Dipl.-Ing. Isabel Hanghofer, BSc

Lithium-ion Dynamics
in
Highly Conductive Solid Electrolytes

Doctoral Thesis

to achieve the university degree of

Doktorin der technischen Wissenschaften (Dr.techn.)

submitted to

Graz University of Technology

Supervisor

Univ.-Prof. Dr. Martin Wilkening

Institute for Chemistry and Technology of Materials

Graz, April 2019

AFFIDAVIT

I declare that I have authored this thesis independently, that I have not used other than the declared sources/resources, and that I have explicitly indicated all material which has been quoted either literally or by content from the sources used. The text document uploaded to TUGRAZonline is identical to the present doctoral thesis.

Place, Date	Signature

EIDESSTATTLICHE ERKLÄRUNG

Ich erkläre an Eides statt, dass ich die vorliegende Arbeit selbstständig verfasst, andere als die angegebenen Quellen/Hilfsmittel nicht benutzt, und die den benutzten Quellen wörtlich und inhaltlich entnommenen Stellen als solche kenntlich gemacht habe. Das in TUGRAZonline hochgeladene Textdokument ist mit der vorliegenden Dissertation identisch.

Ort, Datum	Unterschrift

Das Halbwissen ist siegreicher, als das Ganzwissen: es kennt die Dinge einfacher, als sie sind, und macht daher seine Meinung fasslicher und überzeugender.

— **Friedrich Nietzsche**

Abstract

Driving 900 km, charging in a minute, a dream of all electric car drivers. Solid-state batteries can bring us one step closer to that goal, due to the higher energy denisty in comparison to conventional Li-ion batteries. In addition, the prices of solid-state batteries are significantly lower due to the simplified manufacturing processes and materials. Furthermore, the safety risks of all-solid-state batteries are lower by having a solid electrolyte instead of a flammable, organic liquid electrolyte.

Therefore, the development of efficient, safe and sustainable solid electrolytes is a central task of materials science. The first step is to find a solid electrolyte which is then prepared and further improved. This also requires a fundamental knowledge of different synthesis routes, structural analysis and also Li-ion dynamics, which is indispensable to study solid electrolytes. Promising candidates for solid electrolytes are materials with high ionic conductivity.

The ionic conduction in solids is influenced by defects in the crystal lattice, and also the morphology and the chemical composition of the material. The transport properties of a material can already be improved during the synthesis and by introducing foreign atoms, but also by high-energy ball milling.

In this thesis, Li-ion conductors with high ionic conductivity were prepared by classical synthesis methods, such as solid-state synthesis and/or hydrothermal synthesis. The structures were analyzed by X-ray and neutron powder diffraction as well as high-resolution *magic angle spinning* (MAS) NMR measurements. Ion dynamics, which contain information about jump processes and diffusion parameters, has been studied through impedance spectroscopy and solid-state NMR over a wide temperature-, time- and length-scale.

In $LiZr_2(PO_4)_3$ the ionic motion in the bulk and across were separated and analyzed. By doping with 10% Ca^{2+}, the grain boundary conductivity has been increased by some orders of magnitude. In the case of Li_3OCl, the structure of the compound was resolved, despite the difficulties the metastable material applies. Li_6PS_5X (X: Cl, Br and I) belongs to the Argyrodite-family and is a very promising solid-state electrolyte due to the very high ionic conductivity at room temperature, which is comparable to liquid electrolytes. Structure-property-relationships (including Rietveld refinement) have been studied in detail as well as the Li and P dynamics. All samples are fundamentally different and vary by their Wyckoff site positions and their Li jump processes. For the ordered compound Li_6PS_5I the Li-Li intercage jump is interrupted. Furthermore, the P-dynamics, which describes the rotation of $[PS_4]^{3-}$-tetrahedra and which interacts with the Li diffusion process, was studied for these materials.

In general, this doctoral thesis is structured in three major solid-state electrolyte classes: i) oxidic, ii) halogenated, and iii) sulfidic solid electrolytes. Part of the results have already been published as peer-review articles. Prior to that relevant, theoretical basics as well as short introductions regarding the employed methods are integrated for a better understanding of the subject.

Kurzfassung

900 km fahren, eine Minute aufladen, ein Traum für alle Elektroautofahrer. Eine Möglichkeit dafür ist der Einsatz von Festkörperbatterien, die eine wesentlich höhere Energiedichte erreichen als herkömmliche Lithium-Ionen-Akkumulatoren. Auch sind die Preise der Festkörperbatterien aufgrund der einfacheren Herstellungsprozesse- und Materialen deutlich geringer. Festkörperbatterien, welche einen Festelektrolyten anstelle einer brennbaren, organischen Flüssigkeit beinhalten, bieten außerdem ein höheres Maß an Sicherheit.

Die Entwicklung von leistungsfähigen, sicheren und nachhaltigen Festelektrolyten ist daher eine zentrale Aufgabe der Materialwissenschaft. Um mögliche Festelektrolyte in Li-Ionen-Batterien zu testen, muss zuerst ein möglicher Festelektrolyt gefunden, verbessert beziehungsweise prepariert werden. Dazu gehören eine grundlegende Kenntnisse über mögliche Synthesemethoden, Strukturanalysen sowie die Li-Ionen-Dynamik, welche unentbehrlich ist, um Festelektrolyte zu studieren. Verwendet werden Verbindungen, die eine gute Ionenleitfähigkeit aufweisen und vor allem in einem großem elektrochemischen Fenster stabil sind.

Die Ionenleitung in Festkörpern wird durch Defekte im Kristallgitter ermöglicht, aber auch die Morphologie und die chemische Zusammensetzung spielen eine bedeutende Rolle. Bereits bei der Herstellung werden Materialen so modifiziert, dass sie geeignete Transporteigenschaften aufweisen. Dies kann durch Einbringen von Fremdatomen, aber auch durch Hochenergie-Kugelmahlen erreicht werden. Letzteres erhöht in vielen Fällen den Grad der strukturellen Unordnung in Ionenleitern.

Im Rahmen dieser Dissertation wurden Li-Ionenleiter mit hoher Ionenleitfähigkeit mittels klassischen Synthesemethoden, wie Festkörper-Synthese und/oder Hydrothermal-Synthese, hergestellt und strukturell mit Röngten- sowie Neutronenstrukturanalyse und hochauflösende *magic angle spinning* (MAS)-NMR-Messungen untersucht. Die Ionendynamik der hergestellten Materialien, welche Informationen über Sprungprozesse und Diffusionsparameter liefert, wurde mittels Impedanzspektroskopie sowie Festkörper-NMR über einen großen Temperatur-, Zeit- und Längen-Bereich untersucht.

Bei $LiZr_2(PO_4)_3$ konnte die Ionenbewegung in Bulk und Korngrenzen-Region getrennt und analysiert werden. Durch Einbringen von 10% Ca^{2+} konnte die Korngrenzenleitfähigkeit bei Raumtemperatur um eine Zehnerpotenz erhöht werden. Im Fall von Li_3OCl konnte die Struktur, trotz der Schwierigkeiten, die ein metastabiles Material mit sich bringt, aufgeklärt werden. Li_6PS_5X (X:Cl, Br und I), gehört zur Familie der Argyrodite und ist, aufgrund seiner sehr hohen ionischen Leitfähigkeit, ein sehr vielversprechender Festkörperelektrolyt. Die Ionendynamik und die

Kristallstrukturen (inkl. Rietveld Verfeinerung) wurden im Detail untersucht. Alle drei Verbindungen sind von Grund auf unterschiedlich und unterscheiden sich einerseits hinsichtlich der Wyckoff Besetzung anderseits aber auch durch ihre elementaren Li-Sprungprozesse. Für Li_6PS_5I konnte gezeigt werden, dass aufgrund der geordneten Struktur und der Größe des Anions der Li-Li *intercage*-Sprungprozess unterbrochen ist. Weiters wurde anhand dieser Materialien auch die P-Dynamik genauer studiert, welche die Rotation von $[PS_4]^{3-}$-Tetraedern beschreibt, welche mit dem Li-Diffusionsprozess wechselwirken können.

Im Allgemeinen kann diese Dissertation in drei große Festelektrolytklassen eingeteilt werden: i) oxidische, ii) halogenierte und iii) sulfidische Festelektrolyte. Die Ergebnisse wurden in Form von publizierten Artikeln sowie Manuskripten zusammengefasst.

Acknowledgement

My biggest thank goes to Prof. Dr. Martin Wilkening for giving me the opportunity to write my doctoral thesis at the Institute for Chemistry and Technology of Materials (ICTM) in Graz. I thank him for many helpful advices, for supporting me with his excellent knowledge and the support that I got to develop aside from scientific topics. I highly appreciated that he gave me the opportunity to present my works at international conferences.

I am also grateful for the interesting discussions with Dr. Daniel Rettenwander and the interesting topics he suggested. Since this work is part of the CD-Lab for lithium batteries that is in cooperation with AVL, my gratitude goes to Dr. Volker Hennige and Dr. Marlena Volck for the good collaboration.

I am deeply grateful for the positive working atmosphere on the ICTM and especially in the AGW, the research group. Many thanks go to Stefan Breuer for his instruction and advice with the impedance spectrometer and also to Denise Tapler and Bernhard Gadermaier for the support during the NMR measurements and the fruitful discussions in the office. Special thank also goes to Veronika Pregartner, who has always supported me in preparative work. Further, I want to thank Liane Hochgatterer and Christina Albering for their assistance and the rest of the AGW for the good time together.

Dr. Brigitte Bitschnau and Prof. Dr. Franz Mautner are kindly acknowledged for the XRD measurements and the support for analyzing the diffraction patterns.

I also want to thank all my friends in Styria, Upper Austria and Voralberg for supporting me and always having a friendly ear to me. *Thank you!*

My sincere thank is owned to my family for being with me and helping me all the time and for their special care in every life sitation.

Finally, I express my honest gratitude Michael for being at my side all the time. *Thank you* for your support, your loving attention and for keeping up your good spirits even during stressful time.

Contents

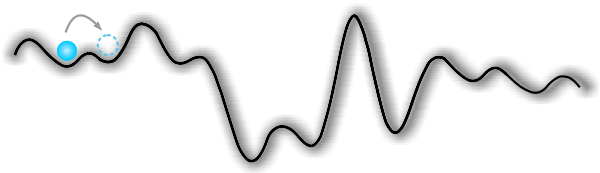

1 Introduction

In today´s world, facing imminent climate change, ever increasing oil prices as it becomes scarce, we are obliged to provide the technological basis for the provision of renewable energy. This implies not only the energy conversion of renewable sources, that is solar, tidal etc., but also, and most importantly, the safe and efficient storage of that energy. Clearly, this has to be achieved in an economic fashion, that is also environmentally benign and sustainable. We find two very different applications for energy storage, stationary and, more familiar to everybody, the mobile sector, as is found in most hand-held devices was well as laptops etc. The latter sector was introduced by the commercialization of the lithium-ion battery by Sony in 1991.[1]

Lithium-ion batteries are used in a wide range of applications including automotive, consumer electronics (like laptops, handys, *etc.*) and also in renewable resources, like solar and wind energy.[2–4] However, commercial available batteries not always satisfy the rigorous and increasing demands of electronic devices, energy storage systems and electric vehicles. Nowadays, batteries require higher energy densities, longer cycle lifetime, acceptable safety levels and lower costs.[4]
In general, the core part of a Li-ion battery is the electrolyte which separates the positive (anode) and negative (cathode) electrode from each other. The electrochemical reaction takes place in the electrodes and the current that is delivered of the battery originates from the chemical reaction in the active materials. In conventional batteries the charge carrier is lithium, that moves through the electrolyte that mainly consist of a lithium salt dissolved in a organic liquid.

In the last hundred years, the research has focused on liquid electrolytes that are used in commercial available batteries. Although, they have high ionic conductivity but they suffer from electrochemical and thermal instabilities and poor safety.[5] To overcome such thermal runaways solid-separators are used in these cells but another more attractive alternative is the usage of a solid electrolyte instead of the liquid electrolyte.[6] Devices with non-flammable ceramic electrolytes have a larger packing density resulting in higher volumetric densities. Therefore, they withstand

higher temperatures and are less sensitive to thermal runaways.[7–10] Solid-state electrolytes have to be improved to have a suitable high ionic conductivity that is comparable to that of liquid electrolytes. Nevertheless, in the recent years, ceramic materials with ionic conductivities in the range of 1 $mS \cdot cm^{-1}$ at room temperature have been reported.[10] Such high ionic conductivities for new solid materials can be reached by different preparation techniques, including a detailed information on the crystal structure.

The aim of this doctoral thesis was to synthesize and characterize new oxide- and sulfide-based solid electrolytes. To understand these materials related to its modifications and structure it is indispensable to study the ion transport. In particular, techniques such as impedance spectroscopy and solid-state nuclear magnetic resonance (NMR) are the methods of choice to investigate lithium ion dynamics and structural behavior.[11] Of course, to synthesize a highly conductive solid electrolyte is not enough. The electrolyte has to be chemically and mechanically stable, compatible with other materials needed for a cell and electrochemically inert to metallic Li.[12] Large-scale production of those materials, and especially the processing of *all-solid-state* batteries will be a challenge for science and industry.

In the course of this work, the well-known sulfide electrolytes Li_6PS_5X (X:Cl, Br, I), the new halide-based electrolyte "Li_3OCl" and oxidic NASICON (*Na super ionic conductor*) electrolytes were characterized and discussed.

The Argyrodite-type Li_6PS_5X (X:Cl, Br, I), which crystallizes in a cubic structure (space group: $F4\bar{3}m$), was characterized and tested in *all-solid-state* batteries (ASSB). The main advantage of Argyrodite electrolytes are their high ionic conductivity as well the low capacitance they can reach. Li_6PS_5Cl can be the electrolyte of choice due to its good processability and stability at high and low temperatures. The impedance measurements result in a very good ionic conductivity for Li_6PS_5Cl and Li_6PS_5Br which are in the range of 10^{-3} to 10^{-2} $S \cdot cm^{-1}$. In contrast, Li_6PS_5I shows a three orders of magnitude lower ionic conductivity at room temperature.[13–18] For all materials, variable-temperature spin-lattice relaxation (SLR) measurements were performed to characterize long- and short-range ion processes in the argyrodite structure.

Another type of solid electrolyte is Li_3OCl that crystallizes in an Anti-perovskite structure. The structural details were untangled *via* X-ray powder diffraction (XRPD) and Neutron powder diffraction (NPD). It was found that "Li_3OCl" is an instable electrolyte that decomposes easily to $LiCl \cdot xH_2O$. Thus, the presence of hydrogen in every compound seems to be responsible for the high ionic conductivity that is sufficient for some applications.

Lithium ion conductors with NASICON structure obeying the general formula $LiM_2(PO_4)_3$ gained interest due to their potential application as solid electrolytes. $LiZr_2(PO_4)_3$ (LZP) shows good ionic conductivities and is stable at air, which makes it an attractive candidate for *all-solid-state* batteries. By doping LZP with Ca^{2+} the grain boundary conductivity can be increased and the rhombohedral phase can be stabilized.

The dissertation is construct into following parts: In the beginning a theoretical part deals with the general principles and the methods, which were used during the thesis. First, the basics of the design of solid electrolytes and the preparation techniques are described (chapter 2). Then it follows with a detailed description of diffusion (chapter 3). XRD and NPD are essential methods (chapter 4) to characterize the solid electrolytes prepared. In chapter 5 the impedance spectroscopy and the NMR measurements are explained in detail. In chapter 6 the results are shown in form of articles that are already published or in form of prepared manuscripts. Finally, a short summary and an outlook is given.

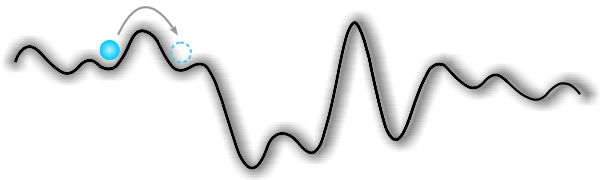

2 Design of Solid Electrolytes

Contents

Solid-state batteries are getting more and more attention to act as candidates for energy storage due to their main advantages in working temperature, safety and energy density in contrast to conventional batteries consisting of liquid electrolyte. Solid-state batteries offer many advantages over conventional liquid-electrolyte-based batteries such as i) the formation of persistent interphases with high cycling stability[19] ii) the possibility of higher power due to the use of metallic Li as anode[20] iii) the transference number is almost unity for Li^+ [21] and iv) the design of multilayer cells that can handled more easily.[22] Despite all this excellent advantages many challenges remain in understanding and manufacturing solid-state batteries. The ionic conductivity, especially for sulfide-based and oxide-based electrolytes, are approaching to those of liquid electrolytes but it has to be mentioned, that a high ionic conductivity is not the only thing that needs to be look at. Lithium dendrites,[23,24] interface stability[25,26] and processing are still obstacles to manufacture solid-state batteries. Additionally, solid-state batteries need a large-scale fabrication at costs that are comparable to that of conventional lithium-ion batteries.

Conventional lithium-ion batteries are made of porous electrodes and a porous separator that is filled with a liquid electrolyte. In contrast, solid-state batteries are made of dense layers, that can be easier handled for large-scale fabrication (see Figure 2.1). Dense layers are suitable for achieving

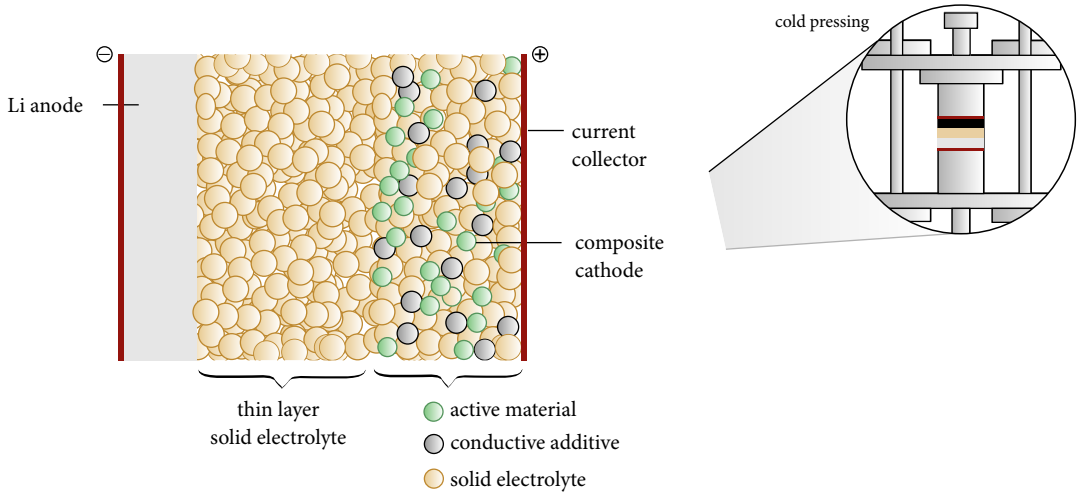

Figure 2.1: Schematic illustration of a solid-state battery fabricated with a ceramic electrolyte, a lithium anode and a composite cathode. The inset shows the cold pressing process used for preparation.

a high volumetric energy density, a good interfacial contact and a fast lithium ion conduction. The cathode of solid-state batteries is in most cases a mixture of the active material, *i.e.* $Li_4Ti_5O_{12}$, TiO_2, graphite, etc., the highly conductive solid electrolyte and a conductive additive (carbon). To avoid volume changes in the active materials a high mechanical strength is necessary.[10,27,28] A dense solid electrolyte is required to avoid Li dendrites and to achieve higher capacities. However, more challenging is to understand the Li dendrite formation, which is preferred along the grain boundaries in porous electrolytes.[26]

The manufacturing of solid-state batteries mainly depends on the mechanical properties of the solid electrolyte. There are three classes of electrolytes that are discussed in that chapter i) sulfide-based, ii) halide-based and iii) oxide-based electrolytes. The solid-state batteries with a sulfide-based solid electrolyte can easily prepared *via* cold pressing and metallic Li as anode can be attached direct to the electrolyte. However, oxidic solid electrolytes show a better mechanical strength and the high sintering temperatures (up to 1000 °C) ensure a good contact between the particles.[29] The main challenge is to achieve a high performance of solid-state cells and to obtain a good contact between the particles within the cathode (includes the active material if Li as anode is used) and between the electrodes and the electrolyte. Moreover, another important aspect is to think of the thickness of the electrolyte.

First, to ensure a good contact between the active material and the solid electrolyte in the cathode solution-processable components have to be used. Especially in the case of sulfide-based solid electrolytes, the electrolyte and the active material are solved in a solution and afterwards the solvent is removed by heat treatment. This results in an good contact and therefore, an efficient

ion transport pathway is obtained contrary to dry electrodes.[30,31] Oxide-based solid electrolytes are known to have a low solubility in many solvents and thus, solid wetting agents are introduced to create a good contact between active material and electrolyte.[27]

Secondly, the contact between the cathode layer and the electrolyte layer is important but often becomes problematic. Sulfides have an excellent deformability and thus, the contact can be achieved through cold-pressing. However, a porous oxide electrolyte can leave gaps between the cathode and the electrolyte layer, resulting in a high interfacial resistance. This can be improved by some advanced sintering techniques, like spark plasma sintering or wetting agent-aided co-sintering or by adding an interlayer between cathode and electrolyte.[32,33]

Third, the solid electrolyte has to be a thin layer to achieve higher specific energy and volumetric energy density. Sulfide-based electrolytes have a smaller mass density (~2 $g \cdot cm^{-3}$) than oxide-based (~5 $g \cdot cm^{-3}$) and hence the break-even thickness is larger for sulfide-based electrolytes. In an all-solid-state battery the thickness of an solid electrolyte should be around 120 μm. Such an thin solid electrolyte can be prepared by coating; mixing a polymer binder, that can be evaporate easily, in the electrolyte. Coating of a solid electrolyte dosed with a binder has been already tried with glassy Li_3PS_4 and results in a layer thickness of 70 μm.[34–36]

To sum up, it is important to prepare a pure, dense and highly conductive solid electrolytes with a relative density $\geq$95%. In the following chapter different preparation methods and different classes of solid electrolytes are described.

2.1 Preparation of Solids

The most famous preparation route to synthesize solids is the classical *solid state reaction* (SSR). Through mixing or milling of solids and further, followed up with an annealing step the desired material can be prepared. It is the most common method due to the good control of purity and composition, and the simple handling, and depending on the milling tool a smaller grain size than in other methods is achieved. Of course there are some disadvantages, like limited homogeneity and high calcination temperatures that result in agglomerations. Therefore, typical other techniques are i) sol-gel method ii) film deposition iii) hydrothermal reactions and iv) crystal growth. In this thesis solid electrolytes were mostly prepared through solid state reactions and hydrothermal reactions so they will be discussed in detail.[37]

2.1.1 Solid State Reaction

A solid state reaction is a reaction between or within solids yielding in a solid product without using solvents. In contrast to a reaction prepared in a solution, solid state reaction occurs within the rigid crystal lattice.[38,39] Therefore, solid state reaction is a good synthesis method for studying the effect of intermolecular forces and the influence on the reaction mechanism. In 1964 Cohen

and Schmidt described the topochemical controlled and the topoactive reaction. Topochemical controlled means that the kinetic features are controlled by the confined environment of the crystal lattice and influences the nature of the product. However, the reaction takes place with a minimum energy and atomic motion requirements. Topoactive reaction is the correlation between the lattice, the product and reactants.[40,41] As already mentioned in the beginning solid state reactions have many advantages over solvent-based reactions referring to the limited formation of side products, no waste (Green chemistry) and higher yields and easier handling for cascade reactions.

In Figure 2.2 the synthesis steps for a classical solid state reaction are shown. The aim of the first steps, like weighing and milling or mixing, is the optimal homogenization of the raw materials to great a good contact between the particles of the different components. Furthermore, after a milling step and a calcination process will follow, *i.e.* a mixture of phases is formed, used for ceramic processing, with a high sintering activity.

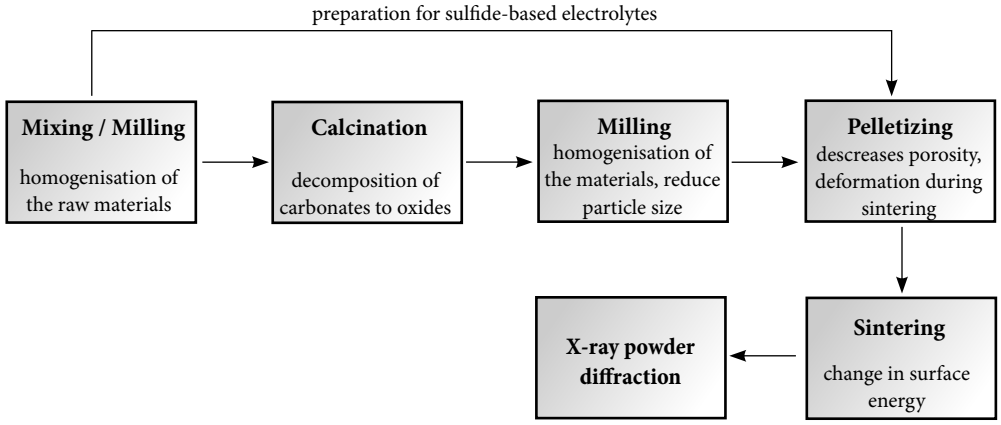

Figure 2.2: Preparation route of a solid state reaction. Calcination and a second milling step is usually used for ceramics that need quite high temperature (up to 1100 °C). Sulfide-based electrolytes were often prepared by milling and pelletizing without the step in between due to the lower sintering temperatures.

Mechanochemistry

Every chemical reaction requires energy to be activated, which is usually introduced in form of heat, light or an electrical potential. When the reaction is caused by absorption of mechanical energy, it is called mechanochemical reaction.[42,43] Besides reducing the particle size in materials mechanochemistry can be also used as independent synthesis. A major advantage of mechanochemical synthesis or a milling step included in the SSR, is the ability to produce nano-crystalline materials that would be inaccessible in conventional manufacturing routes. These compounds include, *i.e.* amorphous phases that would crystallize at higher temperatures or metastable non-equilibrium phases that have a different crystal structure than their thermodynamically more stable modification. Thus, mechanochemistry provides a simple preparation technique.[42]

During the milling process the materials are subjected to mechanical stresses which can have several effects: i) a reduction in particle size and therefore change of the defect structure without

a chemical reaction, ii) the change of chemical structure by means of a chemical reaction, *i.e.* by forming or breaking chemical bonds. However, for a solid state synthesis the reduction of the particle size is the most important step. It describes the structural changes in the materials in macroscopic and microscopic nature. By shearing, frictional or impact forces the small crystals were broken into smaller nanoparticles (<50 nm). Although, a variety of models for the mechanochemical processes can be found in literature but the exact reaction mechanism is not yet clearly defined.[42–45]

In general, the milling process uses two grinding beakers with grinding balls further the materials are filled in an sealed, see Figure 2.3. The grinding tools consist of very durable, hard compounds like zirconia or tungsten carbide that is suitable due to the high mechanical forces. The two milling beakers are fixed on a supporting disk. The contra-rotation of the beakers and the supporting disk lead to an acceleration of the milling balls that they move through the beaker and impact on the opposite side. The resulting centrifugal forces act alternately in the same or in the opposite directions which leads to friction and shear forces during the rotation of the milling balls along the beaker. However, the milling balls move along the milling beaker and crash on the opposite side with very high energy against the crystallites. The energy generated by the mechanical treatment is large enough to split the materials, introduce defects and allow chemical reactions. Depending on the materials and the desired product different settings for the milling process can be used. Important parameters that can be modified are the rotation speed, the number of milling balls or the mass of the materials used.[42–44,46]

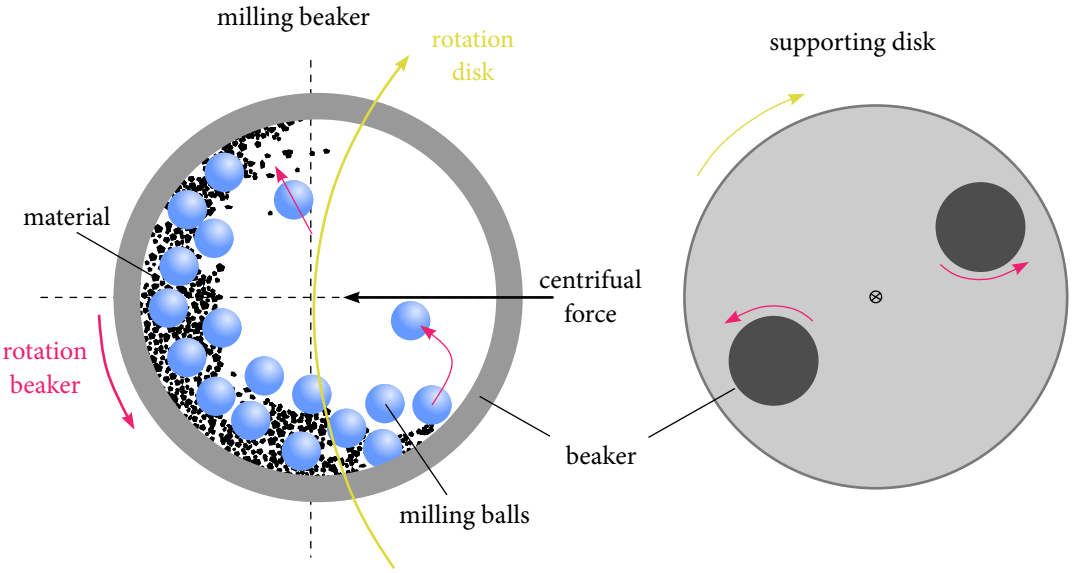

Figure 2.3: Illustration and principle of a planetary ball mill. The arrows indicate the counter rotation of the supporting disk and the beakers. This figure has been adapted from reference 42.

Sintering

Sintering is a technique that is used to combine powder materials together *via* thermal energy (temperature) in combination with mechanical energy (pressure). Many years ago this technique is known well due to the fabrication of pottery and ceramics. During the sintering process two fundamental phenomena occur: densification and grain growth; to understand this phenomena thermodynamics and kinetic have to be understood. For sintering the thermodynamic driving force is a change in the total interfacial surface energy (free surface enthalpy ΔG_s) of the system. In general ΔG_s depends on the grain size and is in the range of J/mol. This can be described as follows

$$\Delta G_s = \Delta(\gamma A) = \Delta\gamma \cdot A + \gamma \cdot \Delta A \tag{2.1}$$

where γ is the specific surface energy and A is the total surface area. The change in surface energy, $\Delta\gamma \cdot A$, results in denisfication and the change in the total surface area, $\gamma \cdot \Delta A$ results in coarsening (grain growth).[47,48]

In general, sintering is divided into solid-state sintering and/or liquid-phase sintering according to the absence or presents of a liquid phase. To choose the correct one, it depends on the desired microstructure and properties of the product. However, the aim of sintering is to produce a dense body and thus, important parameters to change the microstructure are: particle size, sintering temperature, atmosphere, pressure and heating/cooling rate.

Furthermore, solid-state sintering can be subdivided into three linked stages, like initial, intermediate and final stage. In Figure 2.4 the typical densification curve of these stages is shown plotting the sintering time against the relative density. Characteristic for the initial stage is the for-

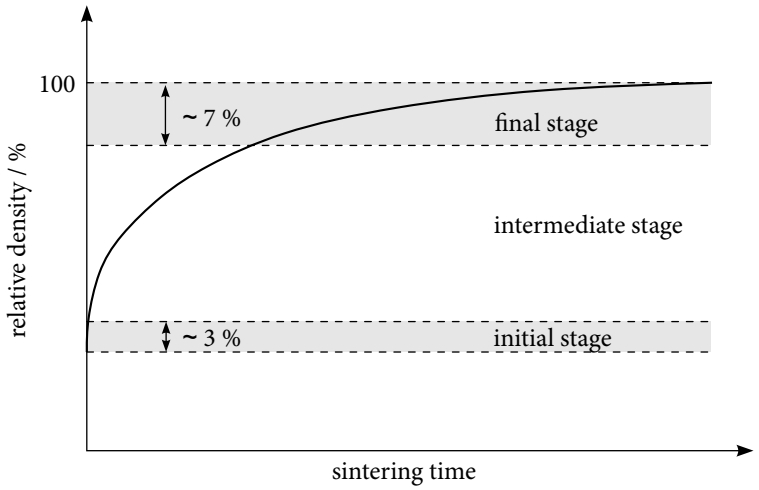

Figure 2.4: Illustration of the three sintering stages. The initial stage indicates the neck formation, the intermediate stage the interconnect pores and the final stage the isolated pores. In the final stage the materials shows a density up to 93 % to the relative density. This figure has been adapted from reference 47.

mation of the necks between particles and a limited shrinkage of 2-3 %. However, the intermediate

stage extend until the formation of isolated pores, which usually occurs up to 93 % of the relative density. Last but no least, the final stage is characterized by full densification of the shrinkage of the isolated pores.[47] To describe these three stages, simpliefied models can be used: two-particle model (initial stage), channel pore (intermediate stage) and the isolated pore model(final stage). All these models exclude grain growth and allow analysis of neck growth and densification.

First, the initial stage of the sintering: the system is idealized as a regular packing of spherical particles with nearly the same size. The sintering of the powders can then be described by two particles in contact with each other (two-particle model). When sintering starts, the material transport occurs form the surface of the particles and/or from grain boundary (g.b.) between the particles to the neck, that is formed between the particles (see Figure 2.5a)). An important

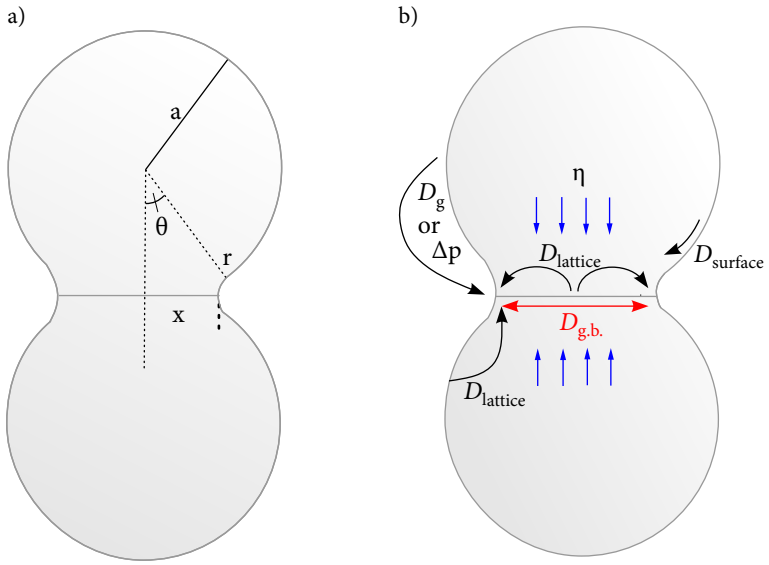

Figure 2.5: Schematic representation of the two-particle moedel for the initial stage sintering. b) Diffusion pathways during sintering. $D_{g.b.}$, D_l, D_b and $D_{surface}$ describe the diffusion coefficients for grain boundary, lattice, gas and surface; η denotes the viscosity.

aspect of sintering is the difference of interface connection of the particle surface (or g.b.) and the neck. Due to the curvature difference, differences in capillary pressure and vacancy concentration come up. Therefore, different mechanisms in material transport occur, whereas the neck growth is the sum of all these mechanisms (see Figure 2.5b)).[48] However, the sintering kinetic depends on the materials that is used and also on the transport mechanisms. If the material source is grain boundary or an viscose flow, the distance between the two particles decreases and therefore, resulting in a shrinkage of the desired material. If the surface is the material source, no shrinkage will be obtained during sintering. The material transport rate from the grain boundary or particle surface to the neck can be described as

$$\frac{dV}{dt} = JAV_m \tag{2.2}$$

where t is the time, V_{m} and A are the volume and the area of the material, J is the material flux. If the material is transported through vacancies, the atom diffusion can be calculated as follows (considering the pressure gradient).[47]

$$J = -\frac{D}{RT}\nabla\sigma = -\frac{D}{RT}(\Delta p)\frac{1}{L} \tag{2.3}$$

$$D = D_0 \cdot \exp^{\frac{E_{\mathrm{a}}}{k_{\mathrm{B}}T}} \tag{2.4}$$

D is the atom diffusion coefficient, $\nabla\sigma$ the sintering stress gradient, p the pressure and L the distance. With equation (2.2) and (2.3) the different sintering mechanism can be calculated. In general there are six different sintering mechanisms:[47,48]

1. lattice diffusion from grain-boundary to neck
2. grain-boundary diffusion from grain boundary to neck
3. viscous flow
4. surface diffusion from particle surface to neck
5. lattice diffusion from particle surface to neck
6. gas-phase transport

Sintering mechanisms 1-3 contribute to the shrinkage, while 4-6 follow redistribution which means no densification but it can affect grain growth in available pores.[47]

2. and 3. or intermediate and final stage: they are the most common one for body-centered-cubic packing. In this theory many assumptions were made but many of them do not take into account the grain boundary as material source. The intermediate stage sintering includes i) lattice diffusion from g.b. to pore and ii) g.b. diffusion from g.b. to pore. The final sintering step obtains grain growth and by increasing the temperature the dominant mechanism of g.b. diffusion changes to lattice diffusion, due to the higher activation energy of the lattice diffusion. At even higher temperatures it can change back to grain boundary diffusion and again back due to the grain growth and coalescence, respectively.[48,49]

The sintering atmosphere is the main property to achieve a good product with high density . It is critical for the densification of the desired product and if the initial size of the pores is large, the maximum density is low due to the decreasing capillary pressure.However, when pore coalescence occurs related to the grain growth the pressure decreases and the porosity is increasing with the sintering time and results in bloating. Therefore, it is important to choose all parameters careful, like temperature, time, pressure, atmosphere, heating and cooling rate.[47,49]

As mentioned in the beginning not only densifictaion is important for sintering also grain growth is a fundamental phenomena during sintering. The driving force is the differences in

capillary pressure of neighboring grains, that can be described *via* boundary energy γ_b and the radius curvature R_o of the boundary. In general there are two types of grain growth, normal and non-normal grain growth. Non-normal can be described by very fine and very large grains, while normal grain growth consists of similar grain sizes (dependence on the annealing time). The latter is the result of boundary migration that is linked with the mobility, which is the main driving force during grain growth. Another example for non-normal grain growth can be the presence of a second phase particle[50,51] or impurities.[52] Additional literature on sintering, sinter activity and grain growth is available in the references 47–49.

2.1.2 Hydrothermal Synthesis

Hydrothermal synthesis is a process were materials can crystallize in an aqueous media direct at elevated temperatures (T > 25 °C) and a defined pressure (p >100 kPa). The reactants that are used in such synthesis conditions are named ”precursors” and ”feedstocks” and can be reacted in form of solutions, gels or suspensions. Hydrothermal synthesis is mostly done in closed vessels, that are called autoclaves (see Figure 2.6) at autogeneous pressure, which corresponds to the saturated vapor pressure of the solution at a specific temperature and composition of the hydrothermal system. Typical conditions for ceramic powders are: a pressure below 30 MPa and a temperature below 400 °C.[48,53] In general, in ceramics synthesis routes chemical reactivity and the mass

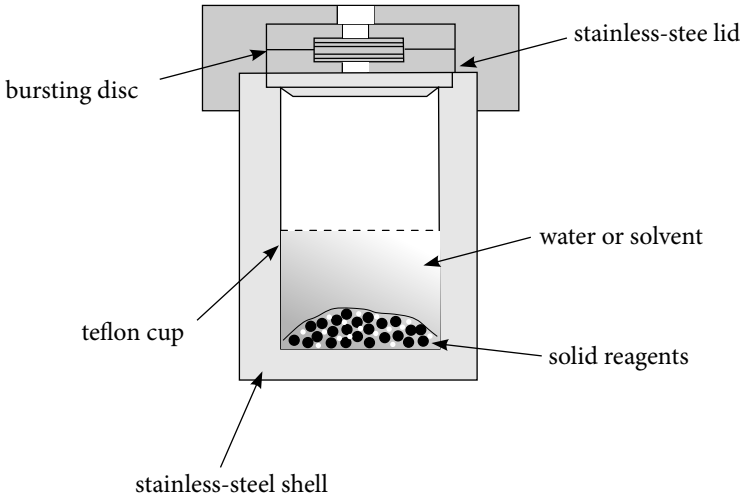

Figure 2.6: Schematic diagram of a autoclave setup used for hydrothermal synthesis of solids.

transport during the reaction are important. In contrast to the classical solid-state reaction the diffusion coefficients for hydrothermal synthesis are several order of magnitude higher. Sluggish diffusion is a reason why for solid-state synthesis high temperatures (T > 1100 °C) are required and therefore, often generates inhomogeneous products.[54]

In the 1980s and 1990s first materials were synthesized hydrothermally and are in most cases oxide-based materials, like $BaTiO_3$, $SrTiO_3$, $LiNbO_3$, etc.[48,55] Meanwhile, this technique is well

suited for pure elements (Si, Ge, Ni, diamond), fluorides (LaF_3, LaF_2), sulfides (CuS, PbS, $PbSnS_3$ and arsenides (InAs, GaAs). The main advantage of this synthesis method is that the powders can be produced with controlled physical and chemical characteristics. The positive attributes of hydrothermal reacted materials are i) the controlled particle size and low degrees of agglomeration and aggregation, ii) controlled particle morphology and iii) direct fabrication of ceramics.[48] For further information about hydrothermal reactions see reference 54 and 55.

In the next sections classes of solid electrolytes are discussed, that were either prepared by solid-state reaction or by hydrothermal synthesis.

2.2 Oxide-based Solid Electrolytes

In the last several years, batteries using a Li anode gain more interest for Li-ion batteries due to the low weight of 6.49 g mol^{-1}, the higher cell voltages and energy densities. Furthermore, Li metal can be handled easier than other alkali metals at room temperature (RT). However, compared to liquid electrolytes, solid electrolytes do not offer problems with corrosion, leakage and evaporation, prevent internal short circuit because of the direct contact with the electrodes with the electrolyte. A ceramic material is used as a solid electrolyte because it should entail a high Li-ion conductivity at RT ($> 10^{-4}$ S cm^{-1}), a negligible low electronic conductivity and a wide electrochemical stability window. Furthermore, it has to be considered that they are stable at high temperatures, have good mechanical properties, show a easier processability and lower costs. When Li metal is used as electrode, it has to be assumed that oxide-based solid electrolytes are stable against it.[56] Taking into account all these properties, oxide-based electrolytes would be a attractive candidate for a solid electrolyte in ASSB.

In general, oxide-based electrolytes can be divided into two groups: i) crystalline and ii) amorphous or glassy materials. The latter have a chemical formula of Li_2O-MO_x (M: Si, Ge, B, P), a highly disordered structure and are formed by network former oxides, *i.e.* SiO_2, B_2O_3, P_2O_5 and the network modifier, *i.e.* Li_2O.[57,58] In 1966 the glassy composition Li_2O-SiO_2-B_2O_3 has been reported with a ionic conductivity of $> 10^{-4}$ S cm^{-1} and a negligible low electronic conductivity. However, the low resistance and corrosive grain boundary and the thin-layer fabrication makes them to an attractive electrolyte.[59] To achieve higher ionic conductivities it was tried to increase the Li_2O concentration or add some lithium salts. Furthermore, the preparation of electrolytes without the network former were tried but the ionic conductivity did not increase. Thus, this type of material is an ideal candidate for thin layered electrolytes.[56,60,61] Another remarkable amorphous/glass oxide electrolyte is $Li_xPO_yN_z$ (LiPON), that has been first discussed in 1992. The nitrogen within Li_2O-P_2O_5 improves the chemical stability and its physical properties. However, LiPON also has a wide electrochemical window (up to 5.5 V vs. Li^+/Li), a higher ionic conductivity and better stability than other glassy oxides.[61]

In the last view years, crystalline oxide materials gained increasing interest due to their significant high ionic conductivity. The first studied crystalline oxide materials include Li_2SO_4-type materials. Another class are antifluorite-type materials[62], *i.e.* Li_5AlO_4, Li_6ZnO_4 and Li_5GaO_4, Li_2WO_4, Li_2CO_3-based materials, and γ-Li_3PO_4 type materials, which include the well-known LISICON[63] (Li Super Ionic Conductor) materials. These materials have a very simple crystal structure although, they can only reach high ionic conductivities at quiet high temperatures. The highest Li-ion conductivity was reported for $Li_{3.6}Ge_{0.6}V_{0.4}O_4$ with 5×10^{-5} S cm^{-1}.[64] This can be described by the strong Li-O bond. Furthermore, to circumvent the strong bond of O^{2-} and to increase the conductivity, it is bonded to four cations resulting in a $[PO_4]^{-3}$, which has fully occupied sp^3 orbitals. NASICON (Na Super Ionic Conductor) also belongs to the family of crystalline solid electrolytes and became interesting due to its 3D framework, with initials space, where Na or the Li can move through caused by the low energy barrier. Thereofore, conductivities up to 10^{-4} S cm^{-1} can be found resulting in a new level of oxide-based electrolytes. In the following table important oxide based solid electrolytes are shown. (see Table 2.1).[56,65]

Table 2.1: Summary of some selected oxid-based solid electrolytes; ionic conductivity σ_{RT}, activation energy E_a and type of the electrolyte is listed.

Sample	σ_{RT} / S cm^{-1}	E_a / eV	type of electrolyte	reference
Li_2O-MO_x	10^{-8} – 10^{-6}	> 0.50	glass	56
$LiTaO_3$	7×10^{-6}	0.38 eV	Perovskite	66
LISICON	10^{-7}	0.73 eV	γ-Li_3PO_4	67, 68
LiPON	2×10^{-6}	0.55 eV	amorphous	56, 69
$Li_{1.3}Al_{0.3}Ti_{1.7}(PO_4)_3$	3×10^{-3} (bulk)	0.20 eV	NASICON	70
$Li_{1.4}Ca_{0.2}Zr_{1.8}(PO_4)_3$	5×10^{-4} (bulk)	0.42 eV	NASICON	71
$Li_{0.34}La_{0.56}TiO_3$	1.5×10^{-3} (bulk)	0.33 eV	Perovskite	72
$Li_7La_3Zr_2O_{12}$	5×10^{-3} (bulk)	0.33 eV	Garnet	73

In the following subsection the NASICON-type of oxide solid electrolytes are discussed in more detail. The focus is on the applications of oxide solid electrolytes as well how to improve the ionic conductivity and the fabrication of ASSB.

2.2.1 NASICON-type electrolyte

The typical NASICON (Na Super Ionic Conductor) has a space group of $R\bar{3}c$ and crystallizes in a rhombohedral structure, as seen in Figure 2.7. The corresponding lithium NASICON material, shown in Figure 2.7 has the general formula of $LiM_2(PO_4)_3$() . In this structure there are two types of polyeder: i) MO_6 octahedra and ii) PO_4 tetrahedra. Both are linked together via corners and form the $[M_2(PO_4)_3]^-$ framework. The whole framework is stabilized by the electrons of the Li-ions, that are located between MO_6 octahedra (A1 site) as shown in Figure 2.7 b). The distorted octahedral coordinated Li can go into an A2 site, that is between the connection of a PO_4 tetrahedra with three MO_6 octahedra. If A1 and A2 are connected, they form a 3D tunnel for the transport process of the Li.

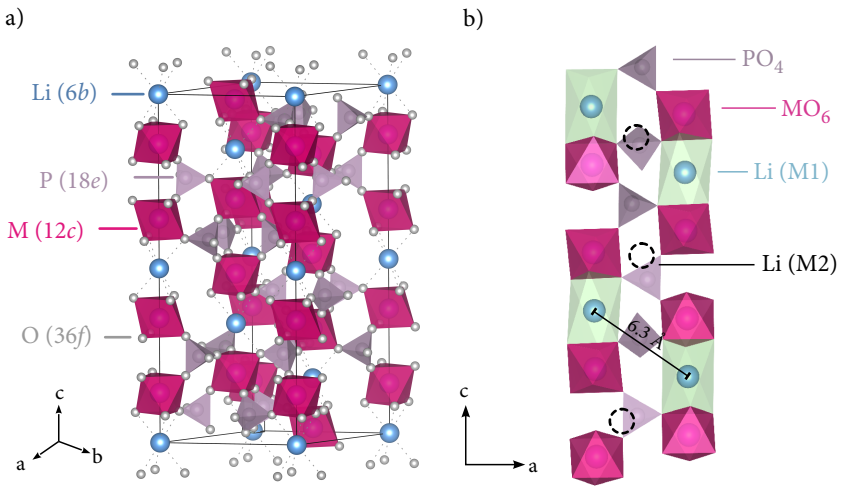

Figure 2.7: Illustration of the NASICON structure $LiM_2(PO_4)_3$ in a) 3D and b) 2D. The purple polyhedra represent the PO_4^{3-} tetrahedra and the pink one the MO_6 octahedra. The Li-ions are octahedrally coordinated between the MO_6 octahedra. In b) the interstitials of the Li are marked in black.

In 1975 Goodenough *et al.* reported a total ion conductivity of 10^{-3} S cm^{-1} on $Na_{1+x}Zr_2Si_xP_{3-x}$. However, Na in the $[Zr_2(PO_4)_3]^-$ framework instead of Li results in a much lower ionic conductivity due to the change in crystal structure at room temperature (rhombohedral – triclinic).[74] Nearly the same results were found for a NASICON framework with M = Sn but the phase transition from triclinic to rhombohedral shifts to lower temperatures.[75] Furthermore, the ionic radii of the M-site (Ge, Zr, Ti and Sn) leads to very small activation energies but the total ionic conductivity is ranging from 10^{-7}-10^{-5} S cm^{-1}. In NASICON materials the low ionic conductivity can be described through the poor sinterability of these ceramics and thus a high porosity.[76]

Substitution of the M^{4+} have been proved to obtain a higher ionic conductivity and a stable rhombohedral crystal structure at room temperature. The highest ionic conductivity was achieved with the Al-substituted $LiTi_2(PO_4)_3$ (LTP). $Li_{1.3}Al_{0.3}Ti_{1.7}(PO_4)_3$ (LATP) results in a total ionic conductivity of 7×10^{-4} S cm^{-1} and a bulk ionic conductivity of 3×10^{-3} S cm^{-1}, which is explained through the better porosity. The improved ionic conductivity can be described through the better porosity in substituted materials and associates increasing grain boundary conductivity.[77] The bulk ionic conductivity is not affected by doping with Al of LTP.

Furthermore, preparation techniques have to be elected careful for NASICON materials. Glass-ceramic processing and wet-chemical synthesis distinguish to be more effective than the classic solid state reaction. For example $Li_{1+x}Al_xGe_{2-x}(PO_4)_3$ (LAGP) prepared through sol-gel method reaches a total ionic conductivity of 1×10^{-3} S cm^{-1} while LAGP prepared through a conventional solid-state reaction results in 6.67×10^{-4} S cm^{-1}.[78,79]

However, the LTP-based oxide electrolytes are good candidates to be used for an ASSB but the obstacle is the reduction of Ti^{4+} ions at a potential below 2.5 V vs Li^+/Li. Therefore, instead of Ti^{4+} the more stable Zr^{4+} can be used that results in $LiZr_2(PO_4)_3$. $LiZr_2(PO_4)_3$ crystallizes in a

rhombohedral structure which can be stabilized by doping, with Y^{3+} or Ca^{2+}, and this affects the ionic conductivity, which increases to values in the order of 10^{-5} - 10^{-4} S cm^{-1}. LZP as well the doped LZP were prepared by a conventional solid-state reaction and spark plasma sintering (SPS) resulting with the same ionic conductivity, which contradicts the statement before.

2.3 Halide-based Solid Electrolytes

In this section the characteristics of halide-based solid electrolytes will be discussed including advantages and disadvantages of these kind of electrolyte. In general, halide-based solid electrolytes can be divided into four different groups: copper, silver, lithium and halide ion conductors.[80] The main advantages of halide-based solid electrolytes in contrast to sulfide and oxide based are the better stability against metallic Li as well the good mechanical strength and mechanical flexibility. However, the air sensitivity, the low oxidation voltage and conductivity is a major drawback of these materials.[81] In this section the focus is on silver and lithium ion conducting solid electrolytes.

One of the most promising candidate of halide-based solid electrolytes is $RbAg_4I_5$ which shows the highest low temperature ionic conductivity 0.27 S cm^{-1}. Therefore, it is an perfect Ag^+ ion conductor. However, the problem of $RbAg_4I_5$ is the low decomposition voltage and the thermodynamical instability above room temperature. $RbAg_4I_5$ is used as a model system to study an Ag^+ solid electrolytes showing a Ag^+ ion transport which is close to unity.[80] In general silver halide electrolytes reach an ionic conductivity of 10^{-6} S cm^{-1} at room temperature, which is not as high as it is suitable for ASSB. However, the ionic conductivity have been improved by addition of additives, *i.e.* Ag_2S to AgCl, resulting in a 5 times higher ionic conductivity. Besides $RbAg_4I_5$, Ag_3SI is another well-known silver containing solid electrolyte, that has been prepared through the mixture of Ag_2S and AgI followed by heat treatment. This highly conductive electrolyte crystallizes in a cubic crystal structure and undergoes many phase transition from α to β to γ phase. The α phase has an order of magnitude higher ionic conductivity than the β phase, due to the increase of the cell volume (decrease in carrier concentration) and the carrier in a unit cell remains the same. Therefore, to increase the ionic conductivity, the Ag^+ ion transport must increase significantly. The quite high difference in ionic conductivity can be described by the anion disorder of the octahedral sites for the Ag^+ ions that occurs in the α phase.[80,82]

Lithium iodide LiI is the most conductive (10^{-7} S cm^{-1})[80] lithium halide at 25 °C and has been utilized in all-solid-state batteries. In Table 2.2 the ionic conductivities of the other lithium halides are shown. In 1971 Schlaikjer *et al.* increases the ionic conductivity by substitution of LiI with a small amount of lithium. The new structure shows an increasing amount of Schottky defects which means an increased number of cation vacancies and as consequence remains a higher ionic conductivity. Doping with Ca^{2+} results in a conductivity of 1.2×10^{-5} S cm^{-1} at room temperature.[83] Liang *et al.* reported an increase of ionic conductivity in LiI, by preparing

Table 2.2: Specific ionic conductivity of lithium halides LiX (X: Cl, Br, I, F) at room temperature[80]

Sample	$\widehat{\sigma}_{RT}$ / S cm^{-1}
LiF	10^{-13}
LiCl	5×10^{-10}
LiBr	2×10^{-9}
LiI	1×10^{-7}

a solid mixture of LiI and Al_2O_3 which results in 1×10^{-5} S cm^{-1}.[84] However, the potential of LiI is limited to 2.8 V vs Li.

Furthermore, a new halide lithium containing solid electrolyte is Li_2ZnI_4. Maekawa *et al.* descirbed the synthesis and the ion dynamics in Li_2ZnI_4 which was used for the fabrication of mesoporous-Al_2O_3. The dc ionic conductivity for (1-*x*)$LiZn_{0.5}I_2$-*x* mesoporous Al_2O_3 with different x were measured. The highest conductivity was achieved for x=0.54 which is 50 times higher than that of pure Li_2ZnI_4 ($\sim 5\times10^{-3}$ S cm^{-1}).

Lithium-rich Anti-perovskites (LiRAPs), such as Li_3OCl and $Li_2(OH)Cl$, are hyped electrolytes due to their great performance in ASSB. They have gained a lot of interest in the last several years due to their highest reported ionic conductivity for a solid oxide electrolyte (2.5×10^{-2} S cm^{-1} at room temperature). Many studies have reported the properties of LiRAPs, but many questions remain unanswered. However, the main question is, does this structure really exist? Lü *et al.* demonstrated the feasibility of Li_3OCl and showed a discharge capacity of 120 mAh g^{-1} and a charge efficiency of 95 %. Therefore, this kind of solid electrolyte will open a new avenue for the development of all solid-state batteries (ASSB).[85]

2.3.1 Anti-perovskite-type Electrolyte

The Anti-perovskite family of compounds show an ideal model to explore the impact of the lattice distortion on ion mobility. The lattice distortion in Anti-perovskites can be changed *via* substitution. The relative simple structure leads to a comprehensive characterization of ion mobility. The disortion in the lattice can correlate with the thermodynamic stability of Anti-perovskites.[86] The degree of lattice distortion, taking into account the general formula of A_3BX, can be calculated through the Goldschmidt tolerance factor[87]:

$$t = \frac{R_A + R_X}{\sqrt{2}(R_A + R_B)} \tag{2.5}$$

where R_A is the radius of the cation X, R_X refers to the halogen and R_B refers to an anion in the octahedron center. If *t* is 1 the ions are ordered perfectly, resulting in perfect symmetry of the cubic structure. The Anti-perovskite (A_3BX) crystallizes in a cubic structure with a $Pm\bar{3}m$ space group. X and B are the anions and A is the cation, where A and X are cubic close-packed layers with octahedral interstices occupied by the B ions. In Figure 2.8 a) the ideal Anti-perovskite structure

is pointed out, which results with a $t \geq 0.83$. If the Goldschmidt tolerance factor is between 0.74 and 0.81 an quasi-orthorhombic structure is achieved with a tilted octahedra while a tilted and distorted octahedra results if $t \leq 0.71$ (see Figure 2.8 b) and c)).[88]

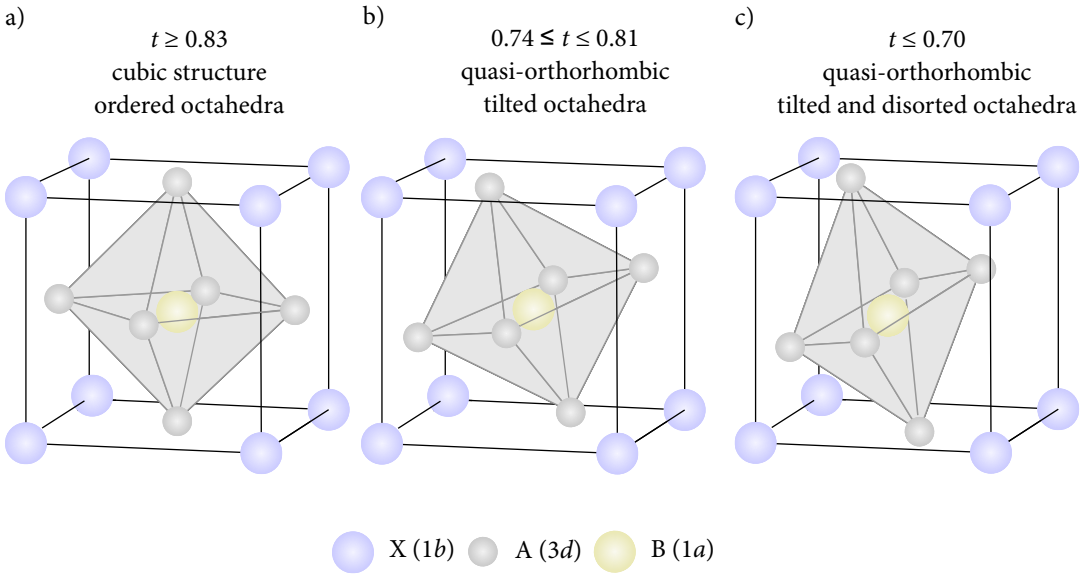

Figure 2.8: The crystal structure of a cubic Anti-perovskite (space group: $Pm\bar{3}m$) A_3BX. The A ion (gray) forms octahedra with the X ion (blue), which occupies the body centered site. The B ion (yellow) occupies the corner sites. a) is the perfect ordered cubic structure, b) a quasi-orthorhombic structure with a tilted octahedra and c) shows a tilted and disorted octahedra.

Examples for Anti-perovskites are A_3OCl (A=Li, Na) and $Li_2(OH)Cl$.[77,89–91] Hippler *et al.* first described the cubic Anti-perovskite Na_3OCl which has a corner-sharing $[ONa_6]$ octahedra with cavities filled by large chloride anions.[92] Li_3OCl gained great attention as a new class of solid electrolytes due to higher energy density and higher ionic conductivities. However, the investigation of energy densities and ionic conductivities are important but it is also crucible to analyze the phase behavior. The lithium-rich anti-perovskites (LiRAPs) belong to the LiOH-LiCl phase system that is the best studied one. The question remaining is does the structure Li_3OCl really exist?[93] Zhao *et al.* reported the synthesis of Li_3OCl through a solid-state reaction of LiOH and LiCl. However, taking a close look on the X-ray powder diffraction (XRPD) data LiCl is present and the differential scanning calorimetry (DSC) shows a phase transition at 40 °C which corresponds to the same of $Li_2(OH)Cl$. Furthermore, it is hard to distinguish Li_3OCl from $Li_2(OH)Cl$ with XRD, due to the similar lattice constant and the poor detection of Li and H. They reached an ionic conductivity of 8.8×10^{-4} S cm^{-1}.[94] It has to be noticed that the same ionic conductivity was measured for $Li_2(OH)Cl$ by Song *et al.*.[95]

2.4 Sulfide-based Solid Electrolytes

Low ionic conductivities of many solid electrolytes hinder the performance of all-solid-state battery. The class of sulfide solid electrolytes opens a new door because of the high ionic conduc-

tivities which are close to that of liquid electrolytes. In general, sulfide solid electrolytes can be divided into following groups: i) glass, ii) glass-ceramic and iii) crystalline electrolytes. The latter demonstrates ionic conductivities in the range of liquid electrolytes. ASSB with a sulfide solid electrolyte offers a higher volumetric and specific energy density that is needed for electric vehicle applications. The mechanical properties, the low-temperature processing as well the nature of the polarizable sulfur anion are the main advantages of sulfur-based solid electrolytes. Additionally, the radius of the sulfur anion is bigger than that of the oxygen which can lead to a larger migration tunnel for Li-ions. As a result they exhibit an ionic conductivity in the range of 10^{-4}-10^{-3} S cm^{-1} at 25 °C. The main drawback of sulfides, used as solid electrolytes, is the smaller electrochemical stability in contrast to other solid electrolytes. However, depending on the degradation products, the solid electrolyte interface (SEI) formed can be passivating. The higher lithiation potentials by using Li-alloy anodes (Li-In) and Li_2S as cathode, avoid degradation of sulfide electrolytes.[96–99]

The first materials that were investigated for lithium-ion conductors were sulfide glasses because of the absence of crystallographic pathways and the absence of grains in the material which eliminates the grain boundary (g.b.) resistance.The absence of g.b. resistance leads to higher ionic conductivities compared to crystalline materials with the same composition.[10,100] The wide range of glass formers makes sulfide glasses attractive. Li_2S is a typical network former and the corresponding modifier can be B_2S_3, P_2S_5 and GeS_2. However, adding a lithium salt can increase the ionic conductivity even more, *i.e.* $Li_2S{-}B_2S_3{-}LiI$ that reaches a value of 1.7×10^{-3} S cm^{-1}.[101] However, the use of lithium salts and the associated decomposition decreases the electrochemical window of this materials but the addition of lithium phosphate or lithium silicates can prevent the debasement.[102] Sulfide-glasses have low preparation temperature and cold pressing creates a good contact between the particles (resulting in a good density). Highly conductive sulfide-glasses can be achieved by modifying the milling parameters.[99]

Another class of sulfide electrolytes are the glass-ceramics, that in general show a lower ionic conductivity. However, the partial crystallization of some glasses results in a higher conductivity, due to the mixture of crystalline and amorphous constituents. Therefore, it was found that an superionic phase is within the glass that can diffuse through the material and the pathway can be maintained through connection of the amorphous region. Sulfide glass-ceramics can be easily prepared through high energy ball milling where the energy in the milling beakers is high enough to locally melt and recrystallize the material.[99,103] The best studied an well-known glass-ceramics is the mixture of xLi_2S-(100-x)P_2S_5 (mol%) which results in more and less conductive compounds. If x < 70 mol% the resulting compounds are $Li_4P_2S_6$ or Li_3PS_4 and they will show a low ionic conductivity.[103] For $x \geq 70$ mol% $Li_7P_3S_{11}$ and $Li_{3.25}P_{0.95}S_4$ result that have a significantly higher ionic conductivity compared to the others (10^{-3} S cm^{-1}).[98,99,104–106]

Finally, the last class of sulfide solid electrolytes are the crystalline one. In principle, crystalline materials that have a well-defined conduction pathway of Li-ion transport show a higher ionic

conductivity than the amorphous materials. $Li_{1.4}Zn(GeO_4)_4$ (Lithium Superionic Conductor = LISICON) is built up of LiO_4, ZnO_4, GeO_4 tetrahedra that are arranged in the γ-Li_3PO_4 structure. The ionic conductivity at room temperature reaches a value of 10^{-7} S cm^{-1}.[68] The maximum conductivity in the thio-LISICON family can reach a value of 10^{-3} S cm^{-1}, *i.e.* $Li_{3.25}Si_{0.25}P_{0.75}S_4$.[107] Another well-known and highly conductive solid electrolyte is $Li_{10}GeP_2S_{12}$ (LGPS); it was the first electrolyte that has a "liquide-like" ionic conductivity of 12 mS cm^{-1} at room temperature. The superionic conductivity in sulfide electrolytes can be described by the arrangement of the anions within the structure. The structure mostly consists of polyhedra connected by ligands in various coordination's and metal ions are used to build up this framework. Li-ions are found either fourfold or sixfold coordinated and thus, are stable in tetrahedral and octahedral sites within the framework. LGPS and β-Li_3PS_4 are assigned to the bcc sublattice, which is an explanation for the high ionic conductivity. γ-Li_3PS_4 and Li_4GeS_4 have a hcp and fcc sublattice which is a motive for the lower ionic conductivity.[99,108] The superionic conductivity in solids can also be investigated in materials without a bcc sublattice, *i.e.* Argyrodite family Li_6PS_5X (X: Cl and Br)[18], $Li_7Ge_3PS_{12}$[109] and Na_3PS_4[110].

The electrochemical stability of an electrolyte is an important consideration for maximizing the energy density of a lithium battery. As early measurements show, sulfide solid electrolytes have a remarkable stability *versus* Li (0 to > 5 V). However, cycling half or full cells over a long time with classical electrodes results in a large cell resistance that leads to a device failure. There are many theories that explain the increasing resistance: i) poor interfacial contact between electrodes and electrolyte, ii) chemical reaction of the components and iii) formation of a space charge layer that hinders the Li-ion diffusion. The decomposition products of most sulfide solid electrolytes are electrochemically active which aggravated the preparation and characterization of solid-state cells. Furthermore, it is also important to identify the SEI products of the electrolytes and their reaction with anode and cathode.[99]

2.4.1 Argyrodites

Lithium Argyrodites are a new and promising class of sulfide-based solid electrolytes. They become more and more important due to the high intrinsic Li-ion conductivity and the stablility within a large (1 V to 5 V) electrochemical window and also the low costs of the starting materials are attractive. Furthermore, in case of lithium Argyrodites cation and anion exchange makes them flexible, that gives an access to many different materials.[16,18,97]

The "parent" Argyrodite component with the general formula Li_7PS_6 crystallizes in a cubic (high-temperature) and an orthorhombic (low-temperature) structure. In general, a mixture of both phases is prepared which results in an ionic conductivity in the order of 10^{-6} S cm^{-1}. The desired cubic structure can be stabilized by substitution with a halogen and thus resulting in an ionic conductivity in the order of 10^{-3} S cm^{-1}. In Li_6PS_5X (X:Cl, Br and I) the ion transport

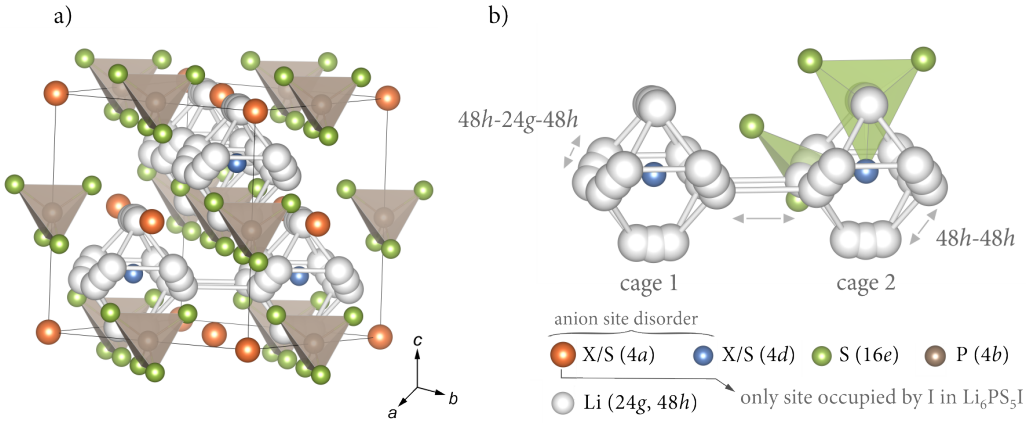

Figure 2.9: a) Cubic crystal structure of the argyrodite-type Li_6PS_5X (X:Cl, Br, I). In the perfect order structure the X^- anions form a cubic close packed lattice with PS_4^{3-} tetrahedra and the Li-ions are coordinated octahedrally. Half of the tetrahedral holes are filled with S^{2-} (4*d*) anions and are placed in the middle of the Li octahedra. b) The two different Li positions form two cages (cage 1 and cage 2) in that three different jump processes can occur: i) 48*h*-24*g*-48*h*, ii) 48*h*-48*h* and iii) cage 1 - cage 2. The jump process between the cages is the diffusion pathway that is responsible for the 3D long-range process.

is determined by the arrangement of the PS_4^{3-} tetrahedra while larger halides result in an ordered structure, see Figure 2.9. Interestingly, Li_6PS_5Br and Li_6PS_5Cl offer an ionic conductivity in the mS cm^{-1} range at room temperature, whereas that of Li_6PS_5I is some orders of magnitudes lower. Deiseroth *et al.* discussed the synthesis of Li_6PS_5X (X:Cl, Br, I) and characterized the long-range diffusion pathways with NMR as well the structure with XRD.[111] Three years later Rao *et al.* reported the first synthesis via ball milling with ethanol.[17] Rayavaruapu and co-workers showed the disorder in structures, especially the site disorder of the anions that promotes the Li conductivity.[18] Over the last decades a large number of studies have been carried out and the ionic conductivity varies from 10^{-7} S cm^{-1} to 10^{-2} S cm^{-1}, while the highest values are found for Cl- and Br-containing Argyrodites and the activation energies are in the range from 0.11 eV to 0.57 eV.[16,18,111] The size mismatch of the halogens, the substitutional disorder in the crystal structure and polarizability of the halogen anion can explain the difference in ionic conductivity of Li_6PS_5X (X: Cl and Br) to Li_6PS_5I.

Comparing all the results of Argyrodites, Li_6PS_5Cl is a good canidate as solid electrolyte for Li-ion batteries either of its high ionic conductivity and the good processability. However, Li_6PS_5Cl shows some interface reactivity towards electrolyte, especially it decomposes in contact with metallic Li. Auvergniot *et al.* cycled $LiCoO_2|Li_6PS_5Cl|Li_4Ti_5O_{12}$ and show that the negative electrode material remains the same after cycling and that the Argyrodite undergoes no chemical reaction or electrochemical degradation in the electrode, but in the positive electrode it decomposes into LiCl, P_2S_5 and polysulfides.[112] In this thesis we focused on the Li ion dynamics of this materials and found out that the diffusion of Li_6PS_5I is almost identical to its relatives (see chapter 6.3.1).

2.5 Other Classes of Solid Electrolytes and Important Facts

Besides oxide, halide and sulfide-based solid electrolytes there are some other important classes, *i.e.* hyrdide ($LiBH_4$, $LiBH_4$-$LiNH_2$, Li_3AlH_6 and Li_2NH), borate ($Li_2B_4O_7$) and polymer based electrolytes. However, in Figure 2.9 the main advantages and disadvantages of the different Li-ion solid electrolyte materials are shown. ASSB have been pursued for many years and have

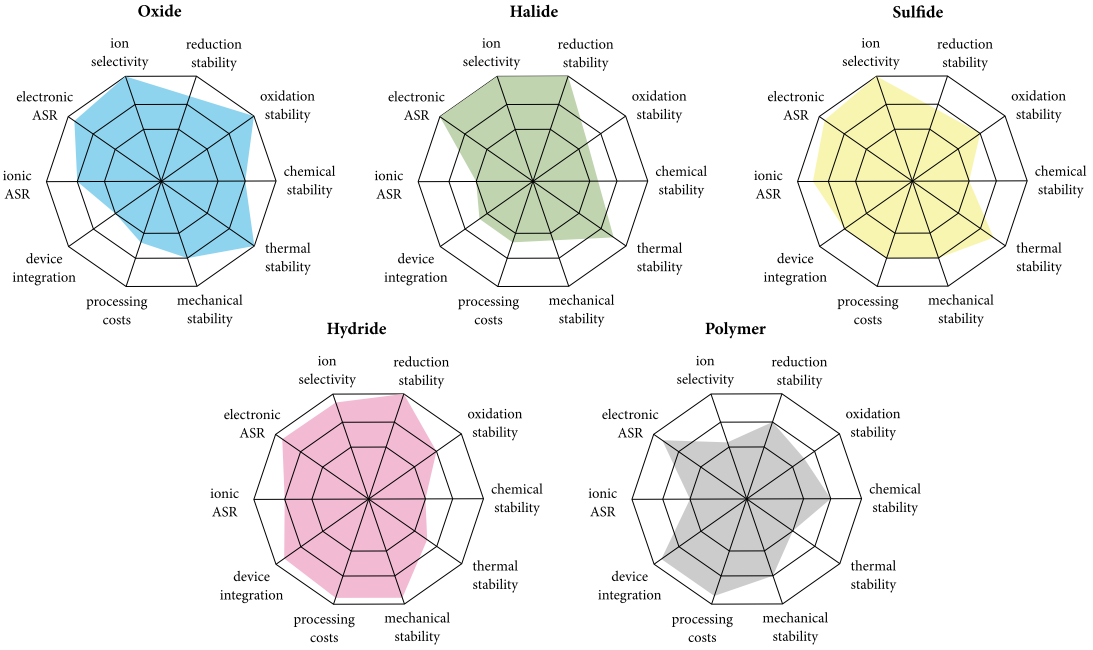

Figure 2.10: Radar plots of the different solid electrolyte classes: i) oxides (blue), ii) halides (green), iii) sulfides (yellow), iv) hydrides (pink) and v) polymer (gray). ASR means area-specific resistance. Illustration according to reference 6.

several important advantages over commercial Li-ion batteries containing a liquid, organic electrolyte. However, for all-solid state batteries with an inorganic solid electrolyte key challenges remain, such as volume change in the electrodes, flexible concerns, interfacial resistance and poor cycling stability. Solid polymer electrolytes can overcome this limitations due to their better flexibility and better contact with the electrodes. However, they have a low ionic conductivity at ambient temperature and a narrow electrochemical stability window. In contrast to liquid electrolytes, solid electrolytes can avoid the issue of high charge-transfer resistance which do not allow large scale battery systems but enable new battery chemistry that were impossible because of the chemical crossover.[6,12]

Batteries based on solid electrolytes show possibilities for electrical vehicles and grid energy storage. The transfer from the laboratory scale to industry requires intensive and systematic research: electrodes, electrolytes, electrode/electrolyte interface and also cell design. Achieving solid materials with high ionic conductivity, good mechanical properties and to overcome the large charge transfer resistance are the main challenges. Additionally, the cost of the production

of a large-scale production have to be low. Insertion of an ionic conductive interlayer between electrode and electrolyte can properly hinder the large charge transfer resistance.[22]

To sum up, realization of solid electrolytes with acceptable parameters would revolutionize the rechargeable battery field, providing good safety levels, higher energy densities and dynamic stability with no self-discharge and long cycle lifetime.[6,22]

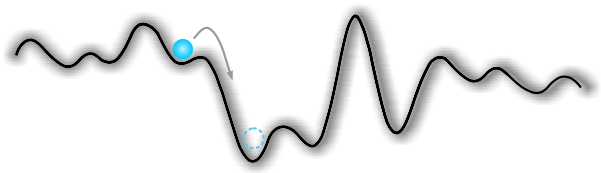

3 Diffusion in Solids

Contents

The ubiquity and importance of solid-state diffusion in the natural sciences are highlighted in many of the texts on this topic, *e.g.* reference 113–115.

Diffusion is derived from latin *diffundere* and means to spread or disperse. Diffusion describes the mixing of substances with each other, especially gases, liquids or solids. The mixing is based on the thermal movement of particles (=*Brownian movement*) for ions, atoms, molecules or colloidal particles and is described through the concentration difference, pressure difference and external field forces. Diffusion that is triggered by concentration differences leads to a degradation of a concentration gradient while the other effects result in a constitution of concentration difference.

Diffusion in solids is an important topic of material science an metallurgy. It has a key role in kinetics during processing of metals, alloys, ceramics, glasses and polymers.The mechanism of diffusion in solids is closely connected to defects, *i.e.* vacancies, interstitials, dislocations, grain boundaries or free surfaces, in the materials. The diffusion in materials with such defects is

much higher due to the better mobility of the atoms. The main driving force of diffusion is the entropy, that increases with the dispersion of the particles. The central points of solid-state diffusion are macroscopic and the microscopic (atomic) diffusion, that will be discussed in detail in the following section.

3.1 Continuum Theory

The equations of diffusion processes are based on the *Fick´s law*. The first system that undergoes diffusion was a salt-water system and was introduced by `Adolf Fick`[116] in 1855. He described the diffusion coefficient that shows a linear response between the concentration gradient and the mixing of two substances. Fick´s law describes the diffusive transport on basic concepts. Diffusion is based on the random walk theory, atomic mechanisms and defects which are treated in this chapter.[115]

3.1.1 Fick´s First and Second Law

In general, diffusion is defined as a temperature depended transport of particles against a concentration gradient by the *Brownian motion*. As already mentioned above, particles statistically move from a region with a higher concentration to a region with lower concentration that results in a thermodynamic equilibrium and an equalization of concentrations. The driving force of this process is the entropy ΔS, that increases with the dispersion of the particles. First, let us consider that the diffusion of particles are in an isotropic medium in an one direction (x-direction) and the concentration gradient $\partial c/\partial x$ is given by the *Fick´s first law*:[114,115]

$$J_{\mathrm{x}} = -D\frac{\partial c}{\partial x}. \tag{3.1}$$

The minus sign in equation (3.1) signifies the fact that the concentration gradient will always result in a particle flux resulting to the equalization of the concentration. The constant D is the *diffusion coefficient* and has the dimensionality $\mathrm{m^2 s^{-1}}$. An extension of the particle flow J to a three-dimensional plane leads to a generalized modification of equation (3.1):[114]

$$j = -D\nabla c. \tag{3.2}$$

The symbol *nabla* $\nabla \equiv (\partial/\partial x, \partial/\partial y, \partial/\partial z)$ describes the vector differential operator and $\boldsymbol{j} \equiv (j_{\mathrm{x}}, j_{\mathrm{y}}, j_{\mathrm{z}})$ the 3D particle flux. In isotropic systems, D as described in equation (3.1) and (3.2) are the same. In principle, D is depended on the direction of the concentration gradient and denoted as tensor $\widehat{D}$. In this thesis, the experiments were done on polycrystalline powders, that have no macroscopic orientation and therefore the average diffusion coefficient $D \equiv \langle D \rangle$. For description of non-stationary processes equation (3.2) has to be combined with the *equation of continuity*[113,115]

$$\frac{\partial c}{\partial t} = -\nabla j \tag{3.3}$$

and results in *Fick´s second law*.

$$\frac{\partial c}{\partial t} = \nabla(D\nabla c). \tag{3.4}$$

Sometimes the *Fick´s second law* is called diffusion equation. This equation is a second order partial differential equation and it is non-linear if *D* depends on the concentration. The composition depended diffusivity is usually denoted with *interdiffusion coefficient*.

If the diffusivity is independent of the concentration, *i.e.* by the tracer diffusion in a homogenous system or in an ideal solid solution, equation (4.6) can be simplified:

$$\frac{\partial c}{\partial t} = D\nabla^2 c \equiv D\Delta c \tag{3.5}$$

where $\Delta \equiv \nabla^2 \equiv (\partial^2/\partial x^2 + \partial^2/\partial y^2 + \partial^2/\partial z^2)$ and is the so called Laplace operator. This equation can also be called *linear diffusion equation*. The diffusivity *D* is determined by recording concentration profiles as a function of position x and time *t* and by fitting these profiles. For a detailed information, see books of Murch[113] and Mehrer[115].

3.1.2 Diffusion Equations and the Dependence in Various Coordinates

As already mentioned above, the Fick´s second law is a linear second-order partial differential equation. The Laplace operatore has different representation in the coordinate system, as seen in Figure 3.1. Using this representation the isotropic diffusion results in following equations for the

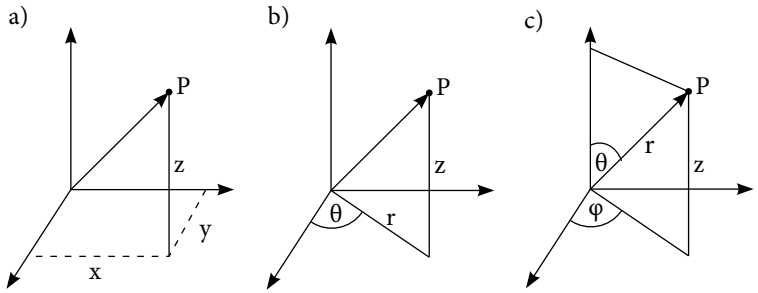

Figure 3.1: a) Cartesian, b) cylindrical and c) spherical coordinates. This figure is adapted from reference 115.

cartesian and cyclindrical coordinates[114,115]:

Cartesian coordinates x,y,z:

$$\frac{\partial c}{\partial t} = D\left(\frac{\partial^2 c}{\partial x^2} + \frac{\partial^2 c}{\partial y^2} + \frac{\partial^2 c}{\partial z^2}\right) \tag{3.6}$$

and *cylindrical coordinates, r, θ, z*:

$$\frac{\partial c}{\partial t} = \frac{D}{r}\left[\frac{\partial}{\partial r}\left((r\frac{\partial c}{\partial r})\right) + \frac{\partial}{\partial \theta}\left(\frac{1}{r}\frac{\partial c}{\partial \theta}\right) + \frac{\partial}{\partial z}\left(r\frac{\partial c}{\partial c}\right)\right] \tag{3.7}$$

Experimental studies use simple geometry which enforce special symmetries on the diffusion field. In following equation some special symmetries are shown, especially the easiest one (linear flow), the axial flow and the spherical flow.

Linear flow in x direction (see Figure 3.1 a)) if $\partial/\partial y = \partial/\partial z$=0:

$$\frac{\partial c}{\partial t} = D\frac{\partial^2 c}{\partial x^2} \tag{3.8}$$

Axial flow in r-direction (see Figure 3.1 b)) if $\partial/\partial z = \partial/\partial\theta$=0:

$$\frac{\partial c}{\partial t} = D\left(\frac{\partial^2 c}{\partial r^2} + \frac{1}{r}\frac{\partial c}{\partial r}\right). \tag{3.9}$$

Spherical flow in r-direction (see Figure 3.1 c)) if $\partial/\partial\varphi = \partial/\partial\theta$=0:

$$\frac{\partial c}{\partial t} = D\left(\frac{\partial^2 c}{\partial r^2} + \frac{2}{r}\frac{\partial c}{\partial r}\right). \tag{3.10}$$

Such symmetries and assumption promote analytical solutions and make it easier to handle.

3.2 Microscopic Diffusion - Random Walk Theory

As already mentioned in the beginning of this chapter, diffusion occurs by the *Brownian motion* of molecules and atoms. In 1905 *Albert Einstein*[117] published the chaotic motion of small particles in a liquid. He said that this motion is due to the attendance of molecules in the fluid and that the molecules are always subjected a thermal movement because of the Boltzmann distribution. Einstein was the first who describes the coherence between the particles and the diffusion coefficient. The same time also the scientist `Smoluchowksi`[118] reported the same and so nowadays the relation is called the *Einstein-Smoluchovski* equation.[113–115]

Diffusion in crystalline powders occurs by jumps in the lattice. An important point is that there is a separation between neighboring lattice sites and the sequence of steps that results in a macroscopic diffusion. For example, the exchange of an atom with a neighboring vacancy has a duration that is approximately the reciprocal Debye frequency ($\approx 10^{-13}$s). In general diffusion in a lattice can be separated into following tasks[113,114]:

1. Random walk of particles: there are diffusive jumps and atomic jumps. Diffusive jumps have a fix length while atomic jumps are driven by defects like vacancies and interstitiales. Therefore, this is a phenomena which makes it possible to calculate jump rates, jump distances and correlation factors.

2. Jump process that occur due to thermal activation and thus a jump rate τ^{-1} can be described:

$$\tau^{-1} = \nu^0 \exp\left(-\frac{\Delta G}{k_\mathrm{B}T}\right) \tag{3.11}$$

where ν^0 describes the frequency, ΔG the Gibbs energy, k_B the Boltzmann constant and T the temperature.

3.2.1 Einstein-Smoluchovski Relation

In this section the diffusion coefficient will be deduced, following the derivation by Mehrer[115], who in term follows that of Einstein.[117] The simplest way how particles can diffuse is through a cubic lattice so the total displacement $\boldsymbol{R}$ = (*X, Y, Z*) of a particle and is the sum of the individual jumps $\boldsymbol{r}_\mathrm{i}$ = (x_i, y_i, z_i) and can be given as

$$\boldsymbol{R} = \sum_{\mathrm{i}} r_\mathrm{i}. \tag{3.12}$$

For the sake of simplicity, we concentrate on the x-axis and keep in mind that the following steps are equal for the other components and describe the *distribution function*. The *distribution function* is described as *W(X,τ)*, where W is the probability that a particle is at a position *X* after some time τ ($\approx \Delta t$). The exact form is not known, so the assumption that the distribution is independent of the starting point of the particle has to be made, and is further normalized:

$$\sum_X W(X,\tau) = 1. \tag{3.13}$$

Additionally, the value X^n has to be introduced, that defines the *n*-th moment of *X* and is a average value of a large number of diffusing particles:

$$\sum_X X^\mathrm{n} W(X,\tau) = \langle X^\mathrm{n} \rangle \tag{3.14}$$

Furthermore, the concentration c of the the diffusing particles is in the x-axis at a time *t*+τ and the particles are located in the plane *x*-*X* at a defined time *t*. This results in:

$$c(x, t+\tau) = \sum_X c(x-X, t) W(X,\tau) \tag{3.15}$$

If τ = 0 and *X* = 0 equation (4.21) results as follwos:

$$c(x,t) + \tau \frac{\partial c}{\partial t} + ... = \sum_X \left(c(x,t) - X\frac{\partial c}{\partial x} + \frac{X^2}{2}\frac{\partial^2 c}{\partial x^2} + ... \right) W(X,\tau) \tag{3.16}$$

For small values τ the high order terms can be discarded and thus the *distribution function* is localized around *X* = 0. Therefore, for very small τ equation (3.15) *c(x, t)* can be missed out and results in:

$$\frac{\partial c}{\partial t} = -\frac{\langle X \rangle}{\tau}\frac{\partial c}{\partial x} + \frac{\langle X^2 \rangle}{2\tau}\frac{\partial^2 c}{\partial x^2} \tag{3.17}$$

The first term is negligible if there is no driving force (*e.g.* electric field) and equation (3.17) can be reduced and results in the diffusion coefficient

$$D_\mathrm{x} = \frac{\langle X^2 \rangle}{2\tau}. \tag{3.18}$$

Additionally, for y- and z- direction the same diffusion coefficients D_y and D_z appear. Assuming that the medium is a cubic crystal, the displacements for all directions (x, y, z) are the same. Hence

$$\left\langle X^2 \right\rangle = \left\langle Y^2 \right\rangle = \left\langle Z^2 \right\rangle = \frac{\langle R^2 \rangle}{3} \tag{3.19}$$

where $\langle R^2 \rangle$ is the *mean square displacement* of a given particle. Combining equation (3.18) and (3.19) and introducing d as dimensionality of the diffusion process, the isotropic diffusion results in coefficient, that is known as the *Einstein-Smoluchowski* relation.[114,115,117–119]

$$D = \frac{\langle R^2 \rangle}{2d\tau} \tag{3.20}$$

3.2.2 Random Walk through the Lattice and Correlation Factor

Macroscopic diffusion in solids results from the concentration of individual microscopic particle jumps. In these elementary jump processes at the atomic level, the atoms or molecules migrate in small random jumps ("random walk") through the solid (see Figure 3.2). The particles move along the grid and the movement is influenced by defects in the lattice such as vacancies and interstitial. The resulting total displacement R is the sum of all individual jumps together

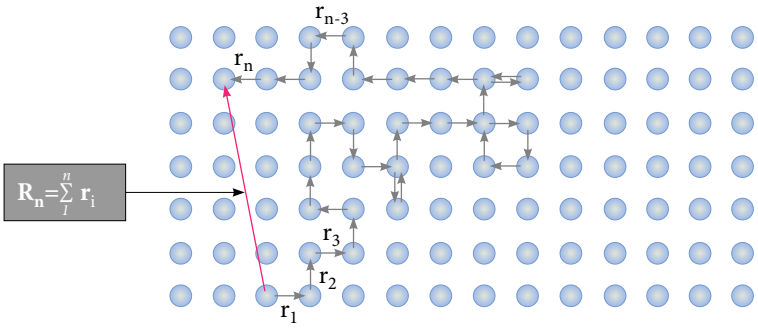

Figure 3.2: Illustration of a jump process of a particle in the lattice. The individual jump processes r_i lead to a total displacement R. This figure has been adapted from reference 115.

$$\mathbf{R} = \sum_{i=1}^{n} r_i \tag{3.21}$$

where r_i are the individual jumps together. The net displacement $\mathbf{R}^2$ is described as follows

$$\mathbf{R}^2 = \sum_{i=1}^{n} r_i + 2 \sum_{i=1}^{n-1} \sum_{j=i+1}^{n} \mathbf{r}_i \mathbf{r}_j \tag{3.22}$$

The first term describes the individual jump length r_i while the second part contains the averages between jump i and all following jumps j. An important term in the random walk theory is the *uncorrelated random walk*, where each jump process is independent of all further jumps. Such jump sequences can also be called Markov sequence. In equation (3.24) the products $\langle \mathbf{r}_i \mathbf{r}_j \rangle$contain

the value $n(n\text{-}1)/2$ which denoted as correlation effect. This second part is for the Markov sequence zero because each pair of $\mathbf{r}_i\mathbf{r}_j$ has a pair with the opposite sign.

$$\left\langle \mathbf{R}^2_{\text{random}} \right\rangle = \sum_{i=1}^{n} \left\langle \mathbf{r}_i^2 \right\rangle . \tag{3.23}$$

Random means no correlation between the jumps. Uncorrelated diffusion processes are governed by the *Einstein-Smoluchowski* relation (see equation (3.20)). This relation describes the microscopic self-diffusion coefficient and the average dwell time τ of a particle at a lattice site, which is also known as the jump rate τ^{-1}. For random uncorrelated movements between two neighbouring lattice sites, the equation can be simplified to

$$D = \frac{x^2}{2d\tau}, \tag{3.24}$$

where x is the jump length between to lattice sites.In this context uncorrelated means that individual jumps are completely independent of each other. To combine this microscopic self-diffusion coefficient and the macroscopic tracer diffusion coefficient D^{tr} (see section 3.1.1) a so-called *correlation factor* f has been introduced:

$$D^{\text{tr}} = f \cdot D \tag{3.25}$$

The correlation factor can assume values between 0 and 1, where 1 corresponds to the completely uncorrelated particle motion.[114,115]

3.3 Diffusion Coefficients

"Different material, different diffusion pathway" and therefore there are three different diffusion coefficient characterized. In this section the focus is on bulk diffusion in binary systems because ternary systems produce mathematical complexities. Therefore, bulk diffusion along the grain boundaries and surfaces will be discussed. For an information in detail; see reference 113–115.

3.3.1 Tracer Diffusion Coefficient

The diffusion coefficient that is appreciable in this thesis is the *tracer diffusion coefficient*. It can be subdivided into the *self-diffusion coefficient* and the *impurity diffusion coefficient*. In the first case the diffusing tracer is chemical the same as the host material while in the second case the species are different.

Basics of self-diffusion are the migration of atoms in a pure metal. To measure the self diffusion coefficient, the applied tracer layer has to be very small compared to the diffusion length. In general tracer atoms are differentiated by the host metal by either their isotropic mass or the radioactivity. To determine the concentration profiles, many methods are known that are descirbed

in detail in reference 115. The distribution of the tracer atom along the concentration gradient can be achieved in all methods through a constant temperature T for a certain duration t. The connection of the tracer self-diffusion coefficient and the atomistic picture of diffusion can be described through the *Einstein-Smoluchowski relation* (see equation (3.20) and (3.24)).

The *tracer diffusion coefficient* can be also applied to much more complex systems like ionic crystals, if there only one mobile species and the rest can be considered as an immobile matrix. The tracer concentration has to be low to avoid interactions between the tracer atoms but also to produce a chemical composition gradient in the sample. In general, the tracer diffusion takes place in the chemical equilibrium

The *impurity diffusion* has nearly the same conditions as the *self-diffusion coefficient* but the tracer atoms are chemically different from the host material. Therefore, the *impurity diffusion coefficient* is dependent on the tracer as well on the host material.[114]

3.3.2 Chemical Diffusion Coefficient

The driving force of diffusion is a concentration gradient but not always. If a chemical composition gradient is present, a *chemical diffusion coefficient* (or *interdiffusion coefficient*) $\widetilde{D}$ is measured. However, the diffusion flux is proportional to the gradient of the chemical potential and is given by (for a binary alloy)

$$\mu_i = \left(\frac{\partial G}{\partial n_i}\right)_{p,T,n_{j\neq i}} \quad i = A, B \tag{3.26}$$

where G is the Gibbs free energy, n_i the number of moles of the product A, B, T the temperature and p the pressure. The *chemical diffusion coefficient* is dependent on the concentration c and thus the Fick´s second law has to be used to calculate the diffusion coefficient $\tilde{D}$(c). It can be analyzed *via* the so called Boltzmann Matano methode that described the diffusion coefficient for a constant volume.

3.3.3 Intrinsic Diffusion Coefficient

Closely related to the chemical diffusion coefficient are the *intrinsic diffusion coefficient* – or also knwown as *compound diffusion coefficient*. In a A-B alloy the diffusion can be described of the components A and B reative to the lattice plane which are denoted as D_{A} and D_{B}. A defined net flux across the plan exists due to the fact that the diffusion rates of A and B are not equal. The shift of the sample to the lattice plane is the so-called *Kirkendall effect*. This effect was first studied by Krikendall and coworkers for Cu/Cu-Zn diffusion.[120] The *Kirkendall effect* is a widespread phenomena that has been discussed over the last decades for alloys.

However, the relation of intrinsic diffusion coefficient, the interdiffusion coefficient and the Kirkendall velocity ν_{K} has been discussed by Darken[121] and Manning.[114,115,122]

3.4 Temperature Dependence of Diffusion

Besides different properties of the samples, the temperature T and the hydrostatic pressure p also influences the diffusion coefficient. The temperature dependence of the diffusion coefficient that is most pertinent to this work. The temperature dependence diffusion coefficients follows an Arrhenius formula

$$D = D_0 \cdot \exp\left(-\frac{\Delta H}{k_\mathrm{B} T}\right) \tag{3.27}$$

where D_0 describes the pre-expontential factor (or frequeny factor), ΔH the enthalpy of diffusion, T the temperature and k_B the Boltzmann constant. ΔH and D_0 can be denoted as *activation parameters*. In principle, the enthalpy of diffusion can be calculated as follows:

$$\Delta H = -k_\mathrm{B} \frac{\partial ln D}{\partial 1/T}. \tag{3.28}$$

The activation enthalpy is the negative slope of the Arrhenius diagramm resulting with a slope of $-\Delta H/k_\mathrm{B}$. At an infinity high temperature ($T^{-1} \rightarrow 0$) it results in the pre-exponential factor D_0 and can be written as:

$$D_0 = D_0^{'} \cdot \exp\left(\frac{\Delta S}{k_\mathrm{B}}\right) \qquad D_0^{'} = g \cdot f \cdot \nu_0 \cdot a^2 \tag{3.29}$$

$D_0^{'}$ contains the geometry factors, such as the geometric factor *g*, the correlation factor *f*, the attempt frequency ν_0 and the lattice parameter *a*, and ΔS denotes the *diffusion entropy*. Combining equation (3.27) and (3.29) the diffusion coefficient results in equation (3.27). Considering the Gibbs free energy, $\Delta G = \Delta H - T\Delta S$, equation (3.27) can be simplified to

$$D = D_0 \cdot \exp\left(-\frac{\Delta G}{k_\mathrm{B} T}\right). \tag{3.30}$$

$$\frac{\partial \Delta H}{\partial T} = T \frac{\partial \Delta S}{\partial T} \tag{3.31}$$

However, enthalpy and entropy can be coupled via the tempertaure dependence of the diffusion coefficient. If ΔH is temperature independent this must also be apply to ΔS.

The interpretation of the physical variables ΔH and D_0 depend on the diffusion mechanism (section 3.6), the type of diffusion process and as well the geometry of the lattice of the sample.[113–115]

3.5 Defects in Crystal Structures

Detailed information can be found in the books Mehrer[115] and Murch[113]. The presence of vacancies or defects in solids is necessary for diffusion. In ideal crystals all lattice sites are occupied by partices that can oscillate around their equilibrium state but can also leave it. However, this ideal structure can only exist at the zero point. Above 0 K each crystal has dislocations due to the second law of thermodynamics that describes that always a certain degree of disorder occurs in thermodynamic equilibrium. Considering the *Gibbs-Helmholtz equation*

$$\Delta G = \Delta H - T\Delta S \tag{3.32}$$

with ΔG as the Gibbs free energy, it becomes clear that with increasing temperatures higher defect concentration occur. Thus, a ideal crystal has a higher degree of entropy ΔS resulting in a thermodynamic lower (favored) energy state G in comparison to its ideal counterpart (see Figure 3.3).[114,123]

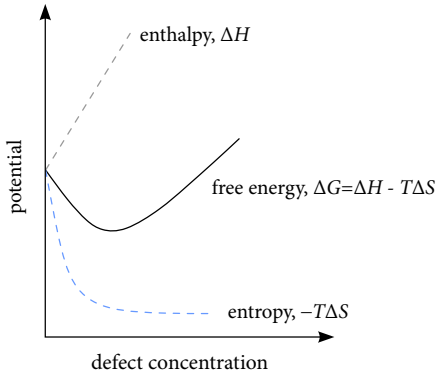

Figure 3.3: Illustration of the energy changes of a imperfect crystal. The number of defects is increasing with temperature, assuming that ΔH and ΔS are independetnt of temperature. Furthermore, with higher temperature $-T\Delta S$ becomes larger and the free energy ΔG is shifted to higher defect concentrations. This figure is adapted from reference 123.

In general, disorders in a crystal structure can be classified in different ways. This crystallographic defects can be subdivided into point defects, line defects and plane defects. Starting with *point defects* (or also known as **zero-dimensional defects**) can be divided into *intrinsic defects*, that are "natural" defects that occur in a "pure crystal", and *extrinsic defects* that are foreign atoms which are intentionally added to the material and are called impurities. Due to the fact, that this defects travel through the crystal it affects the reactivity and the diffusion of the solid. Point defects include the so-called *Frenkel-* and *Schottky-defects* and such typical defects are shown in Figure 3.4. Foreign building blocks are substitution atoms, which are usually smaller or larger than the foreign atoms of the crystal lattice whose place is occupied. The substitution can be done through doping or contamination of the starting materials. The different size of the impurity atom leads either to an expansion or a compression of the grid and thus has a great influence on the properties of

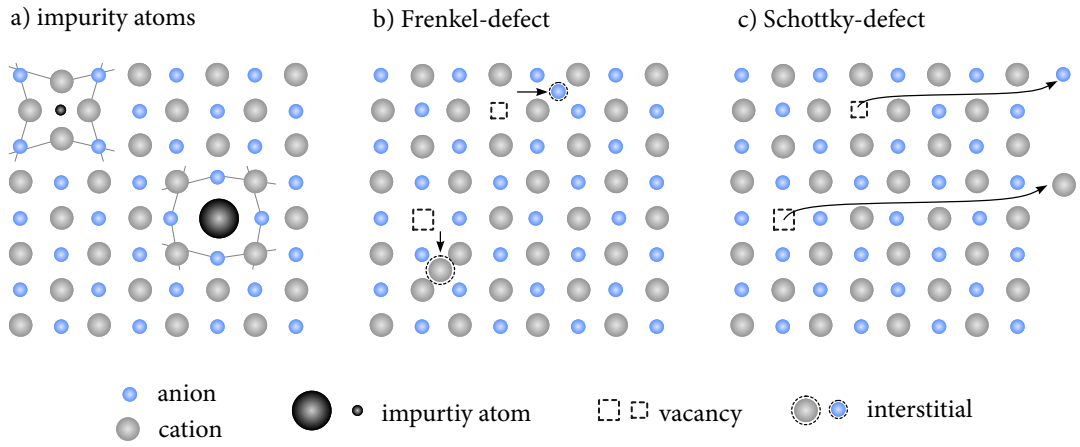

Figure 3.4: Schematic representation of the most important point defects in crystal lattice. a) in case of substitution with a foreign atoms leads to expansion or compression of the crystal lattice. b) Frenkel-defect, where the ions move to interstitial sites and leave vacancies in the crystal. c) By the migration of ions the crystal surface in Schottky dislocations leads to a formation of vacancies in the lattice. This figure has been adapted from reference 124.

the crystal. Additional vacancies can be generated if atoms of other valance are introduced while maintaining charge neutrality. In a Schottky defect, cations or anions migrate to the surface of a crystal leaving voids in the lattice. Furthermore, the Frenkel defect occurs because ions leave a regular lattice site and position themselves on a normally vacant interstitial sites. Additionally, they create both, vacancies and interstitial.[123,124]

Also **one dimensions defects** have been noted and are also knwon as *line defects*. Their most important representatives are dislocations (see Figure 3.5 a) and b)) that are characterized by misalignment in the lattice plan and can extend over the whole crystal lattice. Therefore, they have a big say on the internal structure and thus on the mechanical properties as well in the diffusivity of the crystal.[123]

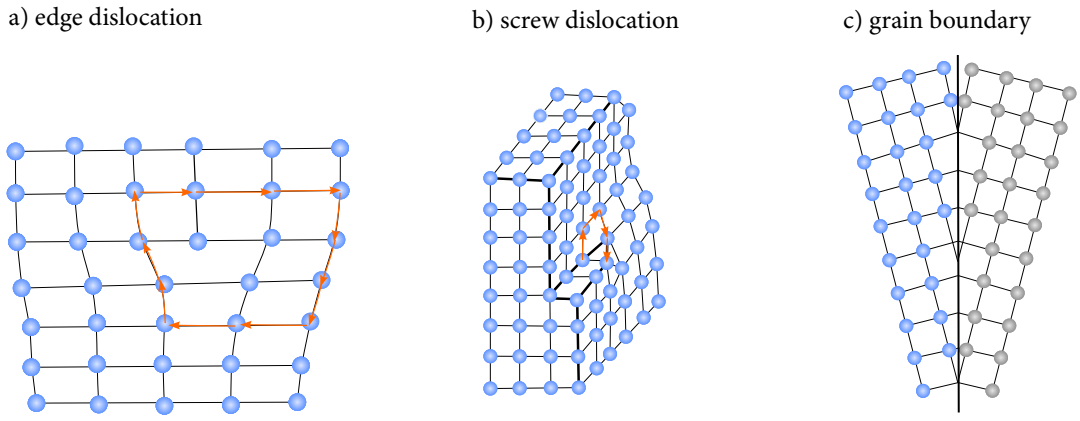

Figure 3.5: a) -c) Schematic representation of one and two dimensional line defects in crystals according to reference 123.

Edge dislocations can be described that there is a stressed and a ”perfect” region as shown in Figure 3.5 a). Outside the stressed region the crystal is arranged perfectly and in the top of the

lattice the atoms are scattered wider than in the middle half. Another dislocation is the *screw dislocations* that is arranged more difficult than the edge dislocation. Taking a look at the bold line (Figure 3.5 b)), at the front site the crystal has a perfect structure but behind its not. For further information about line defects and the dislocation see reference 123.

Two dimensional defects are so-called *plane defects* (or *extended defects*). In polycrystalline materials two dimensional surface defects occur, especially when two or more crystals are in contact. These includes grain boundaries (Figure 3.5 c), stacking faults or twin boundaries. *Grain boundaries* represent interfaces between grains and are important for this thesis due to their fast diffusion pathways in contrast to bulk diffusion. *Stacking faults* are common in materials with a layered structure, especially those that exhibit polymorphism like graphite. It occurs when the "normal" stacking sequence is interrupted by wrong layer, *i.e.* ...ABABABAB**C**ABAB... the bold letter is the corresponding layer that is wrong.[124]

Finally, **three dimensional defects** that include volume and bulk defects. Both results in a much bigger scale than the other defects discussed in this section. However, this type of defects influences the movement of dislocations and has to be considered for bulk. It includes voids or pores. Another type of bulk defect occurs when impurity atoms cluster together to form small regions of a different phase. The term "phase" refers to that region of space occupied by a physically homogeneous material. These regions are often called precipitates.

3.6 Diffusion Mechanisms

The crystal lattice restricts the migration paths and the positions of the atoms and allow a simple description of atom displacement. However, in this chapter is has been already discussed that the diffusivity is affected by jump rates and jump distances. Another important question of atom diffusion is how does do the atoms move? This mechanism can be described through many different diffusion mechanisms.

Interstitial mechanism. – Is the simplest diffusion mechanism and is also known as *direct interstitial mechanism*.This mechanism works without defects and results in high diffusion coefficients compared to other mechanisms. An interstitial atom can diffuse by jumping – through a saddle point – from the interstitial site to a neighboring one (see Figure 3.6 a)). If a jump has been successful, no change in the whole matrix occur. Due to the fact, that no defect concentration and no formation energy is needed, it is the simplest diffusion mechanism.[115]

Collective mechanism. – For atoms with similar size the *collective mechanism* has to be mentioned, in which no defects are involved. This can be either a direct exchange of adjacent particles or a ring mechanism, that is a rotation of three or more atoms by one place as can be seen in Figure 3.6 b). Both types are valid due to their high activation energies as highly unlikely in crystals, but may be common in amorphous systems.[115]

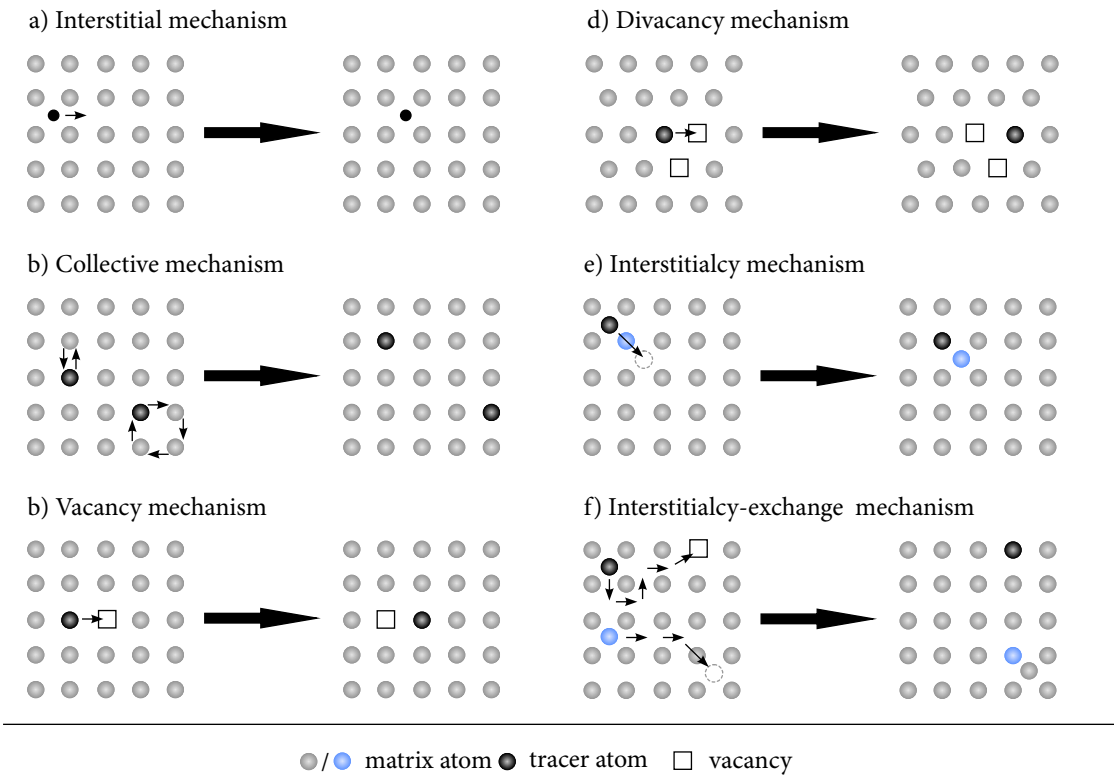

Figure 3.6: Representation of different diffusion mechanism that can occur in a crystal lattice: a) Interstitial mechanism, b) collective mechanism, c) vacancy mechanism, d) divacancy mechanism, e) interstitialcy mechanism and f) interstitialcy-exchange mechanism. The interstitialcy exchange mechanism can be divided into the dissociative mechanism (black) and kick-out mechanism (blue). The figure has been adapted from reference 115 and 114.

Vacancy mechanism. – Is the most common and most important diffusion mechanism and is preferred in metals and alloys (see Figure 3.6 c)). An atom jumps from its position to an adjacent space and leaves its originally site with a vacancy. So there is an exchange of site and site in which subsequently an adjacent atom can jump again. This kind of diffusion depends strongly on the vacancy concentration and its mobility.[114,115]

Diavancy mechanism. – Closely related to the vacancy mechanism an very similar to it is the *diavacancy mechanism*. Providing enough binding energy, vacancy pairs (diavancancies) can simple form vacancies (monovacancies). Both, monovacancies and divacancies are thermally induced. The overall concentration of both types of vacancies increases with increasing temperature. However, the divacancy concentration increases with a higher concentration rate, which makes the pair of vacancies at higher temperatures more important as assigned (see Figure 3.6 d)).[124]

Interstitialcy mechanism. – The *interstitialcy mechanism* or also called indirect interstital mechanism can be found when interstitial atoms in a crystal are present, that are almost the same size as regular atoms and is seen in Figure 3.6 e). Therefore, an atom in a regular place is displaced by large interstitial particle and jumps itself to an interstitial site. This diffusion process is linked with high building enthalpies and are therefore rarely used under equilibrium conditions.[114,115,124]

Interstitial-substitutional exchange mechanism. – If an atom can occupy both, a interstitial and also substitutional sites in a crystal. This two-step jump processes can take place at two different varieties. In both cases, a particle first passes through the crystal lattice via interstitial mechanism. If it jumps onto a vacancy site it is called the dissociative mechanism. The other case is, if the atom displaces another atom at a regular lattice site, it is called the kick-out mechanism (see Figure 3.6 f)).[124]

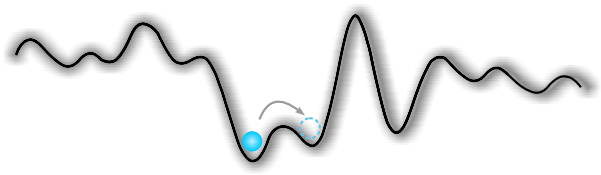

4 Structural Analysis

Contents

Determining the structure of a crystalline material remains the most powerful way to understand that materials properties – which may explain why so many Nobel Prizes have been awarded in the field of crystallography. The standard tools of crystallography are powder diffraction, such as X-ray powder diffraction (XRPD) and neutron powder diffraction (NPD), and single-crystal diffraction. Twenty years ago it has been found that powder diffraction can not be used for solving a new crystal structure but it can be used for determining the presence of already known crystal phases. Therefore, it was necessary to grow large crystals to unravel the position of each atom. However, this limitation disappeared after *H.M. Rietveld* developed a approach for resolving the powder diffraction patterns. This technique, also known as *Rietveld analysis*, has opened up relative rapid structure analysis for all crystalline materials. This section presents the fundamentals of XRPD and NPD and how to solve a crystal structure.[122,125,126]

4.1 Brief History through Powder Diffraction

X-ray diffraction and neutron powder diffraction studies have been used for many years to study structural properties of crystalline or amorphous materials on an atomic scale. In 1910 the method of powder diffraction was understood shortly after *Laue* and *von Kipping* and six years later the method was developed by *Debye* and *Scherrer* in germany (and from *Hull* in the United States). Hull introduced a simple model that was used for determining simple structure, especially graphite, diamond and iron. Furthermore the filter of $K_\beta$through metal foils has also be known so far. With further developments the powder diffraction method has been used for solving the crystal structure of minerals, metals and organic frameworks. From that time on crystal structres can be solved with powder diffraction data; the first structure that was determined was the cubic NaCl structure.[127,128] The first non-cubic structure was determined by *Zachariasn* in 1948.[129]

The fundamental limitation of powder diffraction is the peak overlap, where information gets lost. The loss of information can be avoided through partitioning peak intensities according to the multiplicity. The overlapping has been a problem for many years and so different software packages have been improved to deconvolute the overlapping reflexes.[127,128]

In the 1960s the *ab initio* structure determination was revised and two new methods were introduced: i) direct method and ii) Patterson method. Furthermore, the well-known Rietveld method has been introduced in the same year and thus the refinement of complex structure increases significantly.[125,127] The Rietveld methode was first used for neutron diffraction data but ten years later it has been introduced in the X-ray laboratory.[127] For further details, informations can also be found in the books 125, 123, 124, 126 and 127

4.2 X-ray Powder Diffraction

The basis for the X-ray analysis on crystals is the diffraction effect that was postulated in 1912 from Max von Laue. This states that the X-rays are diffracted at the crystal lattice because the wavelength of X-rays and lattice constants of the crystals are in the same order of magnitude. X-rays are electromagnetic waves with a wavelength (10^{-8} to 10^{-13} m). The demarcation to the two neighboring areas of the UV radiation and the gamma radiation is not strictly set.[127] The wavelength is generated by energy loss of electrons, that can be divided into two different ways how to lose energy. First they can loose kinetic energy and interact with any material, *i.e.* elastic and inelastic scattering. The loose of kinetic energy results in an continuous spectrum, that is illustrated in the following sections. Secondly, electrons can loose energy when changing the energy level but depending on the material.[124,125]

If X-rays hit a material at a certain angle the radiation is scattered. If this scattering is carried out while maintaining the wavelength, and if the scattering centers are not separated at arbitrary distances then interferences and thus diffracted waves occur – with higher or lower intensity depending on the angle. The analysis of the resulting diffraction pattern makes it possible to make a statement.[124,127]

4.2.1 Characteristic X-ray Spectrum

The typical X-ray spectrum (see Figure 4.1) is generated in a typical X-ray tube. The spectrum cons tits of typical sharp peaks, the also known as spectral lines, and a superimposed background, which is known as "white radiation". This continuous part is also known as *Bremsstrahlung* (german for "braking radiation") and is generated when charged particles are accelerated, decelerated or deflected. The distribution of the wavelength depends on the acceleration voltage (see Figure 4.1) and not on the anode material of the X-ray tube. By increasing the acceleration voltage, the intensity of the Bremsstrahlung increases as can be seen in Figure 4.1. However, it is hard to

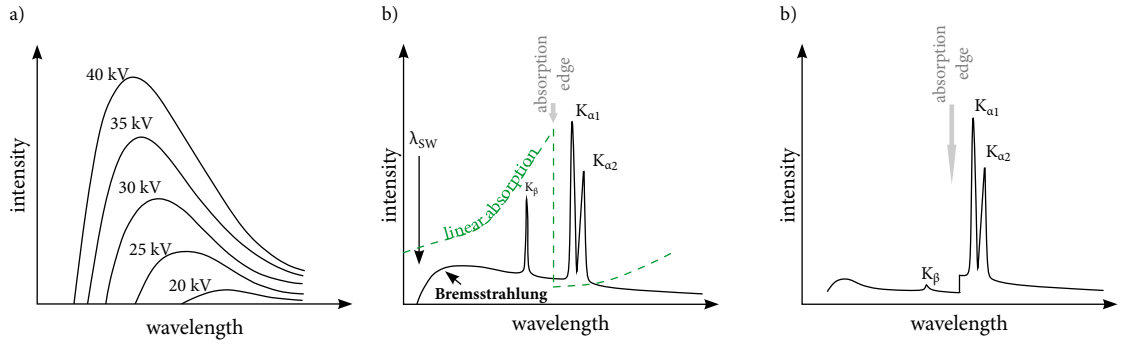

Figure 4.1: a) Bremsspectrum of wolfram that illustrates with increasing acceleration voltage the intensity in increasing. b) Typical X-ray emission spectrum that indicates the continoius background (Bremsstrahlung) and the three characteristic wavelengths: K_β, $K_{\alpha1}$ and $K_{\alpha2}$. The intensities of the spectral lines are approximatey scaled and also the ratio of $K_{\alpha1}$:$K_{\alpha2}$ is exaggerated. The vertical arrow indicates the shortest wavelength of the Bremsstrahlung, λ_{SW}. The dotted line represents the β-filter. c) Spectrum after filtering as a function of wavelength.

establish the exact distribution of wavelengths in the Bremsspectrum analytically but it is possible to establish the shortest wavelength λ_{SW} as a function of acceleration voltage. The X-rays with a small wavelength (phonons with high energy) are emitted by electrons and this electrons are afterwards stopped by a target.[124,125,127] The electron has a defined kinetic energy

$$\frac{mv^2}{2} = eV \tag{4.1}$$

that is completely formed into a photon with a energy of

$$h\nu = \frac{hc}{\lambda}. \tag{4.2}$$

where m is the rest mass, v the velocity, e the charge of an electron (= 1.602×10^{-19} C), V the voltage and c the speed of light (=3×10^8 m s^{-1}), ν is the frequency, h the Plank´s constant (= 6.26×10^{-34} Js) and λ is the wavelength of the photon.[125] By combining equation (4.1) and (4.2):

$$\lambda_{SW} = \frac{hc}{eV}. \tag{4.3}$$

the shortest possible wavelength λ_{SW} can be caculated.[125]

For X-ray powder diffraction the X-ray beam has to be monochromatized which means to reduce the intensity of the Bremsstrahlung and for eliminating undesirable wavelength. The most common method to monochromatize the X-ray beam is the use of a β-filter. In that case, a K absorption edge is present to eliminate the K_β radiation and transmit the $K_{\alpha 1}$ and $K_{\alpha 2}$ parts of the spectrum. The presence of a $K_{\alpha 2}$ describes the presence of dual wavelength in the standard X-ray sources and makes it difficult to determine the peak position in the powder pattern. The intensities of $K_{\alpha 1}$ (λ=1.540Å) and $K_{\alpha 2}$ (λ=1.544Å) are proportional to each other (2:1) whereas the *d*-spacing remains constant. This results in a slightly different Bragg angle of $K_{\alpha 2}$ compared to $K_{\alpha 1}$. However, the peak positions of $K_{\alpha 2}$ have to be eliminated. Both position can be described as follows using the Bragg´s law (as shown in section 4.2.3.3)[122,125] :

$$\frac{\sin\theta_1}{\lambda_{K\alpha_1}} = \frac{\sin\theta_2}{\lambda_{K\alpha_2}}. \tag{4.4}$$

The β-filter has to be made up of a chemical element which is one atomic number lower than the anode material. For a heavy atom this number can be increased by a number of two, however, it is important that the adsorption edge (see Figure 4.1 c) is between K_β and $K_{\alpha 1}$. For a Cu anode the best β-filter is a Ni foil. However, the major disadvantages of β-filters are: i) not all K_β radiation can be eliminated and ii) a small amount of Bremsstrahlung is visible after fileting. Other filters that can be used are crystal monochromator or using a solid state detector.[125]

4.2.2 Fundamentals of X-ray Radiation and Diffraction

Besides Bremsstrahlung a *X-ray radiation* can occur. In general, an atom has been ionized when the material is hit by high energy electrons which has a defined binding energy. Electron from a higher energy level relax to vacant electronic states and during this change of energy level an X-ray phonon has been emitted. This binding energies of the two energy levels are characteristic for each material that has been used. In this thesis Cu is mostly used and has a wavelength of 1.54 Å.

In an atom there are different shells, such as K-, L-, M-,..., and an emitted electron can be hit from one shell to another due to the kinetic energy. The nomenclatur is related to the shells as well to the transition that can take place, *i.e.* L→K emits K_α radiation, M→K emits K_β radiation. In some cases there can be more than one spin-orbit coupling in the energy levels, then the notation is extend with numbers. For example in the L→K transition they are pronounced with $K_{\alpha 1}$ and $K_{\alpha 2}$ radiation, which have a very small splitting. A chracteristic radiation spectrum has been shown in Figure 4.1 b).[124,125]

When X-rays pass through a substance / material following process have to be mentioned and have to be considered in the phenomena of *diffraction*[125] :

1. Coherrent scattering. – The beams that were produced and have the same wavelength as the incident beam (primary beam). It can be also described that the energy of the photons in the coherently scattered beams are unchanged compared to the primary beam.

2. Incoherrent scattering. – The scattered beam wavelength increases due to the loss of energy of the photon that has a collision with the core electrons. This effect is also known as *Compton-effect*.

3. Absorption. – Some photons have been degraded and scattered in random directions and also some photons loose energy by ionization or photoelectric effects.

Coherrent scattering results in diffraction from a crystal lattice whereas incoherent scattering is neglect able low. When absorption of X-rays becomes important it has been taken into account as seperate effect. For further information about X-ray radiation and the fundamentals of diffraction see reference 125.

4.2.3 Diffraction of X-rays in Crystals

A crystal can pass through a grid in space, whose lattice points are the same related to the arrangement of atoms. The grid describes the translational symmetry of the crystal. The base of the grid is generally formed by several atoms, in the simplest case however also only from one atom.In the following subsection the reciprocal lattice, the Laue equation and the Bragg´s law is described in detail. The letters point out in bold are vectors.

4.2.3.1 Reciprocal Lattice

The scattering of X-rays occurs only at electrons of atoms (Thomson-scattering). When X-rays hit a crystal they can be seen by the individual atom scattering, especially the constructive interference. The scattering process can be described through the wave vectors $\mathbf{k}_1$ and $\mathbf{k}_2$ of the incident and scattered X-rays. The scattering is elastic, so that the magnitude of the wave vector does not change in the scattering process (see Figure 4.2).[122,124,126] Consequently it results in

$$k_1 = k_2 = k = \frac{2\pi}{\lambda} \tag{4.5}$$

where k denotes the magnitude of the wave vector of the X-ray radiation. The stray waves interfere

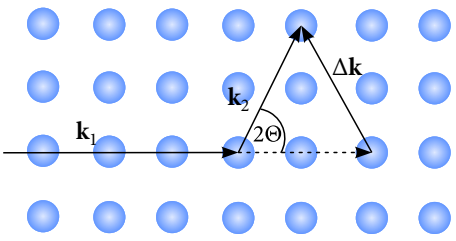

Figure 4.2: Visualization of the Ewald sphere with the vectors $\mathbf{k}_1$ and $\mathbf{k}_1$. The figure has been adapted from reference 124.

constructive, if the change of $\Delta\boldsymbol{k}$ of the wave vector corresponds to a vector $\mathbf{G}$ of the reciprocal lattice. Therefore, following equation is obtained

$$\Delta\mathbf{k} = \mathbf{k}_1 - \mathbf{k}_2 = \mathbf{G} \quad \text{with} \quad \mathbf{G} = h\mathbf{b}_1 + k\mathbf{b}_2 + l\mathbf{b}_3 \tag{4.6}$$

$$\mathbf{b}_{\mathrm{i}} = \frac{2\pi(a_{\mathrm{j}} \times a_{\mathrm{k}})}{(a_1 \times a_2} \cdot a_3) \tag{4.7}$$

For the sake of simplicity, here a simple cubic lattice has been considered. In this case also the reciprocal lattice is cubic with its lattice parameter *a*. The grid points can be described through the coordinates *h*, *k* and *l*. As already mentioned in a powder sample all orientations are present. Combining Figure 4.2 an equation (4.6) it results in

$$\Delta k = 2k\sin\theta = \frac{2 \cdot 2\pi}{\lambda}\sin\theta = a\sqrt{h^2 + k^2 + l^2} = \frac{2\pi}{a}\sqrt{h^2 + k^2 + l^2} \tag{4.8}$$

which is ident to the formula below (4.5). It can be seen that the refection indices in a scattering process correspond to the coordinates of the reciprocal lattice point, that describes the scattering process according to (4.5). The number of surface frequencies as the number of grid points with the same $|\Delta\, k\,|$.

4.2.3.2 Laue Equation

To understand the geometry of the diffraction by a lattice direct and reciprocal spaces can be used. Reciprocal space is very useful to describe the diffraction pattern from a powder. A well-known *Laue equation*, named after *Max Laue* is used to describe the geometry of diffraction from a lattice. In principle, it means that the incoming and outgoing waves are related to each other. In the Laue equation three simultaneous equations are used which are described as follows[124]:

$$a(cos\psi_1 - cos\varphi_1) = h\lambda \tag{4.9}$$

$$b(cos\psi_2 - cos\varphi_2) = k\lambda \tag{4.10}$$

$$c(cos\psi_3 - cos\varphi_3) = l\lambda \tag{4.11}$$

a, *b* and *c* are the dimension of the unit cell, λ is the wavelength, ψ_{1-3} and φ_{1-3} are the angles of the incoming and outgoing waves and *h*, *k* and *l* indicates the Miller indices. The Miller indices are different for each diffraction peak and define the position of the peak in the reciprocal space. When all three equations are satisfied simultaneously a sharp diffraction peak occurs as illustrated in Figure 4.3.

In general, Laue equation defines that a lattices produces diffraction maxima at defined angles and they are defined through the distances of a unit cell (*a*, *b* and *c*) and also of the incoming wave with its wavelength (λ). The result is a three dimensions diffraction pattern that is in most cases used for single crystals but can also be used for powders.[125]

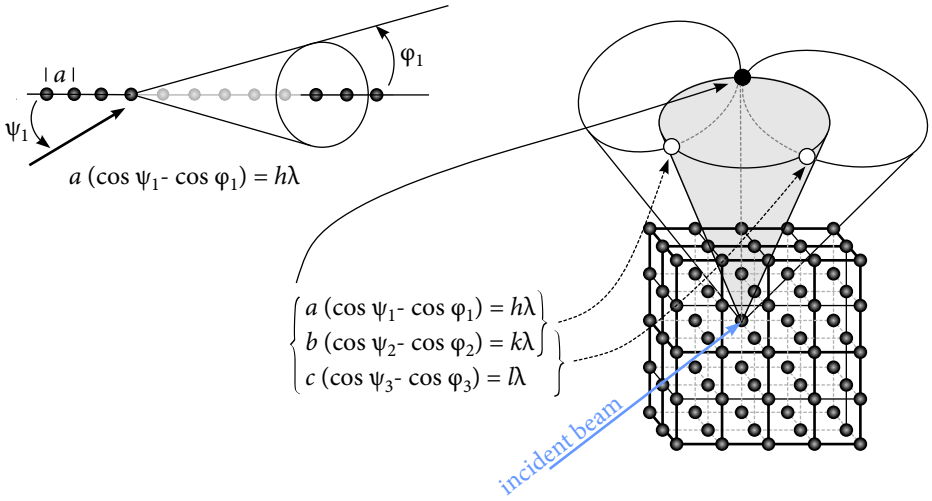

Figure 4.3: Graphical representation of the Laue equation. Top left: representation of the cone of a diffracted beam with a angle φ_1. Bottom right: All three cones of the diffraction are shown. By combining all three equations, a very sharp peak results in the diffraction pattern, that is marked with a black arrow. A combination of two equation is seen with the dotted arrows. This figure has been adapted from reference 125.

4.2.3.3 Bragg´s Law

More useful for powder diffraction patterns is the law which has been formulated by *W.H. Bragg* and *W.L. Bragg*. The so-called Bragg equation describes the occurrence of constructive interference (= two in-phase waves resulting in a new wave with double of the amplitude) in scattering of waves on a three-dimensional grid. The diffraction of the material can be considered as a reflexion of X-rays on lattice planes (*hkl* planes). If an parallel monochromatic X-ray at a certain angle θ hits on a lattice plane, that is parallel and consists of planes with a distance of d_{hkl}, a scattering appeared as far as the rays are in phase. Before and after the waves have been reflected by the neighboring planes, L, are calculated by the distance and the angle as $L{=}d_{\mathrm{hkl}}\ \sin\theta$. As shown in Figure 4.4 the total difference is $2L$ and the constructive interference is defined as $2L{=}\mathrm{n}\lambda$ where n is an integer multiple of the wavelength. By combining this two waitresses the Bragg law results[122,124–126]:

$$2 \cdot d_{\mathrm{hkl}} \cdot \sin\theta_{\mathrm{hkl}} = n \cdot \lambda \tag{4.12}$$

4.2.4 Debye-Scherrer-Method

For the structural analysis of the powder samples produced in this thesis were mainly powder diffractograms recorded according to the *Debye-Scherrer principle*. For this, the samples were ”fired” with monochromatic X-rays. Due to the statistical distribution of the crystals in the powder, for each lattice plane, there are numerous crystallites in the reflection position and are thus able to reflect the rays. The diffracted rays, which lie on a cone sheath, result in an opening angle of

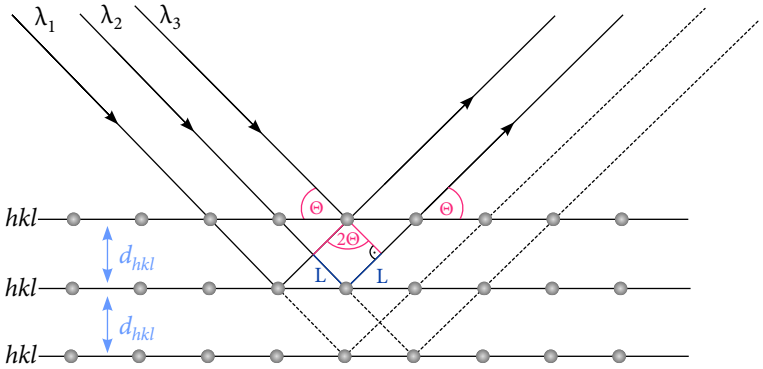

Figure 4.4: Scattering of monochromatic X-rays at lattice planes that consist of parallel planes. Illustration from reference 124 and 125.

4θ. Accordingly, a powder sample emits radiation in form of a coaxial reflection cones. To record the diffraction pattern in this diffraction method a camera is used which consists of a metallic circular cylinder with a photographic film in the inner side. The X-ray stands perpendicular to the cylinder axis. The resulting reflection cones cut the photographic film into so-called Debye-Scherrer lines and result in a characteristic powder diagram in which intensities occur at a specific angle and are plotted against 2θ. The angle between two lines of the same diffraction cone is $4\theta r$,whereby r is the radius representing the camera. With the Bragg´s equation it is possible to determine the interplanar spacing d_{hkl} by wavelength λ and the angle θ. For a complete elucidation of the unknown structure it is necessary to determine the individual lattice parameter a, b, c and the Miller indices (hkl).[122,124]

Miller indices are the smallest integer multiples of the reciporcal interceps defines and describes the lattice plane closest to the origin. The location of a plance which intersects the axes x, y and z is represented by the points (u00), (0v0) and (00w). These intercepts are given in form of reciprocal values in following form

$$h = \frac{1}{u} \tag{4.13}$$

$$k = \frac{1}{v} \tag{4.14}$$

$$l = \frac{1}{w}. \tag{4.15}$$

It is important to note that the indices describe not just a single pain but the position of an infinite number of specific parallel lattice planes, where all have the same distance d from each other.

The determined interplanar distance can be established for an orthorhombic system as follows

$$\frac{1}{d_{\mathrm{hkl}}} = \sqrt{\frac{h^2}{a^2} + \frac{k^2}{b^2} + \frac{l^2}{c^2}} \tag{4.16}$$

However, for a cubic crystal structure this equation can be simpified to

$$d_{\mathrm{hkl}} = \frac{a^2}{\sqrt{h^2 + k^2 + l^2}}. \tag{4.17}$$

From the equation above follows as well

$$\sin\theta = \frac{\lambda}{2a} n\sqrt{h^2 + k^2 + l^2} \tag{4.18}$$

The last equation shows the possibility of an alternative description for higher reflections order. Instead of a reflex *i.e.* third order (n = 3) at (110)-lattice plan (Miller indices h' = 1, k' = 1 and l' = 0) it is also possible to speak of a (330)-reflex, where the ordering degree and Miller index can be contracted with a single refelx index $h = n\,h' = 3$, $k = n\,k' = 3$ and $l = n\,l' = 0$. This description is particularly suitable when scattering processes are described by the reciprocal lattice. It will also be used that the degree of order n no longer appears in the equation.[122,124]

4.2.4.1 Intensity of Bragg-Reflexes

In the Debye-Scherrer method, the intensity I(h, k, l) of the Bragg reflections is given by the following equation

$$I(h,k,l) = I_0 \cdot \left|F(h,k,l)^2\right| \cdot p \cdot \frac{1 + \cos^2 2\theta}{2\sin^2\theta \cdot \cos\theta} \tag{4.19}$$

In this equation I_0 is a constant, F(h,k,l) which depends on the refelx indices is the structure factor and p the number of surface frequencies. The *structure factor* indicates thes scattering power of the base atoms and is described as follows

$$F(h,k,l) = \sum_r f_r \cdot \mathrm{e}^{2\pi i(hu_r + kv_r + lw_r)}. \tag{4.20}$$

The sum goes over all basis atoms, whereby for the *atomic form factor* f_r of the r-th basis atom. u_r, v_r and w_r are the coordinates of the r-th atom in the unit cell. The surface frequency p takes into account that the intensity is proportional to the number of lattice planes that have the right orientation, *i.e.* the Bragg angle to the incident beam. In the cubic crystal lattice p is the number of possibilities how h, k, and l are arranged. For example there are 6 equivalent (100)- and 8 equivalent (111)- planes that means that p = 6 or 8. But why? It can be described through the polarization factor P

$$P = \frac{1 + \cos^2 2\theta}{2} \tag{4.21}$$

It applies to unpolarized X-rays (*i.e.* not to synchotron radiation) and takes into account the angular dependence of the Thomson scattering of the electrons. For further information see reference 125 and 122. Finally, the Lorentz factor takes into account the special geometry of the Debye-Scherrer recordings. If all base atoms have the same atomic form factor, the atomic form factor can be substracted from the sum. The remaining sum is[122,125]:

$$S(h,k,l) = \sum_r \mathrm{e}^{2\pi i(hu_r + kv_r + lw_r)}. \tag{4.22}$$

This of course applies in particular if all base atoms are equal. This remaining sum is the so-called *geometrical structure factor* S(h,k,l). Finally, it should be noted that the structure factor can have the value 0 even if the Bragg equation itself allows a reflex (e.g. in the case of forbidden reflections).

4.2.4.2 Width of Bragg-Reflexes

The Bragg reflexes are not arbitrarily sharp, but broadened. Quantitatively, this is described by the width $\Delta 2\theta$ of observed reflections, which are a function of the scattering angle 2θ. The peak breadth depends on the value of 2θ as given by the formula of Caglioti[130]

$$\text{FWHM} = H = \sqrt{u \cdot \tan^2\theta + v \cdot \tan^2 + w} \tag{4.23}$$

The width $\Delta 2\theta$ is the full width at half maximum (FWHM) and depends on the width of the wavelength distribution of the used X-ray radiation. If this is the characteristic radiation, the lifetime of the involved electronic states is ideally determined. Furthermore, $\Delta 2\theta$ is influenced by several parameters, such as the thickness of the sample layer. The spectral resolution $\Delta 2\theta$ resulting from these effects is experimentally determined by measurements on samples which have a very uniform lattice parameter and not too small grain size so that these samples do not cause (appreciable) additional widening of the Bragg reflexes. The finite grain size (crystallite size) of the investigated powder leads to an additional broadening of the reflexes. This broadening can be explained through the Scherrer equation[125,126]

$$\Delta 2\theta = \frac{0.89 \cdot \lambda}{B \cdot \cos\theta} \tag{4.24}$$

where *B* describes the thickness of the grains. For further information and derivation of the Scherrer equation reference 125 can be used.

4.3 Analysis of Powder Diffraction Patterns

The classical powder diffraction pattern is obtained by fourier transformation of the electron density $\rho_{\text{x,y,z}}$ as described in equation (4.25). Thus, it is obtained from the diffraction pattern of a crystal structure.

$$\rho_{\text{xyz}} = \frac{1}{V} \sum_{h,k,l} F(hkl) \cdot \text{e}^{-2\pi i(hx+ky+lz)} \tag{4.25}$$

The right image of the pattern is obtained by adding the correct amplitudes and phases of the diffracted beams. However, the diffraction pattern only contains an information about the intensities and not about the phase problem that results in a so-called phase problem. This problem makes it difficult to calculate the electron density from the powder pattern. The resulting intensities are proportional to the square modulus of the structure factor. The phase problem can be rectified by using a "direct method" that describes the statistic and probability and therefore the values for the phase can be calculated. This value can be either between 0 or π (centrosymmetric) or between 0 and 2π (see Figure 4.5 and equation (4.26)).

$$I(\varphi) \propto N^2, \text{when } \varphi = h\pi \text{ and } h = ..., -2, -1, 0, 1, 2, ... \tag{4.26}$$

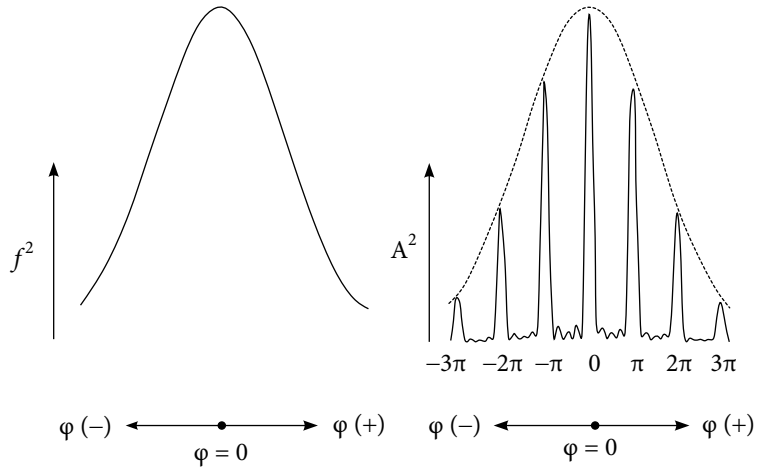

Figure 4.5: a) Graphical representation of the dependence of the intensity scattered by an atom, *i.e.* the atomic scattering factor $f^2 \propto A^2$ as a function of the phase angle φ. b) The decrease of the intensity of five order atoms also a function of the phase angle.

In X-ray powder diffraction (XRPD) there are many crystallites that satisfy the Bragg´s law, for diffraction planes (hkl) in contrast to single crystals. However, for powder data cone-shaped Debye rings are formed, that means that the data were collected by taking a slice through the Debye rings along 2θ and thus result in 1D data that often result in a peak overlap. This can be a problem if the sampes have a large unit cell and a low symmetry which leads to a high peak density. Therefore, to extract the right peak position and the intensity can be quite challenging related to single crystals. However, XRPD data provide a good information if qualitative good crystals cannot be grown or there are problem with crystal growth.[122,125]

In general, XRPD is most commonly used as a qualitative method to identify crystal phases, *i.e.* analysis of mixtures or fingerprinting of materials. In the last decades, the power of X-rays sources have been improved (e.g. synchotron radiation) through coupling of devices and improvement of structure determination method. The structure determination can be described through the three general steps: Indexing, structure solution and refinment.[125]

Indexing. – The indexing of a powder pattern is an essential requirement to determine the structure from powder data. It is the main process of data analysis because if indexing cannot be determined the whole process cannot be continue. The most common used method is the zone-indexing which has been derived from Runge, Ito and Wolff (ITO method)[131]. Furthermore there are two more well studied methods such as TREOR[132] that is based on the permutation of Miller indices for selecting the base line and the direct-space methode DICOL[133]. Peak overlap can make it difficult to index the reflection in the powder pattern but there are also other factors that can avoid fast indexing, such as impurity phases. Furthermore, a source of error is also introduced by a zero-point correlation that means that the position of the sample is different to the calibrated one but for all that it can be corrected by the use of internal and external standards. However,

it is also influenced by synthesis parameters such as grinding or poor quality powder that can result in peak broadening.[125,126]

Space group allocation. – In general, each crystal system has its own space group and different notations to distinguish easily between them. To find the right one it is necessary to study the pattern in detail and find some absences in the diffraction pattern. Due to the different symmetries in the crystal structures some reflections (hkl) are absence regardless the unit cell content. To find the right space group, is has to be required that the peaks are distinguishable from each other (0.02° in 2θ). If there is no systematically absence found a run with a selection of possible space groups is needed. Therefore, solid-state NMR (nuclear magnetic resonance see chapter 5) measurement can help.

Pattern decomposition. – After indexing the correct unit cell, a "structureless" refinement (LeBail or Pawley) known as pattern decomposition is used to achieve a more accurate description of the lattice parameters, zero-point and Pseudo-Voigt peak shape.The peak shape encountered is neigh purely Gauss nor Lorentzian, but a superposition of these two and can be represented by a weighed sum of these two as shown in following equation and known as pseudo-voigt

$$y(x) = PV(x) = \eta \frac{C_G^{1/2}}{\sqrt{\pi} H} \exp(-C_G x^2) + (1-\eta) \frac{C_L^{1/2}}{\pi H} (1 + C_L x^2)^{-1} \tag{4.27}$$

wherein H is the FWHM, $x = (2\theta_\mathrm{i} - 2\theta_\mathrm{k})/H_\mathrm{k}$ is essentially the the Bragg angle of the i$^{\mathrm{th}}$ point in the powder diffraction pattern with its origin in the position of the k$^{\mathrm{th}}$ peak divided by the peak´s FWHM, $2\theta_\mathrm{k}$ is the i$^{\mathrm{th}}$ point of the powder diffraction pattern and $2\theta_\mathrm{k}$ is the calculated (or ideal) Bragg angle of the k$^{\mathrm{th}}$ reflection. With the instrumental settings, the diffraction maxima can be influenced that account for zero-point error through a series of refinement cycles. In contrast to the Rietveld refinement, where the intensities are also refinable variables. If the pattern decomposition is completed it is going on with the solution step and can be used for the final steps. From the pattern decomposition produces a agreement (R_wp / %), which is the structure solution,can be found. It can also integrate intensities from the pattern and results in a χ^2, which is also known as goodness of fit and is defined in equation(4.30), direct space approach.[126]

Structure solution. – To solve the crystal structure, two different methods can be used: i) traditional method and ii) direct space method. The first is based on the same principle that is used for single crystals where the intensities I_hkl are taken from the individual reflection direct out of the diffraction pattern. But the main problem of this method is the peak overlapping and thus it is hard to extract reliable intensities.[125,126]

The latter method is the direct method which is used to isolate the diffraction data. The R_wp factor describes the different between the trial structure and the experimental diffraction pattern. It is taken from the Rietveld program and can be used to compare the fitting profile.

$$R_\mathrm{wp} = 100 \times \sqrt{\frac{\sum\limits_i w_\mathrm{i}(y_\mathrm{i,obs} - y_\mathrm{i,calc})^2}{\sum\limits_i w_\mathrm{i}(y_\mathrm{i,obs})^2}} \tag{4.28}$$

where R_{wp}, $y_{\text{i,obs}}$ describes the experimental intensities at a value of 2θ and $y_{i,calc}$ the calculated intensities at 2θ. w_i is the weight assigned at a data point i. Another important factor is χ^2 which denotes the goodness of fit, that means the ratio between observed against theoretical distribution. Before describing the χ^2 the R_{exp} has to be introduced[125]:

$$R_{\text{exp}} = \left[\frac{n-p}{\sum_{i=1}^{n} w_i (y_{\text{i,obs}})^2}\right]^{1/2} \times 100\% \tag{4.29}$$

where R_{exp} is the expected profile residual. The goodness of fit, χ^2 or also knwon as chi-squared is defined as:

$$\chi^2 = \frac{\sum_{i=1}^{n} w_i (y_{\text{i,obs}} - y_{\text{i,calc}})^2}{n-p} = \left[\frac{R_{\text{wp}}}{R_{\text{exp}}}\right]^2 \tag{4.30}$$

The peak shape parameters, like lattice parameters have been already calculated in the patter decomposition and this factors are important to calculate the R_{wp}. In general, at the direct method the variables can be subdivided into three sections: i) the unit cell parameters (x,y,z), ii) the angles of the molecule (θ, ϕ, ψ) and iii) the conformation that means that the free rotating sections of a molecule are taken into account. Therefore, the R_{wp} factor is important and includes most of the crystallographic information.

Final, another important figure of merit which has to be mentioned is the Bragg residual (R_{Bragg}, that is an intensity based R factor and can be described as

$$R_{\text{Bragg}} = \frac{\sum_{j=1}^{m} \left| I_j^{\text{obs}} - I_j^{\text{calc}} \right|}{\sum_{j=1} I_j^{\text{obs}}} \times 100\% \tag{4.31}$$

Rietveld refinement. – Before starting with the Rietveld refinement[134], a crystal structure has to be generated through structure solution in many cases from the differential evolution (DE). The differential evolution describes the optimization of the fitting parameters, that uses the concept of fitness to find a global minimum. The refinement is successful when the DE is in a good agreement or perfectly matches with the final structure.[122,125] The Rietveld refinement treats every point with its individual intensities and then compares the experimental data with the fitting parameters by using the R_{wp} factor. A perfect match has been achieved when the R-value is below 10%. During the refinement different parameters can be refined, such as atomic coordinates, occupancies, ..., and are adjusted to the refinement of the diffraction pattern. There are also two different restraints which are called tight and soft restraints that are based on geometries based on chemical knowledge. In general, soft restraints allow a more stable refinement than the other.

However, there are several programs that are used for Rietveld refinement like TOPAS[135] and FULLPORF[136] but there are a lot more. For a good refinement following factors have to

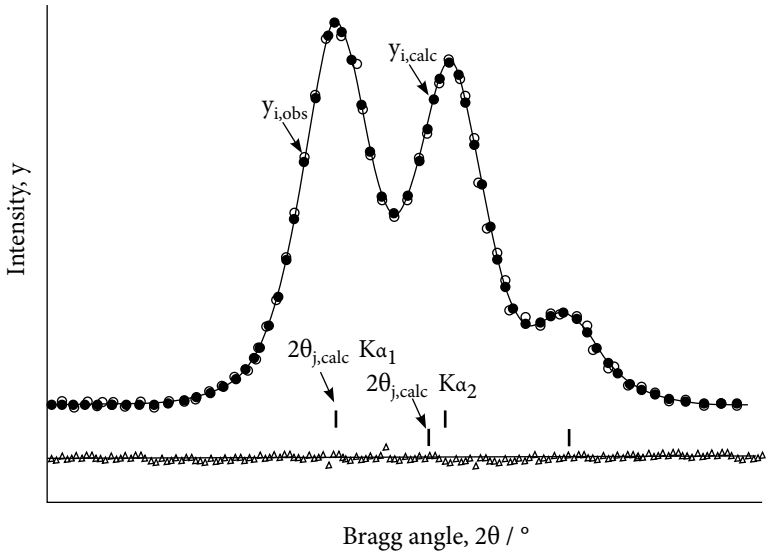

Figure 4.6: A section of a powder diffraction pattern using a Cu Kα radiation. The open circles show the observed scattered intensities $y_{i,obs}$ and the filled circles are connected to the calculated intensities $y_{i,calc}$. The difference between observed and calculated intensities is drawn with open triangles and the vertical bars are the peak position from the diffraction pattern. This figure has been adapted from reference 125.

be taken into account: i) a good model have to be used which matches with the experimental data, ii) the R_{wp} factor has to be close to the agreement factor of the LeBail and Pawley fit and finally, iii) the determined crystal structure have to be meaningful. In Figure 4.6 an example for Rietveld analysis is shown. To sum up, it is important to use the right structure solution thus the refinement will fail.[125]

4.4 Neutron Powder Diffraction

X-ray powder diffraction has been established for a long time for many application such as material science and engineering. However, neutron powder diffraction is another method which is similar to X-ray diffraction. Contrary to X-ray diffraction, which interact with electrons of each atom, the scattering of neutrons occurs at the atom nuclei (see Figure 4.7), that leads to a information that is not visible in X-ray powder diffraction pattern. In Figure 4.7 an atomic cross section with increasing atomic number is shown. It is hard to distinguish between, *i.e.* between Cl and S due to the similar radii. Due to the magnetic moment which is involved in NPD it is an excellent method to determine the magnetic properties of matter. The main advantage of NPD is that it is sensitive to atoms with low atomic number, such as protons, lithium, borates, etc. and it is also possible to distinguish between atoms with similar radii. In some structures it is advisable to combine both techniques to get the right crystal structure, especially when more atoms are on the same crystallographic site.

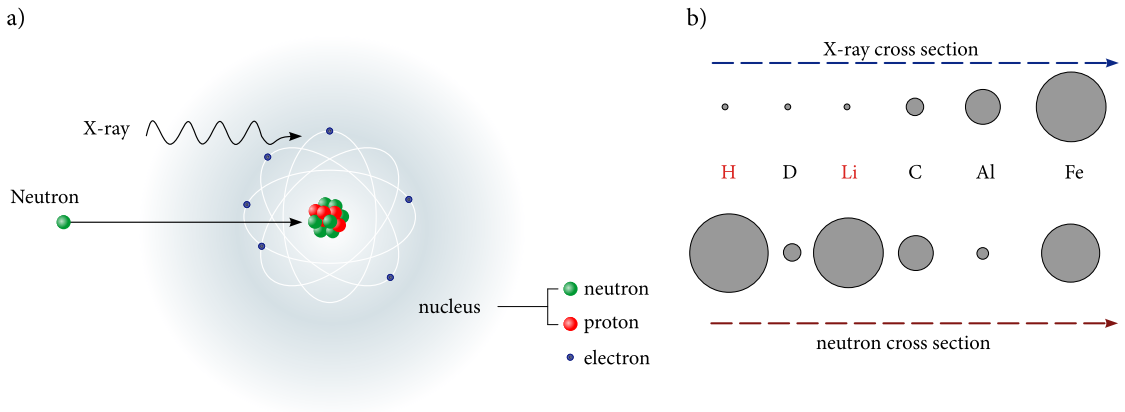

Figure 4.7: a) Graphical illustration of X-ray and neutron scattering. b) cross section of the intensity of the atoms obtained from XRPD and NPD. This figure is adapted from reference 137

Following information can be extracted from a NPD: i) symmetry of the lattice, ii) dimension of the unit cell, iii) the fractional coordinates and iv) occupancy of the atoms at a typical crystallographic site. Finally, also microstructure parameter, grains size and stresses in the crystal lattice can be determined. For further information on neutron powder diffraction see reference 138

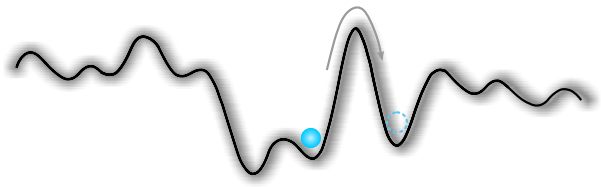

5 Methods to Study Diffusion Parameters

Contents

Before starting to introduce these chapter, it has to be mentioned that there are two different methods to study diffusion parameters.

- *Direct methods.* – are based on Fick's laws of diffusion and are exclusively macroscopic methods due to the sensitivity to long-range processes. Such methods are often more reliable and include the wide variety of physicochemical methods like mass spectrometry, radio-active tracer technique, spectrophotometry etc.

- *Indirect methods.* – is not necessary based on the Fick´s law; takes physical phenomena into account that are influenced by atomic jump processes. The advantage of these methods is that they do not need to determine the change in composition. In this section, the more common and modern methods will be introduced.

There are several different methods to study diffusion parameters. In Figure 5.1 there are some of the methods shown and in general this methods can be divided into microscopic and macroscopic methods. Macroscopic diffusion methods are: i) dc-conductivity method, ii) magnetic

field gradient (MFG) NMR and iii) mechanical relaxation spectroscopy. However, microscopic methods can be described through the sensitivity of localized motion like NMR relaxation or β-NMR studies. Other methods can be quasielastic neutron scattering (QENS) and Mössbauer-spectroscopy (MS). In between this methods impedance spectroscopy can be disposed due to the obtaining information about local diffusion at high temperatures and frequencies.

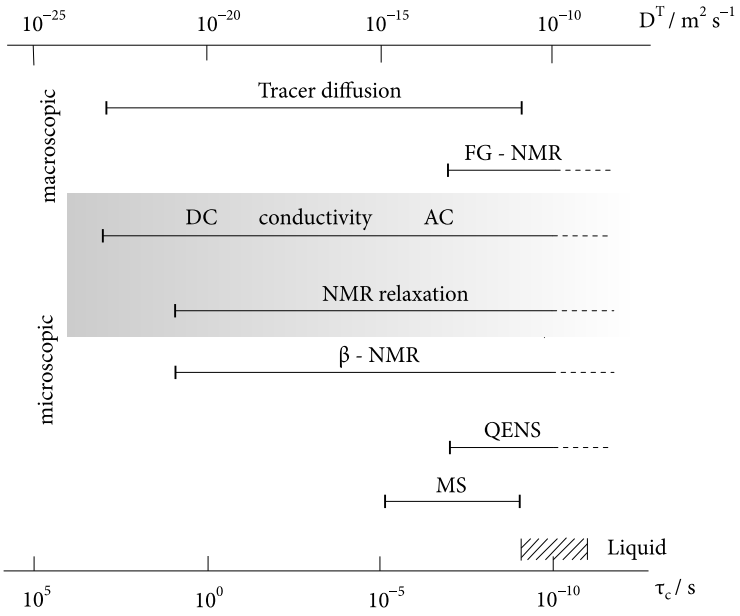

Figure 5.1: Schematic representation of measurement methods for the determining diffusion coefficients and to discuss the long- and short-range ion transport in solids. Marked in gray are the methods which have been used in this thesis. The figure has been adapted from reference 114 and 115. The scala contains the jump rate τ_c and the tracer diffusion coefficient D^T.

In this thesis, impedance spectroscopy and ^{7}Li and ^{31}P NMR relaxation spectroscopy were used to investigate the diffusion process in different solid electrolytes with different crystal structure. In general, it is important to know the crystal structure in detail to make statements of the diffusion process that can occur. In the following sections the basics of NMR and impedance spectroscopy will be discussed and detailed information on these topics can be find in 114, 115, 139–141

5.1 Impedance Spectroscopy

Impedanz spectroscopy is common used analytical method in material science to study ion transport in solids. It provides information on the dynamic of mobile charge carriers in solids and allows the determination of the diffusion parameters. Modern impedance analyzers offer the possibility to determine the frequency-dependence conductivity $\sigma(\nu)$ and the frequency-dependence dielectric function $\epsilon(\nu)$ of a sample in the range from mHz to MHz. The term *impedance* is in connection for a complex resistance, that is the ratio of the complex alternating current (AC) voltage

applied to a sample and the resulting complex AC. From the resulting impedance data a variety of information and characteristics relating to the solid state diffusion can be derived.[139,141,142] The following section introduces this method, that plays and essential role in the analysis of characterisation of the samples considered in this work. Additional literature on this topic is also available in the references 139, 141 and 142.

5.1.1 The Basics of Impedance Spectroscopy

Impedance (or also known as complex electrical resistance) are based on the simply concept of the Ohm´s law, which describes the relation between the voltage U and the current I:

$$R = \frac{U}{I}. \tag{5.1}$$

R denotes the resistance to describe the flow of electric current. However, Ohm´s law applies only to ideal resistors, which operates at all current, voltage and AC frequency levels. The resistance of a resistor is independent of the AC frequency and the current and the AC voltage are in phase with each other. In an ideally homogeneous material it is assumed, that the volume between two electrodes is completely filled and has a defined area A and a defined electrode spacing d, and thus, the resistance is described as

$$R = \rho\frac{d}{A} \tag{5.2}$$

where ρ is the electrical resistivity. The inverse resistivity $1/R$ is the conductivity σ (in S cm^{-1}) that reflects the ability of one material to conduct electrical current between two electrodes.[139,141]

In contrast let us assume an ideal resistor (also called capacitor), it is a circuit element that does not conduct electricity but can store energy in the form of carriers on the electrodes when a dielectric material is placed between them . The voltage and phase signal are out of phase, whereas the current follows the voltage. An important parameter for a capacitor is the ability to store energy, the so-called capacity, and can be described through the following relationship

$$C = \frac{\epsilon_0\epsilon_\mathrm{r}A}{d} \tag{5.3}$$

C is the capacity in Farad and depends on the relative permittivity ϵ_r, the constant electrical permittivity ϵ_0 of the vacuum (8.85×10^{-14} F cm^{-1}), the area A of the electrodes and the distance d between the electrodes.[139]

The complex impedance $\widehat{Z}$, which has a real and a imaginary part (Z' and Z'') combines both concepts from resistivity and the condensator. The real part of the impedance Z' reflects the resistance of a system against the flow of the electric current, thus the imaginary part Z'' stores the electrical engery. Experimentally impedance can be measured by using a AC voltage signal U with a amplitude U_0 applied at a frequency ν. It is a function of time and can be explained as follows:

$$U(t) = U_0\,\sin(2\pi\nu t) = U_0\,\sin(\omega t) \tag{5.4}$$

where ω is the radial frequency and is defined as $\omega = 2\,\pi\,\nu$. The resulting current is also sinusoid at the same frequency but has a phase shift and another amplitude I_0 (see Figure 5.2):

$$I(t) = I_0\,\sin(\omega t + \varphi) \tag{5.5}$$

If there is no phase shift it is an ideal resistor and the Ohm´s law can be used to determine

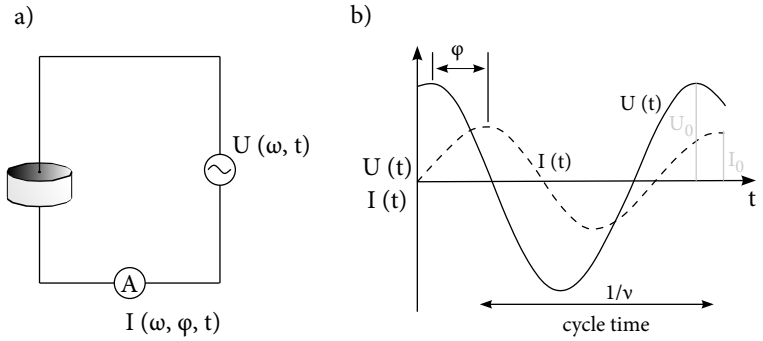

Figure 5.2: a) Fundamental impedance experiment with a sample with a defined thickness d and electrode area A. b) Sinusoidal voltage input U at a single frequency and current response I. This figure has been adaped from reference 139.

the resistance. In dielectric materials there is always a phase shift and thus the equation for the complex impedance of a system is used, which combines equation (5.1), (5.4) and (5.5):

$$\widehat{Z} = \frac{U(t)}{I(t)} = \frac{U_0\,\sin(\omega t)}{I_0\,\sin(\omega t + \varphi)} = |Z|\,\frac{\sin(\omega t)}{\sin(\omega t + \varphi)} \tag{5.6}$$

Therefore, the impedance is expressed through the absolute value of the impedance $|Z|$ and the

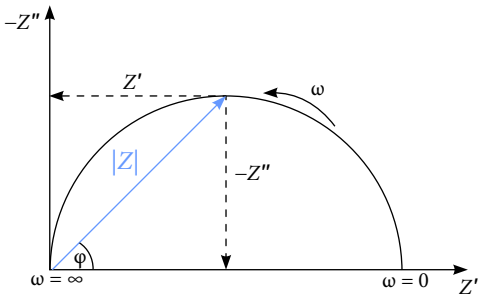

Figure 5.3: Nyquist plot of the impedance data in a complex plane. The real part Z' is plotted against the negative imaginary part Z''. ω represents the radial frequency that is rising in the direction of origin. Figure according to reference 139 and 141

phase shift φ. For an easier treatment of the time-dependent quantities, it is advantageous for the others mathematical description of the complex resistance to switch in the complex number plane. Let us introduce the Euler´s relationship:

$$\widehat{Z} = |Z|\,(\cos(\varphi) + i\,\sin(\varphi)) \equiv Z' + iZ'' \;\text{ if }\; 0 < \varphi \leq 90 \tag{5.7}$$

where the real part is $Z' = |Z|\cos(\varphi)$ and the imaginary part is $Z'' = |Z|\sin(\varphi)$. In Figure 5.3 the complex plane plot is displayed which represents the impedance as a vector and Z' and Z'' are the

coordinates. In addition, combining Figure 5.3 and equation (5.7) it is seen that $|Z|^2 = Z'^2 + Z''^2$ and φ = arctan (Z''/Z').

5.1.2 Admittance, Permittivity and Modulus

Another important parameter is the admittance $\widehat{Y}$, that is defined as the inverse of the impedance and in polar coordinates is defined as:

$$\widehat{Y} = |Y|\,(\cos(\varphi) - i\,\sin(\varphi)). \tag{5.8}$$

The absolute value $|Y| = \left|Z^{-1}\right|$ can be also defined in rectangular coordinates:

$$\widehat{Y} = \frac{Z'}{|Z|^2} - i\frac{Z''}{|Z|^2} \equiv Y' + iY'' \tag{5.9}$$

Dielectric analyzes provides two important quantities, the permittivity and the conductivity, each as a function of time, temperature and the radial frequency. The dielectric permittivity can be noted analogously to equation (5.9) and the arctan relation between the real and imaginary part of the impedance:

$$\widehat{\epsilon} = \frac{\widehat{Y}}{i\omega C_0} \equiv \epsilon' - i\epsilon'', \tag{5.10}$$

where C_0 denotes the capacitance of the empty cell and can be determined through $C_0 = \epsilon_0 A/d$. A describes the area of the electrode and d the distance between them. As the impedance, the permittivity also consists of a real and a imaginary part, whereas the real part of the permittivity ϵ' is the inverse of the imaginary part of the impedance: $1/Z''$. The real part is often called the *dielectric constant*, the imaginary part ϵ'' as *loss factor*. The other way round the real part is $\epsilon'' = 1/Z'$. ϵ' can be determined by using equation (5.3):

$$\epsilon' = \frac{C_0 d}{\epsilon_0 A} \tag{5.11}$$

Other important values of impedance spectroscopy are the ionic conductivity σ, that offers the possibility to characterize the materials related to their conductivity. However, it is also necessary to introduce the resistance R and the specific resistance ρ, that are both influencing the conductivity measurements. However, the loss factor can be calculated with [139,141,142]

$$\epsilon'' = \frac{d}{RA\omega\epsilon_0} = \frac{\sigma}{\omega\epsilon_0} = \frac{1}{\rho\omega\epsilon_0}. \tag{5.12}$$

Both resistivity and conductivity are material dependent values that are strongly influenced by the sample geometry, as in the following relationships becomes clear

$$\left.\begin{aligned} \widehat{\sigma} &= \sigma' + i\sigma'' \\ \widehat{\rho} &= \widehat{Z}\frac{A}{d} = \rho' - i\rho'' \end{aligned}\right\} \quad \widehat{\sigma} = \frac{1}{\widehat{\rho}} = \frac{1}{\widehat{Z}} \cdot \frac{d}{A} = \widehat{Y}\frac{d}{A} \tag{5.13}$$

Probably, the most important size for this thesis is the dc conductivity σ_{DC}, which appears from ion motion in the material and is derived from the real part of the complex conductivity.[139,142]

Another representation is the the complex modulus $\widehat{M}$. Its analysis is different to the impedance analysis and the data representation differs a bit. Dielectric spectroscopy is based on the concept of "relaxation" and is important for this thesis to compare it with the NMR data. The concept of dielectric relaxation was introduced by Maxwell and Debye, and described the relaxation time $\tau = 1/2\pi\nu$. The measurement measures the relaxation time by different frequencies of the complex permittivity $\widehat{\epsilon}$. However, it results in a peak function (see section 5.1.3 / Dielectric and modulus representation) which can be also described through the $\widehat{M}$. $\widehat{M}$ can be described as the inverse part of the permittivity but can also be derived from the impedance[139]:

$$\begin{aligned} \widehat{M} &= \frac{1}{\widehat{\epsilon}} = i\omega\epsilon_0\widehat{Z} = \omega\epsilon_0 Z'' + i\omega\epsilon_0 Z' \\ &\equiv M' + iM'' \end{aligned} \tag{5.14}$$

For a better overview: in table 5.1 a summary of the relations between impedance, admittance, permittiviy and modulus is given.

Table 5.1: Relation of the four basic functions of impedance spectroscopy[141]

	M	Z	Y	ϵ
M	M	μZ	μY^{-1}	ϵ^{-1}
Z	$\mu^{-1}M$	Z	Y^{-1}	$\mu^{-1}\epsilon^{-1}$
Y	μM^{-1}	Z^{-1}	Y	$\mu\epsilon$
ϵ	M^{-1}	$\mu^{-1}M^{-1}$	$\mu^{-1}Y$	ϵ

$\mu \equiv \mathrm{i}\omega C_0$, where C_0 is the capacity of the empty cell.

5.1.3 Analyzing Impedance Data

Ion transport in crystalline solids and ion-conducting glasses occurs through ionic jumps over free grids and interstitial spaces or over vacant spaces in the glass network. The course of the frequency-dependent conductivity $\sigma'(\nu)$ can provide information about the details of such a "hopping motion". In Figure 5.4 the typical run of a frequency dependency of the conductivity is shown.

Conductivity isotherms. – In Figure 5.4 a conductivity isotherm with the characteristic regions is shown, the real part of the conductivity is plotted against the frequency ν applied in a double logarithmic form. It can be seen that σ_{DC} reaches a frequency-independent plateau at low frequencies, that describes the long-range ion transport through the material and is shifted towards higher frequencies at higher temperatures. Both plateaus seen in Figure 5.4 can be separated into grain boundary (pink) and bulk conductivity (blue) (considering several parameters especially permittivity, capacity, etc.).[144] At higher frequencies a so called frequency-dependent regime has been observed which is the dispersive regime. This dispersive regime accrues of a

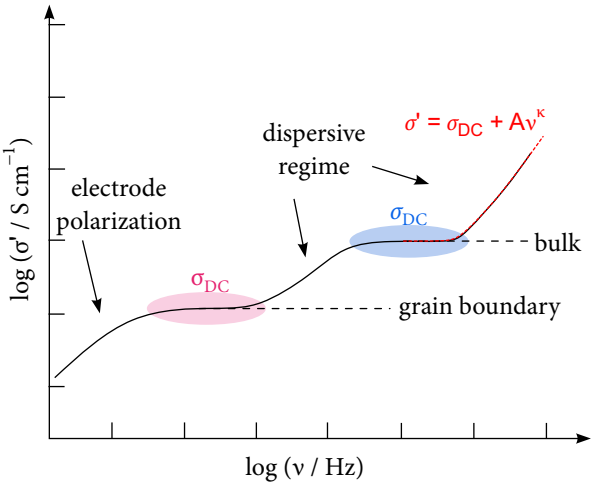

Figure 5.4: Representation of a conductivity isotherm with its characteristic regions in a standard frequency range from a few hertz to a few Megahertz. More detailed information on this figure (according to reference 143) can be found in the following text.

non-ideal behavior of solids. However, various correlation effects influence the frequency dependence of the conductivity. In solids, the temperature dependence can be described through the Arrhenius behavior[145]:

$$\sigma_{DC}T \propto \exp(-E_a^{DC}/k_BT) \tag{5.15}$$

with the activation energy E_a^{DC} and the Boltzmann´s constant k_B. The isotherms can pass, with increasing frequency into the dispersive regime, which can be described through the *Jonscher´s power law*:

$$\sigma'(\nu) = \sigma_{DC}\left[1 + \left(\frac{\nu}{\nu_H}\right)^{\kappa}\right] \tag{5.16}$$

where κ is usually between 0.6 and 0.7 and describes the dimensionality of the ion conductor and ν_H is the cross-over frequency from the σ_{DC}-plateau into the dispersive regime. ν_H is considered to be in the same order of magnitude as the hopping rate of the mobile ions and at this frequency the conductivity is given by $\sigma'(\nu_H) = 2 \cdot \sigma_{DC}$.[146] However, with decreasing temperature the onset of the dispersive regime is shifted towards lower frequencies and also the temperature dependence of the conductivity. This results in $\epsilon'' \neq f(\nu)$, if $\kappa \rightarrow 1$ which is known as nearly constant loss (NCL). The NCL can be described as non-successful motions or relaxation of forward and backward jumps.[147–149] The frequency-dependence at the beginning of the isotherms is described as electrode polarization, from the blocking electrodes. At sufficient high frequencies, a so-called high-frequency plateau occurs, in which every atomic jump contributes to the conductivity. In solids the high-frequency plateau is superimposed from lattice vabriations and thus hard to detect.[143,150]

Dielectric and modulus representation. –In Figure 5.5 a schematic representation of the ϵ' and M'' is detected. As already mentioned in the beginning of the chapter the complex modulus $\widehat{M}$ is proportional to the inverse permittivity and $\omega = 2\pi\nu$.

Before we start with the modulus model, a brief insight into the frequency dependence of dielectric properties, such as capacitance C, permittivity ϵ' and conductivity σ can be expressed. The permittivity (as well the modulus) can be explained through the "Debye model", that can illustrate the bulk relaxation process in an ideal dielectric. Figure 5.5 (solid line) depicts a transition from high-frequency permittivity ϵ_∞ (or C_{bulk}) to the low-frequency limit ϵ_s (or $C_{\text{g.b.}}$) and follows an non-Debye impedance response.[139,142] The curves reveal the well-known features of impedance spectroscopy and show an almost 'ideal' frequency dependence that is expected for a non-Debye impedance response. It can be explained as: If ϵ' is given by $\epsilon' = \epsilon_\infty + A_\epsilon \nu^{-p}$ an AC storage-to-loss ratio of one is obtained if p + κ=1, where κ results from the Jonerscher´s power low above.[151] Additional, it has to be taken into account that $C_{\text{g.b.}} > C_{\text{bulk}}$ and the transition between the permit-

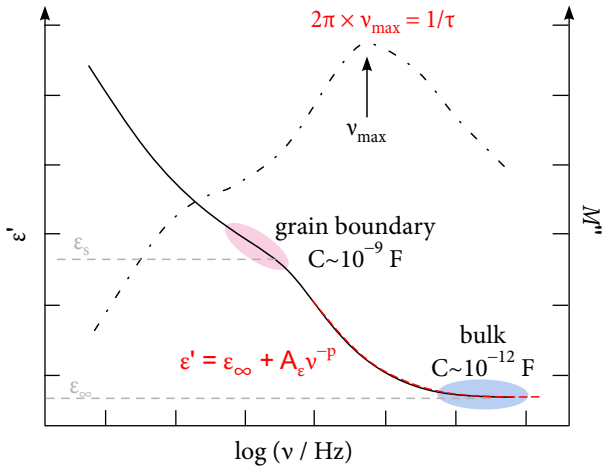

Figure 5.5: Schematic representation of the imaginary modulus M'' (dashed-dotted line) and real part of the permittivity ϵ' (solid line) vs. the frequency ν. The characteristic regions, such as grain boundary (g.b.; pink) and bulk (blue), were marked with their characteristic capacities. The dashed-dotted line represents the modulus spectra; indicated with the maxima conditions $\omega 2\pi = 1/\tau$.

tivities is denoted as $\Delta\epsilon = \epsilon_s - \epsilon_\infty$. This leads to following equation of the complex permittivity:

$$\widehat{\epsilon}(\omega) = \epsilon' - i\epsilon'' = \epsilon_\infty + \frac{\Delta\epsilon}{1 + i\omega\tau} \tag{5.17}$$

$$\text{with } \epsilon'(\omega) = \epsilon_\infty + \frac{\Delta\epsilon}{1 + (\omega\tau)^2} \tag{5.18}$$

$$\text{and } \epsilon''(\omega) = \frac{\Delta\epsilon\tau}{1 + (\omega\tau)^2} \tag{5.19}$$

where ω is the radial frequency and τ is the relaxation time.[139]

However, another data representation is the modulus. The real and imaginary part of the modulus M'' are related to the complex permittivity $\widehat{\epsilon}$ through following relations:

$$M'(\omega) = \frac{\epsilon'}{\epsilon'^2 + \epsilon''^2} \tag{5.20}$$

$$M''(\omega) = \frac{\epsilon''}{\epsilon'^2 + \epsilon''^2} \tag{5.21}$$

The electrical modulus is a widely accepted technique to study the relaxation phenomena to understand the ion conduction mechanism and the relaxation process by suppressing the electrode polarization (in the low frequency region). The imaginary part of the modulus M'' as a function of frequency, results in a maximum which corresponds to the conductivity relaxation process. The high temperature flank is characteristic for the long-range mobility and on the low-temperature side the ions exhibit confined localized motion. By increasing the temperature the peak maxima shift toward higher frequencies, which results in a decrease in relaxation time. So the complex modulus for a material that results in a σ_{DC} plateau can be desribed as follows:

$$\widehat{M}(\omega) = M_{\mathrm{s}} \frac{(\omega\tau_\sigma)^2}{1+(\omega\tau_\sigma)^2} + iM_{\mathrm{s}} \frac{\omega\tau_\sigma}{1+(\omega\tau_\sigma)^2}, \tag{5.22}$$

where $M_{\mathrm{s}} = 1/\epsilon_s$ and τ_σ is the relaxation time of the conductivity. The resulting peak maxima ν_{max} (as seen in Figure 5.5 - dashed-dotted), is related to

$$\frac{1}{\tau_\sigma} = 2\pi\nu_{\mathrm{max}}. \tag{5.23}$$

The modulus realation can be used to study the conductivity and the ion motion; in contrast to the permittivity, which suffers from a low space charge capacitance at low frequencies.[139,142,151,152]

Resistivity plot. – Ion dynamic studies are important to characterize new solid-state materials and thus it is important to compare different methods with each other. In this thesis the focus is on impedance studies and NMR studies and therefore the resistivity plot, that includes the impedance data, makes it possible to compare NMR and impedance data. In Figure 5.6 a resistivity plot is depicted at different temperatures but with the same frequency.[151,153] This measurement can be

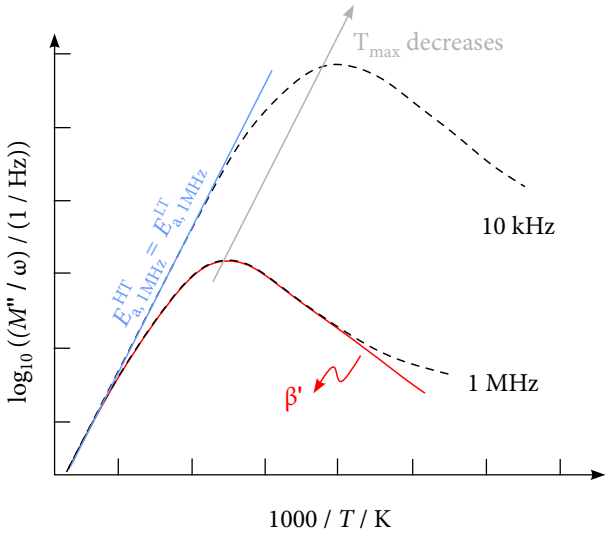

Figure 5.6: Real part of the complex resistivity as a function of the inverse temperature at a frequency of 1 MHz and 10 kHz. The different flanks are characteristic for long- and short-range motion.

done by a different set up, where σ' and ϵ' were recorded at a single frequency but varying the

temperature. The real part of the complex resistivity is given by $\widehat{\rho} = 1/\widehat{\sigma}$ and is related to the complex modulus through $\widehat{M} = 1/\widehat{\epsilon}$ *via* $\widehat{M} = \widehat{M}/i\omega\epsilon_0$, where $\rho' \propto M''/\omega$. Therefore, the real part of the complex resistivity ρ' passes through a distinct maxima, that is comparable to the $1/T_{1(\rho)}$-peaks of the NMR data (see section 5.2). The resistivity shifts to higher temperatures by increasing the frequency, see Figure 5.6. ρ' is given by a Lorentzian-shaped function containing the relaxation time τ_σ [153]

$$\rho' \propto \frac{\tau_\sigma}{1 + (\omega\tau_\sigma)^{\beta'}} \tag{5.24}$$

where $\beta' \leq 2$ and describes the symmetry of the peak. Symmetric peaks are obtained if $\beta' = 2$ and if $\beta' < 2$ the high-temperature flank becomes higher than the low-temperature side. The latter, describes a correlated motion in disordered ion conductors, such as Li_6PS_5Cl [153] or $Ba_{0.6}La_{0.4}F_{2.4}$ [151]. The activation energy E_a^{HT} of the high-temperature flank can be comparable to those resulting from the conductivity isotherms $E_{a,DC}$. [151,153]

Nyquist plot. – A widespread method for the representation of the complex impedance is the visualization of a Nyquist diagram, in which the real part of the impedance Z' is plotted against the negative imaginary part $-Z''$. The resulting graph constists of one or more semicircles and each of them are forming one electrical phenomena which corresponds in the material. Electrode

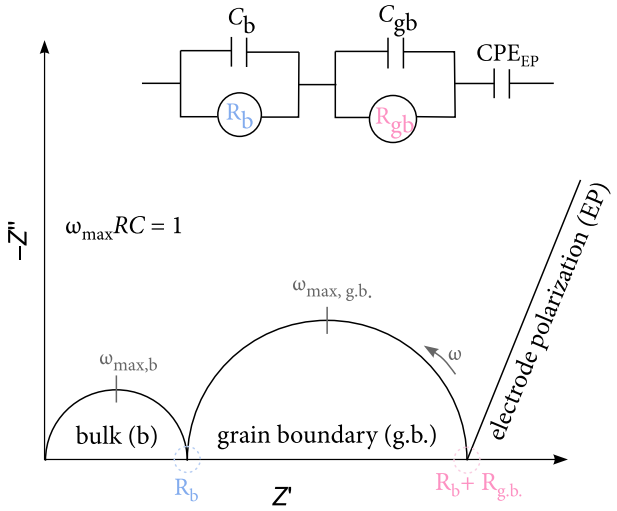

Figure 5.7: Schematic representation of the complex impedance of a ceramic sample including its equivalent circuit diagram for interpretation of the data. The image was adapted from reference 144.

polarization or different diffusion contributions (*i.e.* grain boundary or bulk) are obtained in a Nyquist plot. The resulting Nyquist plot is shown in Figure 5.7. At very low frequencies, seen here on the right, a sharply rising straight line is visible coming from the blocking metal electrodes. In one equivalent circuit diagram, as shown in Figure 5.7 above, this effect is similar to a resistor R_{EP}. Going to higher frequencies, the different diffusion phenomena are visible. Since the complex impedance has both resistor and capacitor contributions, each process can be described with

a resistance *R* and a capacitance *C*. In a equivalent circuit diagram each diffusion contribution corresponds to a parallel connected RC-element, which is calculated through

$$\tau = RC \text{ and} \tag{5.25}$$

$$\omega_{\text{max}} RC = 1. \tag{5.26}$$

τ represents the relaxation time and ω_{max} the radial frequency at maximum loss of the respective phenomenon and is marked with gray lines in Figure 5.7. The resistance *R* can be calculated from the intersection of the semicircles with the abscissa from the real part of the impedance. Thus it is possible to calculate the capacities, identify different RC-elements and assign them to the corresponding regions of the sample. The order of magnitude of the capacities provides information about the processes as described by Irvine et al.[144]. As already mentioned in the permittivity plot the capacities of grain boundaries are larger than that of bulk.

5.1.4 Correlation between Diffusion and Conductivity

The ionic conductivity σ_{DC} through the elementary charge *e*, the mobility μ and the number of charge carriers *n*:

$$\sigma_{\text{DC}} = e \cdot n \cdot \mu \tag{5.27}$$

and further, the mobility can be described as

$$\mu = \frac{D_\sigma \cdot e}{k_{\text{B}} \cdot T}. \tag{5.28}$$

By combining equation (5.27) and (5.28) it results in the Nernst-Einstein relation[117,154,155]:

$$D_\sigma = \frac{\sigma_{\text{DC}} \cdot k_{\text{B}} \cdot T}{e^2 \cdot n} \tag{5.29}$$

where *n* is the charge carrier density, *e* the number density of mobile ions, k_{B} the Boltzmann constant, *T* the temperature and μ the mobility of the ions. The *charge carrier diffusion coefficient* D_σ is closely related to the ionic conductivity σ_{DC} obtained from the impedance spectroscopy. It should be kept in mind that D_σ can not be measured through the Fick´s law. The Haven ratio measures the correlation effects and provides information on whether the conductivity is based on either charge carrier species or on superposition of several different posts.

$$H_{\text{R}} = \frac{D^*}{D_\sigma} \tag{5.30}$$

where D^* is the tracer diffusivity which has been already introduced in section 3.3.1. For the ideal case of arbitrary jumps of a single species of ions, $H_{\text{R}} = f = 1$[113,143] which leads to $D^* = D_\sigma = D$ (equation (3.26) and (5.30)). If a value less than 1 is obtained for H_{R}, this indicates correlation in the motion of the charge charriers or the presence of electronic conductivity.[113,114]

If there are vacancies, which can not be detected via impedance spectroscopy, which are involved in the diffusion process, H_R can be greater than 1.[114]

For uncorrelated motion of the ions, the Haven ratio takes a value of 1 and the measurement of σ_{DC} gives a direct access to the jump rate τ^{-1} via the microscopic diffusion coefficient discussed in section 3.2[113]

$$\frac{1}{\tau} = \frac{2dk_B T}{e^2 n a^2}\sigma_{DC}. \tag{5.31}$$

Here, d denotes the dimension of the diffusion process and a the jump length, in this thesis usually the Li-Li distance.

5.2 Nuclear Magnetic Resonance Spectroscopy

Nuclear magnetic resonance (NMR) is a phenomenon that is an integral part of modern times and is represented in scientific disciplines such as physics, chemistry, medicine or material sciences. The measurement is based on a nuclear magnetic resonance, *i.e.* a resonant interaction between the magnetic moment of the atomic nucleus of a sample, which is in a strong magnetic field, with a magnetic field. NMR spectroscopy can be used both for structure elucidation but also for the investigation of reaction mechanisms or dynamic processes in solids. In the context of this thesis, this method was used in conjunction with impedance spectroscopy to differentiate between long - range and short - range ion transport, respectively, thus establishing a relationship between local structures and ion dynamics in the synthesized samples. Important parameters in this section are diffusion induced-parmeters such as the jump rate τ^{-1} and the activation energy E_a and thus, resulting diffusion coefficient D.

The following section gives a short overview of the most important theoretical basics of solid-state magnetic resonance spectroscopy. More detailed information on this topic can be found in references 119, 156, 157, 158 and 140.

5.2.1 Vector Model of Pulsed NMR

All atomic nuclei with an odd number of neutrons, protons or both have a special fundamental quantum mechanical property called a spin. Each nuclei has a so-called nuclear spin, which can be described by means of a nuclear spin quantum number l and has an angular momentum $\boldsymbol{I}$ (all bold letters in the following chapter represent vectors). As a quantum mechanical quantity, the magnitude of the angular momentum assumes only discrete values, which are determined by the spin quantum number I

$$|\mathbf{I}| = \hbar\sqrt{I(I+1)} \tag{5.32}$$

where $\hbar = h/2\pi$ and h is the Planck constant. By definition, I can only assume discrete values (I=0, ½, 1, 3/2, ...). If a nuclei has a spin unequal zero ($I \neq 0$), a magnetic moment μ can be

introduced. The dipolar magnetic moment $\boldsymbol{\mu}$ is linearly related to the spin angular momentum $\boldsymbol{I}$ of the atomic nucleus

$$\boldsymbol{\mu} = \gamma \mathbf{I} \tag{5.33}$$

where γ is the gyromagnetic ratio, which is different for each nuclei and if $\gamma \neq 0$ it can be detected by NMR spectroscopy and the nuclei is NMR active. Thus, the amount of $\boldsymbol{\mu}$ is equally quantized

$$|\boldsymbol{\mu}| = \gamma \mathbf{I} = \gamma \hbar \sqrt{I(I+1)}. \tag{5.34}$$

If the magnetic moment is exposed to an external magnetic field $\boldsymbol{B}_0$ (see Figure 5.8) with alignment along the z-axis, $\boldsymbol{\mu}$ starts a time-dependent movement about this axis and can be described through:

$$\boldsymbol{\mu} \times \mathbf{B}_0 = \frac{dI}{dt}. \tag{5.35}$$

By combining this equation with equation (5.34) it results in

$$\boldsymbol{\mu} \times \mathbf{B}_0 = \frac{1}{\gamma} \frac{d\mu}{dt}. \tag{5.36}$$

The angular frequency ω_0, with which μ rotates around the z-axis, is the so-called called *Larmor*

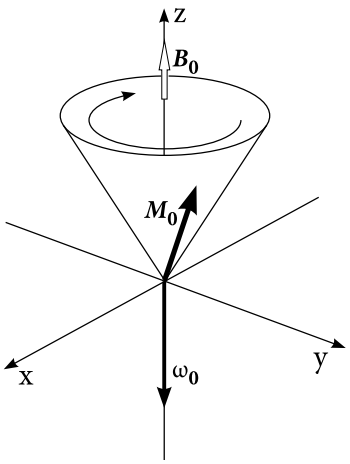

Figure 5.8: Schematic representation of the circular movements of the total magnetization vector $\boldsymbol{M}_0$ in an external magnetic field $\boldsymbol{B}_0$; in thermodynamic equlibirum. ω_0 corresponds to the Lamor frequency. Adapted figure of reference [158]

frequency (see Figure 5.8).

$$\boldsymbol{\omega}_0 = -\gamma \mathbf{B}_0 \tag{5.37}$$

Zemann Splitting

The presence of an magnetic field $\boldsymbol{B}_0$, that in the NMR conditionally always deigned as lying

in the z-direction ($\boldsymbol{B}_z$=$\boldsymbol{B}_0$) , leads to a directional quantization of the spin and thus also of the nuclear magnetic moment

$$\mu_z = \gamma p_z = \frac{\gamma h}{2\pi} m_\mathrm{I} \;\text{ or }\; I_z = m_I \hbar. \tag{5.38}$$

Here, m_I denotes the magnetic quantum number: m_I = *I*, *I-1*,...-*I*. Without the presence of an external magnetic field, the states m_I are energetic degenerate. In contrast, in a magnetic field for m_I and subsequently for I_z, (2*I* + 1), different discrete orientations are possible, which can be split analogously to the angular momentum into (2*I* + 1) different Zeeman energy levels. The determination of the energy levels are done through

$$E_\mathrm{m} = -\mu_z B_0 = \gamma \hbar m_\mathrm{I} B_0. \tag{5.39}$$

The two most important atomic nuclei for this doctoral thesis are ^{7}Li (spin *I* = 3/2) and ^{31}P (spin *I* = 1/2)and thus there is a splitting into four or two energetically different levels, as in Figure 5.9 is shown.

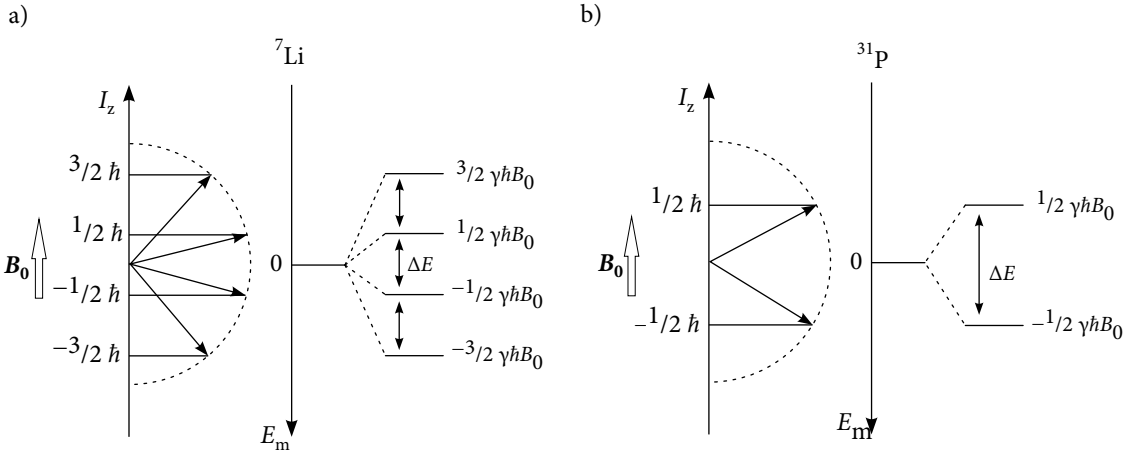

Figure 5.9: a) and b) Illustration of the Zeeman levels of different nuclei in an external magnetic field $\boldsymbol{B}_0$. I_z can take different orientations here and leads in different equidistant energy levels *E*. a) Representation for a ^{7}Li nucleus with a spin of *I* = 3/2. b) Splitting of a ^{31}P nucleus with a spin of *I* =1/2. Illustration according to reference 158 and 157.

Spin transition between the Zeeman levels are allowed, if the conditions $\Delta m_\mathrm{I} = \pm 1$ is satisfied. The energy leveles are equidistant and their absolute values are field dependent (see Figure 5.8b) and c)). This effect is the so-called *Zeeman splitting*. The energy that required depends on the gyromagnetic ratio, the external magnetic field and the frequency.

$$\Delta E = h\nu = \gamma B_0 \hbar = \omega_0 \hbar. \tag{5.40}$$

Here, ν is the frequency and ω_0 the radial frequency. The distribution to the individual energy levels take place in the thermodynamic equilibrium according to the Botzmann distribution.

Let´s take a look a spin $I = {}^3/_2$, such as ^{7}Li:
The distribution to the individual energy levels takes place in the thermodynamic balance according to a *Boltzmann distribution* and is temperature dependent. For nucelei with a spin of I = 1/2 (e.g. Li) it would require the occupation of a lower Zeeman energy levels N_β and a higher N_α look like this

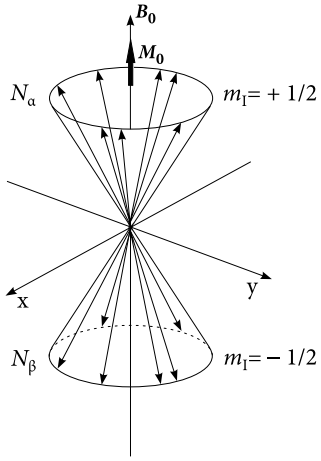

Figure 5.10: Representation of the macroscopic magnetization for the spin $^1/_2$; marked with the Zeemann energy levels N_β and N_α.

The summation of all z-components results in a net magnetization along the z-axis called $\mathbf{M}_0$

$$\mathbf{M}_0 = \sum_i \mu_{z,i} \cdot e_x. \tag{5.41}$$

Consequently the macroscopic magnetization is directly related to the occupation of the different states which for example can be described by a Boltzmann distribution. For a spin$^1/_2$ nucleus with z-components α and β it is

$$\frac{N_\alpha}{N_\beta} = \exp\left(-\frac{\Delta E}{k_B T}\right) = \exp\left(\frac{\gamma h B_0}{2\pi k_\mathrm{B} T}\right). \tag{5.42}$$

where k_B is the Boltzmann constant, T the temperature and N are the Zeeman levels, where N_β is the low and N_α the high energy level as seen in Figure 5.8 b) and c). The total magnetization, as already mentioned in equation (5.41), is composed of the sum N of all magnetic moments μ_I The transition in both directions, from the lower to the higher energy levels and iversely can be described through the population difference, where adsorption is an dominant process. *i.e.* the detected signal is the population difference

$$N_\beta - N_\alpha = N_\mathrm{s} \frac{\gamma h B_0}{4\pi k_\mathrm{B} T}. \tag{5.43}$$

where N_s is the number of all protons (in the case of I=1/2 in the sample.[142,157,158]

Radio Frequency pulses

The macroscopic total magnetization already mentioned above is composed of the sum N of all the magnetic moments μ_I in a defined sample volume V. Equation (5.34) can be modified to

$$\frac{d\mathbf{M}}{dt} = \gamma(\mathbf{M} \times \mathbf{B}_0). \tag{5.44}$$

If the magnetization is at the equilibrium and the magnetic moment precess in field $\boldsymbol{B}_0$ it can be written

$$\mathbf{M} = \mathbf{M}_0 = \mathbf{M}_z \quad \text{and} \quad \mathbf{M}_x = \mathbf{M}_y = 0 \tag{5.45}$$

and is seen in Figure 5.8. During a NMR measurement, the thermal equilibrium is disturbed by applying a radio frequency (rf) -field $\boldsymbol{B}_1$. A small coil is placed perpendicular to the field $\boldsymbol{B}_0$ in xy-plane. The time-dependent linearly oscillating magnetic field $\boldsymbol{B}_1$ can be written as

$$\mathbf{B}_1 = \mathbf{B}_1 \cos(\omega t) \cdot \mathbf{e}_x \tag{5.46}$$

where e_x is the vector in x-direction in the laboratory coordinate system. The polarized field can also be described with two counter rotating fields rotating around the z-axis; clockwise and anti-clockwise.

$$\mathbf{B}_1 = \frac{1}{2}B_1 \cos(\omega t)\mathbf{e}_x + \frac{1}{2}B_1 \sin(\omega t)\mathbf{e}_y + \frac{1}{2}B_1 \cos(-\omega t)\mathbf{e}_x + \frac{1}{2}B_1 \cos(-\omega t)\mathbf{e}_y \tag{5.47}$$

The second term rotates in the opposite direction as the magnitization does and thus it has no influence and can be ingnored. Consequentely, equation (5.47) can be re-written as $\boldsymbol{B}_0$ in xy-plane. The time-dependent linearly oscillating magnetic field $\boldsymbol{B}_1$ can be written as

$$\frac{d\mathbf{M}}{dt} = \gamma\mathbf{M} \times (\mathbf{B}_0 + \mathbf{B}_1(t)). \tag{5.48}$$

One last important point is the introduction of the *rotating coordinate system*. During an NMR measurement, a radio frequency pulse (rf pulse) designed to bring the spins from their relaxed state to an excited non-equilibrium state, thus creating spin transitions. To eliminate the time dependence of this radio frequency field, a rotating coordinate system around $\boldsymbol{B}_0$ can be used. In this the rf pulse leads to two oppositely rotating fields: one that is in the opposite direction of the magnetization and can be ignored (as already mentioned above), and one that appears stationary along the rotating x-axis, here referred to as $\boldsymbol{B}_1$. The two fields lead to one effective magnetic field $\boldsymbol{B}_{\text{eff}}$

$$\mathbf{B}_{\text{eff}} = \mathbf{B}_1 + \frac{\boldsymbol{\omega}}{\gamma} \tag{5.49}$$

The term ω/γ results from transformation of the stationary to the rotating coordinate system. If the frequency of $\boldsymbol{B}_1$ is equal to ω_0 and the magnetization $\boldsymbol{M}$ preciss around $\boldsymbol{B}_1$. The precission

frequency is ω_1 and so if the rf pulse is applied for a time t_p, the angle ϑ, through which the rotation of the magnetization is given as

$$\vartheta = \omega_1 t_p = |\gamma| B_1 t_p \tag{5.50}$$

ϑ is the so-called *flip angle*. By altering the time for which the rf-pulse is applied, the angle can be changed with which the magnetization is rotating. The most common used angles are based on the pulse angles 90° ($\pi/2$) and 180° (π). In case of a 90° pulse the magnetization rotates from the equilibrium state to the y′ axis. In contrast to that the 180° pulse ends up at the z′ axis and is called the inversion pulse. In Figure 5.11 the direction of the magnetization vectors are shown. The receiver coil (generates the rf pulses) is in the xy-plane and the transverse magnetization $M_{y'}$ is important for the detection of the signal. It records a free induction decay (FID) which reaches a signal with its maximum intensity at a 90°, whereas no signal is detected for a 180° (π) pulse (as shown in Figure 5.11).[114,142,157,158]

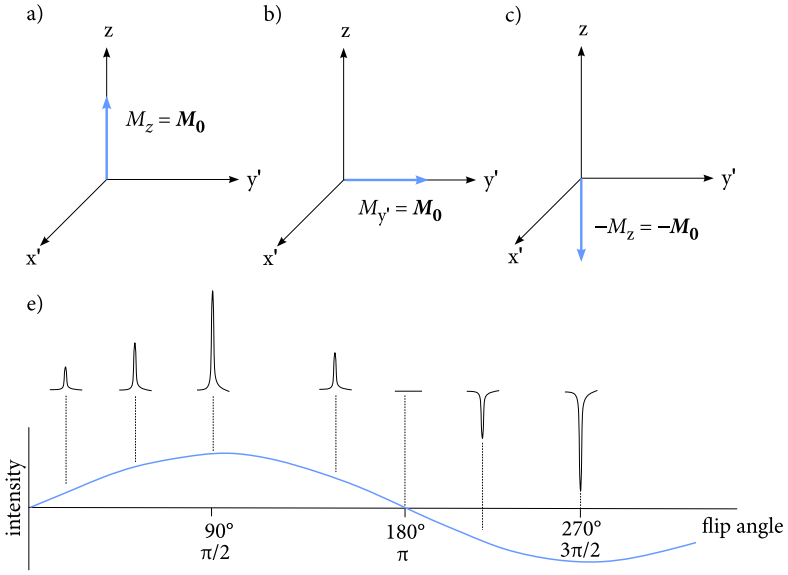

Figure 5.11: Direction of the magnetization a) at the equilibrium state, b) at a $\pi/2$-pulse and c) at a π-pulse. The radio frequency pulse that disturbs the net magnetization is perpendicular to the "static" magnetic field $\boldsymbol{B}_0$. However, the result is a magnetic field $\boldsymbol{B}_1$ which is at the x′ axis. e) Illustrates the pulse-acquire experiment in which the ϑ is varied and results in the different intensities. At a flip angle of 180° no signal can be detected and at 90° the maximum intensity results. Adapted from reference 158.

5.2.2 Spin-lattice Relaxation and Diffusion

As already mentioned in the previous section, in an external magnetic field $\boldsymbol{B}_0$ all spins are thermodynamically balanced and according to the Boltzmann distribution the spins are occupied in different energy levels (N_α and N_β; see also Figure 5.10and 5.9). In a NMR experiment the spins change from a equilibrium state into a non-equilibrium state by applying a rf-pulse and the *relaxation* immediately starts back into the equilibrium state. These relaxation processes and

the therefore associates rates provide a detailed information about the dynamics of the respective charge carrier diffusion in the materials.[114,115,119]

The rf-pulse deflects the magnetization in the x,y-plane. In the subsequent return to the initial state can be distinguish between two different phenomena: i) the relaxation in the direction of the external magnetic field, characterized by the *spin-lattice* (SLR) or *longitudinal relaxation* time T_1 and ii) the relaxation perpendicular to the direction of the applied magnetic field leading to *spin-spin* or *transversale relaxation* time T_2. This phenomena has been described by Felix Bloch with the following equations:

$$\frac{dM_z}{dt} = -\frac{M_z - M_0}{T_1} \tag{5.51}$$

$$\frac{dM_{x\prime}}{dt} = -\frac{M_{x\prime}}{T_2} \text{ and } \frac{dM_{y\prime}}{dt} = -\frac{M_{y\prime}}{T_2} \tag{5.52}$$

The reciprocal relaxation times T_1^{-1} and T_2^{-1} correspond to rate constants for both relaxation processes.

In the case of the longitudinal relaxation time T_1, energy is exchanged between the spins and the lattice, that is the reason calling it spin-lattice relaxation. The rate $1/T_1$ of this process can be described with equation (5.51). As a result, the magnetization again builds up along the z-axis towards the thermal equilibrium M_z=M_0. Relaxation is mainly induced by the motion of atoms or ions that induce fluctuations in the field of the nuclei and thus results in a function of time:

$$M_z(t) = M_0 \left(1 - exp\left(-\frac{t}{T_1}\right)\right). \tag{5.53}$$

The time-dependent return to the equilibrium state induces this AC signal, which decays exponentially and is known as FID ("free induction decay"). With the aid of a Fourier transformation, this time-dependent signal can be generated in be converted to a frequency-dependent, which ultimately leads to the typical NMR spectrum.[114,115,140,157,158]

An alternative method to T_1 is to measure $T_{1\rho}$ in a rotating coordinate system using a weak rf pulse, to measure the magnetization and to fix it the transversal plane. The relaxation then again leads to a time-dependent rate $1/T_{1\rho}$. $T_{1\rho}$ delivers times shorter than T_1, allowing detection slower atomic movements.[157,158]

Correlation and Spectral Density Function

In general, relaxation processes can be decribed via the *spectral density function* $J(\omega)$ and is the Fourier transformation of its *autocorrelation function* G(t), which describes the ensemble average of the transition between the spins i and j. $G^{(q)}$ denotes the spin transitions with $\Delta m = \pm q$, where q describes the change in total angular momentum, hereby describing single or multiple quantum transitions. The autocorrelation function measures the correlation of the time τ with the field $\tau = 0$ and can be written as

$$G^{(q)}(\tau) = G^{(q)}(0) exp(-|\tau|/\tau_c) \tag{5.54}$$

where $G(0)$ is the local field at $\tau = 0$. The time between these fluctuations is the correlation time τ_c. Additional, the spectral density function can be calculated through

$$J_{ij}(\omega) = \int_{-\infty}^{+\infty} G_{ij}(\tau) exp(-i\omega\tau) d\tau. \tag{5.55}$$

The spectral density function of the spin lattice relaxation is related to $1/T_1 \propto J(\omega_0)$ and at $\omega = \omega_0$ the relaxation has been induced. The relaxation rates of spin-lattice relaxation T_1 in the laboratory frame can be determined as follows

$$R_1 \equiv \frac{1}{T_1} = \frac{3}{2}\gamma^4\hbar^2 I(I+1)\left[J_D^{(1)}(\omega_0) + J_D^{(2)}(2\omega_0)\right] \tag{5.56}$$

and $J^{(q)}$ denotes the spin transition. A second equation also add to a total relaxation rate as also seen in equation (5.56)

$$R_1 \equiv \frac{1}{T_1} = \frac{9}{128}\left(\frac{eQ}{\hbar I}\right)^2\left[J_D^{(1)}(\omega_0) + J_D^{(2)}(2\omega_0)\right]. \tag{5.57}$$

Here, eQ describes the electrical quadropol moment. R_2, spin-spin relaxation, can be calculated in a similiar way.

Furthermore, plotting the curve of the spectral density function against ω the area (A) under curve is independent of τ_c

$$A = \int_0^{+\infty} G(0)\frac{2\tau_c}{1+(\omega\tau)^2} d\omega \tag{5.58}$$

which means, when the area is constant $J(\omega)$ has a maximum at $\omega = 0$. Additional τ_c is getting smaller and also the maximum is decreasing which results in $J(\omega)$ with higher frequencies. This is an important deliberation, if thinking about the spectral density at Lamor frequency vs the correlation time τ_c. Plotting both parameter against each other it also results in a peak maximum, which occurs at $\omega_0\tau_c = 1$. However, taking all facts into contrast a *reduced spectral density function* j(ω) results[119,156–158]:

$$j(\omega) = \frac{2\tau_c}{1+(\omega\tau)^2}. \tag{5.59}$$

Rotating frame – $T_{1\rho}$

As already mentioned another important method is the measurement in a rotating coordinate system. Spin-locking NMR records the ionic motion that is too slow for the spin-lattice relaxation measurement and can be recorded in the kHz range. The static external field $\boldsymbol{B}_0$ is replaced by a locking field $\boldsymbol{B}_1$. During the locking pulse the magnitization is polarized along $\boldsymbol{B}_1$ and the magnetization M_ρ is locked to the x′, y′-plane. The relaxation rate can be determined via

$$R_{1\rho} \equiv \frac{1}{T_{1\rho}} = \frac{3}{2}\gamma^4\hbar^2 I(I+1)\left[J_D^{(0)}(2\omega_1) + 10J_D^{(1)}(\omega_0) + J_D^{(2)}(2\omega_0)\right] \tag{5.60}$$

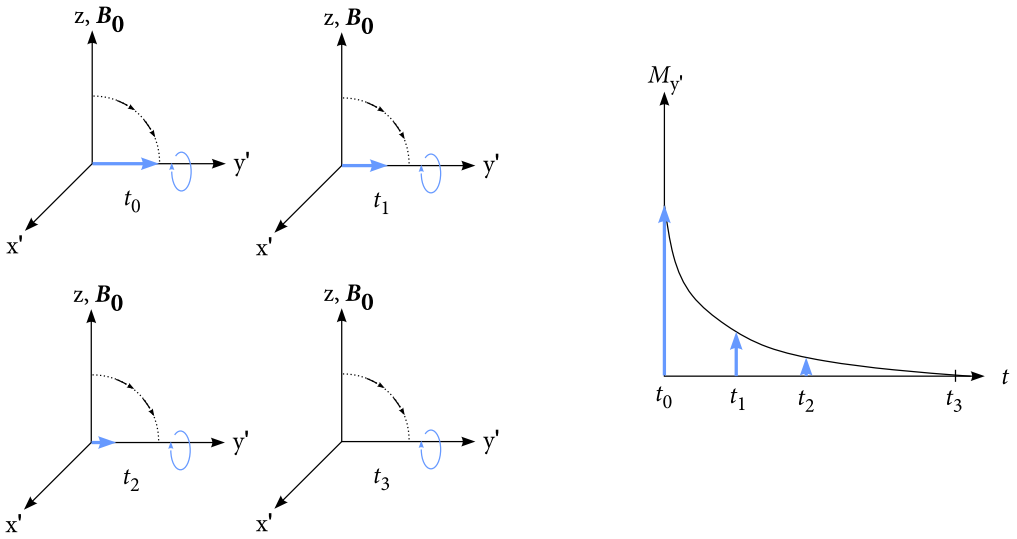

Figure 5.12: Graphical representation of a $T_{1\rho}$ experiment after applying a spin-lock field. On the right side the corresponding FID is shown. Figure according to equation (5.60) and (5.61).

and

$$R_{1\rho} \equiv \frac{1}{T_{1\rho}} = \frac{9}{640}\left(\frac{eQ}{\hbar I}\right)^2 \frac{2I+3}{2I-1}\left[J_{\mathrm{D}}^{(0)}(2\omega_1) + 10J_{\mathrm{D}}^{(1)}(\omega_0) + J_{\mathrm{D}}^{(2)}(2\omega_0)\right]. \tag{5.61}$$

In Figure 5.12 the $T_{1\rho}$ experiment is visualized.[140,157,158]

3D Diffusion and BPP Model

The interpretation of the NMR data obtained in relaxation measurements are very complex in most cases. Therefore, simplifications are mostly used to interpret the data. Most frequently, the relaxation rates are analyzed using an Arrhenius diagram, in which the logarithm of $1/T_1$ or $1/T_{1\rho}$ is plotted against the inverse temperature, as shown in Figure 5.13. The black solid lines in Figure 5.13 represent a three-dimensional, ordered diffusion process that uses the commonly used BBP model which has been introduced by Bloembergen, Purcell and Pound[159]. So remember from section "spectral density function" that this model describes a correlation function that shows a simple exponential decay as seen in equation (5.54). τ corresponds to the correlation time, which is directly related to the average residence time of an ion between two successful jumps. The Fourier transform of G(t) leads to a Lorentzian-shaped spectral density function J(ω), which is directly proportional to the relaxation rate $1/T_1$

$$\frac{1}{T_1} \propto J(\omega) = G(0)\frac{2\tau}{1+(\omega_0\tau)^2}. \tag{5.62}$$

The temperature dependence can be described through the Arrhenius connection

$$\tau = \tau_0 \cdot \exp\left(\frac{E_a}{k_{\mathrm{B}}T}\right) \tag{5.63}$$

where τ_0 is the pre-factor, E_a the activation energy of a successful jump between two lattice sites, k_B the Boltzmann constant and T the temperature.

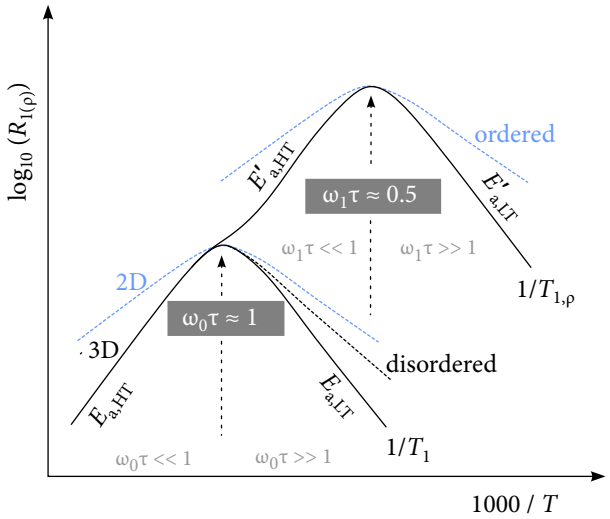

Figure 5.13: Graphical illustration of the relaxation rates R_1 and $R_{1\rho}$. Additionally, $R_{1(\rho)}$ rate peaks observed for 3D diffusion according to the BPP model (solid line), 2D difusion (dashed-blue line), and also the disorder of a system (dashed-black line). If the resulting rate peak is symmetric ($E_{a,HT} = E_{a,LT}$) an ordered system occurs. A lower dimensionality leads to a smaller slope of the high-temperature flank, whereas the disorderd system influences the low-temperature limit. Adapted figure of reference 158.

With increasing temperature T and with a defined Lamor frequency ω_0 the relaxation rates $R_{1(\rho)}$ are increasing and pass through a distinct maximum at T=$T_{\max}$ (see Figure 5.13). Furthermore, in a spin-lattice relaxation experiment $T_{\max}$ can be described through the relation $\omega_0\tau_c \approx 1$. It has to be mentioned that through the relation of $\tau_c^{-1} = \tau^{-1}$ the jump rate can be determined. Accordingly, plotting the inverse temperature against the logarithm of R_1 or $R_{1\rho}$ two flanks appear, which are usually denoted as high-temperature (HT) and low-temperature (LT) flank. In the LT limit following relation has been observed

$$R_1 \propto \frac{1}{\tau_c \omega_0^2} \quad \text{for} \quad \omega_0\tau_c \gg 1 \tag{5.64}$$

and results in a symmetric rate peak as seen in Figure 5.13. However, at $T > T_{max}$ (HT-flank) the Lamor frequency is much greater than the correlation, $\omega_0\tau_c \ll 1$, and equals to

$$R_1 \propto \frac{1}{\tau_c} \quad \text{for} \quad \omega_0\tau_c \ll 1 \tag{5.65}$$

In Figure 5.13 both flanks a represented, whereas the LT-flank indicates the short-range motion and the HT-flank the long-range motion of the ions or atoms.

The same phenomena can bee explained for the rotating frame $R_{1\rho}$, however, the condition of SLR $\omega_0\tau_c \approx 1$ can be replaced to $\omega_1\tau_c \approx 0.5$. The SLR operates in a much higher and longer time scale than the rotating frame, which is sensitive to jump rates with a frequency of $\omega_1 = 10^5 s^{-1}$. Due to the lower locking field the $R_{1\rho}$ rate maxima are shifted towards lower temperatures as graphical illustrated in Figure 5.13.

In addition, it is still possible from the slope of each flank to calculate an activation energy calculate, $E_{\mathrm{a,HT}}$ for high temperatures and $E_{\mathrm{a,LT}}$ for low temperatures. The BBP model assumes

symmetric rate peaks in which the two activation energies are identical $E_{a,HT} = E_{a,LT}$. However, in reals samples and also in this thesis investigated materials, however, will receive asymmetric rate peaks. Correlation effects such as structural disorder and / or Coulomb interactions affect the low temperature region on the right side and lead to lower activation energies.[160] Dimensionalities affect the activation energies in the HT-flank. If a material is a two-dimensional (2D) ion conductor, for example in layered materials, the slope is flatter than in a 3D behavior. Furthermore, the HT-flanks of R_1 and $R_{1\rho}$ run parallel, whereas in a 3D conductor both have the same activation energies.[114] This asymmetric peaks can be described with a modified BPP-model

$$J(\omega) = G(0)\frac{2\tau_c}{1+(\omega\tau_c)^\beta} \tag{5.66}$$

where $1<\beta \leq 2$. Thus, $R_{1(\rho)}$ can be written as

$$R_1 = C_1\left[\frac{\tau_c}{1+(\omega_0\tau_c)^\beta} + \frac{4\tau_c}{1+(2\omega_0\tau_c)^\beta}\right] \tag{5.67}$$

$$R_{1\rho} = C_{1\rho}\left[\frac{6\tau_c}{1+(2\omega_1\tau_c)^\beta} + \frac{10\tau_c}{1+(\omega_0\tau_c)^\beta} + \frac{4\tau_c}{1+(\omega_0\tau_c)^\beta}\right] \tag{5.68}$$

where *C* is the coupling constant. As already mentioned, the LT-flank influences the correlation parameters and therfore, the slope and the frequency changes. The HT-flank have no influence on the correlation only on the dimensionality.

$$R_1 \propto \tau_c \text{ for } \omega_0\tau_c \ll 1 \tag{5.69}$$

$$R_1 \propto \tau_c^{1-\beta}\omega_0^{-\beta} \text{ for } \omega_0\tau_c \gg 1 \tag{5.70}$$

Resulting in an asymmetric rate peak, two different activation energies for the HT and LT flank can be calculated as shown in the following equation

$$E_{\text{a,LT}} = (\beta-1)E_{\text{a,HT}}. \tag{5.71}$$

To sum up, all these values can be interpreted via the length scale of diffusion. A small activation energy on the LT side describes a short range motion, whereas the HT-side is characteristic for the long-range motion. 1D or 2D diffusion leads to small slopes and therefore small activation energies, which are typical for materials with chanel structure or layered structure, especially glasses. However, SLR depends on the frequency and on the magnetic field that has been used.

Linewidth

For insights into the ion dynamic of solids, can be deduced from the motional narrowing (MN) from the static NMR measurements by varying the temperature. At very low temperatures a so-called rigid lattice can be observed, where the jump process τ^{-1} is much smaller than the spectral width. In this region the line follows a dipolar broadened Gaussian line shape. By increasing the temperature the jump process becomes faster and faster and is comparable to the jump process

τ^{-1}. The resulting dipol-dipol interaction are resulting in a motional narrowed line which has usually a Lorentzian NMR line shape.[114,153,161,162]

Besides the SLR the MN is another method, sometimes considered to be less reliable, to extract activation energies from *i.e.* Li diffusivity. Abragam[156] and Hendrickson and Bray[163,164] introduced models to use the change in line widths to deduce activation energies for the hopping process behind.[153] The Hendrickson and Bray equation can be written as[163]

$$\Delta\nu(T) = \Delta\nu_0 \left\{ 1 + \left[(\Delta\nu_0/B) - 1 \right] \exp\left(-\frac{E_{\mathrm{a,HB}}}{k_{\mathrm{B}}T} \right) \right\}^{-1} + \nu_\infty \tag{5.72}$$

where $\Delta\nu(T)$ is the line width at a defined temperature and B describes the number of ions that are thermally activated.[163] The final line width ν_∞ is determined by the inhomogeneities of the external magnetic field $\boldsymbol{B}_0$.

Another formalism to investigate the linewidth is that found by Abragam[156]:

$$\Delta\nu^2(T) = \Delta\nu_0^2 \frac{2}{\pi} \arctan\left[\alpha\Delta\nu(T)\tau_\infty \exp\left(\frac{E_{\mathrm{a,A}}}{k_{\mathrm{B}}T} \right) \right] + \Delta\nu_\infty^2. \tag{5.73}$$

Here, α is a fitting parameter, which is mostly set to one and τ_∞ is the pre-factor that is comparable to τ_c from the underlying Arrhenius law.[98,153,156,162]

Diffusion Coefficient

From the rate peaks of the relaxation measurements it is the possible to determine a microscopic diffusion coefficient. Additionaly, from the maximum condition $\omega_0\tau_c \approx 1$ (and in case of the rotating frame $\omega_1\tau_c \approx 0.5$) a jump rate τ^{-1} can be calculated through equation (3.24). If the mean jump distance between two lattice sites is known, the microscopic NMR self-diffusion coefficient D_{NMR} can be determined. The correlation between NMR and impedance spectroscopy, has already been discussed in section 5.1.4.

5.2.3 Spin Alignment Echo

Spin-alignment echo or also known as *stimulated-echo* (SAE), which was first measured by Spiess et al.[165,166], measures the direct access of single-spin motional correlation function. SAE is sensitive to ultra-slow hopping processes, *i.e.* the Li hopping process can be detected with the jump rate lower than 10^{-4} s^{-1}. However, the amplitudes of this technique are damped by the diffusion process and long-range transport parameters can be measured from a macroscopic point of view.[114,167,168]

In general, the SAE NMR technique takes advantages of the interaction of the quadrupole moment Q of the nucleus with an electric-field gradient (EFG). The specific quadrupole frequency can be monitored as a function of time and is correlated to two different points of time. Therefore,

SAE can be used to detect a jump between two electric in-equivalent atomic sites with the pulse sequence of Jeener-Broekart[169]:

$$(\beta_1)_{\phi 1} - t_{\mathrm{p}} - (\beta_2)_{\phi 2} - t_{\mathrm{m}} - (\beta_3)_{\phi 3} - t. \tag{5.74}$$

This sequence is separated through a preparation time t_p and a mixing time t_m and consists of three pulses with different pulse length β_i and ϕ_i. In Figure 5.14 an classic SAE experiment is shown with three 90° pulses. If β_1=90° and β_2=β_3=45° the amplitude of the spin-alignment echo

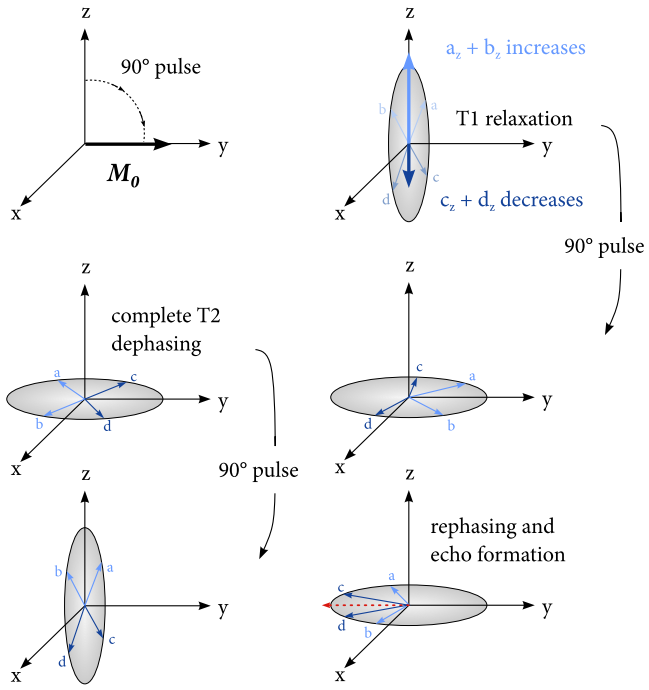

Figure 5.14: Formation of a stimulated echo of three 90° pulses. After the second pulse, the z-components of the spins that do not precess but grow in the $+z$-direction by T_1 relaxation. These "stored" longitudinal components are flipped back into the transverse plane by the 3rd RF-pulse, then re-phase and form an spin alignment echo. Adapted figure 170.

is maximal, which means that it is a two-time hopping correlation function and can be describes as follows, where $\langle ... \rangle$ is a notation to describe a average

$$S_2(t_p, t_m, t) = \frac{9}{20} \langle \sin\left[\omega_Q(0) t_p\right] \sin\left[\omega_Q(t_m) t\right] \rangle \tag{5.75}$$

Here, the decay of the echo amplitude, which observes the diffusive motion of the ions, is controlled by a quadrupole relaxation. Furthermore, Spin-spin and spin-lattice relaxation have to be take into account. The echo can be described through a exponential decay and the longitudinal decay of R_1 and the transverse decay t_{p} that are influencing the spin-alignment. At very low temperatures the echo can be absorbed by the influence of spin-diffusion. Thus, the correlation function can further be described with a stretching factor resulting in an independent quadrupole

frequency the so-called SAE decay rate $1/\tau_{\mathrm{SAE}}$. The time constants are not influences by the magnetic field.[161,167,168,171]

For the study of spin-alignment decay processes it is first necessary to have an exact knowledge of the T_1 and T_2 relaxation parts of S_2. For a constant evolution time $t_{\mathrm{p}} \rightarrow 0$, the time-dependent recording of the alignment echo at the location $t = t_{\mathrm{p}}$ becomes the direct auto correlation function with a correlation time $\tau_c \approx \tau_{\mathrm{SAE}}$. In general, the $S_2(t_{\mathrm{p}}, t_{\mathrm{m}}, t)$ equation can be introduced as follows[161,167,168]

$$S_2(t_p, t_m, t) = S_0 + (A\exp(-(t_m/\tau_{SAE})^{\gamma 1}) + B \cdot \exp(-(t_m/T_1)^{\gamma 2}) \tag{5.76}$$

Equation (5.76) and Figure 5.15 indicate the general case that the stretched-exponentially decaying correlation function $Aexp(-(t_m/\tau_{SAE})^{\gamma 1} + B)$ contained in S_2, falls to a finite value *B*. The residual correlation S_∞ is then given with S_∞=B/(A+B). However, with a further decay process or isotropic motion process $S_2 = S_0 = 0$ can be reached. In Figure 5.15 the pathway of the SAE measurement with $S_\infty = 0$ and $S_\infty \neq 0$ is shown. However, t_p provides information about the

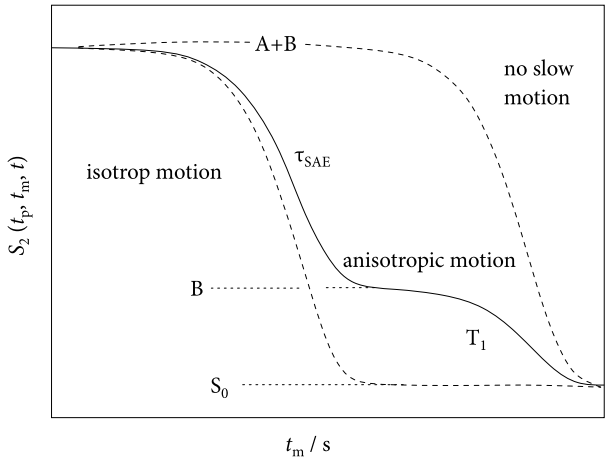

Figure 5.15: $S_2(t_p, t_m, t)$ run according to equation (5.76) for a constant evolution time t_p in dependence of the mixing time t_m. *B* marks the residual correlation value in general the trap of an anisotropic motion process. In case of isotropic motion S_2 falls to zero. The residual correlation S_∞ is here given to S_∞ = *B*. Figure has been adapted from reference 167.

geometry, whereas t_m gives a approach about the timescale and the dynamics in a material. If $t_p \rightarrow 0$ the number of in-equivalent sites can be calculated through

$$\lim_{t_p \rightarrow 0} S_\infty(t_p) = 1/N \tag{5.77}$$

and is adequate for equal site populations with a limited number on in-equivalent occupied sites. Therfore, the jump process of the atom is hindered. Otherwise, S_∞ has to be considered, that is correlated to the quadrupole coupling.

$$S_\infty(t_p) = \frac{S_2(t_p, t_m \rightarrow \infty, t_p)}{S_2(t_p, t_m \rightarrow 0, t_p)} \tag{5.78}$$

If ther is a number of infinite in-equivalent sites, the correletion function tends to zero and is infuenced by a weighting factor w_i and of the sites *i*.

$$\lim_{t_p \to \infty} S_\infty(t_p) = \sum_i^N w_i^2 \tag{5.79}$$

5.2.4 MAS-NMR

Solid-state NMR measurements are not only used to study charge carrier dynamics but also allow the structural elucidation of samples. *Magic-Angle-Spinning* (MAS) NMR is an important method for obtaining high-resolution data for clarification of the structure of solid samples to obtain. In liquids anisotropic interactions, such as dipolar couplings and chemical shifts by the fast motion of molecules are averaged out, resulting in sharp and thus well-resolved signals. In solids, however,

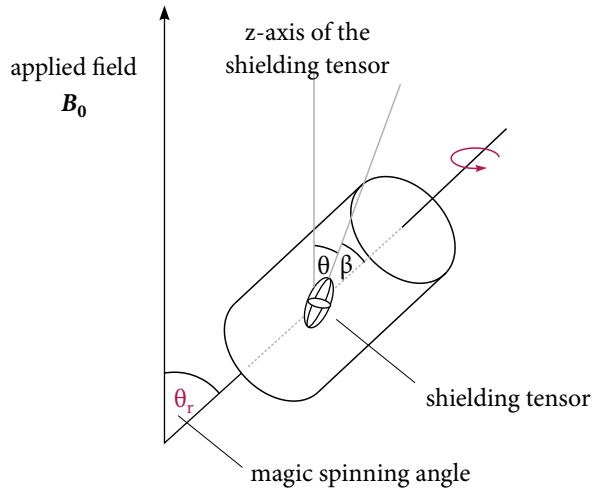

Figure 5.16: Schematic representation of the MAS NMR technique. The sample rotates with a magic angle of 54.74° against the extern magnetic field $\mathbf{B}_0$. The figure has been adapted from reference 172 and 173.

these interactions result in broad NMR lines that prevent accurate analysis or interpretation of the data. To do this and to achieve a high resolution, it is possible to rotate the sample very fast at an angle of 54.74° (magic angle; see Figure 5.16) against the external magnetic field $\mathbf{B}_0$. It results in a narrow well-defined signal due to the inhibition of the anisotropic interactions.

In solids, interactions such as chemical shift anisotropy or dipolar or quadrupole coupling leads to a broad signal. The chemical shift provides information about the crystallographic positions. The anisotropic portions lead to sidebands, which are arranged symmetrically to the left and right of the isotropic line. However, their position depends on the rotation speed, so they are relatively easy to identify and can be assigned to crystallographic positions.[157,172,173]

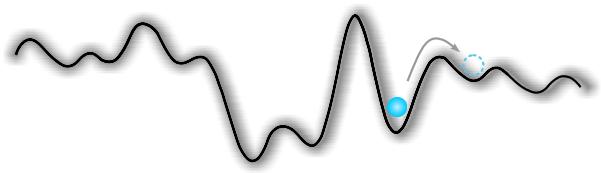

6 Results and Discussion

Contents

In this work different, especially oxide-based, halide-based and sulfide-based, solid electrolytes were examined. The synthesis of nearly all products was done *via* classical solid state reaction, which contains a milling step as well as an annealing step. For some compounds, the hydrothermal reaction was carried out because more pressure was needed to produce the products. The subsequent structural analysis of the products was analyzed through X-ray powder diffraction and the clarification of the structure was done through Rietveld analysis. The focus of this thesis was mainly on the investigation of the microscopic and the macroscopic ion motion and the charge carrier dynamic of the different materials. On the one hand impedance spectroscopic conductivity measurements were realized and on the other hand complementary NMR (spin-lattice relaxation) measurements to study different dynamic parameters on different length scale.

The following chapter describes the results of the experimental work of this doctoral thesis. The results are presented in cumulative form of already published or submitted *peer-reviewed*

journals (P) and manuscripts (M). They are divided into two sections relating to the investigated materials. Each article comes up with a short introduction and eventual additional information.

6.1 Oxide-based Solid Electrolytes

Over the past decades, the interest in modern, electrochemical energy storage systems has increased. In particular, the development of solid-state batteries containing a solid electrolyte. All solid-state batteries can on the one hand operate at higher temperatures and on the other hand increases the energy density which allows the direct use of lithium metal as anode. In addition the use of solid-state electrolytes leads to a improved cycle stability, durability and safety compared to liquid, flammable electrolytes.[10,69] As most promising candidate of solid electrolytes are oxide-based electrolytes with high lithium-ion conductivity. There are two groups of oxide electrolytes, the crystalline group (NASICON, perovskite, garnet) and the amorphous/ glass group, like Li_2O-MO_x (M= B, Si, P, etc.). Compared to other inorganic solid lithium-ion conductors, oxide ion conductors are stable at high temperatures and at ambient air, thus the manufacturing is easy to handle.[56]

The following published article includes the investigation of a NASICON-type (Na superionic conductor) material with the formula $Li_{1+2x}Zr_{2-x}M_x(PO_4)_3$, with M=$Ca^{2+}$ and x=0.0-0.2, relating to the lithium-ion dynamic and doping effects. Of course other dopants, especially x=Hf^{2+} have been prepared and examined. Furthermore, the well-known material $LiTi_2(PO_4)_3$ including a defined amount of Fe^{2+} are examined via impedance spectroscopy. Both $Li_{1+2x}Zr_{2-x}M_x(PO_4)_3$ (M: Hf) and $Li_{1+2x}Ti_{2-x}M_x(PO_4)_3$ (M: Fe) are not implemented in this thesis but both publications are under preparation.

6.1.1 Ion Dynamics in $LiZr_2(PO_4)_3$ and $Li_{1.4}Ca_{0.2}Zr_{1.8}(PO_4)_3$

The aim of this publication is to separate and analyze the total conductivity of a ion conductor ($LiZr_2(PO_4)_3$-LZP). LZP is a material that is due to its good bulk ionic conductivity and its negligible electronic conductivity a suitable solid-state ionic conductor.[174] It crystallizes with NASICON structure (*sodium superionic conductor*), a structure in which the charge carriers move along the interstitial site and which are known for their high ionic conductivity.[74] There are many results known for the highly conductive $LiTi_2(PO_4)_3$ (LTP) (same family as LZP). This solid electrolyte is difficult to sinter and has a very high g.b. resistance and also the Ti ion can be easily reduced from +4 to +3 in contact with metallic Li as anode. Therefore, an alternative electrolyte can be $LiZr_2(PO_4)_3$, which has Zr^{4+} as a more stable cation. But in contrast to LTP a very low ionic conductivity, $\sim 10^{-8}$ S cm^{-1}, is reached. By increasing the sintering temperature the rhombohedral phase can be prepared and results in a bulk value of $\sim 10^{-5}$ S cm^{-1}.[71,175]

$LiZr_2(PO_4)_3$ and $Li_{1+2x}Ca_xZr_{2-x}(PO_4)_3$ (x= 0.1 and 0.2) were prepared through solid-state reaction, with a calcination step at 900 °C and a sintering step at 1150 °C. The characterization

of the structure was done *via* X-ray powder diffraction, and therefore the associated Rietveld analysis. To differ between grain boundary (g.b.) and bulk processes impedance spectroscopy was used. Measurments at very low temperatures (-100 °C) made it possible to differ between both processes. Furthermore, it was shown that the ionic conductivity, prepared with different starting materials, increases at higher temperatures by one order of magnitude. As mentioned at the beginning, LZP has been doped with 5 % and 10 % Ca^{2+} and subsequently characterized with impedance spectroscopy. It has to be noticed that the conductivity of the doped sample with 10 % Ca shows a two orders of magnitude higher g.b. conductivity.

M1:
Ion Dynamics in $LiZr_2(PO_4)_3$ and $Li_{1.4}Ca_{0.2}Zr_{1.8}(PO_4)_3$
I. Hanghofer, B. Gadermaier, A. Wilkening, D. Rettenwander and H. M. R. Wilkening, *in preparation*

Ion Dynamics in $LiZr_2(PO_4)_3$ and $Li_{1.4}Ca_{0.2}Zr_{1.8}(PO_4)_3$

Isabel Hanghofer,[1,*] Bernhard Gadermaier, Alexandra Wilkening, Daniel Rettenwander and H. Martin R. Wilkening[1,2,†]

[1] *Institute for Chemistry and Technology of Materials, Christian Doppler Laboratory for Lithium Batteries, Graz University of Technology (NAWI Graz), Stremayrgasse 9, A-8010 Graz, Austria*

[2] *ALISTORE – European Research Institute, CNRS FR3104, Hub de l'Energie, Rue Baudelocque, 80039 Amiens, France*

* *corresponding author, e-mail: isabel.hanghofer@tugraz.at*
† *see also for correspondence, e-mail: wilkening@tugraz.at*

Abstract. High ionic conductivity, electrochemical stability and small interfacial resistances against Li metal anodes are the main requirements to be fulfilled in powerful, next-generation all-solid-state batteries. Understanding ion transport in materials with sufficiently high chemical and electrochemical stability, such as rhombohedral $LiZr_2(PO_4)_3$, is important to further improve their properties with respect to translational Li ion dynamics. Here, we used broadband impedance spectroscopy to describe the electrical responses of $LiZr_2(PO_4)_3$ and Ca-stabilized $Li_{1.4}Ca_{0.2}Zr_{1.8}(PO_4)_3$ that were prepared following a solid-state synthesis route. We investigated the influence of the starting materials, either ZrO_2 and $Zr(CH_3COO)_4$, on the final properties of the products and studied Li ion dynamics in the crystalline grains and across grain boundary (g.b.) regions. The Ca^{2+} content has only little effect on bulk properties (4.2×10^{-5} S cm^{-1} at 298 K, 0.41 eV), but, fortunately, the g.b. resistance decreased by 2 orders of magnitude. Whereas, ^{7}Li spin-alignment echo NMR confirmed long-range ion transport as seen by conductivity spectroscopy, ^{7}Li NMR spin-lattice relaxation (SLR) revealed much smaller activation energies (0.18 eV) and points to rapid localized Li jump processes. The diffusion-induced rate peak, appearing at $T = 282$ K, shows Li^+ exchange processes with rates of ca. 10^9 s^{-1} corresponding, formally, to ionic conductivities in the order of 10^{-3} S cm^{-1} to 10^{-2} S cm^{-1}.

Keywords: NASICON, electrolytes, conductivity, ceramics, diffusion

1. Introduction

In the years to come all-solid-state Li or Na batteries[1] are expected to replace conventional systems[2] still relying on flammable aprotic electrolytes. Ceramic cells may take advantage of highly flexible design possibilities if batteries with dimensions in the mm range are considered.[3, 4] Moreover, ceramic batteries will withstand higher temperatures than their analogous cells with liquid electrolytes.[5]

For their realization, ceramic electrolytes with sufficiently high ionic conductivities are, however, needed.[5-9] The overall performance of NaSICON-type (Na SuperIonic CONductor) conductors[10, 11] have attracted renewed interests to study the influence of synthesis conditions and dopants on morphology and ion dynamics. Earlier reports have shown that $LiM_2(PO_4)_3$ (*M*: Ge, Ti, Sn, Hf, Zr) exhibit good chemical stabilities under ambient conditions. This property comes along with a wide electrochemical stability window.[12, 13] $LiTi_2(PO_4)_3$ is known as a very good Li-ion conductor but it suffers from the fact that Ti(IV) can easily be reduced to Ti(III) when in contact with metallic Li.[14]

In contrast to $LiTi_2(PO_4)_3$-based ceramics, including those in which Ti^{4+} is partly replaced by Al^{3+}, $LiZr_2(PO_4)_3$ (LZP) shows a much better stability against Li anodes. LZP crystallizes with different

structures, ionic conductivities sensitively depend on both the overall morphology and the defect chemistry involved. The ionic conductivity can be improved by incoporating different metals such as Y^{3+}, Sc^{3+}, Al^{3+}, La^{3+} or Ca^{2+}; this strategy is usually accompanied by a stabilization of the rhombohedral structure.[13, 15-21] LZP is typically prepared at relatively low calcination temperatures of ca. 1173 K, the phase appearing under these conditions is denoted as the α-phase of LZP, which is subdivided in a orthorhombic form (α) and a monoclinic one (α′). At higher sintering temperatures, that is, approximately 1423 K, the highly conductive rhombohedral structure α-$LiZr_2(PO_4)_3$ crystallizing with *R*-3*c* symmetry is formed. α′-$LiZr_2(PO_4)_3$, obtained at lower temperatures, is usually a mixture of monoclinic LZP and triclinic LZP; its ionic conductivity is reported to be in the order of of 10^{-8} S/cm whereas the α-$LiZr_2(PO_4)_3$ shows values of 10^{-5} S cm^{-1}.[21-24]

In this work, the structure variation of different educts on the product formed is discussed. We analysed Li ion dynamics in $LiZr_2(PO_4)_3$ and $Li_{1+2x}Ca_xZr_{2-x}(PO_4)_3$ (LCZP) by both broadband impedance spectroscopy[25, 26] and ^{7}Li NMR spectroscopy, *i.e.*, by recording diffusion-induced spin-lattice relaxation (SLR) rates[27-29] that are sensitive to both short-range and long-range ion transport through the crystal lattice of LZP. As we deal with powder samples with crystallite diameters in the μm range, NMR is solely sensitive to bulk ion dynamics.

2. Experimental

2.1. Sample preparation

$LiZr_2(PO_4)_3$ (LZP) was prepared via a classic solid state reaction by mixing stoichiometric amounts of Li_2CO_3 (Sigma Aldrich ≥ 99 %), $(NH_4)_2HPO_4$ (Sigma Aldrich ≥ 99.9 %) with either ZrO_2 (Sigma Aldirch ≥ 99 %) or $Zr(CH_3COO)_4$. The starting compounds were mechanically milled for 2 hours by using a high-energy planetary ball mill (Fritsch Pulverisette 7 Premium line) at a rotation speed of 400 rpm. We used ZrO_2 beakers (45 mL), which were filled with 180 balls made of ZrO_2 (5 mm in diameter). The subsequent calcination process was carried out in Al_2O_3 crucibles at 900 °C (heating rate 10 °C/min) for 10 hours, where the decomposition of the hydrogen phosphate starts and initiates the reaction with Li_2CO_3. The resulting white powder was milled again for 2 hours at 400 rpm to guarantee a good contact between the particles. Finally, the mixture was pressed with 0.4 tons into pellets with a diameter of 5 mm. The pellets were filled into Al_2O_3 crucibles and sintered at 1150 °C (heating rate 10 °C/ min) for 20 hours. To incorporate Ca^{2+} into LZP we used $CaCO_3$ (Alfa Aesar > 99 %). An excess of 10 % wt.-% Li_2CO_3 should compensate the loss of lithium during the high temperature heating process leading to $Li_{1.4}Ca_{0.2}Zr_{1.8}(PO_4)_3$ (LCZP). For the synthesis of LZP (and LCZP) using $Zr(CH_3COO)_4$ we needed to prepare the acetate as follows. 20 mmol Zirconium oxochloride (Sigma-Aldrich 99.99 %) was dissolved under reflux in 100 ml of a mixture of MeCOOH (Sigma-Aldrich ≥99.5 %) and Me(COO)2O (Sigma Aldrich ≥99 %) mixture (1:9). After the mixture was cooled to room temperature, a white crystalline deposit appeared. Finally, it was filtered and vacuum dried at 60 °C.

2.2. X-ray powder diffraction

The sample obtained after the calcination process and the finally sintered product was characterized by X-ray powder diffraction (XRPD). We used a Bruker D8 Advance diffractometer operating with Bragg

Brentano geometry and Cu K_α radiation. Diffractgrams were reorded in air atmosphere and at room temperature covering a 2θ range from 20° to 100° with a step size of 0.02° (2s per step). Rietveld refinement was carried out with X-PertHighScorePlus (PANanalytical).

2.3. Impedance spectroscopy

For the impedance measurements the sintered samples were equipped with gold electrodes by a sputtering process. Gold electrodes with a layer thickness of 100 nm on both sides were applied with a sputter coater (LEICA EM SCD 050) to ensure a good electrical contact. To avoid any influence of moisture, the samples were dried at 60 °C under vacuum before the impedance measurements.

Impedance spectra were analyzed with a Novocontrol Concept 80 broadband dielectric spectrometer equipped with a BDS 1200 cell combined with an active ZGS cell (Novocontrol). We measured complex impedances over a frequency range of nine decades (10 mHz – 10 MHz). The temperature in the sample holder was varied from 173 K to 473 K in steps of 20 K; the temperature program is automatically controlled by a QUATRO cryosystem (Novocontrol). During the measurements a dry nitrogen atmosphere is build up around the sample in the cryostat to avoid any contamination with water and/or oxygen.

2.4. Nuclear magnetic resonance measurements

For the time-domain NMR measurements, the powder samples $LiZr_2(PO_4)_3$ and $Li_{1.4}Ca_{0.2}Zr_{1.8}(PO_4)_3$ were sealed in Duran glass rubes (ca. 4 cm in length and 3 mm in diameter). They were kept under dynamic vacuum to protect them from any reactions with humidity. We used ^{7}Li NMR line shape measurements, spin lattice relaxation (SLR) experiments as well as ^{7}Li spin alignment echo (SAE) NMR to collect information about Li activation energies and jump rates. Longitudinal NMR SLR rates ($1/T_1$) as well as spin-lock rates ($1/T_{1\rho}$) were measured with a Bruker Avance III spectrometer that is connected to a shimmed cryomagnet with a nominal magnetic field of 7 T. This field corresponds to a ^{7}Li Lamor frequency of $\omega_0/2\pi$ = 116 MHz. For the measurements at T ranging from 173 K to 583 K a ceramic high probe (Bruker Biospin) was used. Depending on temperature at a power level of 180 W the π/2 pulse length ranged from 2.2 µs to 2.4 µs.

^{7}Li NMR SLR rates ($1/T_1 = R_1$) in the laboratory frame were acquired with the well-known saturation recovery pulse sequence. This sequence uses a comb of closely spaced π/2 pulse to destroy any longitudinal magnetization M_z. The subsequent recovery of M_z was detected as a function of waiting time t_d with a π/2 reading pulse: $10 \times \pi/2\text{-}t_d\text{-}\ \pi/2$ – acquisition.[30, 31] To construct the magnetization transients $M_z(t_d)$, we plotted the area under the free induction decays vs. t_d. The transients $M_z(t_d)$ were parameterized with stretched exponentials, $M_z(t_d) \propto 1 - \exp(-(t/T_1)^\gamma)$, to extract the rates R_1. Additionally, rotating frame ^{7}Li NMR SLRρ rates $1/T_{1\rho}$ ($= R_{1\rho}$) were measured by means of the spin lock technique: $\pi/2\text{-}p_{lock}$ – acquisition.[30] Here, we used a locking frequency $\omega_1/2\pi$ of 20 kHz. The duration of the spin-lock pulse t_{lock} was varied from 10 µs to 460 ms. The ensure full longitudinal relaxation between each scan the recycle delay was set to $5 \times T_1$. The $R_{1\rho}$ rates were obtained by analyzing the resulting transients $M_\rho(t_{lock})$ with stretched exponentials with the form $M_\rho(t_{lock}) \propto \exp(-(t_{lock}/T_{1\rho})^\kappa)$. The stretching exponent γ varied from 1 to 0.8, the exponent κ ranges from 1 to 0.6.

Finally, mixing time (t_m) dependent ^{7}Li SAE NMR decay curves were recorded with the help of the Jeener-Broekaert[32, 33] three-pulse sequence: (90°)X-t_p-(45°)Y-t_m-45°-acq. We used a fix preparation time t_p of 25 μs to acquire two-time sinus-sinus single-spin correlation functions. The mixing time was varied from 30 μs up to several seconds. A suitable phase cycle[32, 34] was employed to suppress unwanted coherences and to eliminate, as best as possible, dipolar contributions to the echo that appears after the reading pulse.[34] Fourier transformation of spin alignment echoes, starting from the top of the signal, results in SAE NMR spectra useful to highlight quadrupole intensities due to the interaction of the quadrupole moment of the ^{7}Li spin (spin-quantum number I = 3/2) and a non-vanishing electric field gradient (EFG).

3. Results and Characterization

3.1. Characterization via X-ray powder diffraction

The purity of the crystalline samples synthesized was examined by XRPD. As mentioned above, diffraction patterns were collected at room temperature and under air atmosphere. The first XRPD pattern was recorded directly after the calcination process, *i.e.*, after removal of CO_2, NH_3 and H_2O at 900 °C, the pattern is depicted in Figure S1. After the calcination step (10 hours), we see that the sample crystallizes with monoclinic structure (space group $P12_1/n$). After the sintering step we obtain a crystalline sample that shows the rhombohedral NASICON structure, the corresponding pattern is shown in Figure 1.

The $Zr_2(PO_4)_3$ framework consists of two ZrO_6 octahedra and three PO_4 tetrahedra sharing O atoms. The octahedral and tetrahedral units are alternating with the cations to form infinite chains parallel to the ternary axis of the structure. Each PO_4 unit shares its oxygen with four ZrO_6 octahedra of three $Zr_2(PO_4)_3$ units to form the NASICON framework (space group R-3c). A 3D network of conduction pathways is formed that is used by the ions to diffuse through the crystal. In our case the Li ions (6b) are octahedrally coordinated by oxygen ions (36f) at the intersection of three conduction channels (A1). The A1 sites are located between pairs of ZrO_6 octahedra along the c-axis, while the (vacant) interstitial sites (□) A2 can be found between $O_3ZrO_3A1O_3Zr$-□-O_3ZrO_3A1. Since the A1-A1 distance in LZP is rather larger, we assume that interstitial sites, such as A2, are involved in Li diffusion. Because of the large spatial separation of Li ions in LZP, we expect rather low homonuclear dipole-dipole interactions resulting in narrow ^{7}Li NMR lines even in the rigid lattice regime, see below.

In Figure 2 the result of our Rietveld analysis of the diffraction pattern of $LiZr_2(PO_4)_3$ synthesized by using ZrO_2 as educt is shown. Our refinement points to rhombohedral symmetry characterized by the space group R-3cH. In addition to the main rhombohedral phase, a minor impurity of ZrO_2 (< 4wt %) is seen (see black bars). Rietveld analysis yields the following lattice properties a = 8.824 Å and c = 22.456 Å; V = 1514.24 Å^3. By doping this sample with 5 wt.-% and 10 wt.-% Ca^{2+} the cell volume decreases (1512.64 Å^3 (5 wt.-% Ca), 1506.22 Å^3 (10 wt.-% Ca)) as expected.

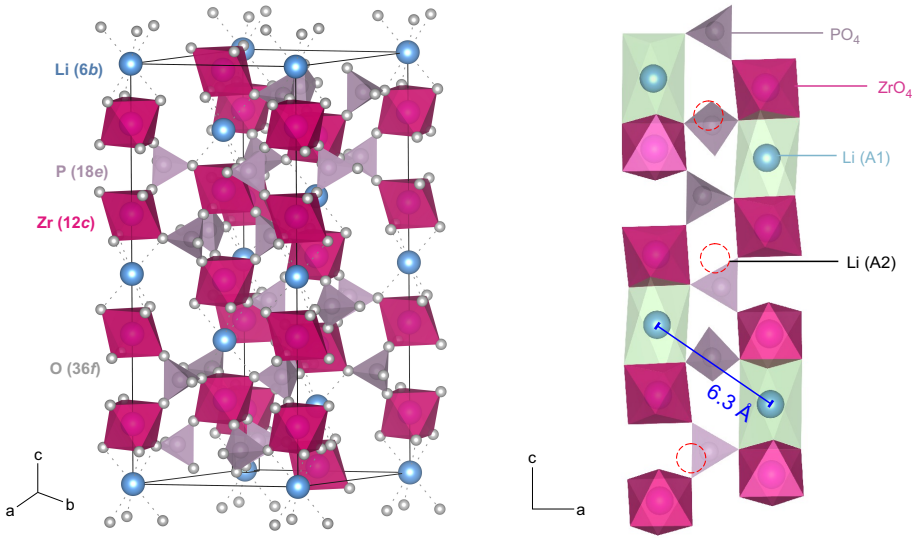

Figure 1: Left: Rhombohedral crystal structure of $LiZr_2(PO_4)_3$. The tetrahedral in purple represent PO_4-units, pink octahedra in pink show ZrO_6, while the blue spheres denote the Li^+ ions. Li^+ is octahedrally coordinated by oxygen anions of the the ZrO_6 octahedra. Right: Section of the rhombohedral crystal structure to show interstitial sites A2 the Li ions may use to jump between the regularly occupied sites A1. The A1-A1 distance turned out to be 6.3 Å, which is, presumably, much too large for a direct jump process.

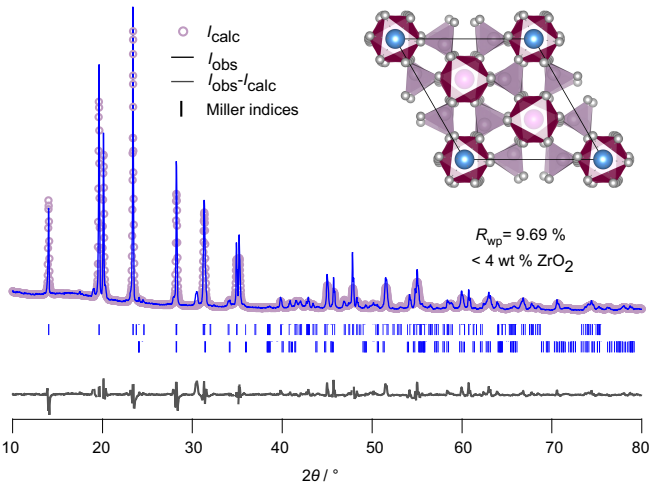

Figure 2: Rietveld refinement of LZP using ZrO_2 as educt. The sample was sintered at 1150 °C for 20 hours in closed Al_2O_3-crucibles. LZP crystallizes with space group *R*-3*cH*. Selected reflections have been indexed with black bars. A very small amount (< 4wt.-%) of ZrO_2 can be seen. The inset shows the ab-plane of the rhombohedral NASICON structure (viewing direction along the c-axis).

The preparation route with $Zr(CH_3COO)_4$ as starting material yields almost the same lattice parameters but the amount of non-reacted material is much higher and reaches values as high as 25 wt.-%.The incorporation of aliovalent Ca^{2+} ions, on the other hand, helps obtaining phase pure LZP with rhombohedral structure, as is illustrated in Figure 3. The amount of unreacted ZrO_2 continuously decreases with increasing Ca-content. This behavior is also found for LCZP prepared with the help of $Zr(ac)_4$. Nonetheless, the amount of ZrO_2 remains much higher (> 15 wt.-%) than that in samples prepared from ZrO_2 directly. Dots in Figure 3 denote reflections belonging to ZrO_2. Worth noting, we

do not find any additional Bragg reflections that belong to triclinic LZP in all diffractograms. These have been mentioned in earlier reports.[21, 35-37]

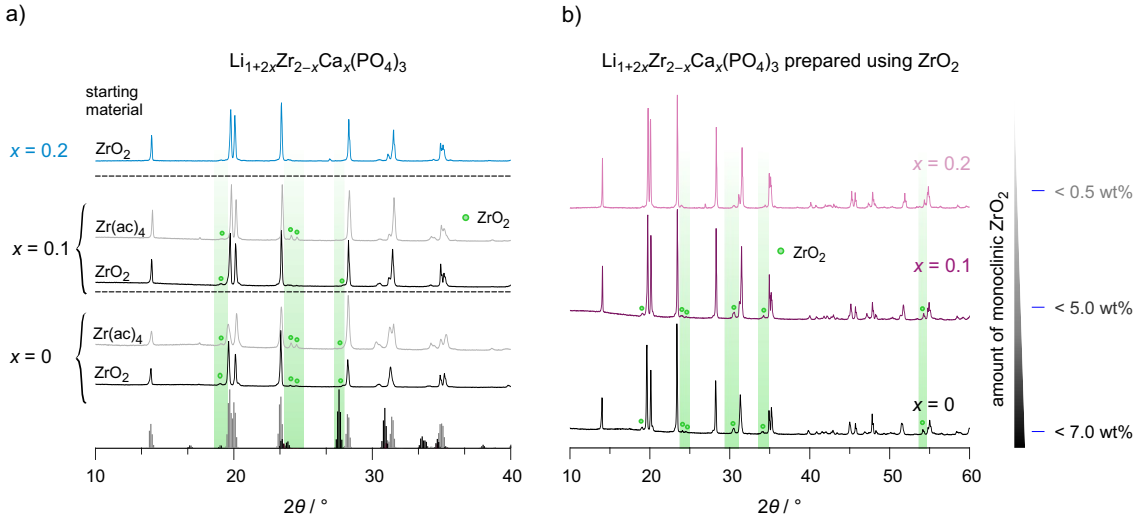

Figure 3 a) X-ray powder diffraction pattern of the crystalline $LiZr_2(PO_4)_3$ and $Li_{1+2x}Zr_{2-x}Ca_x(PO_4)_3$ ($x = 0.1$ and 0.2). All samples were prepared by following a classical solid-state route with either ZrO_2 as starting material (black) or $Zr(CH_3COO)_4$ (light grey). The vertical lines at the bottom denote the reflections of rhombohedral LZP (pink) and monoclinic ZrO_2 (black), respectively. b) XRPD pattern of $Li_{1+2x}Zr_{2-x}Ca_x(PO_4)_3$ prepared with the help of ZrO_2. The diffraction pattern reveal that the amount of the impurity phase ZrO_2 decreases with increasing Ca^{2+}-content.

According to XRPD we decided to study, in detail, ion dynamics of the following samples: $LiZr_2(PO_4)_3$ prepared from ZrO_2 and $Zr(ac)_4$ as well as $Li_{1+2x}Zr_{2-x}Ca_x(PO_4)_3$ ($x = 0.10$ and 0.20) prepared with the help of ZrO_2. Similar to $LiTi_2(PO_4)_3$ and other NASICON-type materials α-$LiZr_2(PO_4)_3$ shows relatively low theoretical densities, here ranging from 78 % to 84 %.

3.2. Impedance spectroscopy

To study how Li^+ ion transport is affected by x as well as to investigate whether the starting materials influence the dynamic parameters, we measured complex impedances over a large temperature and frequency range.[25, 38] Exemplarily, in Figure 4a conductivity isotherms of $LiZr_2(PO_4)_3$ are shown. Isotherms are obtained by plotting the real part, σ', of the complex conductivity $\boldsymbol{\sigma}$ of $LiZr_2(PO_4)_3$ as a function of frequency ν.

The isotherms shown in Figure 4a are composed of four regimes. (i) At low frequencies (and sufficiently high temperatures and, thus, high ionic mobility) electrode polarization (EP) appears owing to the piling-up of ions near the surface of the blocking Au electrodes applied. In many cases a stepwise decay of σ' is seen (*cf.* the two arrows in Fig. 4a)). (ii) The polarization regime passes into so-called conductivity plateaus (P1) governing the isotherms at intermediate temperatures and low frequencies. If this plateau is identified with a bulk response, it reflects long-range ion transport and is given by the dc-conductivity σ_{dc}. By moving to higher frequency a shallow dispersive regime with a weak frequency dependence shows up. It directly merges into another plateau (iii, P2), which finally passes over in the high-frequency dispersive regime (iv) which can roughly be approximated with Jonscher's power law.

In Figure 4a the inflexion points of the plateaus P1 and P2 are highlighted by filled circles; straight lines connect these circles. The dispersive region belonging to plateau P2 is best seen at 173 K, the solid

line shown in Figure 3a corresponds to a Jonscher power law:[39] $\sigma' = \sigma_{dc} + A_0\nu^n$. Here A_0 is the so-called dispersion parameter and n represents the power law exponent, which takes a value of 0.73 at 173 K. To analyse our data in terms of dimensionality effects, we also studied the frequency dependence of the real part of the complex permittivity; the corresponding isotherms (ε' vs. ν) are plotted in Figure 4c; the plateaus P1 and P2 produce a two-step increase of ε' when coming from high frequencies. As for σ', also $\varepsilon'(\nu)$ can be approximated with exponents around 0.75 for P2, see Figure 4c. As summarized in ref. 19, such Jonscher exponents are expected for 3D ionic conduction.[40]

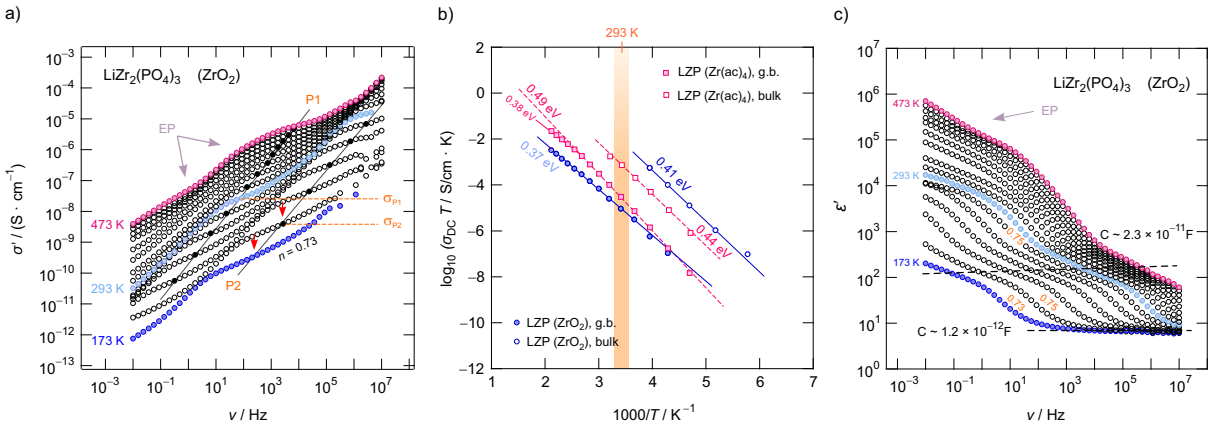

Figure 4: a) Conductivity isotherms of Ca-free LZP (synthesized from ZrO_2) recorded at temperatures ranging from 173 K to 473 K; isotherms have been recorded in steps of 20 K. We observed two plateaus P1 and P2 that correspond to the grain boundary (g.b., P1) and bulk response (P2). b) Arrhenius plot of the DC conductivities associated with P1 and P2. The solid and dashed line show line fits with an Arrhenius law yielding activation energies ranging from 0.39 eV to 0.52 eV. Circles represent LZP synthesized from ZrO_2 and rectangles show results of LZP that was synthesized from $Zr(ac)_4$. LZP prepared from ZrO_2 shows the highest bulk ion conductivity that is characterized by 0.41 eV. c) Real part of the complex permittivity as a function of frequency. P1 and P2 seen in Figure 4a produce a two-step increase of ε' characterized by permittivities and capacities being typical for a bulk electrical response and a response including ion-blocking grain boundaries. The same characteristics are seen for LZP prepared from $Zr(ac)_4$. Both processes can be approximated with a power law of the form $\varepsilon'(\nu) = \varepsilon(\infty) + A_s\nu^{-p}$ with $p \neq f(T) \approx 0.75$, wherein $\varepsilon(\infty)$ represents the permittivity at very high frequencies.

To determine which capacitances C govern the responses P1 and P2, we used the equation for a parallel-plate capacitor for an estimation $C = \varepsilon_0\varepsilon_r A/d$. Here ε_0 represents the electric field constant (8.854×10^{-12} F m^{-1}), A the area and d the thickness of the sample. While the DC plateau (P2) at high frequencies is characterized by $C = 1.2 \times 10^{-12}$ F, for the plateau at lower ν we found $C = 2.3 \times 10^{-11}$ F. Therefore, the plateau associated with C in the pF range represents the bulk response, whereas P1 seen at lower frequencies is additionally governed by grain boundary contributions (g.b.) for which capacitances in the order of 10^{-11} F are typically expected.[41]

In the Arrhenius plot of Figure 4b, $\sigma_{DC}T$ of the two plateaus P1 and P2 is plotted vs. the inverse temperature T. $\sigma_{DC}T$ does not change when several heating and cooling runs were performed. The lines in Figure 4b refers fits according to $\sigma_{DC}T(P1, P2) \propto \exp(-E_a/(k_BT))$; k_B denotes the Boltzmann's constant and E_a the corresponding activation energy. For $LiZr_2(PO_4)_3$ prepared from ZrO_2 we obtain $E_a(P2)$ of 0.413 eV, whereas for $LiZr_2(PO_4)_3$, when using $Zr(ac)_4$ as starting material, E_a increases to 0.44 eV (see Figure 3b). At room temperature, the ionic conductivities of P2 are of 3.6×10^{-5} S cm^{-1} and 3.4×10^{-6} S cm^{-1}, respectively. For the sake of clarity, in Table 1 all activation energies E_a are listed.

Table 1: Comparison of activation energies E_a and pre-factors σ_0 of the Arrhenius lines shown in Figure 3b. The values refer to Ca-free and Ca-containing $LiZr_2(PO_4)_3$. Values in the brackets represent data determined by blocking grain boundaries (P2).

composition	E_a / eV	$\log_{10}$ (σ_0 / S cm^{-1} K))	starting material
$LiZr_2(PO_4)_3$	0.444 (0.476)	4.97 (3.86)	$Zr(ac)_4$
$LiZr_2(PO_4)_3$	0.413 (0.372)	4.91 (1.49)	ZrO_2
$Li_{1.2}Ca_{0.1}Zr_{1.9}(PO_4)_3$	0.428 (0.516)	5.44 (4.14)	ZrO_2
$Li_{1.4}Ca_{0.2}Zr_{1.8}(PO_4)_3$	0.408 (0.381)	5.08 (3.49)	ZrO_2

Unfortunately, by using Nyquist diagrams, which show complex plane plots of the imaginary part Z′ of the complex impedance, **Z**, vs. its real part Z'', the faster relaxation process, corresponding to P2, cannot be resolved properly. Instead, we used the complex modulus $M''(\nu)$ representation[42] to visualize the two processes further, see Figure 5a and Figure 6. At sufficiently low temperatures two relaxation peaks M1 and M2 appear (see grey arrows in Figure 5a). These peaks are separated by two orders of magnitude on the frequency scale. This distance on the frequency scale is comparable with the ratio of $\sigma_{DC,P2}$:$\sigma_{DC,P1}$; thus, they refer, as is seen in Figure 6 to the plateaus P1 and P2 governing $\sigma'(\nu)$. As expected the two electrical relaxation frequencies mirror the ratio in conductivities. The peak with the large amplitude (M2) corresponds to P2 in $\sigma'(\nu)$, the one with the smaller amplitude (M1) represents a relaxation process with a longer relaxation time (*cf.* P1), see also Figure 6. As an estimation, M'' is proportional to the inverse capacitance, $M'' \propto 1/C$.[41, 43] Thus, we expect peak M2 to be characterized by a larger amplitude (3.4 pF) than M1 (30.1 pF). $C_1/C_2 \approx 10$ is in good agreement with the amplitude ratio seen in Figure 5a and Figure 6.

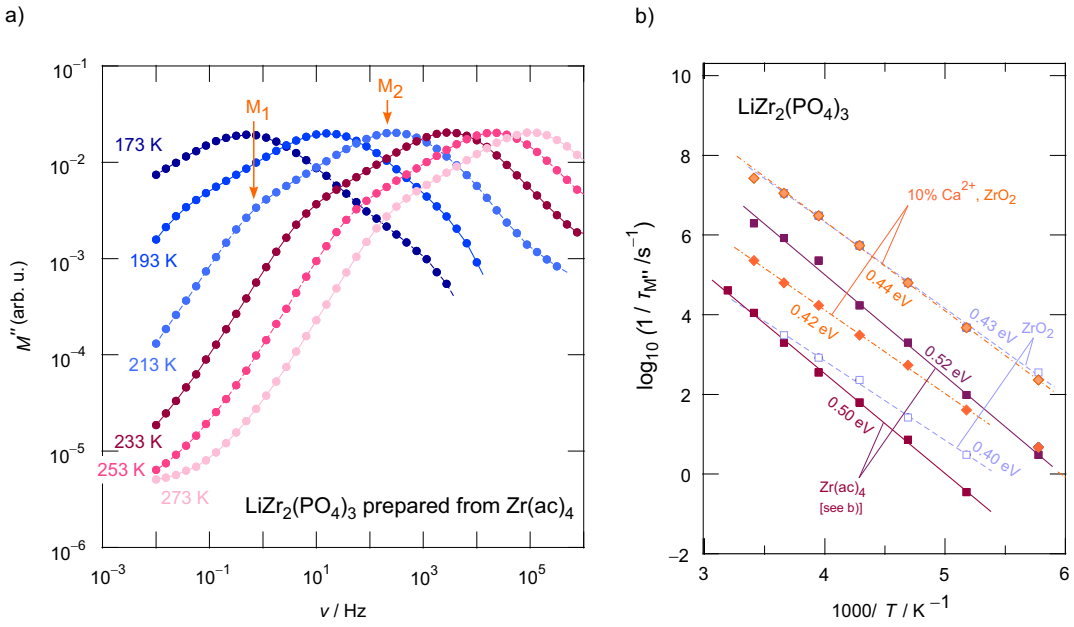

Figure 5: a) Frequency dependence of the imaginary part of the electric modulus M'', of $LiZr_2(PO_4)_3$ prepared from $Zr(ac)_4$. Spectra were recorded at the temperatures indicated. The lines are to guide the eye. As suggested by $\sigma'(\nu)$, two distinct peaks are visible denoted as M1 and M2. The temperature dependence of the corresponding relaxation rate τ_M^{-1} is shown in b). For comparison, the results of $LiZr_2(PO_4)_3$ (prepared from ZrO_2, symbols in light blue) and $Li_{1.4}Zr_{1.8}Ca_{0.2}(PO_4)_3$ (also prepared from ZrO_2, symbols in orange) are included as well.

In order to compare activation energies extracted from σ_{DC}(P1, P2) we determined characteristic electrical relaxation frequencies $1/\tau_M$ using the modulus peaks of Figure 5a. $1/\tau_M$ refers to frequencies at which the peaks appear at fixed temperature. A comparison of activation energies for selected compounds is shown in Figure 5b.

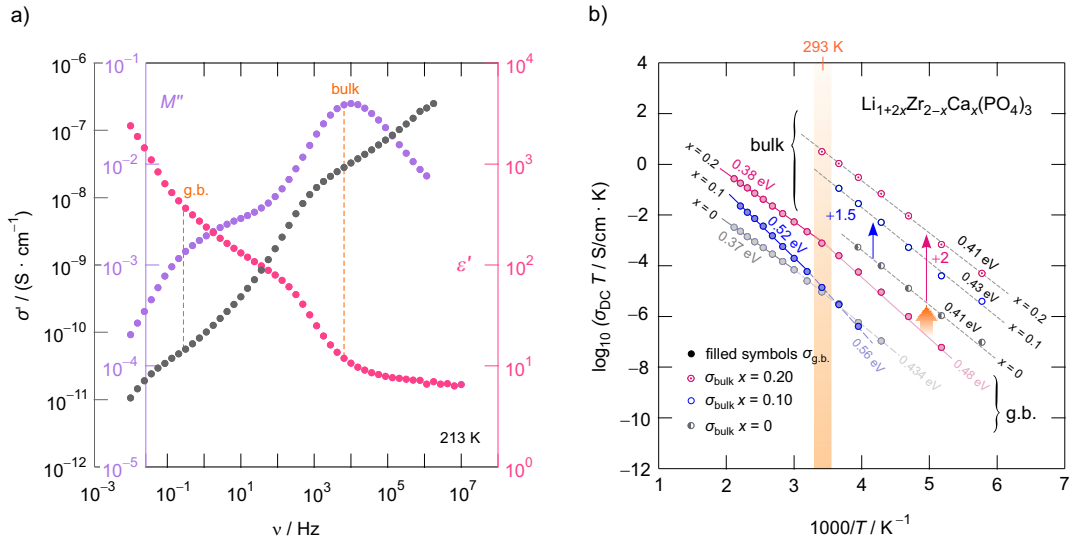

Figure 6: a) Frequency dependence of the complex modulus M'', the real part, ε', of the permittivity as well as the real part, σ', of the complex conductivity of $LiZr_2(PO_4)_3$ (prepared from ZrO_2). The isotherms were recorded at 213 K. The maxima in M'' clearly refer to the plateaus P1 and P2 seen in $\sigma'(\nu)$. For comparison, the change of $\varepsilon'(\nu)$ is shown, too. b) Arrhenius plot of the ionic conductivities referring to the plateaus P1 and P2 ($\sigma_{DC}T$ vs $1000/T$) of cation-mixed crystalline $Li_{1+2x}Zr_{2-x}Ca_x(PO_4)_3$. Solid lines and dashed lines represent fits according to an Arrhenius law yielding the activation energies E_a indicated. While solid lines refer to conductivities influenced by the grain boundary contributions, the dashed lines represent bulk ion dynamics in $Li_{1+2x}Zr_{2-x}Ca_x(PO_4)_3$. For the sake of clarity, the bulk ion conductivities for the samples with $x = 0.20$ and $x = 0.10$ have been plotted using an offset of +2 and +1.5 on the logarithmic scale. These conductivities coincide with those of the Ca-free sample.

As mentioned in the beginning, Ca^{2+} incorporation increases the ionic conductivity of LZP. Figure 7 shows the change in $\sigma_{DC}T$(P1, P2) of $Li_{1+2x}Ca_xZr_{2-x}(PO_4)_3$ prepared from ZrO_2 for $x = 0$, $x = 0.1$ and $x = 0.2$. Most importantly, while $\sigma_{DC}T$(P2), which refers to bulk ion dynamics, is almost unaffected by x, Ca^{2+} incorporation reduces the g.b. resistance. We clearly see that $\sigma_{DC}T$(P1) is by two orders of magnitude larger than that of the sample with $x = 0$, see arrow in Figure 6. Most likely, the sintering process clearly benefits from a Ca-rich composition, which helps reducing the blocking nature of surface regions of the $Li_{1+2x}Ca_xZr_{2-x}(PO_4)_3$ crystallites.

3.3. Ion dynamics as seen by NMR measurements

Figure 7a gives an overview of the ^7Li NMR SLR rate measurements performed using an Arrhenius representation plotting the $R_{1(\rho)}$ rates as a function of the inverse temperature. To identify the thermally activated regions, we measured $R_{1(\rho)}$ of $Li_{1.4}Ca_{0.2}Zr_{1.8}(PO_4)_3$ over a wide temperature range to detect the maxima of diffusion-induced rate peaks.[44] Here we focused on the sample with the composition $Li_{1.4}Ca_{0.2}Zr_{1.8}(PO_4)_3$ as it shows the lowest bulk activation energy and the lowest amount of residual ZrO_2.

Below 183 K the rates R_1 reveal a non-diffusive background regime. In this temperature range longitudinal relaxation is induced by lattice vibrations or coupling of the Li spins with paramagnetic impurities.[44-46] At higher temperatures we expect the SLR rate to be increasingly induced by Li^+ hopping

processes. Such processes lead to magnetic and electric field fluctuations that cause longitudinal relaxation.[44] Indeed, the rates increase with temperature and, in both cases R_1 and $R_{1\rho}$, characteristic diffusion-induced rate peaks appear. Importantly, we recognize that R_1 passes through two maxima located at T_{max} = 282 K and 492 K, respectively. In general, at T_{max} the motional correlation rate $1/\tau_c$ is related to ω_0 via the relation $\tau_c\omega_0 \approx 1$. The so-called motional correlation rate $1/\tau_c$ is identical, within a factor of two, with the Li^+ jump rate $1/\tau$.[44, 46] For $R_{1\rho}$, this maximum condition changes to $\tau_c\omega_0 \approx 0.5$.[47] As ω_0 and ω_1 differ by more than three orders of magnitude, we are able to characterize Li^+ motional correlation rates in LCZP with values in both the kHz and MHz range.[48]

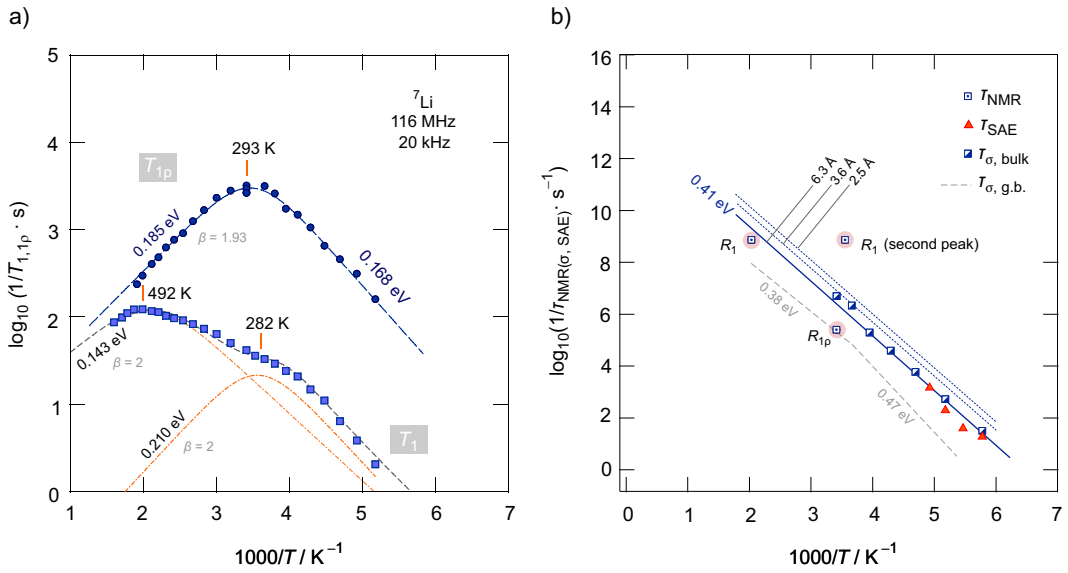

Figure 7: a) Arrhenius plot of the ^{7}Li NMR relaxation rates R_1 and $R_{1\rho}$ measured in the laboratory frame of reference (116 MHz) and in the rotating frame of reference (20 kHz, nominal locking frequency). Dashed lines represent BPP-type fits to determine activation energies, pre-factors and asymmetry parameters β. Temperatures indicate T_{max} of the rate peaks. The superposition of the R_1 rate peaks can be approximated with two symmetric peaks (β = 2). b) Li jump rates as deduced from the diffusion-induced rate peaks R_1 and $R_{1\rho}$. For comparison, we also included jump rates which we estimated from frequency-dependent conductivity measurements and ^{7}Li SAE NMR. The text for further explanations.

Here, we approximated the superposition of the two R_1 rate peaks by a sum of two Lorentzian-shaped spectral density functions $J(\omega_0, T) \propto \tau_c/(1+(\omega_0\tau_c)^{\beta})$ according to the concept introduced by Bloembergen, Purcell and Pound (BPP) for 3D isotropic diffusion,[49, 50] see dashed line in Figure 7a that follows the R_1 rates. For each peak we used a single term to deconvolute the temperature dependence of the overall R_1 rates measured, *cf.* the dashed-dotted lines in Figure 7a, which will be discussed below. τ_c is given by $\tau_c = \tau_{c,0} \exp(-E_a/(k_B T))$; $\tau_{c,0}$ represents the pre-exponential factor that is typically identified as the "attempt frequency" of the jump process.[51]

In general, $J(\omega_0, T)$ is the Fourier transform of the underlying motional correlation function $G(t')$.[44] If $G(t')$ is or can be well approximated with a single exponential, β equals 2. Values smaller than 2 are expected for correlated motion, which is, *e.g.*, seen for cations exposed to an irregularly shaped potential landscape. In such a landscape short-ranged Li^+ diffusion will be different to long-range ion transport. In particular, forth-and-back jumps or, more generally speaking, localized motions will govern the rate R_1 in the low-temperature regime, which is characterized by $\tau_c\omega_0 \gg 1$. In this regime we have $J(\omega_0)$

$\propto \tau_c^{-1}\omega_0^{-\beta}$ with $(1< \beta \leq 2)$. $\beta < 2$ produces asymmetric rates peaks which are often found for structurally complex ion conductors with a non-uniformly shaped energy landscape. Ion dynamics in this regime are anticipated to be affected by correlation effects because of both structural disorder and strong Coulomb interactions of the moving ions.[52] As the peak is asymmetric, the activation energy on this side of the peak, $E_{a,\,low}$, is lower than that of the high-temperature flank, $E_{a,\,high}$; the two values are linked to each other via $E_{a,\,low} = (\beta_{(\rho)} - 1)E_{a,\,high}$. In the regime $\tau_c\omega_0 \ll 1$, that is, on the high-temperature side of the peak, many jump events are sensed during one Larmor precession and the probability is high that also those jumps contribute to longitudinal relaxation which are characterized by higher activation energies. Usually, on this side of the rate peak $R_1(1/T)$ long-range Li ion dynamics is sensed; in this limit we obtain $J(\omega_0) \propto \tau_c$.[28]

In the present case, the analysis of the rate peak analysis with a sum of two BPP-type spectral densities yields activation energies of $E_{a,1} = 0.210$ eV and $E_{a,2} = 0.143$ eV. As both rate peaks join up, information on β are difficult to obtain. Here, the fitting routine yields $\beta = 2$ for the two peaks resulting in symmetric peaks with $E_{a,\,low} = E_{a,\,high} = E_{a,i}$ $(i = 1, 2)$. Note that the peak at higher T $(i = 2)$ is only partly visible which influences the precise determination of $E_{a,\,high}$. We clearly recognize that $E_{a,i}$ as determined from R_1 SLR NMR turned out to be significantly lower than E_a obtained from σ_{DC} measurements describing bulk ion dynamics. The fact that $E_{a,i} < E_{a,\,DC}$ shows that the number of jump events seen by NMR does not include all types of jumps needed for long-range diffusion. Obviously, the spin-fluctuations sensed by NMR are already sufficient to generate a full R_1 peak. Thus, we conclude that the Li^+ motions in LCZP are highly mobile on a short-range length scale while long-range ion transport is, however, characterized by much larger activation energies than 0.2 eV. This situation resembles that of Li^+ ion dynamics in argyrodite-type Li_6PS_5I, which has been studied recently by our group. Here, we assume that rapid forward-backward exchange processes between the sites A1 and A2 might be responsible for the peaks seen in NMR spin-lattice relaxometry. A2 sites might be occupied in samples with $x > 0$. Here, especially the peak appearing at $T_{max} = 282$ K for $Li_{1.4}Ca_{0.2}Zr_{1.8}(PO_4)_3$ points to rapid (localized) exchange processes with residence times in the order of several ns. According to $\omega_0\tau_c \approx 1$ we estimate that at T_{max} the jump rate should be in the order of $1/\tau = 7.3 \times 10^8\ s^{-1} \approx 10^9\ s^{-1}$. A very similar behavior has recently been seen also for NASICON-type $Na_{3.4}Sc_{0.4}Zr_{1.6}(SiO_4)_2PO_4$.

To complement our R_1 measurements, we carried out spin-lock NMR SLR measurements at a locking frequency of 20 kHz. As expected we detected a prominent spin-lock NMR peak $R_{1\rho}(1/T)$ at much lower temperature than 492 K. A single peak appears at $T_{max} = 293$ K. Its turned out to be slightly asymmetric with an activation energy of $E_{a,\,high} = 0.185$ eV and $E_{a,\,low} = 0.168$ eV. At first glance it looks like that the $R_{1\rho}$ peak corresponds to the R_1 peak seen at $T_{max} = 492$ K. Keeping, however, both the locking frequency of only 20 kHz and the rather low activation energy of 0.185 eV in mind, the $R_{1\rho}$ peak belonging to $R_1(1/T)$ with $T_{max} = 492$ K would be expected to appear at much lower temperatures than ambient. Even if we replace ω_1 by an effective frequency $\omega_{1,\,eff}$ $(> \omega_1)$, which takes into account local magnetic fields that increase ω_1, no satisfactory joint fit results that is characterized by the same E_a and the same $\tau_{c,0}$ for the two peaks. Here, only unreliably high $\omega_{1,\,eff}$ values reaching the MHz range would result in a joint fit connecting the two peaks. Table 2 shows an overview of the results obtained from analyzing the three peaks individually by BPP-type spectral density functions. It also includes the amplitudes C_{NMR} in $R_{1(\rho)} = C_{NMR}\,J(\omega_0, T)$. We see that the amplitudes of the two R_1 rate peaks differ by approximately one order of

magnitude. Most likely, stronger quadrupolar relaxation governs the peak appearing at higher T. The corresponding prefactor $1/\tau_0$ is relatively low, while that of the peak showing up at 282 K ($1/\tau_0 = 5.9 \times 10^{12}$ s^{-1}) is consistent with frequencies typically expected for phonons.

Table 2: Results of analyzing the ^{7}Li NMR rate peaks R_1 and $R_{1\rho}$ of $Li_{1.4}Ca_{0.2}Zr_{1.8}(PO_4)_3$. The coupling constant C_{NMR}, which is the amplitude of the rate peak, $J(\omega_0) = C_{NMR}\tau_c/(1+(\omega_0\tau_c)^\beta$, turned out to be in the range of 10^{10} and 10^{11} s^{-2}. Values in the order of 10^{-13} s for τ_0 correspond to phonon frequencies.

	E_a (= $E_{a,\,high}$)	C_{NMR}	$\beta_{(\rho)}$	τ_0
R_1 (T_{max} = 492 K)	0.143 eV	1.8×10^{11} s^{-2}	2	4.1×10^{-11} s
R_1 (T_{max} = 282 K)	0.210 eV	2.5×10^{10} s^{-2}	1.93	1.7×10^{-13} s
$R_{1,\rho}$ (T_{max} = 293 K)	0.185 eV (0.165 eV)[a]	1.5×10^{9} s^{-2}	2	2.8×10^{-9} s

[a] the value in brackets refers to $E_{a,\,low}$ of the $R_{1\rho}$ peak seen at 293 K.

The above-mentioned jump rate derived from SLR NMR at T_{max} ($1/\tau = 7.3 \times 10^8$ s^{-1}) can be converted into diffusion coefficients with the help of the Einstein-Smoluchowski equation according to $D_{NMR} = a^2/(6\tau)$, which is valid for 3D diffusion.[28] As an estimation, by inserting a = 6.3 Å, which is simply the maximum Li-Li distance, we obtain $D_{NMR} = a^2/(6\tau) = 4.8 \times 10^{-11}$ m^2 s^{-1}. Assuming the interstitial sites A2 participating in exchange processes D_{NMR} reduces to 1.8×10^{-11} m^2 s^{-1}. A distance of a = 6.3 Å is, of course, by far too long for a single hopping process.

In the Arrhenius plot of Figure 7b we compare the rates $1/\tau$ from NMR ($1/\tau_{NMR}$) with those obtained after converting σ_{DC} into jump rates by using the Nernst Einstein equation. As we do not know the exact jump distance, we calculated $1/\tau_\sigma$ for three different values of a. $1/\tau_\sigma$ represents an average value mainly influenced by Li^+ jumps necessary for long-range ion transport. Most likely, the R_1 peak appearing at 492 K is more related to jump processes enabling the ions to move over longer distances. The large discrepancy between $1/\tau_{NMR}$(282 K) and $1/\tau_\sigma$ once again visualizes that the $R_1(1/T)$ peak at low T reflects localized jump processes. For comparison, we also included $1/\tau_\sigma$ rates estimated from conductivity values that characterize the influence of grain boundaries. Interestingly, $1/\tau_{NMR}$(293 K, $R_{1\rho}$) = 2.5×10^5 s^{-1}, which we estimated via the relation $\omega_1\tau_c \approx 0.5$, see above, agrees with $1/\tau_{\sigma,\,g.b.}$. The corresponding spin-lock NMR rate peaks seems to be sensitive to ion dynamics influenced by interfacial processes. This behaviour is consistent with the following comparison. At frequencies in the kHz range ($\omega_1/2\pi$ = 20 kHz) and at T = 282 K the isotherms $\sigma'(\nu)$ are mainly influenced by the g.b. response rather than bulk ion dynamics.

To shed more light on long-range ion dynamics, we used ^{7}Li NMR line shape measurements and ^{7}Li SAE NMR experiments[42, 53-56] to further characterize ionic transport in LCZP. Via SAE NMR we should be able to get access to diffusion parameters that characterize ion transport over longer distances as the method is sensitive to exchange processes on the time scale that is comparable to that of DC conductivity measurements.[44] In Figure 8a variable-temperature ^{7}Li NMR spectra of $Li_{1.4}Ca_{0.2}Zr_{1.8}(PO_4)_3$ are shown. Remarkably, at temperatures as low as 213 K a relatively narrow NMR line is detected whose width is only 1.4 kHz. Usually, we would expect a width in the order of several kHz due to ^{7}Li-^{7}Li dipolar interactions. Here, the large Li-Li distance of 6.3 Å between the A1 sites, and between A1 sites and Li ions occupying interstitial sites in samples with $x > 0$, leads to relatively weak dipole-dipole interactions

producing a narrow line already in the rigid-lattice regime. With increasing temperature, the line undergoes a slight narrowing process because of Li diffusion that averages dipolar couplings. Finally, at even higher temperatures, *i.e.*, in the extreme narrowing regime, its width is only governed by the inhomogeneity of the external magnetic field.

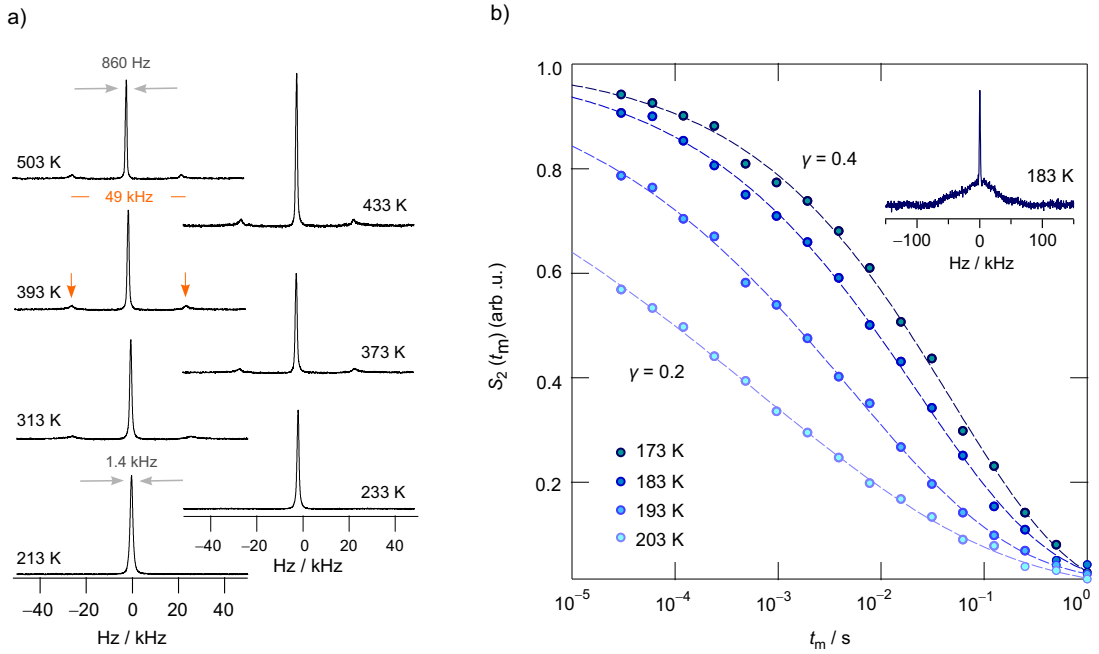

Figure 8: a) ^{7}Li NMR spectra of $Li_{1.4}Ca_{0.2}Zr_{1.8}(PO_4)_3$ recorded at the temperatures indicated. The NMR line transforms from a Gaussian shape at low temperatures to a Lorentzian one at elevated T. Clearly visible and well-defined quadrupole powder patterns emerge at temperatures higher than 313 K. b) ^{7}Li SAE NMR decay curves of LCZP whose spectra are shown in a). Decay curves follow stretched exponentials ($0.20 < \gamma < 0.4$) which are shown as solid lines. Data have been recorded at a Larmor frequency of 116 MHz. See text for further details. Inset: Fourier transform of a spin-alignment echo, starting from the top of the echo, which was recorded at a fixed t_p of 20 µs and a short mixing time of t_m = 100 µs. In addition to a "central line" a rather broad quadrupole foot is visible illustrating the distribution of EFGs seen by the Li ions in the dynamic regime of the rigid lattice.

Interestingly, at 313 K two satellite lines emerge that belong to a first-order quadrupole powder pattern arising from the interaction of the quadrupole moment of the ^{7}Li nucleus (I = 3/2) with a non-vanishing electric field gradient (EFG) at the nuclear site. The EFG is produced by the electric charge distribution in the direct neighborhood of the ^{7}Li nucleus. This additional interaction alters the Zeeman levels and, thus, also the associated (angular) Zeeman frequency ω_0 towards $\omega_0 \pm \omega_Q$.[30,50] The singularities seen in Figure 8a correspond to the 90° satellite transitions of a powder pattern, which typically show up at sufficiently high T; this feature belongs to the universal characteristics of crystalline materials studied by NMR.[30, 46,57] Their distance on the frequency scale, if we simply assume an EFG with axial symmetry, corresponds to $\delta/2$. δ is the quadrupole coupling constant. A distance of 49 kHz leads to δ = 98 kHz.[54] This value should, however, be interpreted as an average value, as we cannot exclude a small distribution of EFGs the ions are exposed to at very low temperatures. At very low T, the intensity of the singularities is too low to be detectable by single pulse experiments. Instead, echo experiments should be used that also avoid receiver dead time effects. In Figure 8b (see inset) a spectrum is shown that is the Fourier transform of a stimulated echo. Indeed, a sharp central line is located on top of a broad quadrupole foot. Hence, we conclude that the Li ions are exposed to a distribution of EFGs.

Fluctuations in ω_Q seen by the ions when jumping between electrically inequivalent sites can be used to record sinus-sinus two-time correlation functions. In Figure 8a the change of the ^{7}Li SAE amplitude S_2 is shown vs. the logarithmic mixing time t_m. In general, S_2 depends on both the preparation time t_p and t_m. Here, we measured the decay curve at fixed t_p (= 20 μs) but variable mixing time. Stretched exponentials of the form $S_2 \propto \exp(-(t_m/\tau_{SAE})^{\delta})$, with a stretching factor δ ranging from 0.21 to 0.37, are best suited to describe the dependence of $S_2(t_p = \text{const.}, t_m)$ in this temperature regime. In general, stretching factors deviating from $\delta = 1$ indicate non-Debye-like motional process. For example, such deviations can arise from motions in disordered matrixes or in confined dimensions[55, 58] leading to motional correlation functions whose decay slows down with increasing time. With increasing T the inflexion point of the echo decay curves shifts towards shorter t_m. At the same time, the shape of S_2 steadily becomes more stretched until values of $\gamma = 0.21$ are reached at $T = 203$ K. At sufficiently long mixing times the curves $S_2(t_p = \text{const.}, t_m)$ always reach $S_{2,\infty} = 0$, which either indicates a rather large number of quadrupole frequencies involved or which points to the influence of dipolarly coupled spins, as is well-described in literature.[34] The rates $1/\tau_{SAE}$ governing the stretched decay functions are included in Figure 7b. We recognize that they are in fair agreement with those rates, $1/\tau_{\sigma,\text{bulk}}$, which were estimated from bulk ionic conductivities of $Li_{1.4}Ca_{0.2}Zr_{1.8}(PO_4)_3$.

4. Conclusion

We used a conventional solid-state reaction procedure to synthesize NASICON-type $LiZr_2(PO_4)_3$ and investigated both ionic conductivity and Li^+ diffusivity. Ca^{2+} incorporation helps prepare $Li_{1+2x}Zr_{2-x}Ca_x(PO_4)_3$ crystallizing with rhombohedral symmetry. While bulk ion dynamics is not influenced by the Ca^{2+} content, the grain boundaries in LZCP turn out to be less blocking for Li^+ ions as compared to the sample with $x = 0$. We observed an increase in the low-frequency ionic conductivity by two orders of magnitude when increasing x from $x = 0$ to $x = 0.2$. For $Li_{1.4}Ca_{0.2}Zr_{1.8}(PO_4)_3$ ^{7}Li NMR relaxometry revealed rapid *localized* Li^+ jump processes with activation energies of 0.2 eV and 0.14 eV. The diffusion-induced rate peak seen at 282 K points to a very high jump rate in the order of 10^9 s^{-1} at this temperature. On the other hand, ^{7}Li spin-alignment echo spectroscopy confirmed that long-range ion transport in the bulk regions of $Li_{1.4}Zr_{1.8}Ca_{0.2}(PO_4)_3$ needs to be characterized by an activation energy of 0.41 eV as determined by variable-frequency conductivity measurements.

Acknowledgements. This project has received funding from the European Union's Horizon 2020 research and innovation programme under grant agreement No 769929. We thank the Deutsche Forschungsgemeinschaft for further support (FOR1277, WI3600(2-1;4-2).

References

1. J. Janek and W. G. Zeier, *Nat. Energy*, 2016, **1**, 16141(16141)-16141(16144).
2. D. Larcher and J. M. Tarascon, *Nat. Chem.*, 2015, **7**, 19-29.
3. J. I. Hur, L. C. Smith and B. Dunn, *Joule*, 2018, **2**, 1187-1201.
4. E. Quartarone and P. Mustarelli, *Chem. Soc. Rev.*, 2011, **40**, 2525-2540.

5. J. C. Bachman, S. Muy, A. Grimaud, H. H. Chang, N. Pour, S. F. Lux, O. Paschos, F. Maglia, S. Lupart, P. Lamp, L. Giordano and Y. Shao-Horn, *Chem. Rev.*, 2016, **116**, 140-162.
6. Z. Z. Zhang, Y. J. Shao, B. Lotsch, Y. S. Hu, H. Li, J. Janek, L. F. Nazar, C. W. Nan, J. Maier, M. Armand and L. Q. Chen, *Energy Environ. Sci.*, 2018, **11**, 1945-1976.
7. Y. Inaguma, K. Funayama, A. Aimi, D. Mori, Y. Hamasaki, K. Ueda, M. Ikeda, T. Ohno and K. Mitsuishi, *Solid State Ion.*, 2018, **321**, 29-33.
8. A. Sakuda, A. Hayashi and M. Tatsumisago, *Sci. Rep.*, 2013, **3**.
9. A. Hayashi, K. Noi, A. Sakuda and M. Tatsumisago, *Nat. Commun.*, 2012, **3**.
10. M. Guin and F. Tietz, *J. Power Sources*, 2015, **273**, 1056-1064.
11. M. Guin, F. Tietz and O. Guillon, *Solid State Ion.*, 2016, **293**, 18-26.
12. H. Xie, J. B. Goodenough and Y. Li, *J. Power Sources*, 2011, **196**, 7760-7762.
13. V. Ramar, S. Kumar, S. R. Sivakkumar and P. Balaya, *Electrochim. Acta*, 2018, **271**, 120-126.
14. S. Hasegawa, N. Imanishi, T. Zhang, J. Xie, A. Hirano, Y. Takeda and O. Yamamoto, *J. Power Sources*, 2009, **189**, 371-377.
15. H. Xie, Y. Li and J. B. Goodenough, *RSC Advances*, 2011, **1**, 1728-1731.
16. M. C. R, P. Kumar, A. Kumar, S. Indris, H. Ehrenberg, G. Vijaya Prakash and R. Jose, *Ceram. Int.*, 2018, **44**, 15509-15516.
17. L. Xiaojuan, F. Xue, L. Wenwei, L. Haitao and Z. Yunjie, *Adv. Engin. Res., International Conference on Advances in Energy, Environment and Chemical Engineering*, 2015, DOI: https://doi.org/10.2991/aeece-15.2015.45, 227-230.
18. D. Petit, P. Colomban, G. Collin and J. P. Boilot, *Mat. Res. Bull.*, 1986, **21**, 365-371.
19. D. Petit and B. Sapoval, *Solid State Ion.*, 1986, **21**, 293-304.
20. M. Casciola, U. Costantino, L. Merlini, I. G. K. Andersen and E. K. Andersen, *Solid State Ion.*, 1988, **26**, 229-235.
21. M. Catti and S. Stramare, *Solid State Ion.*, 2000, **136–137**, 489-494.
22. M. Catti, S. Stramare and R. Ibberson, *Solid State Ion.*, 1999, **123**, 173-180.
23. M. Catti, A. Comotti and S. Di Blas, *Chem. Mater.*, 2003, **15**, 1628-1632.
24. H. El-Shinawi, C. Greaves and J. Janek, *RSC Adv.*, 2015, **5**, 17054-17059.
25. F. Preishuber-Pflügl, P. Bottke, V. Pregartner, B. Bitschnau and M. Wilkening, *Phys. Chem. Chem. Phys.*, 2014, **16**, 9580-9590.
26. S. Lunghammer, Q. Ma, D. Rettenwander, I. Hanzu, F. Tietz and H. M. R. Wilkening, *Chem. Phys. Lett.*, 2018, **701**, 147-150.
27. B. Stanje, D. Rettenwander, S. Breuer, M. Uitz, S. Berendts, M. Lerch, R. Uecker, G. Redhammer, I. Hanzu and M. Wilkening, *Ann. Phys.*, 2017, **529**, 1700140(1700141)-1700140(1700149).
28. M. Uitz, V. Epp, P. Bottke and M. Wilkening, *J. Electroceram.*, 2017, **38**, 142-156.

29. V. Epp, Q. L. Ma, E. M. Hammer, F. Tietz and M. Wilkening, *Phys. Chem. Chem. Phys.*, 2015, **17**, 32115-32121.
30. V. Epp, Ö. Gün, H. J. Deiseroth and M. Wilkening, *Phys. Chem. Chem. Phys.*, 2013, **15**, 7123.
31. E. Fukushima and S. B. W. Roeder, *Experimental Pulse NMR. A Nuts and Bolts Approach.*, Addison-Wesley Publ. Comp., Reading, 1981.
32. R. Böhmer, *J. Magn. Reson.*, 2000, **147**, 78-88.
33. J. Jeener and P. Broekaert, *Phys. Rev.*, 1967, **157**, 232-240.
34. F. Qi, G. Diezemann, H. Böhm, J. Lambert and R. Böhmer, *J. Magn. Reson.*, 2004, **169**, 225-239.
35. K. Arbi, M. Ayadi-Trabelsi and J. Sanz, *J. Mater. Chem.*, 2002, **12**, 2985-2990.
36. I. A. Stenina, Y. A. Velikodnyi, V. A. Ketsko and A. B. Yaroslavtsev, *Inorg. Mater.*, 2004, **40**, 967-970.
37. J. Sanz, J. M. Rojo, R. Jiménez, J. E. Iglesias and J. Alamo, *Solid State Ion.*, 1993, **62**, 287-292.
38. I. Hanghofer, M. Brinek, S. L. Eisbacher, B. Bitschnau, M. Volck, V. Hennige, I. Hanzu, D. Rettenwander and H. M. R. Wilkening, *Phys. Chem. Chem. Phys.*, 2019, DOI: 10.1039/C9CP00664H.
39. A. K. Jonscher, *Nature*, 1977, **267**, 673-679.
40. D. L. Sidebottom, *Phys. Rev. Lett.*, 1999, **83**, 983-986.
41. J. T. S. Irvine, D. C. Sinclair and A. R. West, *Adv. Mater.*, 1990, **2**, 132-138.
42. B. Ruprecht, H. Billetter, U. Ruschewitz and M. Wilkening, *J. Phys.: Condes. Matter*, 2010, **22**, 245901.
43. S. Breuer, D. Prutsch, Q. L. Ma, V. Epp, F. Preishuber-Pflügl, F. Tietz and M. Wilkening, *J. Mater. Chem. A*, 2015, **3**, 21343-21350.
44. M. Wilkening and P. Heitjans, *ChemPhysChem*, 2012, **13**, 53-65.
45. M. Wilkening, V. Epp, A. Feldhoff and P. Heitjans, *J. Phys. Chem. C*, 2008, **112**, 9291-9300.
46. A. Kuhn, S. Narayanan, L. Spencer, G. Goward, V. Thangadurai and M. Wilkening, *Phys. Rev. B*, 2011, **83**, 094302(094301)-094302(094311)
47. A. Kuhn, M. Kunze, P. Sreeraj, H. D. Wiemhöfer, V. Thangadurai, M. Wilkening and P. Heitjans, *Solid State Nucl. Magn. Reson.*, 2012, **42**, 2-8.
48. M. Wilkening, V. Epp, A. Feldhoff and P. Heitjans, *J. Phys. Chem. C*, 2008, **112**, 9291-9300.
49. N. Bloembergen, E. M. Purcell and R. V. Pound, *Physical Review*, 1948, **73**, 679-712.
50. A. Abragam, *The Principles of Nuclear Magnetism*, Claredon Press, Oxford, 1961.
51. P. M. Richards, in *Topics in Current Physics*, ed. M. B. Salamon, Springer, Berlin, 1979, vol. 15.
52. A. Bunde, P. Maass and M. Meyer, *Physica A*, 1992, **191**, 433-437.
53. P. Bottke, D. Rettenwander, W. Schmidt, G. Amthauer and M. Wilkening, *Chem. Mater.*, 2015, **27**, 6571-6582.
54. M. Wilkening and P. Heitjans, *J. Phys.: Condes. Matter*, 2006, **18**, 9849-9862.

55. M. Wilkening and P. Heitjans, *Phys. Rev. B*, 2008, **77**, 024311(024311)-024311(024313).

56. M. Wilkening, A. Kuhn and P. Heitjans, *Phys. Rev. B*, 2008, **78**.

57. R. Bertermann, W. Müller-Warmuth, C. Jansen, F. Hiltmann and B. Krebs, *Solid State Ion.*, 1999, **117**, 245-255.

58. P. Bottke, Y. Ren, I. Hanzu, P. G. Bruce and M. Wilkening, *Phys. Chem. Chem. Phys.*, 2014, **16**, 1894-1901.

TOC Graphic

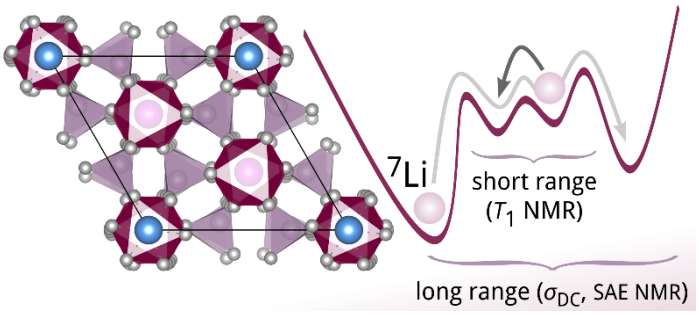

^{7}Li NMR reveals rapid cation exchange processes in NASICON-type $Li_{1.4}Ca_{0.2}Zr_{1.8}(PO_4)_3$ on a local length scale.

6.2 Halide-based Solid Electrolytes

Several classes of halogenide solid electrolytes have been investigated for ASSB. In general, halide-based solid electrolytes are divided into the following groups: i)silver ion conductors, ii) copper ion conductors, iii) halide ion conductors and iv) lithium ion conductors. Halide solid electrolytes can reach a total ionic conductivity in the range of 10^{-8} to 10^{-5} S cm^{-1}, are stable against metallic lithium and have a good mechanical strength and mechanical flexibility that results in a high electrochemical oxidation stability. However, they are attractive candidates due to the nature of halogen anions and the monovalent halogen anions which do not interact with Li like sulfur and oxygen anions do. The bigger ionic radii of halogens (r > 167 pm) lead to a long ionic bond length and higher polarizabilities. In contrast to the oxide-based solid electrolytes they have a lower ionic conductivity, a low oxidation voltage and are sensitive to moisture.[80,81]

The following pubished article contains the development and advancement of potential solid electrolytes for all-solid-state batteries. This topic deals with the disentanglement of structure and ion dynamics of lithium-rich anti-perovskites (Li_3OCl), which gain a great interest as solid electrolyte that can be used to realize all solid-state batteries.[93]

6.2.1 Untangling the Structure and Dynamics of Lithium-Rich Anti-Perovskites Envisaged as Solid Electrolytes for Batteries

The first publication aims at the detailed structural analysis of the lithium-rich anti-perovskites (LiRAPs), Li_3OCl and $Li_2(OH)Cl$, as well as the ion dynamic in this "new" solid electrolytes. LiRAPs got great attention as a new class of solid electrolytes due to the work of Braga *et al.* claiming that Li_3OCl can realize battery systems with energy densities 3 times higher than already known all-solid-state cells.[89] There are many studies that have reported the properties of LiRAPs, but many questions remain unanswered. However, the main question is, does this structure really exist? To shed light on this aspect, we synthesized "Li_3OCl" and $Li_2(OH)Cl$ *via* both hydrothermal reaction and classical solid state reaction as Braga *et al.* and Hood *et al.* did.[89,90]

X-ray powder diffraction (XRPD) and neutron powder diffraction (NPD) were used to characterize the structure of the samples and further the ion dynamic in this glassy materials was analyzed *via* impedance spectroscopy as well as nuclear magnetic resonance (NMR). It is hard to distinguish between the structures *via* X-ray powder diffraction due to the similar lattice parameters and the difficulty to detect H and Li. Even Rietveld analysis of the PND data turned out to be not as easy at it seemed at first. Here, however, we managed to separate the cubic structure as well as a new orthorhombic structure. *in situ* XRD, showed that "Li_3OCl" rapidly decomposes to Li_2CO_3 and LiCl·xH$_2$O. This instability of "Li_3OCl" explains the unusual high ion conductivity because LiCl·xH$_2$O offers a quite good electrical conductivity that is sufficient for some applications. However, the only stable LiRAPs are $Li_4(OH)_3Cl$[176] and $Li_{3-x}(OH_x)Cl$, where x > 0.

P1:

Untangling the Structure and Dynamics of Lithium-Rich Anti-Perovskites Envisaged as Solid Electrolytes for Batteries

I. Hanghofer, G. J. Redhammer, S. Rohde, I. Hanzu, A. Senyshyn, H. M. R. Wilkening and D. Rettenwander, *Chemistry of Materials*, 2018, **30**, 8134–8144.

Erratum: The fractional atomic coordinates *x*, *y*, *z* listed in table 3 have to be changed. All values 1 must be changed to $^1/_4$.

CHEMISTRY OF MATERIALS
Cite This: Chem. Mater. 2018, 30, 8134−8144
Article
pubs.acs.org/cm

Untangling the Structure and Dynamics of Lithium-Rich Anti-Perovskites Envisaged as Solid Electrolytes for Batteries

Isabel Hanghofer,[†] Günther J. Redhammer,[‡] Sebastian Rohde,[†] Ilie Hanzu,[†] Anatoliy Senyshyn,[§] H. Martin R. Wilkening,*[,†] and Daniel Rettenwander*[,†]

[†]Institute for Chemistry and Technology of Materials and Christian Doppler Laboratory for Lithium Batteries, Graz University of Technology, Stremayrgasse 9, A-8010 Graz, Austria

[‡]Department of Chemistry and Physics of Materials, University of Salzburg, 5020 Salzburg, Austria

[§]Heinz Maier-Leibnitz Zentrum (MLZ), Technische Universität München, 85748 Garching, Germany

Supporting Information

ABSTRACT: Lithium-rich anti-perovskites (LiRAPs) have attracted a great deal of attention as they have been praised as another superior group of solid electrolytes that can be used to realize all-solid-state batteries free of flammable liquids. Despite several studies that have reported on the properties of LiRAPs, many questions remain unanswered. In particular, these include fundamental ones concerning the structure, stability, and Li-ion conductivity and diffusivity. Moreover, it is not clear whether some of the previously reported compounds do really exist. To untangle the current picture of LiRAPs, we synthesized "Li_3OCl" and Li_2OHCl polymorphs and applied a wide spectrum of methods, such as powder X-ray diffraction (PXRD), powder neutron diffraction (PND), nuclear magnetic resonance spectroscopy, and impedance spectroscopy to carefully shed some light on LiRAPs. Here we self-critically conclude that the cubic polymorph of the two compounds cannot be easily distinguished by PXRD alone as the lattice metrics and the lattice parameters are very similar. Furthermore, PXRD suffers from the difficulty of detecting H and Li. Even Rietveld refinement of our PND data turned out to be complicated and not easily interpreted in a straightforward way. Nevertheless, here we report the first structural models for the cubic and a new orthorhombic polymorph containing also structural information about the H atoms. *In situ* PXRD of "Li_3OCl", intentionally exposed to air, revealed rapid degradation into Li_2CO_3 and amorphous $LiCl{\cdot}xH_2O$. Most likely, the instability of "Li_3OCl" explains earlier findings about the unusually high ion conductivities as the decomposition product $LiCl{\cdot}xH_2O$ offers an electrical conductivity that is good enough for some applications, excluding, of course, those that need aprotic conditions or electrolytes free of any moisture. Considering "H-free Li_3OCl" as well as $Li_5(OH)_3Cl_2$, $Li_5(OH)_2Cl_3$, $Li_3(OH)_2Cl$, and $Li_3(OH)Cl_2$, we are confident that $Li_4(OH)_3Cl$ and variants of $Li_{3-x}(OH_x)Cl$, where $x > 0$, are, from a practical point of view, so far the only stable lithium-rich anti-perovskites.

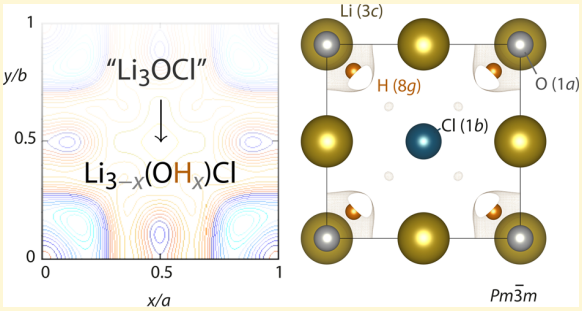

INTRODUCTION

Today's societies need to develop sustainable devices that can efficiently convert and store energy in its various forms.[1,2] Over the past few years, lithium-rich anti-perovskites (LiRAPs) have attracted a great deal of attention as another opportunity to soon realize high-performance electrochemical energy storage systems that take advantage of nonflammable solid electrolytes.[3−8] Without doubt, such systems, including Li-based and Na-based batteries,[9−12] are urgently needed to efficiently store electricity from solar, wind, or tidal sources and, thus, to ultimately cut our dependency on fossil fuels.

In 2017, Braga et al. claimed that the LiRAP "Li_3OCl", if prepared in a modified glassy form,[7] can be the heart of a game-changing new strategy for introducing all-solid-state batteries whose energy densities exceed those of conventional systems by factors of 5−10.[4] Such an announcement must be taken with a grain of salt as we have heard similar statements quite a few times before. In many cases, these possibly record-breaking new batteries never made the jump from the laboratory to the show room, and for LiRAPs, despite all efforts and studies published so far,[4,8,7] our knowledge of crystal structure, stability, phase transitions, and, finally, Li-ion dynamics is still very limited; even the existence of several LiRAPs discussed in the literature remains at least questionable[13] (also see Table S1). This fragmentary understanding is rather surprising as LiRAPs belong to the LiOH-LiCl group being best studied as part of the general system "alkaline hydroxide−alkaline halogenide".[14,15] Obviously, before we can begin to untangle the current state of knowledge, we need to take a closer look at previous reports on lithium halide

Received: June 18, 2018
Revised: October 24, 2018
Published: October 25, 2018

DOI: 10.1021/acs.chemmater.8b02568
Chem. Mater. 2018, 30, 8134−8144

hydroxides and lithium oxyhalides to evaluate the status of research today.

Lithium Halide Hydroxides (LHHs). The first investigations of LiRAPs go back to Scarpa et al.[16] On the basis of their thermochemical measurements in 1915, they supposed $Li_5(OH)_3Cl_2$ as a phase in this system. Decades later, in 1958, Rshetnikov and Unzhakov again addressed this system and confirmed $Li_5(OH)_3Cl_2$ and additionally Li_2OHCl thermochemically as phases within the LiOH-LiCl phase diagram.[17] More than 20 years later, Weppner and co-workers considered these materials as potential Li-ion-conducting solid electrolytes and started to synthesize and characterize them in more detail.[18] They prepared samples with nominal compositions of Li_2OHCl and $Li_5(OH)_3Cl_2$ by melting stoichiometric amounts of the binaries and observed Li-ion conductivities of 3×10^{-5} and 7×10^{-4} S cm^{-1} at 200 °C, respectively. They were, however, not able to confirm the phases with the help of their diffraction data. In 1993, Barlage and Jacobs structurally reinvestigated the compounds and used powder X-ray diffraction (PXRD) to confirm that Li_2OHCl crystallizes with orthorhombic symmetry [space group (SG) *Pmma*].[19] Additionally, they identified a second phase, viz., $Li_4(OH)_3Cl$ (space group $P2_1/m$), by taking advantage of single-crystal XRD. Surprisingly, they could not find any other compound in the LiOH-LiCl system, which contrasts with previous claims, e.g., the $Li_5(OH)_3Cl_2$ mentioned above.

Very recently, Hood et al. reported several new OH-based compositions, namely, $Li_4(OH)_3Cl$, $Li_5(OH)_3Cl_2$, two polymorphs of $Li_2(OH)Cl$, $Li_5(OH)_2Cl_3$, and $Li_3(OH)Cl_2$. They prepared the compounds by mixing stoichiometric amounts of the corresponding binaries.[13] Unfortunately, no Rietveld refinements were carried out to support the statements made. It is obvious from their PXRD patterns that reflections belonging to LiCl systematically increase as a function of the intentionally added amount of LiCl. The authors observed a splitting of the Li_2OHCl reflections. This observation is similar to the findings of Schwering et al., who studied $Li_{3-x}(OH_x)Cl$, where $0.83 \leq x \leq 2$.[14] It has been suggested that the substitution of Li^+ with H^+ forms OH^- or OH_2 units in the Li_3OX compound and, thus, introduces vacancies in the fully occupied Li sites.[14] Those OH^- groups rotate freely as long as the Li ions can move. With a decrease in temperature, the Li-ion conductivity decreases and the rotational motions of the OH^- units freeze. Consequently, at sufficiently low temperatures, the Li ions are statistically distributed among the available sites leading to a reduction in symmetry. Such a behavior has also been observed previously for the $LiCl{\cdot}H_2O$ system[15] and for $Li_2(OH)Cl$.[20] The phase transition is accompanied by a strong increase in the Li-ion conductivity, which suggests increased Li-ion dynamics in the cubic polymorph.

A very similar correlation of Li-ion mobility and OH^- has recently been reported by Howard et al.[21] for $Li_2O{\cdot}HCl$; the authors presented a comprehensive experimental and computational study of this system. Moreover, they found evidence of a theoretical ground state with tetragonal symmetry, which was not observed experimentally; this observation is in contrast to the cubic and orthorhombic polymorph. Song et al. also suggested such a tetragonal modification to be an intermediate phase existing at temperatures ranging from 26 to ∼60 °C. At 60 °C, they observed that the sample decomposes. The release of LiCl upon exposure of the sample to elevated temperatures indicates that the composition of the samples is highly sensitive to any post-heat treatments.[22]

Recently, Li et al. showed that the highly conductive cubic $Li_2(OH)Cl$ polymorph can also be stabilized at room temperature through substitution of OH^- with F^-.[5] Furthermore, it has been suggested that decreasing the amount of sterically hindering H causes an increase in Li-ion conductivity. It has to be noted, however, that F^- preferably replaces Cl^- instead of OH^-. This preference would explain the finding that as more F is added, more LiCl appears as an extra phase. At least this observation raises the fundamental question of whether the target phase has really been obtained.

Lithium Oxyhalides (LOHs). LiRAPs with the formula of Li_3OX (X = Cl or Br) have been reported by Zhao et al.[8] The samples that were studied were synthesized following a solid-state route using LiCl and LiOH as starting materials.[8] Zhao et al. used PXRD (without any refinement) to characterize the phases that were prepared. A closer look at the published pattern reveals, however, that the two compounds synthesized contain significant amounts of extra phases. The patterns shown clearly reveal LiCl as the main extra phase. Its presence indicates the formation of a Cl-deficient compound giving evidence that OH-based LiRAPs have been formed rather than "OH-free Li_3OCl". Both differential scanning calorimetry and PXRD reveal a phase transition at ∼40 °C, which is very similar to what is expected for $Li_2(OH)Cl$. Astonishingly, Zhao et al. reported that the symmetry decreases with an increase in temperature;[8] usually the opposite trend is observed when the temperature increases. Furthermore, the Li-ion conductivity is reported to strongly depend on the preparation conditions and on the history of the samples. An increase in ionic conductivity of 2 orders of magnitude was observed after the samples were annealed at 250 °C under vacuum for 24 h. Under ambient conditions, the ionic conductivity turned out to be on the order of $\sim 8.8 \times 10^{-4}$ S cm^{-1}.[8] For comparison, Song et al. reported that LHH variants decompose at temperatures as low as 60 °C.[22] No X-ray analyses were, however, carried out to evaluate possible structural or phase changes being presumably responsible for such a strong increase in Li-ion transport properties.[22]

In 2014, Braga et al. introduced a "glassy modification" of the "Li_3OCl" polymorph and presented doped analogues with the formula $Li_{3-2x}M_xOCl$, where M = Mg, Ca, Sr, or Ba.[4,7] For Li_3OCl doped with 0.005 Ba pfu, the authors report incredibly high Li-ion conductivities of ≲25 mS cm^{-1} at 25 °C and 240 mS cm^{-1} at 100 °C. Such values would even exceed those of liquid electrolytes. Pristine Li_3OCl showed considerably lower conductivities of only 0.12 mS cm^{-1} at 27 °C. Importantly, and this is what the authors had to admit, such high values were, however, not achievable without manipulating the samples in air.[4,7] Even more critically, as the synthesis itself was performed with water as the solvent, the occurrence of extra phases such as $Li_5(OH)_2Cl_3$ as well as the formation of another LHH phase, such as Li_2OHCl, is at least very likely (see above). In 2016, Li et al. tested several synthesis approaches to achieve highly pure Li_3OCl.[23] In all except one of their approaches, LiOH was used as the starting material. Therefore, the formation of $Li_2(OH)Cl$ instead of Li_3OCl cannot be excluded. In the approach in which Li_2O was used instead of LiOH and the authors strictly avoided the influence of moisture or humidity in any step of the synthesis, the formation of "Li_3OCl" is reported. Unfortunately, no experimental evidence is provided that would underpin this conclusion.

DOI: 10.1021/acs.chemmater.8b02568
Chem. Mater. 2018, 30, 8134−8144

To shed light on the existence and properties of LiRAPs, we prepared Li_2OHCl and "Li_3OCl", intended to be free of H, either via a hydrothermal route or by taking advantage of a solid-state sintering approach. We combined PXRD and neutron powder diffraction (PND), measured at 4 and 300 K, to analyze the crystal structures by considering all elements, i.e., Li, O, Cl, and H. Impedance spectroscopy using blocking electrodes covering a wide temperature range (153−473 K) together with ^{7}Li nuclear magnetic resonance (NMR) spin−lattice relaxation was used to characterized both long-range and short-range Li-ion dynamics. Here we show that cubic polymorphs of both compounds cannot be distinguished by PXRD. Even the analysis of PND data by Rietveld refinement turned out to be difficult in the cases of Li_2OHCl and "Li_3OCl". Nevertheless, with the help of neutron diffraction, we managed to present structural models for both the cubic and the orthorhombic polymorphs, including details about H positions. ^{7}Li NMR and impedance spectroscopy revealed rapid Li-ion bulk dynamics; the overall long-range Li-ion transport is, however, limited by highly resistive grain boundaries. Moreover, we used *in situ* PXRD to study degradation processes that were initiated when the samples were exposed to air. Taken together, we have to relativize previous claims about the existence of "glassy Li_3OCl" as well as of other compounds such as $Li_5(OH)_3Cl_2$, $Li_5(OH)_2Cl_3$, $Li_3(OH)_2Cl$, and $Li_3(OH)Cl_2$. Here we conclude that $Li_4(OH)_3Cl$ and $Li_{3-x}(OH_x)Cl$ variants, where $x > 0$, seem to be the only stable LiRAPs presented so far.

EXPERIMENTAL SECTION

Hydrothermal Synthesis and Solid-State Sintering. The hydrothermal synthesis was performed in a manner similar to the approach followed by Braga et al.[7] Stoichiometric amounts of LiCl (Sigma-Aldrich, 99%), LiOH (Sigma-Aldrich, ≥98%), and $BaOH_2$ (Sigma-Aldrich, ∼95%) were weighed under an Ar atmosphere [all chemicals were predried at 333 K under dynamic vacuum (∼10^{-3} mbar) for 24 h]. The starting materials were ground with a mortar and pestle to synthesize a 25 g batch of $Li_{2.99}Ba_{0.005}OCl$, intended to be free of H; this sample is, if not stated otherwise, named LRAP_1. The powders were mixed with distilled water in a Teflon reactor with a volume of 240 cm^3 and then placed in an autoclave for 72 h at a temperature of 493 K. Afterward, the pressure was released at 493 K until the autoclave reached a temperature of approximately 373 K. The final powder was placed in a vacuum chamber and kept there at 373 K for 24 h. Compared to the route presented by Braga et al.,[7] the drying step was changed to increase the purity of our product. The $Li_2(OH)Cl$ variants were synthesized using a solid-state sintering method. LiCl and LiOH powders were mixed according to the desired stoichiometric ratio followed by hand grinding in an agate mortar for 10 min and pressed into pellets, by applying a uniaxial pressure of ≤1 GPa. We estimated that the density of the pellets was >85% of the theoretical value. The pellets were assembled in a corundum crucible and placed in Duran glass tubes. The tubes were heated to 673 K at a heating rate of 7 K/min without (LRAP_3) or with (LRAP_2) dwelling for t_{dw} = 30 min. After the dwelling period, they were allowed to immediately cool naturally in a tube furnace.

Powder X-ray Diffraction and Neutron Diffraction. To identify main and side phases, measurements of symmetries and unit cell dimensions were taken using a Bruker D8 Advance diffractometer operating with Cu Kα radiation. Data were collected at 2θ angles ranging from 10° to 80°. The patterns were evaluated by performing Rietveld refinement with X'Pert HighScore Plus version 3.0 (PANalytical). Powder neutron diffraction experiments were performed at the Maier-Leibnitz Zentrum (FRM-II, Munich, Germany). Powder diffraction data were acquired at 4 and 300 K in constant wavelength mode using the high-resolution powder diffractometer SPODI[24] with Ge331 monochromatized neutron radiation (λ = 2.5360 Å). Experiments were performed in a 2θ range of 3−154°, and the step width was 0.04°. We used a closed cycle cryostat with the sample contained in a vanadium can. Data were treated and evaluated using JANA2006, EXPO2014, and the FULLPROF suite of programs.[25−27] VESTA was used to display crystal structures and to calculate geometric properties.

NMR Spectroscopy. ^{7}Li NMR spin−lattice relaxation and line shape measurements were used to determine Li jump activation energies. Prior to the NMR experiments, the powders were fire-sealed in Duran glass tubes with a length of ∼4 cm and a diameter of ∼3 mm. Sealing was performed under vacuum to avoid any contact of the samples with traces of humidity. Variable-temperature NMR measurements (258−433 K) were taken with a Bruker Avance III spectrometer that was connected to a shimmed cryo-magnet with a nominal magnetic field of 11.4 T. This external magnetic field corresponds to a ^{7}Li NMR Larmor frequency of $\omega_0/2\pi$ = 194 MHz. The temperature in the sample chamber was adjusted with a stream of dry and freshly evaporated nitrogen gas. At a power level of 180 W, the $\pi/2$ pulse length slightly varied from 3.0 to 3.5 μs. The saturation recovery pulse sequences was used to acquire longitudinal spin−lattice relaxation rates: $R_1 = 10 \times \pi/2 - t_d - \pi/2 - acq$.[28,29] At the beginning, a train of ten 90° pulses destroys any longitudinal magnetization M_z. After a variable delay t_d, the (diffusion-induced) recovery of M_z is detected with a final $\pi/2$ pulse. The area under the free induction decay (FID) generated was plotted as a function of t_d to construct magnetization transient M_z, which was parametrized with stretched exponentials to extract R_1 as a function of the inverse temperature. We accumulated up to 16 scans for each FID.

Impedance Spectroscopy. For the impedance measurements, the powder samples were cold pressed into cylindrical pellets that were 5.0 mm in diameter using a uniaxial pressure of 0.5−1.0 GPa. We prepared pellets with a thickness of approximately 1 mm. Gold electrodes with a layer thickness of 100 nm on both sides of the pellet were applied with a Leica EM SCD 050 sputter device. Impedance spectra were recorded with a Novocontrol Concept 80 broadband dielectric spectrometer covering a frequency (ν) range from 10 mHz to 10 MHz (173 to 453 K in steps of 20 K). A QUATRO cryosystem (Novocontrol) controlled the temperature in the (active) sample cell (BDS 1200, Novocontrol).[30] Measurements were taken under a stream of freshly evaporated dry nitrogen to strictly avoid any influence of water or oxygen on the samples. To follow how the overall conductivity changes when the samples are exposed to air, impedance measurements were taken in air at a fixed temperature (298 K) in the same cell but outside the dewar. Conductivity spectra were then recorded every 30 min.

RESULTS AND DISCUSSION

Phase Behavior of LiRAP. In Figure 1, the PXRD pattern of LRAP_1, i.e., Ba-doped "Li_3OCl", synthesized by the hydrothermal approach, which is similar to that used by Braga et al.,[4,7] is shown. It clearly exhibits reflections indicating cubic symmetry. Only minor amounts of unidentified extra phases, as is indicated by the reflection at 31° with low intensity, are observed. Most likely, this reflection originates from $Li_2(OH)Cl$; traces of humidity might have led to the formation of $Li_2(OH)Cl$ during handling of the sample.

The XRD pattern of $Li_2(OH)Cl$ synthesized by the solid-state synthesis route described above indicates that Li_2OHCl crystallizes in different polymorphs depending on the dwelling time (t_{dw}). LRAP_2 with a t_{dw} of 30 min exhibits reflections that point to cubic symmetry. Only a small amount of an extra phase is observed by PXRD, which could be identified as LiCl. Interestingly, for a t_{dw} of 0 min, a splitting of the reflections is observed (LRAP_3) (see Figure 1). At first glance, the reduced symmetry could be associated with a decrease in the OH content, which is indicated by the increased amount of

DOI: 10.1021/acs.chemmater.8b02568
Chem. Mater. 2018, 30, 8134−8144

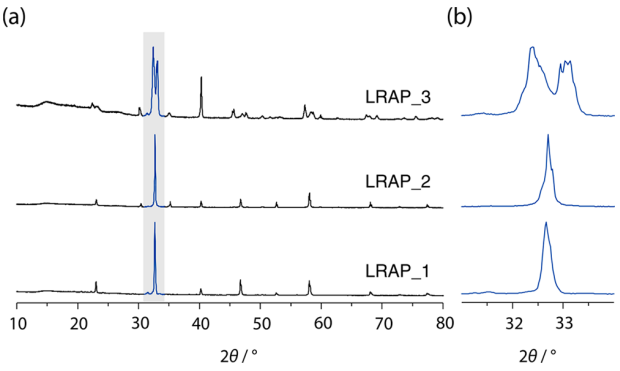

Figure 1. (a) Powder X-ray diffraction pattern of LRAP_1, LRAP_2, and LRAP_3. (b) Magnification of the most intense reflection of the LRAP's pattern shown in panel a.

LiCl. This observation is similar to that of Schwering et al.[14] Depending on the OH content for $Li_{2.17}(OH_{0.83})Cl$, they observed a phase transition from tetragonal to cubic symmetry [space group $Pm\bar{3}m$; a = 3.9035(1) Å] at 213 K. For comparison, $Li_2(OH)Cl$ revealed a phase transition from orthorhombic ($Amm2$) to cubic [$Pm\bar{3}m$; a = 3.9103(1) Å] at 308 K. The behavior of $Li_{2.17}(OH_{0.83})Cl$ is similar to that of "Li_3OCl" without any OH groups. Because both "Li_3OCl" and $Li_{2.17}(OH_{0.83})Cl$ (and presumably also other hydrates) appear in the same symmetry with very similar lattice parameters, it is difficult to distinguish the two types by using PXRD alone (see Table S1). The formation of $Li_2(OH)Cl$ is especially very likely if a water-based synthesis route has been chosen to prepare the samples. To clarify this point, we performed PND at 300 and 4 K.

PND data revealed that besides LiCl $Li_4(OH)_3Cl$ is also an impurity phase in LRAP_1. Because of the small amount of Ba in the intended composition, it is not possible to refine Ba on certain crystallographic positions or to detect Ba-containing extra phases. Indexing of the neutron diffraction pattern of LRAP_1 (see Figure 2a) yields a cubic unit cell with a = 3.89442(11) Å at 300 K and space group $Pm\bar{3}m$. Structure solution with a combination of EXPO2014 and difference Fourier analysis (see above) with subsequent Rietveld refinements using FULLPROF revealed that the compound adopts the typical anti-perovskite structure (see Table 1, which lists the corresponding fractional atomic coordinates). O and Cl fully occupy the 1a and 1b Wyckoff positions; the Li atoms are located at the 3d sites, which are only partly filled. This result gives rise to a distinct deviation from ideal chemical stoichiometry Li_3OCl. Interestingly, distinct residual negative nuclear densities are identified at the 8g (x, x, x) position (cf. Figure 2b) indicating H occupying sites being close to the oxygen positions. Without the application of any restraints, a charge-balanced chemical formula of $Li_{1.84(1)}H_{1.16(1)}OCl$ was obtained for nominally "Li_3OCl" with Li at position 3d being partly replaced by H at position 8g. As mentioned previously by Eilbracht et al.[20] for $Li_2Br(OD)$, hydrogen is statically disordered over four possible positions. The amount of H obtained from site occupation refinements is >1 and thus suggests that at least some of the oxygen atoms are fully hydrated forming H_2O molecules. At room temperature, the O−H bond distance amounts to 0.863(2) Å, which is somewhat short but still in a range typically expected for this type of bond. Li is coordinated by two O atoms at a distance of 1.947(1) Å and four Cl atoms at a distance of 2.753(1) Å (see Figure 2c and Table S2). These distances give rise to a slightly distorted octahedral coordination sphere.

Cooling the sample to 4 K does not alter the crystal structure; the lattice parameter was reduced to a = 3.86466(8) Å, and the O−H bond length turned out to be 0.929(6) Å, which is more ideal. On the other hand, the Li−O and Li−Cl bond lengths decreased to 1.931(1) and 2.731(1) Å, respectively. The atomic displacement parameters are distinctly reduced for the anions, while they are still large for Li and H. The amount of H, obtained from unconstrained refinements, was slightly too large to give a balanced formula with respect to charges. Thus, the amount of both Li and H was restrained to give three formula units. Accordingly, the chemical composition at 4 K turned out to be $Li_{1.77(5)}H_{1.33(5)}OCl$, which deviates even more from the nominal one, "Li_3ClO", being the hypothetical end-member compound. It is, however, still in agreement with cubic symmetry. We conclude that even if great care is taken to avoid any contamination with traces of moisture, "Li_3ClO" readily reacts with H sources under so-called "dry conditions".

Quantitative evaluation of the composition of LRAP_1 from neutron diffraction data obtained at 4 K resulted in 60(1) wt % "Li_3ClO" [$Li_{1.77(5)}H_{1.33(5)}OCl$], 31 wt % $Li_4(OH)_3Cl$, and 9 wt

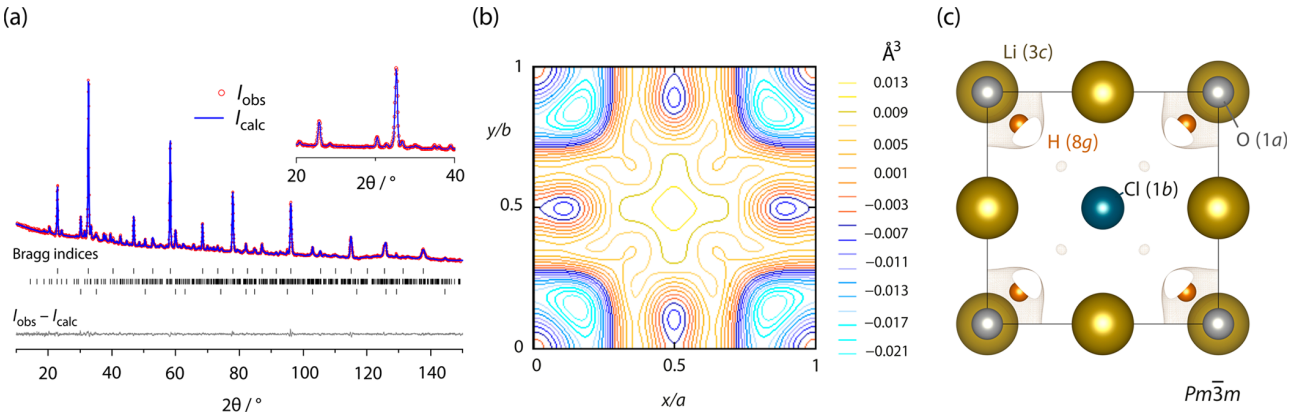

Figure 2. (a) Rietveld refinement of the powder neutron diffraction pattern of LRAP_1 ("Li_3OCl"). (b) Contour plot of the difference electron density map of the 001 plane. (c) Illustration of the crystal structure of LRAP_1 with cubic $Pm\bar{3}m$ (No. 221) symmetry showing the refined hydrogen positions based on neutron diffraction.

DOI: 10.1021/acs.chemmater.8b02568
Chem. Mater. 2018, 30, 8134−8144

Table 1. Fractional Coordinates, Isotropic Displacement Parameters, and Occupancy Factors for the Cubic $Pm\bar{3}m$ (No. 221) Structure of LRAP_1 Measured at 300 and 4 K by Powder Neutron Diffraction[a]

atom	T (K)	Wyckoff	x	y	z	B_{iso}	Occ.
O	300	1*a*	0	0	0	1.60(5)	1.00
	4		0	0	0	0.78(5)	1.00
Cl	300	1*b*	1/2	1/2	1/2	1.99(6)	1.00
	4		1/2	1/2	1/2	0.77(5)	1.00
Li	300	3*d*	1/2	0	0	7.6(4)	06.14(5)
	4		1/2	0	0	5.8(2)	0.592(5)
H	300	8*g*	0.1279(14)	0.1279(14)	0.1279(14)	4.02(14)	0.145(5)
	4		0.1389(12)	0.1389(12)	0.1389(12)	4.01(13)	0.153(5)

[a]Atomic coordinates ($\times 10^4$ Å). Equivalent isotropic displacement parameters ($\times 10^3$ Å^2). B_{iso} is defined as one-third of the trace of the orthogonalized $\mathbf{B}_{ij}$ tensor. Occ. is the site occupation number with 1.00 corresponding to a fully occupied site, independent of the Wyckoff position. It should be mentioned that an alternative setting is possible with an identical quality of refinement, i.e., Cl at 1*a*, O at 1*b*, Li at 3*c*, and H at 8*g* with $x = 0.3580$.

% LiCl, while at 300 K the composition was 67 wt % "Li_3ClO", 26 wt % $Li_4(OH)_3Cl$, and 7 wt % LiCl (see Table 2).

Table 2. Compositions of the LiRAP Samples Prepared As Obtained from Neutron Diffraction Data

LiRAP	T (K)	"Li_3OCl", $Pm\bar{3}m$	$Li_2(OH)Cl$, *Pban*	$Li_4(OH)_3Cl$	LiCl
1	4	60(1)	–	31(1)	9(1)
	300	67(1)	–	26(1)	7(1)
2	300	32(1)	64(1)	–	4(1)
3	4	–	91(1)	–	9(1)
	300	–	92(1)	–	8(1)

As we have collected the data at 4 K a few days after the measurement at 300 K, we suppose that the difference observed already originates from an ongoing decomposition process. Even if we handle and seal the sample in an Ar-filled glovebox with <0.2 ppm of H_2O, traces of water seem to initiate the decomposition of the "Li_3OCl" sample, pointing out its extremely high air sensitivity. This sensitivity is problematic for (aprotic) battery applications. For comparison, PXRD patterns of the "fresh" samples and those recorded after a storage period of 3 months, i.e., after the neutron diffraction measurements, are shown in Figure S1. The changes in chemical composition also show that the sample successively incorporates hydrogen. Also, Reckeweg et al.[31] noticed an extreme sensitivity to air and moisture leading to $LiCl{\cdot}xH_2O$ as a decomposition product. Schleid and co-workers[31] used Li_2O and LiCl as starting materials and carefully report on a compound with the formula Li_3OCl that crystallizes with cubic symmetry [$a = 3.9070(4)$ Å]; their study is one of the first on Li_3OCl and, in our opinion, belongs to the group of reliable investigations of lithium oxide chlorides Li_5OCl_3 and Li_5OCl.[31]

With respect to LRAP_3, it turned out that it crystallizes with orthorhombic symmetry characterized by the following unit cell parameters: $a = 7.74898(17)$ Å, $b = 8.00248(19)$ Å, and $c = 3.82528(8)$ Å. The space group symmetry is *Pban* (No. 50, origin choice 2). The corresponding Rietveld refinement of the ND pattern is shown in Figure 3a (for further details about indexing, symmetry analysis, and structure determination see Figure S2 and Tables S2 and S3). The crystal structure is illustrated in Figure 3c. This unit cell setting roughly corresponds to a 2*a*, 2*b*, *c* setting with respect to the cubic $Pm\bar{3}m$ structure. Similar to the case in the cubic parent form, the oxygen atom is placed into the origin at 0, 0, 0, with site symmetry 4*e*. The oxygen atom has two hydrogen positions nearby depicting similar positional disorder as already observed for LARP_1. These positions are only partially occupied, i.e., roughly by $^1/_4$ (see Table 3). Hydrogen positions H1 and H2 themselves are oriented in a common plane. This plane is, however, not coplanar to any of the main directions, *a*, *b*, or *c*.

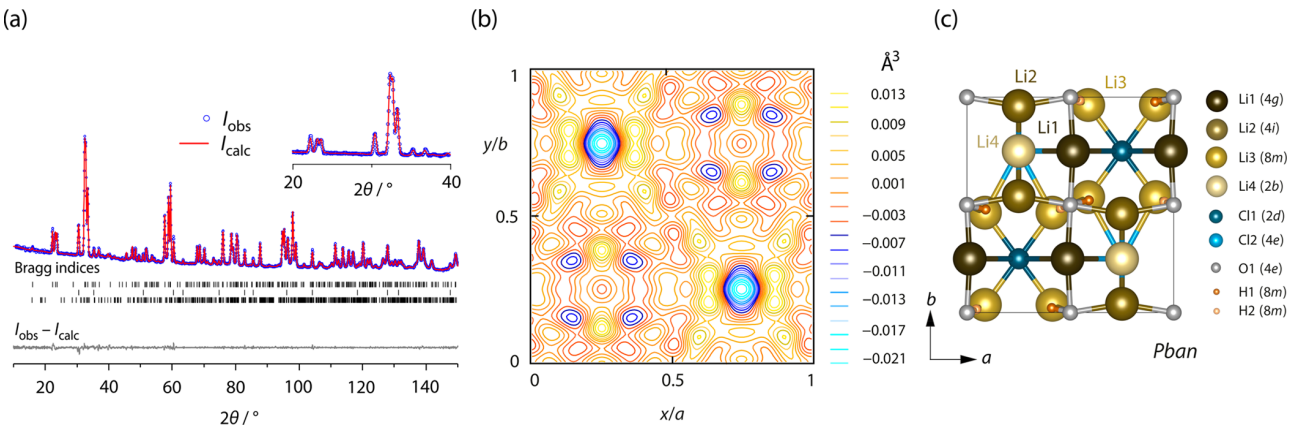

Figure 3. (a) Rietveld refinement of the powder neutron diffraction pattern of LRAP_3 [$Li_2(OH)Cl$]. (b) Contour plot of the difference electron density map of the 001 plane. (c) Illustration of the crystal structure of LRAP_3 with orthorhombic symmetry (*Pban*, No. 50) revealing the refined lithium and hydrogen positions based on neutron diffraction.

DOI: 10.1021/acs.chemmater.8b02568
Chem. Mater. 2018, 30, 8134–8144

Table 3. Fractional Atomic Coordinates, Isotropic Atomic Displacement Parameters, and Occupation Factors for the Orthorhombic *Pban* (No. 50, origin choice 2) Structure of LRAP_3 [i.e., the almost phase pure $Li_2(OH)Cl$ sample] Measured at 4 and 300 K[a]

atom	Wyckoff	x	y	z	B_{iso}	Occ.
			T = 300 K			
O1	4*e*	0	0	0	1.64(4)	0.5
Cl1	2*d*	1	1	1/2	2.39(9)	0.25
Cl2	2*c*	0.75	1	1/2	1.01(6)	0.25
Li1	4*g*	0.0373(8)	1	0	2.43(11)	0.5
Li2	4*i*	1	−0.0049(12)	0	3.68(37)	0.218
Li3	8*m*	0.0741(17)	0.0037(13)	0.454(9)	2.97(42)	0.297
H1	8*m*	0.0834(15)	0.0016(5)	0.1296(24)	2.46(25)	0.244
H2	8*m*	0.0399(14)	0.4681(17)	0.2168(33)	2.46(25)	0.244
			T = 4 K			
O1	4*e*	0	0	0	1.27(3)	0.5
Cl1	2*d*	1	1	0.5	2.44(6)	0.25
Cl2	2*c*	0.75	1	0.5	0.29(3)	0.25
Li1	4*g*	0.0136(11)	1	0	1.35(7)	0.5
Li2	4*i*	1	−0.0041(13)	0	1.35(7)	0.188
Li3	8*m*	0.0867(15)	0.0367(16)	0.475(6)	1.35(7)	0.261
Li4	2*b*	1	0.75	0	1.35(7)	0.052
H1	8*m*	0.0895(11)	0.0209(15)	0.1220(19)	1.29(18)	0.252
H2	8*m*	0.0459(8)	0.4870(20)	0.196(20)	1.29(18)	0.252

[a]Atomic coordinates (×10^4 Å). Equivalent isotropic displacement parameters (×10^3 Å^2). B_{iso} is defined as one-third of the trace of the orthogonalized $\mathbf{B}_{ij}$ tensor

It is slightly inclined so that this positional shift forces, among others, a doubling of the unit cell along the *a* and *b* directions. Two atomic positions for Cl at 2*d* and three Li atomic positions were identified. It is evident from Table 3 that Li1 and Li2 are slightly displaced from their "ideal" positions at (0, 1, 0) and (1, 0, 0), respectively. This fact is one of the main reasons for doubling of the unit cell along *a* and *b* (Figure S3). Li3 is distinctly more displaced from (0, 0, 1/2) toward the general position 8*m*; this site is only partially occupied, and the Li atoms show a positional disorder here between two nearby lying Li3 sites having a Li3−Li3 distance of 1.27(4) Å. Because of the Li1 and Li2 site displacements, two different Li−Cl atomic distances exist (see Table S2) and Li1 and Li2 are still octahedrally coordinated; the Li3 site is, however, tetrahedrally coordinated by two oxygen and two Li atoms. Compared to the LiO_2Cl_4 octahedron in the cubic phase, the Li2 site is similar to it in terms of bond lengths and distortion parameters, while the Li1 site is distinctly elongated and more distorted. From site unconstrained occupation factor refinement, the chemical composition of the compound can be determined as $Li_{2.03(1)}H_{0.98(1)}OCl$, which is almost balanced in charge and very close to the ideal $Li_2(OH)Cl$ composition. The LiCl impurity level turned out to be <10 wt % (see also Figure S4).

Recently, Song et al.[22] reported on $Li_2(OH)Cl$ with orthorhombic *Pmmm* symmetry and lattice parameters of *a* = 3.8945 Å, *b* = 3.9937 Å, and *c* = 7.6634 Å. Unfortunately, no further structural information was given. A similar cell with *Pmmm* symmetry, again without any further structural characterization, was suggested by Barlage and Jacobs.[19] On the basis of the first full structural investigation in this study, there is firm evidence that both axes have to be doubled and the cell, used by these authors, turned out to be too small. Only Schwering et al.[14] recognized the same 2*a*, 2*b*, *c* setting, however, with *Amm*2 symmetry. The determination of the space group, solely based on Pawley/Le Bail refinements, is shown in the Supporting Information (see also Tables S2 and S3 and Figure S2).

Decreasing the temperature to 4 K does not alter the crystal symmetry. Some differences were, however, observed. The most prominent one is the appearance of a fourth Li position at 2*b* (Table 3), which evidently can be identified form the negative residual nuclear density from the difference Fourier analysis (see Figure 3b). This Li4 site is populated to the extent of both the Li2 sites and the Li3 sites, while Li1 still shows a full occupation. The chemical formula, derived from the structural refinement, is $Li_{2.00(1)}H_{1.00(1)}OCl$. During cooling, the geometry of the three Li sites distinctly changes (see Table S4), which is indicative of a strong response of the structural topology to temperature variations.

Structural data for orthorhombic phase LRAP_2 are very close to those of LRAP_3, as one can see from Table S2. The composition was determined to be $Li_{2.02}H_{0.96}OCl$ from occupation factor refinement (without constraints). Note that LRAP_2 contains 32(1) wt % cubic phase with *a* = 3.90367(4) Å.

Unfortunately, estimated Li contents reported together with structural data are hardly given in the literature. Schwering et al.[14] provided such data from which one can estimate that for the cubic phase an enhanced Li content in compounds with the general formula "$Li_{3-x}OH_xCl$" causes the cubic lattice parameter to increase. The very same is observed here. Using the small amount of data and extrapolating this trend to the ideal end-member composition Li_3OCl, one should observe a lattice parameter of approximately 3.945 Å (see Figure S5). Such large values, however, have not yet been reported in the literature. Most of them range from 3.90 to 3.91 Å, which would invoke the fact that most of the samples investigated in the literature have to be characterized by $x \approx 1$.

Stability in Air. Although the U.S. patent of Owens and Hanson already has reported on the instability of LiRAPs upon exposure to air,[32] in recent publications "Li_3OCl"-type

DOI: 10.1021/acs.chemmater.8b02568
Chem. Mater. 2018, 30, 8134−8144

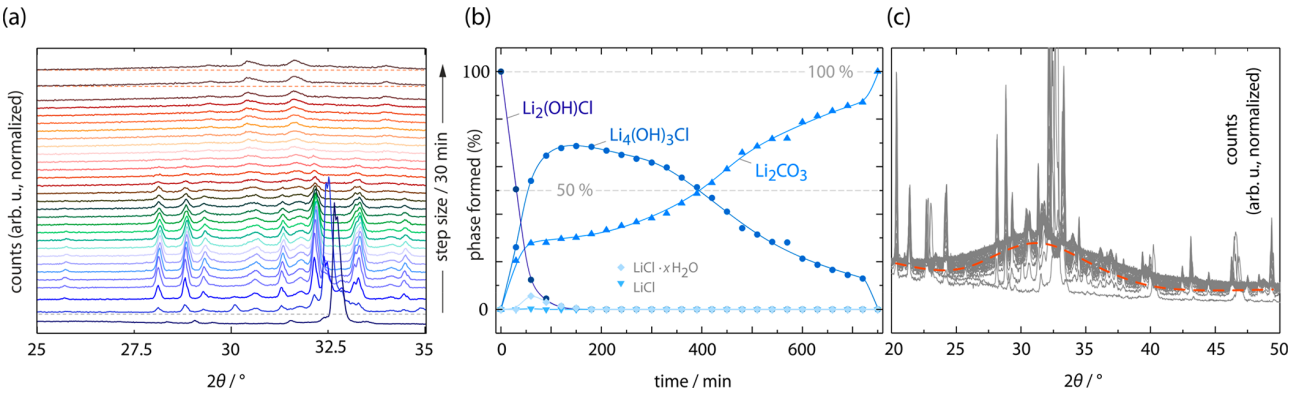

Figure 4. (a) Diffraction patterns of LRAP_1 taken in steps of 30 min to illustrate its instability in air. Even during the first scan, significant degradation occurs. (b) Phase composition as a function of exposure to air. Note the portion given in panel b does not represent the real composition because LiCl hydrates (see panel c) are seen only in the form of a broad background signal. (c) Overlay of the PXRD patterns from panel a to illustrate that with an increasing level of formation of LiCl hydrates a pronounced hump with its center at 32° emerges. This X-ray amorphous background is most likely caused by LiCl·xH$_2$O forming ionic melts, e.g., with the composition LiCl·7H$_2$O.

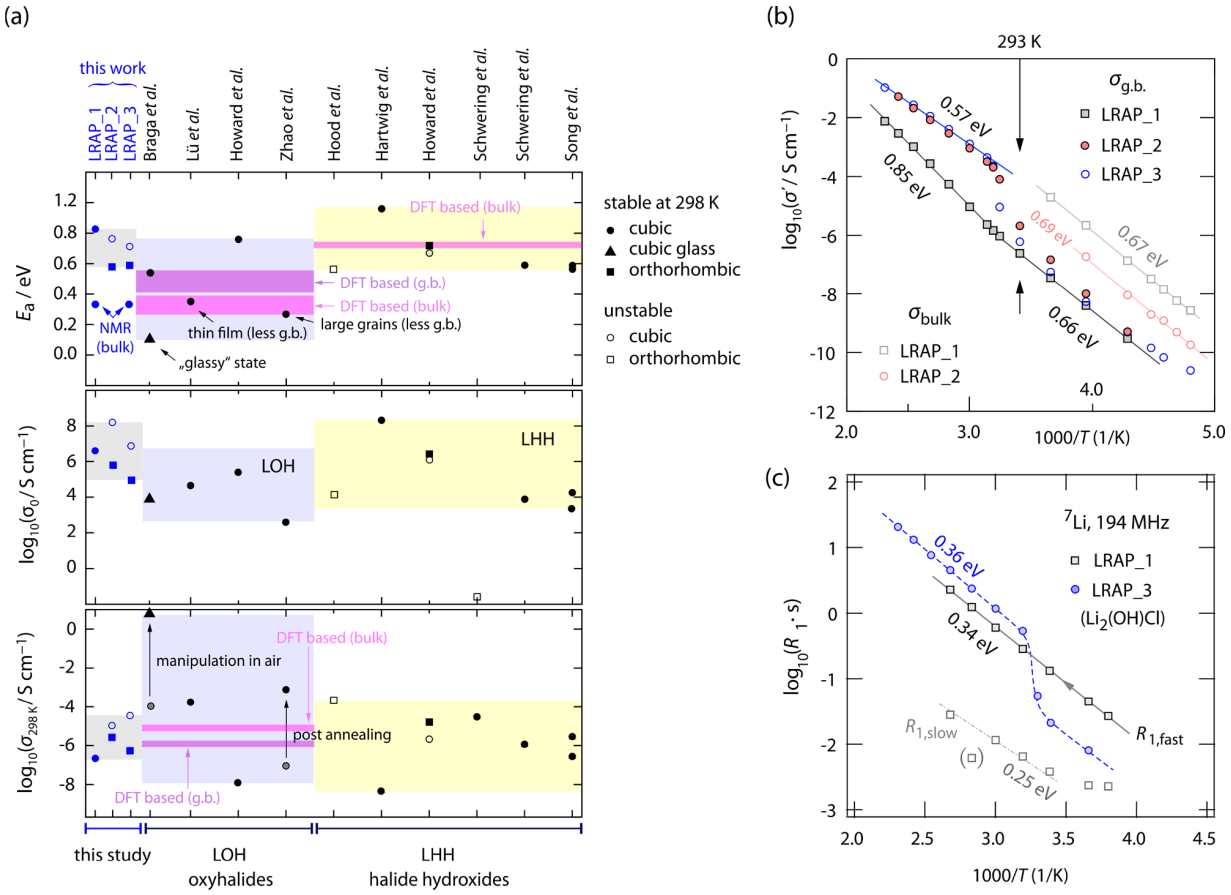

Figure 5. (a) Comparison of Li-ion conductivities ($\sigma_{298\ K}$), activation energies (E_a and $E_{a,NMR}$), and Arrhenius prefactors (σ_0) of LRAP_1, LRAP_2, and LRAP_3 (first row) with results from the literature. The studies mentioned refer to refs 19, 38, 37, 8, 13, 18, 21, 14, 14, and 22 (from left to right, respectively). Data referring to LOH and LHH are highlighted with light blue and yellow backgrounds, , respectively. The areas marked with light and dark purple indicate limits of bulk and g.b. properties calculated with the help of DFT.[35] (b) Electrical conductivities of the three samples that were investigated. For LRAP_1 and LRAP_2, the conductivity isotherms allowed for the separation of the electrical bulk response from the g.b. response (see also Figures S6 and S7). (c) Variable-temperature (diffusion-induced) ^{7}Li NMR spin−lattice relaxation rates. Well above room temperature, the cubic forms of LRAP_1 and LRAP_3 reveal an activation energy of ∼0.35 eV. LRAP_3 [Li$_2$(OH)Cl] undergoes a phase transition at 308 K and transforms at lower temperatures into the orthorhombic form.

compounds, which we believe were actually variants of Li$_2$(OH)Cl, have intentionally been manipulated in air to improve their Li-ion conductivity.[7] To monitor possible structural and compositional changes in this material and to

DOI: 10.1021/acs.chemmater.8b02568
Chem. Mater. 2018, 30, 8134−8144

understand the underlying mechanism that is responsible for such extremely high Li-ion conductivity changes, we performed *in situ* PXRD measurements on similarly prepared samples. We exposed sample LRAP_1, a mixture of $Li_{1.84(1)}H_{1.16(1)}OCl$ and $Li_4(OH)_3Cl$ [2:1 ratio (see above)] to air and recorded PXRD in steps of 30 min.

As illustrated in Figure 4, degradation starts immediately, even during the first scan, as indicated by small reflections at approximately 28°. These increase with time over the next 3 h. Through Rietveld refinement analysis, we could assign the new reflections to monoclinic $Li_4(OH)_3Cl$ [P_121/m_1 (No. 21)]. As soon as $Li_4(OH)_3Cl$ has been formed, it may react with H_2O to disproportionate into LiCl and LiOH. It has to be noted that LiOH is not observed herein. Either LiOH starts immediately to react with CO_2 from air to form Li_2CO_3, or $Li_4(OH)_3Cl$ reacts with CO_2 and HCl directly from the very beginning. In both cases, LiCl forms its hydrates afterward, which are energetically favored compared to water-free LiCl. As the highly hydrated forms of $LiCl{\cdot}xH_2O$ form a glassy-like structure, only a broad hump is seen in the PXRD pattern.[33] Therefore, the phase portion, as illustrated in Figure 4b, has to be taken with care and does not take into account X-ray amorphous compounds. The same broad hump (see the dashed line in Figure 4c) has been observed by Braga et al.[4,7] In contrast to the interpretation presented here, they claimed that this featureless background would represent a new "glassy" form of "Li_3OCl". Most likely, this hump simply reflects $LiCl{\cdot}xH_2O$, as we will discuss below. Finally, $Li_4(OH)_3Cl$ fully disappears until the only observable phases are $LiCl{\cdot}xH_2O$ and Li_2CO_3. On the basis of our observations, we propose the following degradation mechanism:

$$2Li_2(OH)Cl + H_2O \rightarrow Li_4(OH)_3Cl + HCl \quad (1)$$

$$Li_4(OH)_3Cl + CO_2 + HCl \rightarrow 2LiCl + Li_2CO_3 + 2H_2O \quad (2)$$

$$LiCl + xH_2O \rightarrow LiCl{\cdot}xH_2O \quad (3)$$

It is well-known that the electrical conductivity of $LiCl{\cdot}xH_2O$ is in the high millisiemens per centimeter range (see below). This high conductivity might also explain the extraordinary ionic conductivities of "glassy Li_3OCl" that have been reported. Needless to say, it cannot be used in applications that must be kept strictly free of moisture.

Li-Ion Dynamics. We used broadband impedance spectroscopy and variable-temperature ^{7}Li NMR spin−lattice relaxation measurements to probe ion dynamics in the LiRAP samples that were prepared. Figure 5a compares our results, i.e., activation energies (E_a), overall conductivities at 298 K (σ), and Arrhenius prefactors [σ_0 (see below)], with those presented in the literature. In panels b and c of Figure 5, results from conductivity measurements and NMR spin−lattice relaxation experiments, respectively, are depicted. Conductivity isotherms $\sigma'(\nu)$, where σ' denotes the real part of the complex conductivity, are shown in Figure S6. For LRAP_1 and LRAP_2, we were able to determine both the bulk and grain boundary (g.b.) ionic conductivities (σ_{bulk} and $\sigma_{g.b.}$, respectively).

$\sigma_{g.b.}$, when read off from the so-called frequency-independent plateau seen in $\sigma'(\nu)$,[30] follows Arrhenius behavior according to the equation $\sigma_{g.b.}T = \sigma_0 \exp[-E_a/(k_BT)]$. The same holds true for σ_{bulk}, which is accessible only at sufficiently low temperatures (see Figure 5b). NMR spin−lattice relaxation rate R_1 $\{\propto\exp[-E_{a,NMR}/(k_BT)]\}$ also reveals Arrhenius behavior (Figure 5b). The corresponding activation energy $E_{a,NMR}$ reflects short-range (i.e., bulk) ion dynamics as the rates correspond to the so-called low-T flank of diffusion-induced rate peak $R_1(1/T_1)$.[34] Deviations from Arrhenius behavior show up in those temperature regions where phase transitions occur. For LRAP_1, grain boundary conductivity $\sigma_{g.b.}$ follows an Arrhenius law with an E_a of 0.66 eV; at approximately 303 K, the slope changes yielding an E_a of 0.86 eV at higher temperatures. For both LRAP_2 and LRAP_3, $\sigma_{g.b.}$ reveals a clear increase at the same temperature. At a low T, which is the region of the orthorhombic phase, we obtain an E_a of 0.66 eV; above 317 K, the activation energy is 0.57 eV. Hence, the cubic modifications clearly exhibit higher conductivities and lower activation energies. The change occurring above room temperature can also be recognized in ^{7}Li NMR spectra (see Figure S7).

The same feature is seen by variable-temperature ^{7}Li NMR spin−lattice relaxation measurements. The diffusion-induced R_1 rates of LRAP_3 [$Li_{2.03(1)}H_{0.98(1)}OCl$ (see above)] sharply increase at 308 K. Above this temperature, they strictly follow Arrhenius behavior, which is characterized by an $E_{a,NMR}$ of 0.36 eV. A very similar activation energy (0.34 eV) is obtained for LRAP_1. Importantly, for LRAP_1, magnetization transients $M_z(t_d)$ show biexponential behavior resulting in two rates, $R_{1,fast}$ and $R_{1,slow}$ (see Figure 5c). The slower relaxation process vanishes at temperatures higher than 373 K and cannot be separated from the main one any longer. It is characterized by a lower activation energy of only 0.25 eV. It is worth remembering that LRAP_1 is a mixture of two components, viz., cubic $Li_{1.84(1)}H_{1.16(1)}OCl$ and $Li_4(OH)_3Cl$, in a ratio of approximately 2:1. At ≤295 K, transients $M_z(t_d)$ reveal two contributions reflecting this ratio. The amplitude of the slower magnetization component, $M_{slow}(t_d)$, yielding R_1 thermally activated with 0.25 eV, represents ∼30% of the total amplitude. Hence, this component is attributed to the Li spins in $Li_4(OH)_3Cl$, while the main part of $M_z(t_d)$ is given by $M_{fast}(t_d)$ governed by $R_{1,fast}$.

It is worth noting that besides Li^+ translational motions, OH reorientations, or even H^+ motions, will affect the R_1 values measured here. Thus, a clear-cut interpretation of relaxation data is always difficult in systems with more than one dynamic species. Of course, the same holds true for data from conductivity measurements. Further studies are needed to clarify which charge carriers other than Li^+ contribute to $\sigma_{g.b.}$ and σ_{bulk}. For comparison, the activation energies deduced from ^{7}Li NMR are very similar to those recently calculated by Islam and co-workers for bulk Li^+ diffusion (see below) in Li_3OCl.[35] Thus, we assume that $R_{1,fast}$ of the cubic forms, which yields similar activation energies of approximately 0.35 eV, is mainly influenced by Li^+ self-diffusion.

Going back to total conductivities found in the literature for oxyhalides (LOH) and halide hydroxides (LHH) (see Figure 5a), we recognize that the reported values cover a relatively large dynamic range of several orders of magnitude (see also Figure S8). This scattering also holds for the reported activation energies and prefactors. Figure 5a illustrates one of the most important difficulties in materials science, viz., satisfactorily establishing a relationship between the structure and dynamic properties. In many cases, it is very difficult to discover the origins of the variations seen in Figure 5a. To advance in the field of LiRAPs, accurate information about ion dynamics needs to be correlated with precise structural data. In

DOI: 10.1021/acs.chemmater.8b02568
Chem. Mater. 2018, 30, 8134−8144

many cases, the unknown morphology of the materials complicates the situation further as microstructural nuances are expected to additionally affect the overall macroscopic properties.

The extraordinarily high conductivity of "glassy Li_3OCl" stands out. Braga et al. report a $\sigma_{298\ K}$ of "25 mS cm^{-1}" and an activation energy of only 0.13 eV (see also the overview of conductivity results shown in Figure S8).[4,7] Such a high (overall) conductivity was suggested to be related to the glassy state of "Li_3OCl". The corresponding differential scanning calorimetry curves did, however, not show any indications that a glassy material is present. Alternatively, the authors simply used discontinuities of the conductivity in Arrhenius graphs to support their hypothesis and to extract a glass temperature (T_g). They gratuitously interpreted the change in conductivity as a result of the glassy structure. In many cases, it is, however, very difficult to extract reliable conductivities from impedance data when σ' reaches values in the range of 10 mS cm^{-1} at ambient temperature. These difficulties simply arise from the extremely high electrical relaxation frequencies, being expected in the gigahertz regime at such temperatures and capacitances in the usual range for g.b. (100 pF) and bulk response (1 pF). Hence, besides structural changes, artifacts, such as electrode polarization, and incomplete conductivity isotherms or Nyquist curves, which have been recorded over a limited frequency range, may easily cause deviations from linearity in Arrhenius plots. In the study by Braga et al., the upper accessible frequency was only 5 MHz. Considering the data provided and taking the impedance data for granted, we recalculated the resistance of the cell measured by Braga et al.[7] (0.24 S cm^{-1} at 373 K) and obtained a value of ∼0.5 Ω, which contradicts the resistance of 30 Ω shown in the corresponding Nyquist plot.[7] A sample with a thickness of 0.2 cm and an area of 1.76 cm^2 would result in a resistance R of only 0.5 Ω. This value is lower than the published Nyquist plot tells us by a factor of 60.

The only similarity, which remains to be discussed, concerns the prominent broad hump in the PXRD pattern shown by Braga et al.[4,7] In contrast to earlier studies, we found no evidence that this feature is proof of having "glassy Li_3OCl" at hand. Instead, there is strong evidence of a trivial explanation. The featureless background signal simply represents amorphous $LiCl{\cdot}xH_2O$ rather than a highly conducting form of "Li_3OCl". $LiCl{\cdot}xH_2O$ is known as a very good Li-ion conductor. While, from a general point of view, ionic conductivity (see below) is good enough to compete with the best solid and liquid electrolytes for batteries, its use in Li-ion batteries, being designed to work with aprotic electrolytes, is hard to imagine. As has been clearly shown above, LiCl is formed during the degradation process. It continuously reacts with H_2O from air. Depending on the final water content, Yim et al.[36] suggested five different forms for $LiCl{\cdot}xH_2O$: (i) a dilute solution, (ii) a concentrated solution, (iii) molten salt hydrates, (vi) hydrous melts, and (v) the pure salt. A molar ratio of ∼4 to 7 favors the formation of a glassy state. As an example, $LiCl{\cdot}7H_2O$ is known to form an undercooled fragile ionic melt with a high ionic conductivity and fast reorientational motions of the water molecules.[37] ^{7}Li spin−lattice relaxation NMR is mainly controlled by extremely rapid thermally activated motions of the hydrate complexes; an activation energy of 0.3 eV in the low-T regime of the R_1 peaks is found, and peaks show up at temperatures as low as 200 K (69 MHz).[38] As in liquid water, conductivity spectroscopy reveals that the corresponding electrical relaxation time is only 7 ps at 298 K.[37] Electrical conductivities of such materials take values ranging from 10 to ∼140 mS cm^{-1}.[36,37] Activation energies of $LiCl{\cdot}7H_2O$, for example, depend on the frequency regime used to acquire the data; depending on whether Vogel−Fulcher−Tamman or Arrhenius-type regimes are analyzed, values range from 0.08 to 0.14 eV.[39] Hence, the formation of $LiCl{\cdot}xH_2O$ could easily explain the high conductivity values reported for "glassy Li_3OCl".[4,7] The activation energy of "glassy Li_3OCl" presented by Braga et al. (0.13 eV) agrees with values found for $LiCl{\cdot}xH_2O$[40] (or $LiCl{\cdot}7H_2O$).[39]

Besides the influence of sample history and morphology, as mentioned above, the amount of OH groups in LiRAPs may also significantly affect ion dynamics.[14,21,22] For instance, Song et al. showed that a short and fast rotating O−H bond provides extra space for the formation of Frenkel defects. Frenkel defects seem to play a capital role to allow rapid Li-ion exchange processes, which are highly correlated, i.e., not independent, of the rotational dynamics of the OH groups.[22] Even small variations in composition may drastically change ion transport properties. Hence, with regard to the instability against moisture or air (see above) as well as with respect to the significant amounts of extra phases that can form, it is easily comprehensible that a broad range of conductivities and activation energies have been reported. Even traces of $LiCl{\cdot}xH_2O$ on experimental conductivity properties should not be underestimated.

Apart from extra phases, which are present in most of the studies in the literature, the ionic conductivity of a sample is generally affected by the nature and volume fraction of grain boundary regions. As mentioned in the Introduction, microstructural effects, such as grain size and density, influence $\sigma_{g.b.}$, which finally dominates the practical conductivities for battery applications. This view also helps rationalize the broad distribution of dynamic properties shown in Figure 5a.

Two reports[8,41] can be found in the literature in which the authors report on samples optimized with regard to their grain boundary structure. These samples show activation energies significantly lower than those usually seen for LHH and LOH. Heat treatment at 250 °C, i.e., slightly below the melting point, is assumed to increase the total Li-ion conductivity by several orders of magnitude, reaching 0.85 mS cm^{-1} under ambient conditions.[8] Here, we found that, well above room temperature, the activation energies extracted from broadband impedance spectroscopy take values of 0.57 eV (LRAP_2 and LRAP_3) and 0.85 eV (LRAP_1) (see Figure 5b). For comparison, values on the order of 0.6 eV are in good agreement with those commonly seen for LHH and LOH. $E_{a,NMR}$ values from ^{7}Li NMR R_1 measurements, which are sensitive to short-range Li jump processes in the bulk, range from 0.25 eV [$Li_4(OH)_3Cl$] to 0.36 eV [$Li_2(OH)Cl$]. In particular, for LRAP_3 [$Li_{2.03(1)}H_{0.98(1)}OCl$ with <10 wt % LiCl (see Figure S6)] above the phase transition temperature, two activation energies, viz., 0.57 eV ($\sigma_{g.b.}$) and 0.36 eV (R_1, bulk), could be precisely determined. Pronounced ^{7}Li NMR line narrowing supports the idea that in LRAP_3 rapid Li^+-ion (bulk) motions take place. For comparison, these activation energies are very similar to those presented by Dawson et al. for LOH.[35] They found, in agreement with other studies,[42−47] that the activation energy for bulk dynamics is 0.29 eV and that Li-ion transport across grain boundaries is characterized by E_a values ranging from 0.4 to 0.56 eV. These results underpin our

DOI: 10.1021/acs.chemmater.8b02568
Chem. Mater. 2018, 30, 8134−8144

assumption that experimental data indeed point to ion blocking g.b. regions in $Li_2(OH)Cl$.

SUMMARY AND CONCLUSIONS

We used both hydrothermal routes and solid-state sintering methods to prepare three different samples of LiRAPs. We took advantage of (*in situ*) PXRD, PND, ^{7}Li NMR, and broadband conductivity spectroscopy to untangle current ideas of structure and ion dynamics in this class of materials. X-ray diffraction turned out to be inadequate for reliably identifying the crystal structures of LiRAPs, calling earlier reports on "Li_3OCl" into question. In our opinion, the formation of H-free Li_3OCl has so far never been proven experimentally. Earlier studies simply use PXRD without any refinement to characterize their samples. Even Rietveld refinement on neutron diffraction data collected at 300 and 4 K needs great care to produce credible results. Here, we managed to present the first structural models for hydrothermally prepared $Li_{1.84}H_{1.16}OCl$ that crystallizes with cubic symmetry ($Pm\bar{3}m$). Via solid-state synthesis, phase pure $Li_2(OH)Cl$ that adopts a new orthorhombic structure, which is based on the *Pnma* space group, was prepared.

The instability of LiRAPs becomes apparent as the samples decompose even in a sealed container that was stored in a glovebox between two neutron diffraction measurements. *In situ* PXRD revealed immediate decomposition into Li_2CO_3 and glassy $LiCl{\cdot}xH_2O$ if $Li_{1.84}H_{1.16}OCl$ was exposed to air. $LiCl{\cdot}xH_2O$ is a very good electrical conductor, and charge carriers other than Li^+ are expected to contribute to the conductivities reported in the literature. Its formation under humid conditions may easily explain the extraordinary transport properties of "glassy Li_3OCl", whose existence had remained unconfirmed until now.

Compositional effects, the influence of morphology, and inappropriate experimental setups lead to a wide distribution of ionic conductivities and activation energies reported for LiRAPs. As we have shown by both conductivity spectroscopy and ^{7}Li NMR relaxation measurements, grain boundaries seem to block long-range ion transport. Activation energies of $Li_2(OH)Cl$ (0.56 eV including g.b.; 0.36 eV for the bulk) perfectly agree with results from theory. It is likely that, as has been suggested by theory, fast ion transport could be achieved for Li halide hydroxides by minimizing the influence of g.b. regions.

In summary, on the basis of our results and the lack of evidence found in previous reports, we are very critical of the existence of "glassy Li_3OCl" as well as $Li_5(OH)_3Cl_2$, $Li_5(OH)_2Cl_3$, $Li_3(OH)_2Cl$, and $Li_3(OH)Cl_2$. To show that these compounds really exist in nature, a systematic reinvestigation by, e.g., (single-crystal) XRD or powder neutron diffraction in combination with proper Rietveld refinement is needed. On the basis of the current state of knowledge, we are quite convinced that $Li_4(OH)_3Cl$ and $Li_{3-x}(OH_x)Cl$, where $0 < x \leq 1$, are the only LiRAPs whose existence has unambiguously been proven experimentally so far.

ASSOCIATED CONTENT

Supporting Information

The Supporting Information is available free of charge on the ACS Publications website at DOI: 10.1021/acs.chemmater.8b02568.

Additional structural parameters, conductivity isotherms, further comparisons with data from the literature, and ^{7}Li NMR line shapes (PDF)

AUTHOR INFORMATION

Corresponding Authors

*E-mail: rettenwander@tugraz.at.
*E-mail: wilkening@tugraz.at.

ORCID

Ilie Hanzu: 0000-0002-9260-9117
H. Martin R. Wilkening: 0000-0001-9706-4892
Daniel Rettenwander: 0000-0002-2074-941X

Notes

The authors declare no competing financial interest.

ACKNOWLEDGMENTS

Financial support by the DFG (FOR1277), the Austrian Federal Ministry of Science, Research and Economy, and the Austrian National Foundation for Research, Technology and Development is greatly appreciated. Furthermore, the authors are thankful for financial support from the FFG (Austrian Research Promotion Agency) in the frame of the competence project "safe battery".

REFERENCES

(1) Tarascon, J. M. Towards sustainable and renewable systems for electrochemical energy storage. *ChemSusChem* **2008**, *1*, 777−779.
(2) van Noorden, R. The rechargeable revolution: A better battery. *Nature* **2014**, *507*, 26−28.
(3) Janek, J.; Zeier, W. G. A solid future for battery development. *Nat. Energy* **2016**, *1*, 16141.
(4) Braga, M. H.; Grundish, N. S.; Murchison, A. J.; Goodenough, J. B. Alternative strategy for a safe rechargeable battery. *Energy Environ. Sci.* **2017**, *10*, 331−336.
(5) Li, Y.; Zhou, W.; Xin, S.; Li, S.; Zhu, J.; Lü, X.; Cui, Z.; Jia, Q.; Zhou, J.; Zhao, Y.; Goodenough, J. B. Fluorine-doped antiperovskite electrolyte for all-solid-state Lithium-ion batteries. *Angew. Chem., Int. Ed.* **2016**, *55*, 9965−9968.
(6) Hood, Z. D.; Wang, H.; Samuthira Pandian, A.; Keum, J. K.; Liang, C. Li_2OHCl crystalline electrolyte for stable metallic Lithium anodes. *J. Am. Chem. Soc.* **2016**, *138*, 1768−1771.
(7) Braga, M. H.; Ferreira, J. A.; Stockhausen, V.; Oliveira, J. E.; El-Azab, A. Novel Li_3ClO based glasses with superionic properties for lithium batteries. *J. Mater. Chem. A* **2014**, *2*, 5470−5480.
(8) Zhao, Y.; Daemen, L. L. Superionic conductivity in Lithium-rich anti-perovskites. *J. Am. Chem. Soc.* **2012**, *134*, 15042−15047.
(9) Hueso, K. B.; Armand, M.; Rojo, T. High temperature sodium batteries: status, challenges and future trends. *Energy Environ. Sci.* **2013**, *6*, 734−749.
(10) Pan, H. L.; Hu, Y. S.; Chen, L. Q. Room-temperature stationary sodium-ion batteries for large-scale electric energy storage. *Energy Environ. Sci.* **2013**, *6*, 2338−2360.
(11) Hartmann, P.; Bender, C. L.; Vračar, M.; Dürr, A. K.; Garsuch, A.; Janek, J.; Adelhelm, P. A rechargeable room-temperature sodium superoxide (NaO_2) battery. *Nat. Mater.* **2013**, *12*, 228−232.
(12) Chu, I. H.; Kompella, C. S.; Nguyen, H.; Zhu, Z.; Hy, S.; Deng, Z.; Meng, S.; Ong, S. P. Room-temperature all-solid-state rechargeable sodium-ion batteries with a Cl-doped Na_3PS_4 superionic conductor. *Sci. Rep.* **2016**, *6*, 33733.
(13) Hood, Z. D.; Wang, H.; Samuthira Pandian, A.; Keum, J. K.; Liang, C. Li_2OHCl Crystalline electrolyte for stable metallic Lithium anodes. *J. Am. Chem. Soc.* **2016**, *138*, 1768−1771.
(14) Schwering, G.; Hönnerscheid, A.; van Wüllen, L.; Jansen, M. High Lithium ionic conductivity in the Lithium halide hydrates

DOI: 10.1021/acs.chemmater.8b02568
Chem. Mater. 2018, 30, 8134−8144

$Li_{3-n}(OH_n)Cl$ ($0.83 \leq n \leq 2$) and $Li_{3-n}(OH_n)Br$ ($1 \leq n \leq 2$) at ambient temperatures. *ChemPhysChem* **2003**, *4*, 343−348.
(15) Hönnerscheid, A.; Nuss, J.; Mühle, C.; Jansen, M. Die Kristallstrukturen der Hydroxyhalogenide $Li_4(OH)_3Br$ und $Li_4(OH)_3I$. *Z. Anorg. Allg. Chem.* **2003**, *629*, 312−316.
(16) Scarpa, G.; Atti, R. Thermal analysis of the mixture of the alkali hydroxides with the corresponding halides. *Accad. Naz. Lincci, Sez. II* **1915**, *24*, 476−482.
(17) Reshcrnikov, N. A.; Unzhakov, G. M. Diagrammy plavkosti sistem LiOH-LiCl, LiOH-NaOH. *Zh. Neorg. Khim.* **1958**, *3*, 1433−1438.
(18) Hartwig, P.; Rabenau, A.; Weppner, W. Lithium hydroxide halides: phase equilibria and ionic conductivities. *J. Less-Common Met.* **1981**, *78*, 227−233.
(19) Barlage, H.; Jacobs, H. Ungewöhnliche Koordinationspolyeder um Sauerstoff in $Li_4Cl(OH)_3$. *Z. Anorg. Allg. Chem.* **1994**, *620*, 471−474.
(20) Eilbracht, C.; Kockelmann, W.; Hohlwein, D.; Jacobs, H. Orientational disorder in perovskite like structures of $Li_2X(OD)$ (X = Cl, Br) and $LiBr \cdot D_2O$. *Phys. B* **1997**, *234-236*, 48−50.
(21) Howard, J.; Hood, Z. D.; Holzwarth, N. A. W. Fundamental aspects of the structural and electrolyte properties of Li_2OHCl from simulations and experiment. *Phys. Rev. Mater.* **2017**, *1*, 075406.
(22) Song, A.-Y.; Xiao, Y.; Turcheniuk, K.; Upadhya, P.; Ramanujapuram, A.; Benson, J.; Magasinski, A.; Olguin, M.; Meda, L.; Borodin, O.; Yushin, G. Ion conductivities: Protons enhance conductivities in Lithium halide hydroxide/Lithium oxyhalide solid electrolytes by forming rotating hydroxy Groups. *Adv. Energy Mater.* **2018**, *8*, 1700971.
(23) Li, S.; Zhu, J.; Wang, Y.; Howard, J. W.; Lü, X.; Li, Y.; Kumar, R. S.; Wang, L.; Daemen, L. L.; Zhao, Y. Enhanced ionic conductivity with $Li_7O_2Br_3$ phase in Li_3OBr anti-perovskite solid electrolyte. *Solid State Ionics* **2016**, *284*, 14−19.
(24) Hoelzel, M.; Senyshyn, A.; Juenke, N.; Boysen, H.; Schmahl, W.; Fuess, H. SPODI: High resolution powder diffractometer. *Nucl. Instrum. Methods Phys. Res., Sect. A* **2012**, *667*, 32−37.
(25) Petříček, V.; Dusek, M.; Palatinus, L. Crystallographic computing system JANA2006: General features. *Z. Kristallogr. - Cryst. Mater.* **2014**, *229*, 345−352.
(26) Altomare, A.; Cuocci, C.; Giacovazzo, C.; Moliterni, A.; Rizzi, R.; Corriero, N.; Falcicchio, A. EXPO2013: A kit of tools for phasing crystal structures from powder data. *J. Appl. Crystallogr.* **2013**, *46*, 1231−1235.
(27) Rodríguez-Carvajal, J. Recent Developments of the Program FULLPROF. Commission on Powder Diffraction (IUCr), 2012.
(28) Epp, V.; Gün, O.; Deiseroth, H.-J.; Wilkening, M. Highly Mobile Ions: Low Temperature NMR Directly Probes Extremely Fast Li^+ Hopping in Argyrodite-type Li_6PSe_5Br. *J. Phys. Chem. Lett.* **2013**, *4*, 2118−2123.
(29) Epp, V.; Gün, O.; Deiseroth, H.-J.; Wilkening, M. Long-range Li dynamics in the lithium argyrodite Li_7PSe_6 as probed by rotating-frame spin-lattice relaxation NMR. *Phys. Chem. Chem. Phys.* **2013**, *15*, 7123−7132.
(30) Lunghammer, S.; Ma, Q.; Rettenwander, D.; Hanzu, I.; Tietz, F.; Wilkening, H. M. R. Bulk and grain-boundary ionic conductivity in sodium zirconophosphosilicate $Na_3Zr_2(SiO_4)_2PO_4$ (NASICON). *Chem. Phys. Lett.* **2018**, *701*, 147−150.
(31) Reckeweg, O.; Blaschkowski, B.; Schleid, T. Li_5OCl_3 and Li_3OCl: Two Remarkably Different Lithium Oxide Chlorides. *Z. Anorg. Allg. Chem.* **2012**, *638*, 2081−2086.
(32) Owens, B. B.; Hanson, H. J. U.S. Patent 4,007,122, 1977 (application 465,432).
(33) Ruiz, G. N.; Bove, L. E.; Corti, H. R.; Loerting, T. Pressure-induced transformations in LiCl-H_2O at 77 K. *Phys. Chem. Chem. Phys.* **2014**, *16*, 18553−18562.
(34) Uitz, M.; Epp, V.; Bottke, P.; Wilkening, M. Ion dynamics in solid electrolytes for lithium batteries. *J. Electroceram.* **2017**, *38*, 142−156.
(35) Dawson, J. A.; Canepa, P.; Famprikis, T.; Masquelier, C.; Islam, M. S. Atomic-scale influence of grain boundaries on Li-ion conduction in solid electrolytes for all-solid-state batteries. *J. Am. Chem. Soc.* **2018**, *140*, 362−368.
(36) Yim, C.-H.; Abu-Lebdeh, Y. A. Connection between phase diagram, structure and ion transport in liquid, aqueous electrolyte solutions of Lithium chloride. *J. Electrochem. Soc.* **2018**, *165*, A547−A556.
(37) Funke, K.; Heimann, B.; Vering, M.; Wilmer, D. Concept of Mismatch and Relaxation Explains DC and AC Conductivities of Fragile Glass-Forming Ionic Melts. *Proceedings of the International Symposium on Molten Salts* **1999**, *12*, 301−312.
(38) Kanert, O.; Hackmann, A.; Küchler, R.; Ngai, K. L. Nuclear spin relaxation in electrolyte glasses. *J. Non-Cryst. Solids* **1994**, *172−174*, 1424−1430.
(39) Cramer, C.; Funke, K.; Buscher, M.; Happe, A.; Saatkamp, T.; Wilmer, D. Ion dynamics in glass-forming systems: Conductivity spectra above the glass transformation temperature. *Philos. Mag. B* **1995**, *71*, 713−719.
(40) Howard, J. W. *Li^+ Ion Transport in Select Lithium-Rich Antiperovskites*. Doctoral thesis, University of Nevada, Las Vegas, 3686123.
(41) Lü, X.; Howard, J. W.; Chen, A.; Zhu, J.; Li, S.; Wu, G.; Dowden, P.; Xu, H.; Zhao, Y.; Jia, Q. Anti-perovskite Li_3OCl superionic conductor films for solid-state Li-ion batteries. *Adv. Sci.* **2016**, *3*, 1500359.
(42) Lu, Z.; Chen, C.; Baiyee, Z. M.; Chen, X.; Niu, C.; Ciucci, F. Defect chemistry and lithium transport in Li_3OCl anti-perovskite superionic conductors. *Phys. Chem. Chem. Phys.* **2015**, *17*, 32547−32555.
(43) Deng, Z.; Radhakrishnan, B.; Ong, S. P. Rational composition optimization of the Lithium-rich $Li_3OCl_{1-x}Br_x$ anti-perovskite superionic conductors. *Chem. Mater.* **2015**, *27*, 3749−3755.
(44) Emly, A.; Kioupakis, E.; Van der Ven, A. Phase stability and transport mechanisms in anti-perovskite Li_3OCl and Li_3OBr superionic conductors. *Chem. Mater.* **2013**, *25*, 4663−4670.
(45) Mouta, R.; Melo, M. Á. B.; Diniz, E. M.; Paschoal, C. W. A. Concentration of charge carriers, migration, and stability in Li_3OCl solid electrolytes. *Chem. Mater.* **2014**, *26*, 7137−7144.
(46) Stegmaier, S.; Voss, J.; Reuter, K.; Luntz, A. C. Li^+ defects in a solid-state Li-ion batteries: Theoretical insights with a Li_3OCl electrolyte. *Chem. Mater.* **2017**, *29*, 4330−4340.
(47) Chen, M.-H.; Emly, A.; Van der Ven, A. Anharmonicity and phase stability of anti-perovskite Li_3OCl. *Phys. Rev. B: Condens. Matter Mater. Phys.* **2015**, *91*, 214306.

DOI: 10.1021/acs.chemmater.8b02568
Chem. Mater. 2018, 30, 8134−8144

6.3 Sulfide-based Solid Electrolytes

These days, sulfide-based solid electrolytes are the most attractive candidates for all-solid-state batteries. The ionic conductivity of lithium thio-phosphates such as $Li_{10}GeP_2S_{12}$,[10,100] $Li_7P_3S_{11}$[177–179] and as well the lithium argyrodite phase Li_6PS_5X (X: Cl, Br)[17,111,180] reaches a value of over 10^{-2} S·cm^{-1} at room temperature and is even higher then of organic carbonate electrolytes.[94,181] In contrast to the other types of solid electrolytes, such as oxides and phosphates, sulfides are robust and flexible and therefore they can be densified easier. However, there are many challenges to commercialize solid-state lithium batteries with sulfide-based solid electrolytes. Most importantly, the stability issues need to be solved and the electrode interface need to be improved. The difference to the oxide-based solid electrolytes is that the sulfur ion is larger than the oxygen ion and therefore the sulfide-based electrolytes can come up with a larger migration tunnel for lithium ions. This strategically important point influences the migration of the lithium ions.[182]

In this part the published articles contain a detailed analysis of argyrodite-type materials, Li_6PS_5X (X: Cl, Br, I) regarding to lithium ion dynamics. Materials that contain more then one type of mobile charge carriers, including for example both Li and P ions, are perfect candidates to serve as a model systems. Analyzing the individual species separately makes it easier to compare results and interpret ion motion. Li_6PS_5Cl, Li_6PS_5Br and Li_6PS_5I were used as model systems for structure analysis *via* X-ray powder diffraction, impedance spectroscopy and NMR measurements.

6.3.1 Substitutional disorder: Structure and ion dynamics of the argyrodites Li_6PS_5Cl, Li_6PS_5Br and Li_6PS_5I

This article deals with the understanding of ion dynamics in Li_6PS_5X (X: Cl, Br, I), as a class of lithium rich solids with high Li^+ mobility. It discusses the correlation of local jump processes with long- and short-range diffusion as well as conductivity processes and the structural properties elucidated *via* X-ray powder diffraction and Rietveld analysis.

All samples of Li_6PS_5X (X: Cl, $Cl_{0.75}Br_{0.25}$, $Cl_{0.50}Br_{0.50}$, $Cl_{0.25}Br_{0.75}$, Br, $Br_{0.75}I_{0.25}$, $Br_{0.50}I_{0.50}$, $Br_{0.25}I_{0.75}$, I and $Cl_{1/3}Br_{1/3}I_{1/3}$) were obtained by a solid state reaction and structurally characterized by X-ray powder diffraction and magic angle spinning (MAS) NMR. To analyze ion dynamics, NMR spin-lattice relaxation experiments and impedance measurements were used. The central statement of this article is, that only a wide range of complementary techniques can provide the complete picture on the long- and the short range diffusion. NMR is able to probe short-range and long-range bulk ion dynamics. Bulk ion dynamics was analyzed with electric modulus data from impedance spectroscopy. We found that the activation energies range from 0.08 eV to 0.48 eV. Furthermore, this article relates anion disorder of the Argyrodite compounds (Li_6PS_5Cl, Li_6PS_5Br, Li_6PS_5I), which were quantified with XRPD. Impedance measurements for Li_6PS_5Cl and Li_6PSBr show an extremely fast lithium ion diffusion process, whereas for Li_6PS_5I the ionic conductivity

turned out to be very poor. Interestingly, NMR relaxometry revealed that in Li_6PS_5I a short-range diffusion process, which is as fast as for the Cl- and Br- containing argyrodites, is present.

In section 6.3.1.1 the characterization of the main Argyrodite component, Li_7PS_6, is shown and discussed separately.

P2:
Substitutional disorder: Structure and ion dynamics of the argyrodites Li_6PS_5Cl, Li_6PS_5Br and Li_6PS_5I
I. Hanghofer, M. Brinek, S. L. Eisbacher, B. Bitschnau, M. Volck, V. Hennige, I. Hanzu, D. Rettenwander and H. M. R. Wilkening, *Phys. Chem. Chem. Phys.*, 2019, **21**, 8489–8507.

PCCP

PAPER

Cite this: *Phys. Chem. Chem. Phys.*, 2019, **21**, 8489

Substitutional disorder: structure and ion dynamics of the argyrodites Li_6PS_5Cl, Li_6PS_5Br and Li_6PS_5I†

I. Hanghofer,*[a] M. Brinek,[a] S. L. Eisbacher,[a] B. Bitschnau,[b] M. Volck,[c] V. Hennige,[c] I. Hanzu,[ad] D. Rettenwander[a] and H. M. R. Wilkening*[ad]

Received 2nd February 2019,
Accepted 27th March 2019

DOI: 10.1039/c9cp00664h

rsc.li/pccp

For the development of safe and long-lasting lithium-ion batteries we need electrolytes with excellent ionic transport properties. Argyrodite-type Li_6PS_5X (X: Cl, Br, I) belongs to a family of such a class of materials offering ionic conductivities, at least if Li_6PS_5Br and Li_6PS_5Cl are considered, in the mS cm^{-1} range at room temperature. Although already tested as ceramic electrolytes in battery cells, a comprehensive picture about the ion dynamics is still missing. While Li_6PS_5Br and Li_6PS_5Cl show an exceptionally high Li ion conductivity, that of Li_6PS_5I with its polarizable I anions is by some orders of magnitude lower. This astonishing effect has not been satisfactorily understood so far. Studying the ion dynamics over a broad time and length scale is expected to help shed light on this aspect. Here, we used broadband impedance spectroscopy and ^{7}Li NMR relaxation measurements and show that very fast local Li ion exchange processes are taking place in all three compounds. Most importantly, the diffusion-induced NMR spin–lattice relaxation in Li_6PS_5I is almost identical to that of its relatives. Considering the substitutional disorder effects in Li_6PS_5X (X = Br, Cl), we conclude that in structurally ordered Li_6PS_5I the important inter-cage jump processes are switched off, hindering the ions from taking part in long-range ion transport.

1 Introduction

Energy from renewable sources can be stored in various ways. Considering electrochemical storage, Li-based batteries offer high energy densities combined with a high degree of design flexibility.[1–3] In particular, batteries using Li^+ as an ionic charge carrier are an emerging option to power electric vehicles.[1–7] Such batteries may, however, suffer from flammable fluorinated liquid electrolytes conventionally used in these energy storage systems. Next-generation Li batteries with, *e.g.*, metallic Li anodes and equipped with solid electrolytes have aroused great interest.[8–12] Devices with non-flammable ceramic electrolytes are anticipated to benefit from increased safety as they easily withstand higher temperatures. Thus, such systems are less sensitive to thermal runaway.

To take full advantage of all-solid-state Li (or Na) batteries, electrolytes with exceptionally high ionic conductivities are needed.[8–15] In the past, only a few ceramics were available fulfilling this requirement.[16,17] This lack of suitable materials prevented any commercialization on a large scale.[18,19] Ideal candidates should (i) show room-temperature ionic conductivities with values comparable to those of liquids, (ii) be chemically stable over a sufficiently wide temperature range and (iii) possess a sufficiently high electrochemical stability over a large potential window.[10,11] For battery applications, the conductivity of a ceramic material should reach a value of 10^{-3} S cm^{-1} at room temperature.[10,14]

Over the last years several classes of materials have been presented whose members show very high conductivities. These materials include sulfides, such as $Li_7P_3S_{11}$ and $Li_{10}GeP_2S_{12}$, oxides including garnets, such as $Li_7La_3Zr_2O_{12}$, or phosphates based on the NASICON structure.[8–15,20–26] Although the ionic bulk conductivities of oxides and phosphates can reach very high values, the materials may suffer from high grain boundary (g.b.) resistances.[27] For the softer sulfides the difference between the bulk and g.b. conductivities[28] is expected to be much lower. Of course, Li-bearing sulfides or thiophosphates are sensitive to air and moisture, thus requiring careful handling and adequate processing. As an example, the Ge-containing thiophosphate $Li_{10}GeP_2S_{12}$ (LGPS),[13] which initiated the renaissance to consider

[a] *Christian Doppler Laboratory for Lithium Batteries and Institute for Chemistry and Technology of Materials, Graz University of Technology (NAWI Graz), Stremayrgasse 9, 8010 Graz, Austria. E-mail: isabel.hanghofer@tugraz.at, wilkening@tugraz.at; Fax: +43 316 873 32332; Tel: +43 316 873 32330*
[b] *Institute of Physical and Theoretical Chemistry, Graz University of Technology, Stremayrgasse 9, 8010 Graz, Austria*
[c] *AVL List GmbH, 8020 Graz, Austria*
[d] *Alistore-ERI European Research Institute, 33 rue Saint Leu, 80039 Amiens, France*

† Electronic supplementary information (ESI) available: Rietveld refinements and structural data, further NMR data. See DOI: 10.1039/c9cp00664h

sulfide-based systems as candidates for solid electrolytes, is characterised by an ionic conductivity of 12 mS cm^{-1}. Meanwhile the expensive element Ge has been replaced by cheaper and naturally abundant materials.[29] The electrochemical stability of LGPS-based systems needs, however, to be improved.[30]

Besides LGPS, Deiseroth and co-workers introduced Li-containing argyrodite-type Li_6PS_5X (X = Cl, Br, I).[31] The crystal structure is shown in Fig. 1; the possible Li exchange processes are illustrated as well. As an example, the ionic conductivity of Li_6PS_5Br and Li_6PS_5Cl is reported to range from 10^{-3} S cm^{-1} to 10^{-2} S cm^{-1} depending on the preparation technique, which influences the type and number of defects as well as the overall morphology.[32,33] Thus, the ionic conductivity of Li-argyrodites is only slightly smaller than that of the LGPS family. Lower costs make this family of electrolytes highly attractive for application in all-solid-state batteries.[31,34]

In 2008 Deiseroth *et al.* reported the solid-state synthesis of Li_6PS_5X (X = Cl, Br, I) and characterised the local and long-range structure by X-ray diffraction and NMR.[31] Three years later Rao *et al.* discussed the synthesis of the lithium argyrodite *via* ball milling.[35] Rayavarapu *et al.* showed that the disorder in both the lithium distribution over the available cation sites and the disorder in the S^{2-}/Cl^- and S^{2-}/Br^- sublattices promotes lithium ion conductivity.[36] This view has further been supported by bond-valence calculations.[37]

Over the last years a number of studies have been carried out to measure the ionic conductivities of the Li_6PS_5X family by using standard impedance measurements.[31–40] The overall goal, not only for Li_6PS_5X, is to relate macroscopic application relevant properties to crystal chemical and morphological properties. So far, the results reported have rarely been related to the length-scale specific properties of the measuring technique applied. The ionic conductivities for Li_6PS_5X vary from 10^{-7} S cm^{-1} to 10^{-2} S cm^{-1}, while the highest values are found for X = Cl, Br. The corresponding activation energies reported, either experimentally probed or calculated, take values from 0.11 eV to 0.57 eV.[31–40] Astonishingly, the I-compound Li_6PS_5I shows the lowest conductivity. According to the strategy of substitutional disorder, size mismatch and polarizability of the halogen anion one could have expected the opposite trend. Replacing S by a larger and more polarizable anion such as I, as compared to the small and unpolarizable Li cation, is expected to cause lattice distortions which on their part lead to a broader distribution of slightly inequivalent Li sites in the Li sublattice. Without any strong site preference of the Li ions they are expected to jump quickly between the local minima of such a heterogeneous, *i.e.*, non-uniformly shaped, potential landscape. Such a situation, sometimes also connected to geometric frustration, is very similar to F diffusion in the recently investigated system $(Ba,Ca)F_2$,[41,42] Li diffusion in $Li_7La_3Zr_2O_{12}$ oxides[43] and Na diffusion in some *closo*-borates.[44] While this situation might be the origin for the high conductivity in Li_6PS_5Br and Li_6PS_5Cl, for the I analogue it seems to incompletely describe the real situation as for Li_6PS_5I relatively low ion conductivities are reported.

In an elegant way, Kraft *et al.*[34] tried to establish a connection between the stiffness (or polarizability) of the anion sublattice in Li_6PS_5X and the macroscopic ionic transport properties. They used impedance spectroscopy and ultrasonic speed of sound measurements to collect information on activation energies and the pre-factors governing the underlying Arrhenius equation. They reported that soft lattices, as is the case for Li_6PS_5I, lead to smaller Arrhenius pre-factors than obtained for Li_6PS_5Cl and Li_6PS_5Br. This decrease in pre-factor, which might originate from a change of the migration entropy or attempt frequencies, has been used to explain the low (overall) ion conductivity in Li_6PS_5I.

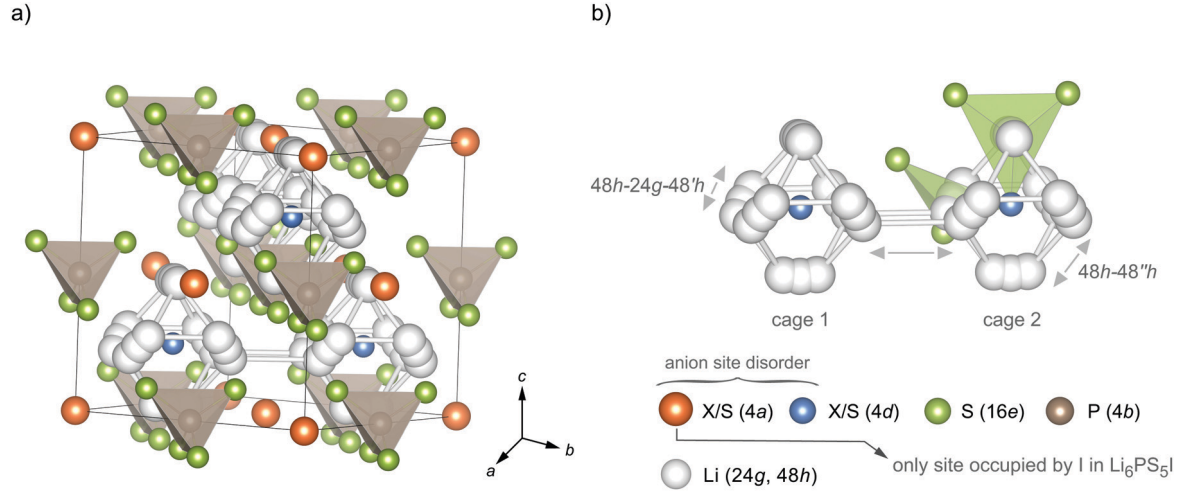

Fig. 1 (a) Crystal structure of argyrodite-type Li_6PS_5X (X = Cl, Br, I). In a perfect ordered structure, a cubic lattice is formed with PS_4^{3-} tetrahedra and Li ions being arranged octahedrally. Some of the S^{2-} (4d) anions are placed in the middle of the Li octahedra; the anions on 4a form a face centred cubic lattice. (b) The two different lithium positions (24g, 48h) form an octahedral arrangement in which three different jump processes can occur: (i) strictly localised jumps between the Li positions 48h–24g–48h′; (ii) intracage jumps (48h–48h″) and (iii) so-called intercage jumps $48h_1$–$48h_2$ between two neighbouring cages 1 and 2. The latter jump process forms interconnected diffusion pathways being responsible for 3D long-range ion transport. Site disorder on the anion positions 4a and 4d, which is absent for Li_6PS_5I, is expected to influence the Li ion diffusivity significantly.

Here, we employed impedance and NMR spectroscopy to shed more light on the effect seen for Li_6PS_5I. The important structural differences between the three argyrodites have to be taken into account to explain the significant changes in ionic conductivities, pre-factors and activation energies. For this purpose we have not only looked at the monosubstituted compounds like Li_6PS_5X, but also at samples with two or three different anions such as $Li_6PS_5Cl_{0.5}Br_{0.5}$ or $Li_6PS_5Cl_{1/3}Br_{1/3}I_{1/3}$. The non-substituted compound Li_7PS_6 served as a reference material. Importantly, complementary techniques which are sensitive to ion dynamics on different length-scales and time-scales are used to fully characterise the transport properties. We will show that, on a short-range length scale, the Li ions in Li_6PS_5I are as rapid as in the Br and Cl analogues. Obviously, the ordered S^{2-}/I^- sublattice, as compared to the disordered situation for Li_6PS_5Cl and Li_6PS_5Br, is responsible for a more regular potential landscape with a higher degree of site preference for the Li ions. As a consequence, we assume that intercage jump processes in Li_6PS_5I occur less frequently. These processes are, however, needed to establish rapid long-range ion dynamics in the iodide.

2 Experimental

2.1 Sample preparation through a solid state reaction

The Li argyrodites Li_6PS_5X, with the compositions shown in Fig. 2b, have been prepared by mixing stoichiometric amounts of Li_2S (Sigma-Aldrich $\geq$99.98%), P_2S_5 (Honeywell Fluka $\leq$99%) and LiCl (Sigma-Aldrich, anhydrous, 99%), LiBr (Sigma-Aldrich, anhydrous, 99.98%) and LiI (Sigma-Aldrich, 99.9%). The starting compounds were mechanically milled using a high-energy planetary ball mill (Fritsch Pulverisette 7 Premium line) at a rotation speed of 400 rpm for 4 hours (15 min milling; 15 min pause). Milling was carried out using ZrO_2 beakers (45 ml) filled with 180 balls (ZrO_2, 5 mm in diameter). Afterwards the mixtures were uniaxially pressed (0.4 tons) into pellets with a diameter of 5 mm, filled into quartz ampoules and sealed under a vacuum. The ampules were preheated at 573 K under a dynamic vacuum to remove traces of water. The reaction was carried out at 823 K (heating rate: 5 K min^{-1}, duration 7 days; cooling rate 10 K min^{-1}). All preparation steps were strictly carried out in an Ar gas atmosphere (H_2O < 1 ppm, O_2 < 1 ppm).

2.2 X-ray powder diffraction (XRPD)

The samples were analyzed by X-ray diffraction using a Bruker D8 Advance diffractometer (Bragg Brentano geometry, Cu K_α radiation). The patterns, shown in Fig. 2, were recorded with a step size of 0.02° (measuring time 2 s) in the 2θ-range 20° to 100°. Rietveld refinement, see Fig. 3 and the ESI† (Fig. S1 and S2), was carried out by using X'PertHighScorePlus (Panalytical).

2.3 Impedance spectroscopy

To measure the impedance responses of the pellets, Au electrodes were applied. We used a LEICA EM SCD 050 sputter coater to equip the samples with a thin Au layer of 100 nm thickness.

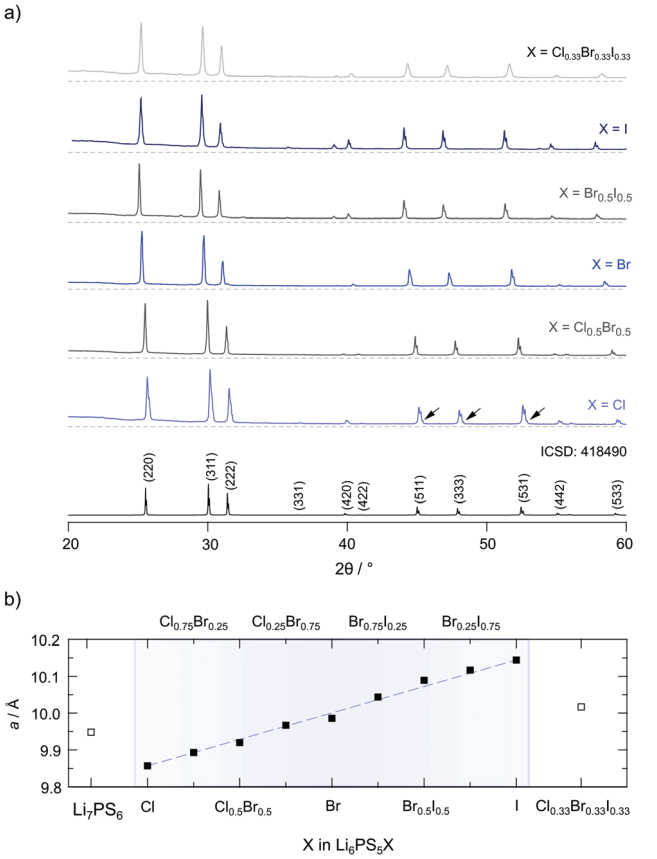

Fig. 2 (a) X-ray powder diffraction patterns of the Li_6PS_5X series investigated within this study (X = Cl, $Cl_{0.5}Br_{0.5}$, Br, $Br_{0.5}I_{0.5}$, I and $Cl_{0.33}Br_{0.33}I_{0.33}$). The XRPD patterns were recorded after the final annealing step at room temperature. In some cases, little, almost negligible, amounts of Li_3PO_4 and LiX are visible; the amount of LiX does not exceed 1.5 wt%. Only for Li_6PS_5Cl *ca.* 3.3 wt% Li_3PO_4 is seen, see the arrows; in all other cases its amount is negligible or less than 1.5 wt%, see the ESI† for Rietveld refinements (Fig. S1 and S2). (b) Lattice parameter of Li_6PS_5X obtained from Rietveld refinements of the patterns shown in (a). The lattice parameter increases continuously with the radius of X.

Impedance spectra were recorded with a Novocontrol Concept 80 broadband dielectric spectrometer; the frequency range covered ranged from ν = 10 mHz to 10 MHz. The temperature T was varied from 173 K to 453 K in steps of 20 K; the temperature in the sample holder was controlled by a QUATRO cryosystem (Novocontrol) that uses freshly evaporated nitrogen and a heater to adjust the temperature with an accuracy of ±0.5 K. The measurements were carried out in a dry nitrogen atmosphere to avoid any contamination with water and oxygen.

2.4 ^{7}Li static NMR measurements

For the time-domain NMR measurements the samples Li_6PS_5Cl, Li_6PS_5Br and Li_6PS_5I were sealed in Duran© glass tubes (*ca.* 4 cm in length and 3 mm in diameter). They were kept under a vacuum to protect them from any reaction with humidity or traces of oxygen. We used ^{7}Li NMR line shape measurements and spin–lattice relaxation (SLR) experiments to collect information about Li activation energies and jump rates. Longitudinal NMR SLR rates ($1/T_1$) as well as spin-lock rates ($1/T_{1\rho}$)

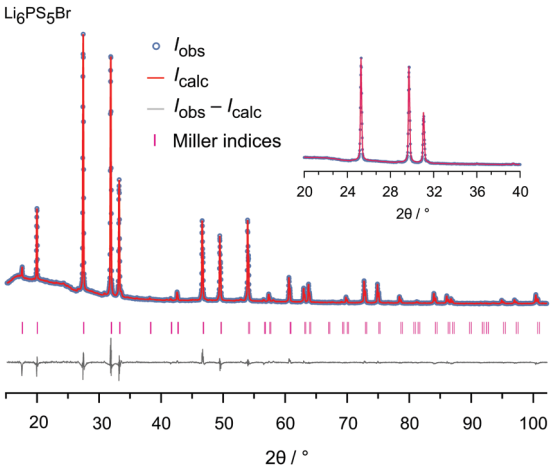

Fig. 3 Rietveld analysis of the XRPD pattern of Li_6PS_5Br recorded at 293 K (R_{Bragg} = 4.633%). In this plot the Bragg positions as well as calculated and observed profiles are depicted. The analysis reveals a phase pure sample. The R_w profile is 10.84% and the GoF amounts to 4.82; see the ESI† for further explanations.

were measured by employing a Bruker Avance III spectrometer connected to a shimmed cryomagnet with a nominal magnetic field of 7 T. This field corresponds to a ^{7}Li Larmor frequency of $\omega_0/2\pi$ = 116 MHz. For the measurements at temperatures T ranging from 173 K to 433 K a ceramic high-temperature probe (Bruker Biospin) was used. At a power level of 200 W the $\pi/2$ pulse length ranged from 2.7 to 3.2 μs slightly depending on temperature. A Eurotherm temperature controller in combination with a type T thermocouple was used to control and to monitor the temperature in the sample chamber. Low temperature measurements down to T = 124 K were performed with a cryo probe (Bruker) that uses freshly evaporated nitrogen to reach temperatures below ambient. The $\pi/2$ pulse length of the cryo probe ranged from 3.0 to 4.3 μs at a power level of 95 W. It is equipped with a LakeShore 331 element equipped with two Cernox temperature sensors.

^{7}Li NMR SLR rates $1/T_1 \equiv R_1$ in the laboratory frame were acquired with the well-known saturation recovery pulse sequence.[45,46] This sequence uses a comb of closely spaced $\pi/2$ pulses to destroy any longitudinal magnetization M_z. The subsequent recovery of M_z was detected as a function of waiting time t_d with a $\pi/2$ reading pulse: $10 \times \pi/2 - t_d - \pi/2 -$ acquisition.[15] To construct the magnetization transients $M_z(t_d)$, we plotted the area under the free induction decays (FIDs) *vs.* t_d. Up to 16 FIDs were accumulated for each waiting time.

The transients $M_z(t_d)$ were parameterised with stretched exponentials, $M_z(t_d) \propto 1 - \exp(-(t_d/T_1)^{\gamma})$, to extract the SLR rates R_1. Additionally, rotating-frame ^{7}Li NMR SLRρ rates $1/T_{1\rho} \equiv R_1$ were measured by means of the spin-lock technique: $\pi/2 - p_{lock}$ acquisition. We used a locking frequency $\omega_1/2\pi$ of 20 kHz.[47,48] The duration t_{lock} of the locking pulse p_{lock} was varied between 22 μs and 460 ms. To ensure full longitudinal relaxation between each spin-lock scan the recycle delay was set to at least $5 \times T_1$. Again, the $R_{1\rho}$ rates were obtained by analysing the resulting transients $M_\rho(t_{lock})$ with stretched exponentials of the form $M_\rho(t_{lock}) \propto \exp(-(t_{lock}/T_{1\rho})^{\kappa})$. While the stretching exponents γ varied from 1 to 0.9, the exponents κ range from 0.4 to 1, depending on the temperature. Some of the $T_{1\rho}$ transients showed bi-exponential behaviour and were analyzed with a sum of two stretched exponential functions.

2.5 Magic angle spinning (MAS) NMR

^{6}Li (73.6 MHz), ^{31}P (202.4 MHz), ^{127}I (100.1 MHz), ^{79}Br (125.3 MHz) and ^{35}Cl (49.0 MHz) NMR spectra under magic angle spinning (MAS) conditions were recorded with a 500 MHz Avance spectrometer (Bruker). The high-resolution MAS NMR spectra were measured at a rotation speed of 25 kHz using 2.5 mm rotors with an ambient bearing gas temperature. Spectra were recorded with a single pulse sequence. We accumulated up to 128 scans for one spectrum. LiCl, KBr, LiI and 85% H_3PO_4 served as ref. 31 to determine chemical shifts δ_{iso}. In order to detect also very slow diffusion processes and to obtain quantitative MAS NMR spectra we varied the recycle delay from 1 s to 180 s. Sufficiently long relaxation delays guarantee full longitudinal relaxation of all spectral components. Further information on pulse lengths, temperature effects and delay times are given in the ESI,† see Table S1.

3 Results and characterization

3.1 Sample characterization by X-ray powder diffraction

To study the ion dynamics in argyrodite-type Li_6PS_5X we used a solid-state synthesis approach to prepare samples with the following compositions: X = Cl, $Cl_{0.75}Br_{0.25}$, $Cl_{0.5}Br_{0.5}$, $Cl_{0.25}Br_{0.75}$, Br, $Br_{0.75}I_{0.25}$, $Br_{0.5}I_{0.5}$, $Br_{0.25}I_{0.75}$, I and X = $Cl_{0.33}Br_{0.33}I_{0.33}$, respectively. Through replacing S^{2-} with X^- we change the average lattice constant of the crystal structure, the polarisability of the anion lattice and the degree of anion disorder. The relative density of our samples, estimated from the sintered pellets used for impedance spectroscopy, reached values ranging from 92% to 98%. Argyrodite-type Li_6PS_5X is expected to crystallise with cubic $F4\bar{3}m$ face centered (fc) symmetry; the crystal structure is depicted in Fig. 1.

In Fig. 2a the XRPD patterns of all samples are shown including a reference pattern taken from the literature (entry no. 418490 in the inorganic crystal structure database (ICSD)). The positions and intensities of the reflections obtained for the different patterns of Li_6PS_5X including Li_7PS_6 match very well with what is expected from the literature. Humps at low diffraction angles originate from the mercapto foil used to protect the samples from reaction with air during the measurements.

To characterise the samples in detail, Rietveld refinements were carried out. As an example, the result of the analysis is shown for Li_6PS_5Br in Fig. 3. The Li_6PS_5Br sample is phase pure and crystallises with cubic symmetry (space group $F4\bar{3}m$); the lattice parameter turned out to be a = 9.986 Å. The same symmetry is found for the other samples; the amount of side phases or impurities turned out to be extremely low, see the ESI.† When going from Li_6PS_5Cl to Li_6PS_5I the lattice parameter a increases from a = 9.857 Å to a = 10.145 Å. Lattice expansion of

the unit cell is expected because the radius r of the anion increases in the order $r_{Cl} < r_{Br} < r_I$. Here, an increasing unit cell volume stabilises the lithium ions in the transition state 24g; the change in lattice constant a seems to also affect the Li occupancies in the Li_6PS_5X series as has been shown by neutron diffraction.[34]

Recent neutron and X-ray synchrotron diffraction studies have shown that in fc cubic argyrodite-type Li_6PS_5Cl and Li_6PS_5Br the S^{2-} and X anions can occupy three different crystallographic positions. Whereas the 16e site is fully occupied by S^{2-} anions, the sites 4a and 4d are shared by the S^{2-} and X anions. For Li_6PS_5Cl Kraft *et al.* found that 38.5% of the 4a site and 61.5% of the 4d site is occupied by Cl^-.[34] The rest is filled by S^{2-} anions; Li^+ only occupies the 48h sites. For Li_6PS_5Br Rietveld analysis yielded occupancies of 77.9% (4a) and 22.1% (4d) with Li^+ distributed over the 48h (44.1%) and 24g (11.9%) sites. Thus, the highest degree of anion disorder is found for Li_6PS_5Cl, while cation disorder for the samples rich in Br. This finding is in contrast to what Rietveld refinement resulted in for Li_6PS_5I. While Li disorder is also present for the split-site (48h (39.1%) and 24g (21.9%)), in Li_6PS_5I the I anions solely occupy the 4a sites. The 4d sites are fully occupied by S^{2-}. Deiseroth and co-workers also reported on the same order/disorder effects earlier.[31,40,49]

The larger difference in ionic radii between I^- and S^{2-} (r_{I^-} = 216 pm *vs.* $r_{S^{2-}}$ = 184 pm, as compared to r_{Cl^-} = 181 pm and r_{Br^-} = 195 pm) might lead to this site preference for the anions. The anion sublattice in Li_6PS_5I is, thus, structurally ordered as compared to Li_6PS_5Cl (and Li_6PS_5Br); simultaneously, cation disorder shows up for Li_6PS_5Br and Li_6PS_5I.[36,37,50] The compounds with mixed halogen compositions agree well with the trend in S^{2-}/X occupancy and cation disorder.[34] As will be discussed below, anion ordering seems to have an important impact on long-range ion diffusion in the I compound.

The 24g site represents an intermediate state used by the Li ions on 48h to diffuse through. As a result of these two lithium positions three different jump processes can occur; they are explicitly shown in Fig. 1b. (i) A strongly localised process is given by 48h–24h–48h′ jumps. Intracage jumps are possible within the octahedral cage when the Li ions jump between the 48h sites: (ii) 48h–48h″. (iii) Long-range ion dynamics needs $48h_1$–$48h_2$ intercage jump processes between two different cages 1 and 2. The latter jump process is expected to be strongly affected by the anion site disorder of X and S^{2-}. We expect that a high degree of substitutional disorder will have a significant impact on the associated jump rate, which characterises exchange processes between the cages.

3.2 Magic angle spinning NMR

To investigate local structures of the argyrodites, we recorded ^{31}P (spin-quantum number $I = 1/2$) MAS NMR spectra of Li_6PS_5X (X = Cl, Br, I) at a spinning speed of 25 kHz. The spectra are shown in Fig. 4a. In line with the report of Deiseroth and co-workers,[31] the ^{31}P MAS NMR resonance of Li_6PS_5I shows a very sharp line centered at δ_{iso} = 96.3 ppm pointing to an ordered anion framework with the I anions non-randomly occupying selected crystal sites. Small shoulders near the main signal might point to defect sites in Li_6PS_5I.

The ^{31}P MAS NMR spectrum of Li_6PS_5I is in stark contrast to the situation that is met for Li_6PS_5Cl, for which we expect the influence of strong S/Cl disorder on the line shape, see above. Indeed, its very broad line, which can hardly be resolved,

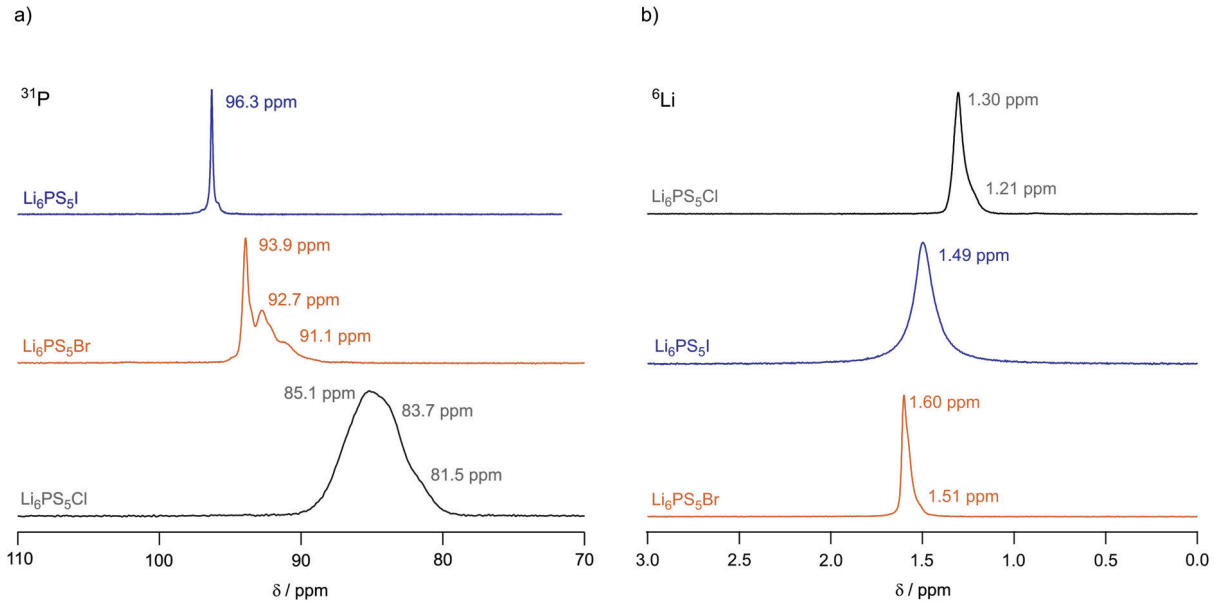

Fig. 4 (a) ^{31}P MAS NMR spectra of Li_6PS_5I, Li_6PS_5Br and Li_6PS_5Cl recorded at 202.4 MHz and a spinning frequency of 25 kHz. The spectra have been referenced to 85% H_3PO_4 and were recorded at an ambient bearing gas temperature.[31] (b) ^6Li MAS NMR spectra of Li_6PS_5Cl, Li_6PS_5Br and Li_6PS_5I recorded at 73.6 MHz and a spinning speed of 25 kHz. All spectra have been referenced to solid $LiCH_3COO$. Values given in ppm indicate the isotropic chemical shifts.

reveals a wide distribution of chemical shifts and strong spin–spin interactions. Chemical shifts of lines constituting the overall line range from 85 to 81 ppm. Therefore, ^{31}P MAS NMR clearly reveals anion disorder in Li_6PS_5Cl. The ^{31}P MAS NMR line of Li_6PS_5Br takes an intermediate position. It is composed of narrower lines than those seen for Li_6PS_5Cl; nevertheless, line broadening, as compared to Li_6PS_5I, reveals disorder in the S/Br sublattice. At least the spectrum is composed of three distinct lines located at 93.9 ppm, 92.7 ppm and 91.1 ppm, respectively. The same increase in substitutional disorder might be seen if we consider the corresponding ^{127}I, ^{79}Br and ^{35}Cl MAS NMR spectra of the three compounds; the corresponding spectra of the three quadrupole nuclei are shown in the ESI,† Fig. S3. Clearly, because of the large quadrupole moment of I ($|Q(^{127}I)| = 0.721b$) the full spectrum including its spinning side bands is rather broad. The isotropic signal, however, is much smaller than that for Li_6PS_5Cl and Li_6PS_5Br with $|Q(^{35}Cl)| = 0.855b$ and $|Q(^{79}Cl)| = 0.330b$. Although exposed to less second order quadrupole effects, the line of Li_6PS_5Cl is as broad as that of the Br compound. Site disorder in Li_6PS_5Cl might explain this additional broadening.

The ordered anion framework seen for Li_6PS_5I by ^{31}P MAS NMR, synchrotron X-ray diffraction and neutron diffraction[34] is fully consistent with results from ^{7}Li SLR NMR on the ion dynamics in the I compound. As we will show and discuss below, an almost symmetric diffusion-induced ^{7}Li NMR rate peak describes longitudinal spin–lattice relaxation in Li_6PS_5I; Li^+ disorder on the split-site does not influence this symmetry. This observation mainly points to the absence of pronounced site disorder in the anion sublattice. Structural anion disorder is, thus, expected to have a significant impact on both the Li ion diffusion and ionic conductivity in Li_6PS_5X.

For the sake of completeness, we also recorded ^{6}Li ($I = 1$) MAS NMR spectra at an ambient bearing gas temperature, these spectra are shown in Fig. 4b. They have been referenced to $LiCH_3COO$. For Li_6PS_5Br and Li_6PS_5Cl we observe a slightly asymmetric line with chemical shifts of $\delta_{iso} = 1.6$ ppm and $\delta_{iso} = 1.3$ ppm, respectively. The line of Li_6PS_5I turned out to be more symmetric in shape and is broader than the other lines. As Li_6PS_5Br and Li_6PS_5Cl show rapid Li ion long-range translational dynamics their lines represent already coalesced spectra at the measurement temperature of 307 K, see the ESI.† This observation is in perfect agreement with ^{7}Li NMR motional line narrowing (see below), which has reached its extreme limit already well below ambient temperature.

In contrast, complete line narrowing of the static ^{7}Li NMR line of Li_6PS_5I is shifted toward much higher temperature, revealing significantly slower long-range ion dynamics (*vide infra*). In addition, the absence of effective Li ion dynamics in Li_6PS_5I, which would be able to also average (small) second order quadrupolar interactions that the spin-1 nucleus ^{6}Li is exposed to, might further increase the width of the NMR line of Li_6PS_5I as compared to the samples with X = Cl or Br. The increased anisotropy seen for Li_6PS_5Cl is in line with the degree of site disorder in Li_6PS_5Cl and Li_6PS_5Br.

Interestingly, according to the halogen anion introduced into the argyrodite struture the isotropic chemical shift values δ_{iso} of the ^{6}Li MAS NMR spectra increase from Li_6PS_5Br to Li_6PS_5I and further to Li_6PS_5Cl. Thus, the paramagnetic component of the NMR line decreases; obviously, the different halogen anions change the electron density distribution in the direct neighborhood of the Li spins with Li_6PS_5Br having the highest density.

3.3 Ion dynamics as seen by conductivity spectroscopy

We used broadband impedance spectroscopy[51–53] covering frequencies from the mHz to the MHz region to study the ion dynamics in Li_6PS_5X to see the change in the overall ionic transport properties with the X substitution. As an example, in Fig. 5a the real part σ' of the complex conductivity $\hat{\sigma}$ of Li_6PS_5Br is plotted *vs.* the frequency ν.

At low frequencies and high temperatures T the isotherms $\sigma'(\nu)$ reveal electrode polarization, which results from the accumulation of ions at the surface of the ion blocking electrodes applied.[52–54] Towards higher frequencies or at sufficiently low T, distinct direct current (DC) plateaus show up, which reflect long-range ion transport. The corresponding σ_{DC} value is governed by both bulk and grain boundary contributions. For the bromide sample, Li_6PS_5Br, $\log_{10}(\sigma_{DC})T$ follows Arrhenius behaviour

$$\sigma_{DC}T = \sigma_0 \exp(-E_{a,DC}/(k_B T)) \quad (1)$$

with an activation energy, $E_{a,DC}$, as low as 0.296 eV. The corresponding Arrhenius line is shown in Fig. 5b. Almost the same behaviour is seen for $Li_6PS_5Cl_{0.5}Br_{0.5}$. Going back to the underlying isotherms $\sigma'(\nu)$ we clearly observe dispersive regions at very low T and high frequencies ν. These regions can be approximated by a Jonscher-type power law, $\sigma' = \sigma_{DC} + A\nu^p$, where A is the alternating current coefficient and p represents the power law exponent. Because of the very high ionic conductivity of Li_6PS_5Br, this behaviour, influenced by short-range ion dynamics including forward–backward jump processes, is only seen at temperatures below 193 K.[52,54] Here, p turned out to be *ca.* 0.75; such a value is expected for 3D correlated motion.[55] Similar isotherms were observed for the other compositions investigated.

For comparison, in Fig. 5b the temperature dependence of $\log_{10}(\sigma_{DC})T$ of the other samples is presented. Li_6PS_5I and Li_7PS_6 are characterised by the lowest conductivities and the highest activation energies $E_{a,DC}$ of 0.47 eV and 0.37 eV. At approximately 250 K we notice a slight deviation from the Arrhenius line determining $\log_{10}(\sigma_{DC})T$ at higher T. This behaviour cannot be related to the phase transition of Li_6PS_5I;[31,39,40,49] the I compound transforms into a low-T phase at $T \approx 160$ K, see below. Such a slight deviation is also seen for Li_6PS_5Cl.

In Fig. 6a the changes in activation energies, ionic conductivities and Arrhenius pre-factors (σ_0, see eqn (1)) are illustrated. In all cases, the replacement of sulfur anions in Li_7PS_6 by heavier halide anions leads to a decrease in activation energies. Except for Li_6PS_5Cl and $Li_6PS_5Cl_{0.75}Br_{0.25}$ the Arrhenius pre-factor σ_0 also decreases. This feature, which is seen when Li_6PS_5Br is compared with Li_7PS_6 (or Li_6PS_5Cl), has been interpreted in terms of the Meyer–Neldel[56] rule and related to a reduction in

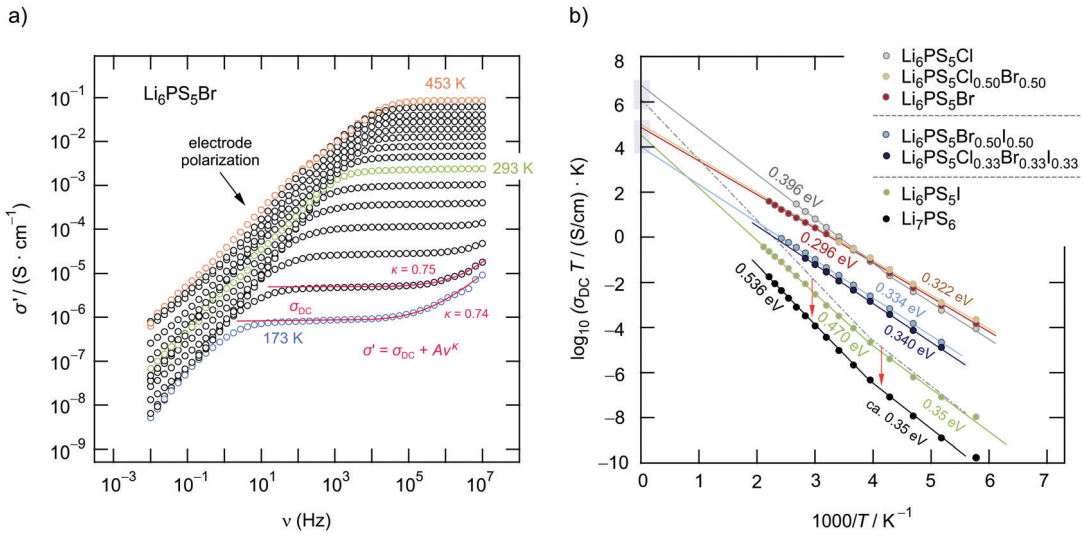

Fig. 5 (a) Conductivity isotherms (10 mHz to 10 MHz) of Li_6PS_5Br at temperatures ranging from 173 K to 453 K; isotherms have been recorded in steps of 20 K. (b) Change of the DC conductivity of Li_6PS_5X as a function of inverse temperature. The highest conductivity is found for Li_6PS_5Cl and the lowest for Li_6PS_5I. Data points and the Arrhenius line referring to Li_7PS_6 have an offset of −2 on the log scale for the sake of clarity.

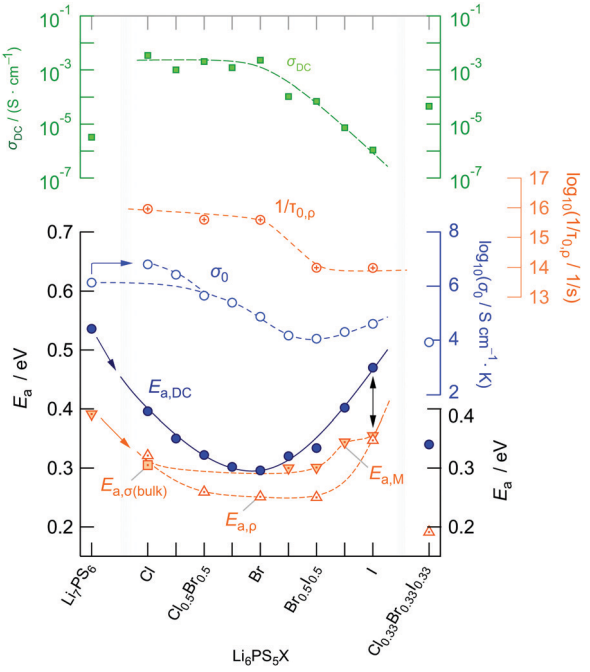

Fig. 6 Activation energies $E_{a,DC}$ of the argyrodite samples prepared. $E_{a,DC}$, determined with the help of conductivity isotherms, characterises the overall ion transport, which is affected by both bulk and g.b. contributions. A minimum is found for Li_6PS_5Br. The dependence of the corresponding Arrhenius pre-factor on anion substitution is also shown. For the sake of completeness, we also included activation energies that, most likely, describe bulk ion dynamics. These have been extracted either (i) from conductivity isotherms (Li_6PS_5Cl), (ii) from modulus spectra or (iii) from variable-temperature resistivity measurements carried out at fixed frequencies (see below). In the upper graph overall ionic conductivities at room temperature are shown. The highest conductivity of 3×10^{-3} S cm^{-1} has been observed for Li_6PS_5Cl, whereas Li_6PS_5I reveals the lowest overall conductivity of only 10^{-6}.

Debye frequencies for soft lattices created by substitution of Br and I for S.[34] If we compare our results for Li_6PS_5Cl with respect to the conductivity behaviour of Li_7PS_6 we witness both a decrease in $E_{a,DC}$ from 0.536 eV to 0.396 eV and an increase in σ_0 by one order of magnitude. This favorable combination of $E_{a,DC}$ and σ_0 results in a room temperature ionic conductivity of σ_{DC} = 3.8 mS cm^{-1}. For Li_6PS_5Br, with its more polarisable anions on the other hand, the low activation energy is compensated by a pre-factor two orders of magnitude lower than that for Li_6PS_5Cl. Considering high temperatures this feature causes σ_{DC} to adopt values lower than those of Li_6PS_5Cl.

Interestingly, the ionic conductivity of ordered Li_6PS_5I is even lower than that of the non-substituted compound Li_7PS_6; this decrease, despite the higher activation energy found for Li_7PS_6, can also be explained by the relatively low value for σ_0. The pre-factor is proportional to the attempt frequencies ν_a, the number of effective charge carriers n_{Li} and an entropy term.[42] Besides the effect of ν_a, trapping effects in Li_6PS_5I, because of a very low intercage jump rate, might reduce N for this sample. If we assume similar ν_a values for Li_6PS_5Cl and Li_6PS_5Br, entropy effects could serve as an explanation for the change in σ_0. Especially for the highly disordered Li_6PS_5Cl sample[50] the migration entropy might take a decisive role in influencing the ion dynamics. For the ordered Li_6PS_5I compound this contribution might be absent.

When going from Li_6PS_5Br to Li_6PS_5I we see that, despite the introduction of polarisable iodine anions, the pre-factor remains almost the same, $A = \log(\sigma_0/(\text{S cm}^{-1}\ \text{K})) = 4.9$ for Li_6PS_5Br and $A = 4.6$ for Li_6PS_5I, but $E_{a,DC}$ increases from 0.296 eV to 0.47 eV. From this point of view, although the lattice gets softer in the case of I, Kraft *et al.* mentioned[34] that Meyer Neldel seems to be not fully applicable to describe the situation in Li_6PS_5I. One could have expected the more polarisable I anions to allow the Li ions to squeeze through smaller voids.[50] Obviously, this concept does not work for Li_6PS_5Br and Li_6PS_5I, at least if we regard the (overall) averaged long-range ion transport process as probed by σ_{DC} measurements.

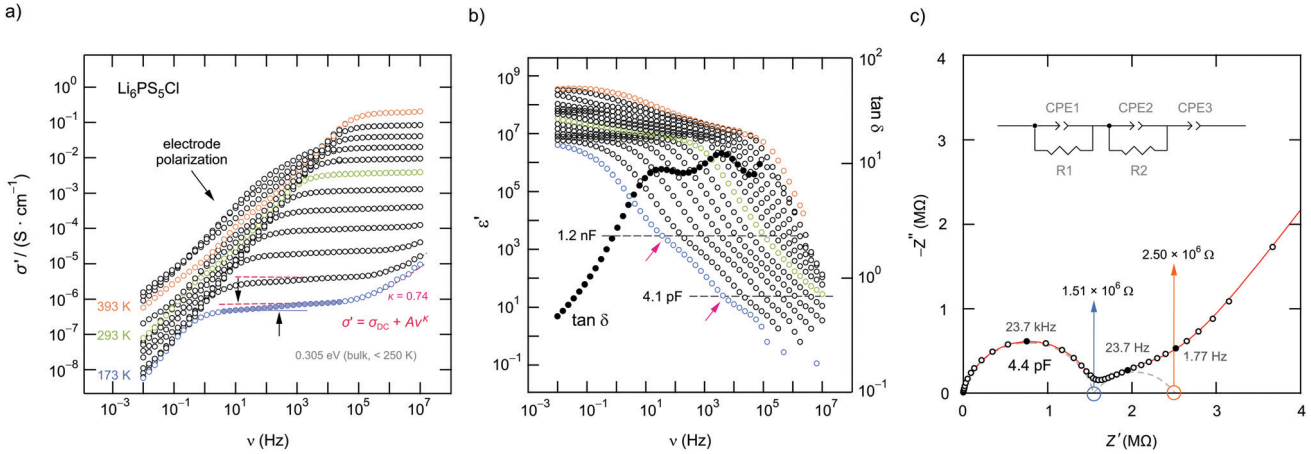

Fig. 7 (a) Conductivity isotherms of Li_6PS_5Cl recorded at temperatures ranging from 173 K up to 393 K. Jonscher-type power laws are used to parameterise the dispersive regions seen at the lowest temperatures. At sufficiently low T we notice a step in the DC plateaus that is attributed to contributions from grain boundaries and the bulk regions. (b) Real part of the permittivity (and loss factor (173 K)) plotted as a function of frequency. Disregarding the polarisation regime, ε' also reveals a two-step frequency decay characterised by the following capacitances: 4.1×10^{-12} F and 1.2×10^{-9} F. Dots show the change of the loss factor $\tan\delta$ passing through two maxima. (c) Complex plane plot (Nyquist plot) of the real part Z' *vs.* the imaginary part Z'' of the complex impedance $\hat{Z}$ of a Li_6PS_5Cl pellet (173 K). Two depressed semicircles are seen reflecting the bulk (4.4×10^{-12} F) and grain boundary response (6.8×10^{-9} F).

The ionic conductivities of the mixed compounds containing I anions, *viz.* $Li_6PS_5Br_{0.5}I_{0.5}$ and $Li_6PS_5Cl_{1/3}Br_{1/3}I_{1/3}$, do not vary much. Obviously, the introduction of I plays the crucial role to lower σ_{DC}. The Cl anions do not affect the ionic transport in these high-entropy compounds in a positive way, at least for compounds containing two anions greatly differing in ionic radius (181 pm *vs.* 216 pm). To take a closer look at the exceptional behaviour of Li_6PS_5Cl with its high degree of anion disorder we tried to separate the bulk and grain boundary contributions of this sample. Moreover, we used complex resistivity measurements to further characterise the ion dynamics.

The $\sigma'(\nu)$ isotherms of Li_6PS_5Cl are shown in Fig. 7a. A careful look at the DC plateau region shows that it contains a small step. Thus, it is composed of actually two plateaus. Below 250 K, the corresponding activation energies turned out to be 0.310 eV and 0.305 eV, see Fig. 7b. The two-step behaviour of the $\sigma'(\nu)$ isotherms of Li_6PS_5Cl are also seen if we plot the real part ε' of the complex permittivity *vs.* ν (Fig. 7b). We used the equation for a parallel-plate capacitor to estimate the corresponding capacitance C of the two steps:

$$C = \varepsilon_0 \varepsilon_r \cdot \frac{A}{d} \qquad (2)$$

Here ε_0 represents the electric field constant (8.854×10^{-12} F m^{-1}), and A is the area and d the thickness of the sample. While the first DC plateau at high frequencies is characterised by C_1 = 4.1 pF, for the one at lower ν we found C_2 = 1.2 nF. Therefore, the plateau associated with C_1 in the pF range represents the bulk response, whereas the response at lower frequencies is governed by grain boundary contributions for which capacitances typically in the nF regime are expected.[57] The estimated capacitances are in good agreement with those that can be inferred from complex plane plots (Fig. 7c). At 173 K the corresponding Nyquist plot is dominated by two depressed semicircles; electrode polarization shows up at low frequencies. If we calculate C *via* $\omega_{el} = 1/RC$, where $\omega_{el} = 2\pi\nu_{el}$ is the electric relaxation frequency and R the resistance at the intercept of the curve with the Z' axis,[57] we obtain C_1 = 4.4 pF and C_2 = 6.8 nF, being in good agreement with the estimation presented above. Only for Li_6PS_5Cl we managed to separate the small difference between the bulk and g.b. contributions. Also for Li_6PS_5I this difference is expected to be very small.

For comparison, the two contributions in the electrical relaxation of Li_6PS_5Cl are also seen in the loss factor $\tan\delta = \varepsilon''/\varepsilon'$ when plotted as a function of frequency ν (see also Fig. 7b). The maxima in $\tan\delta$, showing up at 15.36 Hz (g.b.) and 4.21 kHz (bulk), correspond to the plateaus or inflection points of $\varepsilon'\nu$, see also Fig. 8. According to $\hat{\sigma} = i\omega\varepsilon_0\hat{\varepsilon} = i\omega\varepsilon_0\varepsilon' + \omega\varepsilon_0\varepsilon''$ the maxima in $\tan\delta$ produce two minima if the frequency dependence of the imaginary part $\sigma''(\propto\varepsilon')$ is analyzed (Fig. 8).

To further characterise ion hopping in Li_6PS_5X, especially if we consider samples with lower conductivity than Li_6PS_5Cl and

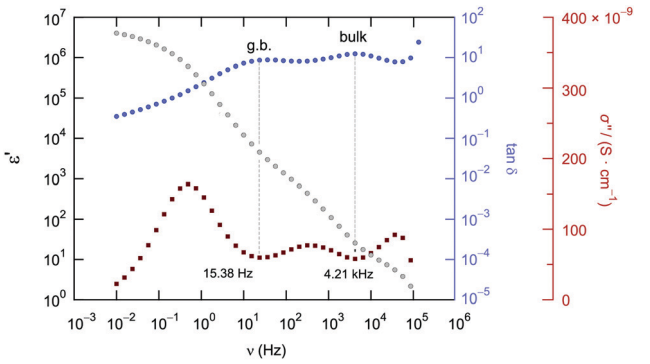

Fig. 8 Comparison of the frequency dependence of $\tan\delta$, ε' and σ'' of Li_6PS_5Cl measured at 173 K. Plateaus (or inflection points) in ε' result in minima in σ'' and maxima in $\tan\delta$, respectively.

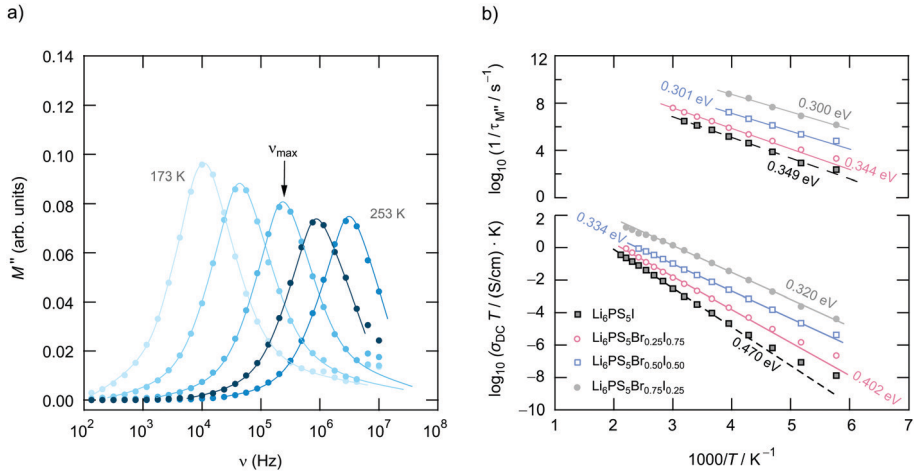

Fig. 9 (a) Frequency dependence of the imaginary part of the modulus, M'', of $Li_6PS_5Br_{0.50}I_{0.50}$ recorded from 173 K to 253 K in steps of 20 K. The lines are to guide the eye. The temperature dependence of the rate τ_M^{-1} is shown in (b). For comparison, the results for $Li_6PS_5Br_{0.25}I_{0.75}$, $Li_6PS_5Br_{0.75}I_{0.25}$ and Li_6PS_5I are also included. The lower part of the graph shows $\sigma_{DC}T(1/T)$; the values given represent activation energies. For the sake of clarity, data of $Li_6PS_5Br_{0.75}I_{0.25}$ (solid line, grey) have been plotted using an offset of +1 on the log scale.

Li_6PS_5Br, we used the electric modulus representation[58,59] to take a look at electrical relaxation frequencies $\tau_{M''}^{-1} = \nu_{max}$. As an example, in Fig. 9 for $Li_6PS_5Br_{0.5}I_{0.5}$ the imaginary part M'' of the complex modulus is plotted *vs.* ν. Since the amplitude of M'' is proportional to $1/C$, bulk processes are mainly seen. For samples with very high conductivities, such as Li_6PS_5Cl, the peaks are shifted to too high frequencies and are, thus, no longer fully visible. Activation energies $E_{a,M''}$ from our $M''(\nu)$ analysis are also included in Fig. 6. For comparison, the bulk activation energy deduced from Fig. 7 is included, too. They reveal that the activation energies, which we ascribe to bulk properties, do not change much if we consider compounds up to the composition $Li_6PS_5Br_{0.5}I_{0.5}$. This behaviour changes if we increase the I concentration. Importantly, for the compounds rich in I, especially if we consider Li_6PS_5I, the observation $E_{a,M''} < E_{a,DC}$ suggests that the charge carrier concentration increases with temperature. For Li_6PS_5I the difference $E_{a,DC} - E_{a,M''}$ turned out to be relatively high, *viz.* 0.121 eV (see the vertical arrow in Fig. 6).

Additionally, after we took a look at the overall and bulk ion dynamics in Li_6PS_5X we used complex resistivity measurements, $\hat{\rho} = 1/\hat{\sigma} = \hat{M}/(i\omega\varepsilon_0)$, carried out at constant frequency but varying temperature, to answer the question of how the bulk ion dynamics depends on the time-scale and length-scale that the technique applied is sensitive to. In Fig. 10a the temperature dependence of the real part $\rho' = M''/\omega$ of the complex resistivity $\hat{\rho}$ is shown for Li_6PS_5Br. The peaks in Fig. 10a have been recorded for two different frequencies *viz.* 1 MHz and 10 MHz.

ρ' is given by a Lorentzian-shaped function containing the electrical relaxation time τ_ρ:[60]

$$\rho' \propto \frac{\tau_\rho}{1 + (\omega\tau_\rho)^{\beta'}} \quad (3)$$

The quantity $\log_{10}(M''/\omega)$ when plotted *vs.* $1/T$ shows similar features to the diffusion-induced NMR spin–lattice relaxation rate.[15,51,60] The higher the frequency the more the peaks shift towards higher temperatures. Symmetric peaks are obtained for $\beta' = 2$; if $\beta' < 2$ the low-T flank becomes lower than that of the high-T side. Indeed, for Li_6PS_5Br we notice an asymmetric peak that strongly points to correlated motion in disordered ion conductors.[15,61–64] While the high-T flank yields an activation energy $E_{a,\rho}$ comparable to $E_{a,DC}$ when bulk processes are probed, short-range motions are seen on the low-T side. The latter motions are characterised by values as low as 0.15 eV, which are also seen for Li_6PS_5Cl and $Li_6PS_5Br_{0.5}I_{0.5}$ (Fig. 10b). $E_{a,\rho}$ of Li_6PS_5Cl is only slightly higher than $E_{\sigma,bulk}$ = 0.305 eV (see above).

We cannot see any strong variation in $E_{a,\rho}$ when comparing the response of $Li_6PS_5Br_{0.5}I_{0.5}$ with that of Li_6PS_5Br. $E_{a,\rho}$ values have also been included in Fig. 6; for the sake of clarity, they are separately shown in Fig. 10c. Obviously, a lower pre-factor of the underlying Arrhenius relation is responsible for this shift. The same effect is seen for Li_6PS_5I. Although the lattice is expected to be much softer in the case of Li_6PS_5I as compared to the situation in Li_6PS_5Cl, $\rho(\omega)$ tells us that the activation energies $E_{a,\rho}$ of the two compounds are very similar (0.32 eV *vs.* 0.35 eV). However, the peak $\rho'(\omega)$ of Li_6PS_5I is clearly shifted toward higher T and shows up at 385 K; the origin of this difference has to be looked for in the bulk ion dynamics, g.b. resistances cannot explain it. As compared to the peak of Li_6PS_5Cl the peak of the I compound is symmetric in shape ($\beta \approx 1.95$) and points to an ordered structure.

Obviously, as in the case of $E_{a,DC}$ the reason for the lower conductivity and, thus, the slower bulk electrical relaxation in Li_6PS_5I (and in $Li_6PS_5Br_{0.5}I_{0.5}$) has been looked for in the prefactor of the underlying Arrhenius relationships. Most likely, the anion site disorder in Li_6PS_5Cl is responsible for this behaviour. Indeed, if we approximate the $\rho'(\nu)$ peaks with eqn (3) we can extract pre-factor $\tau_{0,\rho}^{-1}$ assuming τ_ρ^{-1} to be depending on temperature according to Arrhenius. $\tau_{0,\rho}^{-1}$ values are also included in Fig. 6; indeed, they clearly reveal lower pre-factors for Li_6PS_5I by approximately two orders of magnitude. If we assume that the attempt frequencies are similar for Li_6PS_5Cl and

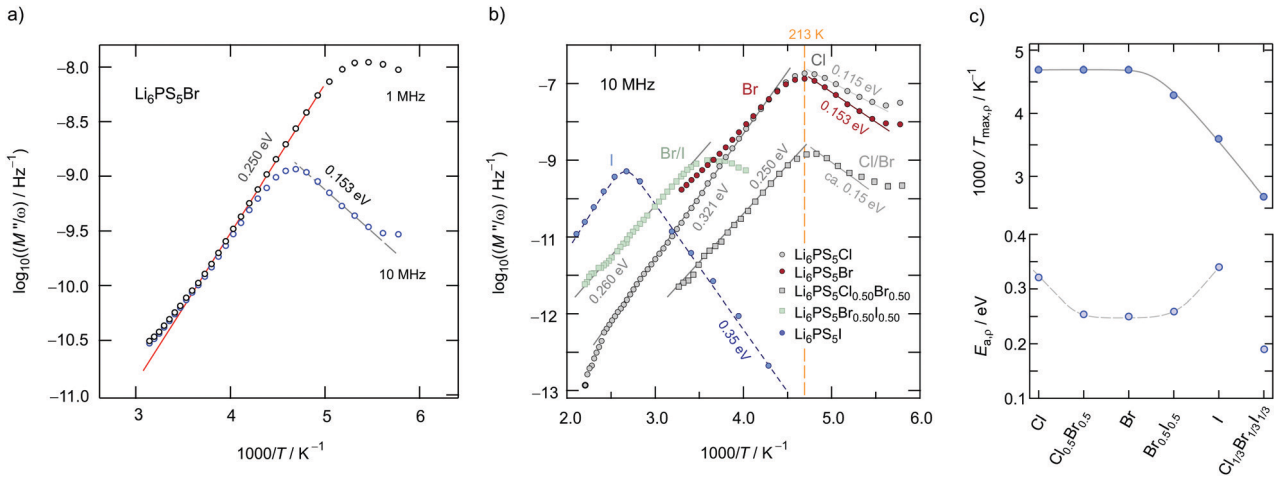

Fig. 10 (a) Real part of the complex resistivity ρ' of Li_6PS_5Br, measured at a fixed frequency (1 MHz and 10 MHz), *vs.* 1000/*T*. (b) $\rho'(\omega)$ peaks (10 MHz) of the argyrodites indicated. Asymmetric peaks point to time-scale dependent (heterogeneous) ion dynamics with local jump processes characterised by activation energies as low as 0.115 eV (Li_6PS_5Cl). (c) Temperatures (shown as 1000/*T*) at which the $\rho'(\omega)$ peaks show up. For Li_6PS_5I the peak is clearly shifted toward higher *T* indicating much slower ion dynamics. The change in $E_{a,\rho}$ is also shown.

Li_6PS_5I a significant change in migration entropy, as mentioned above, might explain the prominent change seen. To check whether this phenomenon is also apparent in SLR NMR, which is in general sensitive to both short-range and long-range ion dynamics, we carried out ^{7}Li NMR measurements in both the laboratory and rotating-frame of reference.[64,65] Line shape measurements carried out at temperatures down to the cryogenic region complement our investigation.

3.4 ^{7}Li NMR relaxometry to probe the bulk ion dynamics

In Fig. 11 an overview of the ^{7}Li NMR spin–lattice relaxation rates $1/T_1 \equiv R_1$ and $1/T_{1\rho} \equiv R_{1\rho}$ measured over a wide temperature range is given. To identify the thermally activated regions the rates of Li_6PS_5X, with X = Cl, Br, and I, were plotted using an Arrhenius representation, *i.e.*, $\log(1/T_1)$ is plotted *vs.* 1000/*T*. The rates have been recorded at a Larmor frequency of $\omega_0/2\pi$ = 116 MHz; for the locking frequency we used a magnetic B_1 field corresponding to $\omega_1/2\pi$ = 20 kHz. At very low temperatures ($T < 160$ K) the R_1 rates shown in Fig. 11a reveal a non-diffusive background; in this *T* range longitudinal relaxation is primarily induced by lattice vibrations or coupling of the Li spins ($I = 3/2$) with paramagnetic impurities.[61,65–67]

At higher *T* we expect spin–lattice relaxation to be increasingly induced by Li self-diffusion.[61] Indeed, the rates sharply increase

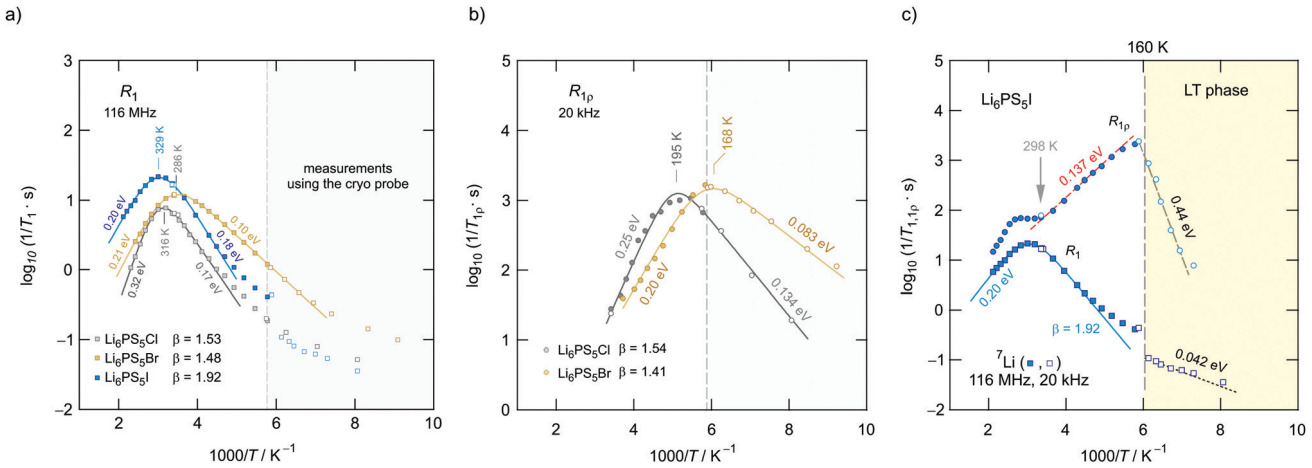

Fig. 11 (a) Temperature dependence of the diffusion-induced ^{7}Li NMR spin–lattice relaxation rates R_1 (116 MHz) of Li_6PS_5X (X: Cl, Br and I). Solid lines refer to BPP-type fits to extract activation energies and pre-factors. (b) Arrhenius plot of the corresponding ^{7}Li SLRρ NMR rates recorded in the rotating frame of reference using a nominal locking frequency of $\omega_1/2\pi$ = 20 kHz. Again, the solid lines represent fits according to a modified BPP relaxation model taking into account the asymmetry of the peaks by parameter β. The further the relaxation peak is shifted to lower *T*, the faster the Li exchange process inducing spin-lock spin–lattice relaxation. Therefore, Li diffusion, as seen by NMR, is increasing in the following order: Li_6PS_5I < Li_6PS_5Br < Li_6PS_5Cl (see also c). (c) R_1 and $R_{1\rho}$ of Li_6PS_5I; at 160 K Li_6PS_5I reversibly transforms into its low-*T* phase. At this temperature the rates R_1 show a jump toward lower values; the $R_{1\rho}$ rates sharply decay with an activation energy of 0.44 eV. The unfilled symbols in (a–c) show rates measured with an NMR probe designed for experiments at cryogenic temperatures; the filled symbols refer to data which were acquired with a standard probe.

with temperature and characteristic diffusion-induced rate peaks show up. We recognise that R_1 passes through well-defined maxima as has been found by some of us in an earlier study on the ion dynamics in Li_6PS_5Br.[15] At the temperature T_{max}, where R_1 reaches its maximum value, the motional correlation rate $1/\tau_c$ is given by $\tau_c\omega_0 \approx 1$. $1/\tau_c$ is identical within a factor of two to the Li jump rate $1/\tau$.[61,65] The same holds for $R_{1\rho}$, for which the maximum condition is $\omega_1\tau \approx 0.5$.[61,65] As ω_0 and ω_1 differ by more than three orders of magnitude, the SLR NMR experiments, when taken together, are able to sense motional processes covering a large time scale.[67,68]

We notice that the rate peak of Li_6PS_5Br shows up at T_{max} = 286 K. The peak is asymmetric and we used a Lorentzian-type (BPP-type)[62,69] spectral density function $J(\omega_0) \propto R_1$ of the form[70]

$$J(\omega_0) \propto \frac{\tau_c}{1 + (\omega\tau_c)^{\beta}} \quad (4)$$

to approximate its shape. Eqn (4) holds for 3D diffusion; $J(\omega_0)$ is the Fourier transform of the underlying motional correlation function $G(t')$. If $G(t')$ is a single exponential, β in $J(\omega_0)$ takes a value of 2. For a 3D diffusion process, at high temperatures, *i.e.*, if $\tau_c\omega_0 \ll 1$, eqn (4) yields $J \propto \tau_c$; in the limit $\tau_c\omega_0 \gg 1$, that is, on the low-T side of the rate peak, we have $J \propto \tau^{-1}{\omega_0}^{-\beta}$ $(1 < \beta \leq 2)$. While we expect $\beta = 2$ for uncorrelated motion,[61,62,69,71] asymmetric peaks are often found for structurally complex ion conductors[15,71–73] whose dynamic processes are affected by correlation effects because of both disorder and strong Coulomb interactions of the moving ions.[71] For such materials the activation energies for short-range and long-range processes might largely differ.[62] In general, β can also be related to a distribution width of motional correlation times; in this sense it has a similar meaning to the exponent in the Cole–Davidson spectral density function used to approximate asymmetric rate peaks.[74–76]

Here, the analysis of the rate peak of Li_6PS_5Br with eqn (4) yields an activation energy $E_{a,NMR}$ of 0.213 eV, which is in perfect agreement with earlier findings for this compound.[15,50] As mentioned above, the parameter β describes the deviation from symmetric behaviour ($\beta = 2$). β turned out to be $\beta \approx 1.5$,[65] which gives rise to a much lower activation energy $E_{a,low}$ on the low-T side of the peak. In this regime, characterised by $\tau_c\omega_0 \ll 1$, short-range or localised ion dynamics in double-well potentials, including also highly correlated forward–backward jumps, are sensed by R_1.[61] The activation energy of the low-T flank is given by 0.10 eV, which is in very good agreement with that seen by $\rho'(\omega)$. Localised intracage jump processes involving the 48h and 24g sites in Li_6PS_5Br could be mainly responsible for spin–lattice relaxation in this region, as has been precisely calculated (0.11 eV) by De Klerk *et al.*[50] The higher activation energy $E_{a,high}$(=$E_{a,NMR}$) seen in the limit $\tau_c\omega_0 \ll 1$ might, however, additionally be affected by 48h–48h jumps. Usually in this regime, in which many jump processes occur during one Larmor precession of the spin, $E_{a,NMR}$ should be comparable with $E_{a,DC}$ (0.296 eV) or $E_{a,\rho}$ (0.250 eV).[61] $E_{a,DC}$ could be influenced by g.b. effects; here, $E_{a,NMR} < E_{a,\rho}$ shows that the number of jump events sensed by NMR, which should not necessarily include all types of jumps needed for long-range diffusion, is sufficient to generate a full R_1 peak.

Table 1 Results of the individual BPP-fits used to analyse the ^{7}Li NMR R_1 and $R_{1\rho}$ peaks of the three argyrodite samples Li_6PS_5X (X = Cl, Br, I). For comparison, the activation energies obtained from the low-T flank, $E_{a,low}$, are also included

	Li_6PS_5Cl[a]	Li_6PS_5Br[a]	Li_6PS_5I[b]
β	1.53(2)	1.48(2)	1.92(1)
E_a	0.320(1) eV	0.213(1) eV	0.198(1) eV
$E_{a,low}$	0.170(4) eV	0.102(5) eV	0.182(5) eV
τ_0	$1.3(5) \times 10^{-14}$ s	$2.3(5) \times 10^{-13}$ s	$8.2(5) \times 10^{-13}$ s
β_ρ	1.54	1.41	—
$E_{a,\rho}$	0.248(9) eV	0.201(9) eV	0.137(3) eV
$E_{a,low}$	0.134(1) eV	0.083(1) eV	—
$\tau_{0,\rho}$	$9.5(5) \times 10^{-13}$ s	$3.3(1) \times 10^{-12}$ s	—

[a] The best $R_{1\rho}$ fit is obtained if we replace $\omega_1/2\pi$ = 20 kHz by a slightly higher effective locking frequency ω_{eff} that also takes into account local magnetic fields. For Li_6PS_5Cl several runs of the global fit procedure yields $\omega_{eff} = 1.68 \times \omega_1$; for Li_6PS_5Br ω_{eff} is given by $\omega_{eff} = 1.41 \times \omega_1$. [b] Li_6PS_5I undergoes a phase transition at 160 K; thus, no β_ρ can be observed. The symmetric rate peak ($\beta \approx 2$) agrees with the ordered anion sublattice as suggested by XRPD, see above.

A very similar behaviour is found for Li_6PS_5Cl. The corresponding rate peak is shifted toward higher temperature revealing that faster ion dynamics is present in Li_6PS_5Br. In agreement with conductivity spectroscopy and our $\rho'(\omega)$ analysis, for Li_6PS_5Cl higher activation energies ($E_{a,high}$ = 0.32 eV, $E_{a,low}$ = 0.17 eV) than those seen for the Br analogue were found. Although $E_{a,high}$ = 0.32 eV perfectly agrees with $E_{a,\rho}$, see Fig. 10, and calculated values,[35] it is higher than expected from $R_{1\rho}$ NMR in the limit $\tau_c\omega_1 \ll 1$ (0.248 eV). Furthermore, the shapes of the $R_1(1/T)$ peaks of the two compounds are very similar. Obviously, similar (local) jump processes influence the NMR rates. In Table 1 an overview of the parameters is given obtained from the analysis with individual BBP-type spectral densities for each peak.

Exactly the same trend is seen when we look at the $R_{1\rho}(1/T)$ peaks of the two compounds, which are shown in Fig. 11b. These have been, independently of the R_1 experiments, also parameterised with Lorentzian-shaped spectral density functions. The activation energies of the peak of Li_6PS_5Br (0.201 eV, 0.083 eV) match with those reported earlier[15] also including calculated values.[50] They also agree with those from the R_1 peak. Here, $R_{1\rho}(1/T)$ of Li_6PS_5Br turned out to be much smaller that that reported by Yu *et al.*;[77] most likely, the difference has to be looked for in the preparation conditions such as milling steps and annealing procedures.

In Fig. 12 so-called joint fits[65] of the two types of NMR experiments, R_1 and $R_{1\rho}$, are shown. For the joint fits the parameters $E_{a,NMR}$ and ${\tau_0}^{-1}$, which is the pre-factor of the Arrhenius equation of ${\tau_c}^{-1}$, have been linked to each other. The best fit is obtained if we use two independent values for β and if we replace ω_1 by effective frequencies $\omega_{1,eff}$, also taking into account local magnetic fields.[73] To estimate the latter, we did not fix ω_1 and looked at how the quality of the fit changes if it is a free parameter. Only a slight change of ω_1 was necessary giving rise to $\omega_{eff} \approx 1.5 \times \omega_1$. A successful joint fit shows that the same overall diffusion processes govern the peaks R_1 and $R_{1\rho}$. The results of our joint fits are shown in Table 2.

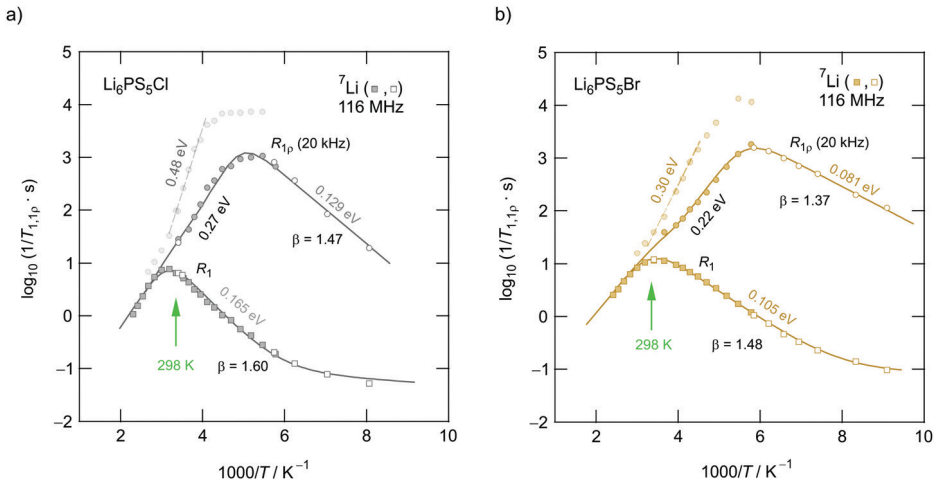

Fig. 12 Arrhenius plot of the ^{7}Li NMR relaxation rates R_1 and $R_{1\rho}$ of (a) Li_6PS_5Cl and (b) Li_6PS_5Br measured in the laboratory frame of reference (116 MHz) and in the rotating frame of reference (20 kHz, nominal locking frequency). The solid lines represent the global fit based on a modified BPP model that takes into account peak asymmetries by the parameter $\beta_{(\rho)}$. The fastest Li diffusion is found for Li_6PS_5Br with the peak maxima showing up at 286 K and 168 K, respectively. The second $R_{1\rho}$ relaxation process, most likely also influenced by spin–spin relaxation to a certain degree, is indicated, too. As mentioned before (see Fig. 11), the open symbols represent rates that were measured with an NMR probe designed for experiments at cryogenic temperatures; the filled symbols show rates which were acquired with the standard probe.

Table 2 Results of the overall fit used to jointly parameterise the ^{7}Li NMR R_1 and $R_{1\rho}$ peaks of Li_6PS_5Br and Li_6PS_5Cl. E_a agrees well with the results if we analyse the peaks individually. For comparison, results for Li_6PS_5I taken from Table 1 are also included

	$E_{a,NMR}$	C	$\beta_{(\rho)}$	τ_0
Li_6PS_5Cl				
R_1	0.273(5) eV	$3.5(5) \times 10^9$ s^{-2}	1.60(1)	$4.9(4) \times 10^{-14}$ s
$R_{1\rho}$		$3.1(5) \times 10^{10}$ s^{-2}	1.47(1)	
Li_6PS_5Br				
R_1	0.218(1) eV	$5.6(7) \times 10^9$ s^{-2}	1.48(1)	$2.0(2) \times 10^{-13}$ s
$R_{1\rho}$		$3.3(9) \times 10^{10}$ s^{-2}	1.47(1)	
Li_6PS_5I[a]				
R_1	0.198(1) eV	$1.1(4) \times 10^{10}$ s^{-2}	1.92(1)	$8.2(9) \times 10^{-13}$ s
$R_{1\rho}$	0.137(3) eV	—	—	—

[a] The best global fits are obtained if we replace ω_1 by the effective locking frequencies $\omega_{eff} = 1.68 \times \omega_1$ (Li_6PS_5Cl) and $\omega_{eff} = 1.41 \times \omega_1$ (Li_6PS_5Br). The coupling constant C, which is the amplitude of the rate peak, $J(\omega_0) = C\tau_c/(1 + (\omega\tau_c)^{\beta})$, turns out to be on the order of 10^9 to 10^{10} s^{-2}.

The activation energies $E_{a,NMR}$ (=$E_{a,high}$) obtained fulfill the relationship

$$E_{a,low} = (\beta_{(\rho)} - 1)E_{a,high}. \quad (5)$$

$\beta_{(\rho)} < 2$ points to correlated Li^+ motion and indicates a sub-quadratic dependence of the diffusion-induced SLR NMR rates in the low-T limit $\tau_c\omega_{0(1)} \gg 1$. Our results are in good agreement with those of Epp *et al.* as well as Rao *et al.*[15,35] We clearly see that correlation effects such as structural disorder and Coulomb interactions[71] have a larger effect on the cation dynamics in Li_6PS_5Br than in Li_6PS_5Cl.

Considering the overall constants C obtained from the joint fits, they reveal that both dipolar and electric quadrupolar interactions govern the diffusion-induced SLR NMR rates. Estimating $C_{dipolar}$ with the help of the rigid lattice line width for Li_6PS_5Br and Li_6PS_5Cl would underestimate C to be on the order of 10^{10} s^{-2}.[46] As we will discuss below, for Li_6PS_5Br quadrupolar interactions have been identified to greatly influence longitudinal relaxation.[15]

Interestingly, a very close look at the $R_{1\rho}$ magnetization transients revealed that they contain a minor magnetization component that leads to activation energies of 0.484 eV (Li_6PS_5Cl) and 0.298 eV (Li_6PS_5Br); the corresponding $R_{1\rho}$ rates are included in Fig. 12. We cannot exclude that these rates are to a certain degree also influenced by spin–spin relaxation. Obviously, the rates sense long-range Li jump processes characterised by higher activation energies. The intercage jumps might contribute to this type of magnetic relaxation, too.

For X = Cl and Br, if we consider activation energies, T_{max}, β and β_ρ, the ^{7}Li SLR NMR data reveal the same trend for the ion dynamics as seen by the conductivity and $\rho'(\omega)$. Li_6PS_5Br shows fast ion dynamics and the lowest activation energies. For Li_6PS_5Cl we witness slightly higher activation energies; simultaneously, the peaks shift toward higher temperature. For Li_6PS_5I, on the other hand, significant differences show up (see the next section).

The NMR rate peaks of Li_6PS_5I, remembering its low σ_{DC} conductivity of 10^{-6} S cm^{-1} at ambient temperature, are expected to show up at temperatures much higher than 320 K. We would expect much higher activation energies, at least similar to or higher than those found for Li_6PS_5Cl. Surprisingly, the R_1 rate peak of Li_6PS_5I shows up at a temperature highly comparable to that of Li_6PS_5Cl *viz.* at T_{max} = 329 K, see Fig. 11a. In stark contrast to our expectation, NMR does not point to slower Li^+ diffusion. Hence, in Li_6PS_5I the same fast (local) jump processes are present as in their parent compounds.[35,40,50] Here, we anticipate that the Li ions in Li_6PS_5I, with its ordered anion sublattice, have access to the same rapid intracage jump processes. According to NMR the barriers have to be characterised by an

activation energy of 0.2 eV. Obviously, only intracage jump processes in Li_6PS_5I are sufficient to produce a full $R_1(1/T)$ peak, see the discussion above.

As expected for a material with an ordered anion lattice such as Li_6PS_5I and without severe influences of motional correlation effects, an almost symmetric rate peak $R_1(1/T)$ ($\beta = 1.92(\approx\beta')$) is obtained for Li_6PS_5I. The same shape was seen in $\rho'(\omega)$. Interestingly, an even lower activation energy determines $R_{1\rho}(1/T)$, see Fig. 11c: in the limit $\tau_c\omega_1 \ll 1$ the rates follow an Arrhenius line whose activation energy $E_{a,high}$ is given by only 0.137 eV. This value is remarkably similar to a cage-like local pathway studied by Rao and Adams (0.15 eV) who used a bond valence approach to investigate the Li ion dynamics in Li_6PS_5I. Our experimental value also coincides with that of Pecher *et al.*[40] (0.14 eV) who studied the local ion dynamics by molecular dynamics simulations.

The amplitude $(R_1)_{max}$ of the $R_1(1/T)$ rate of Li_6PS_5I turned out to be higher that that of the peaks belonging to Li_6PS_5Cl and Li_6PS_5Br. This could be because of stronger heteronuclear Li–X interactions and the fact that Li ions on the distorted 24g sites give rise to stronger dipolar and electric quadrupolar couplings constants. These are lowest for the Li_6PS_5Cl compound. In general, $(R_1)_{max}$ is proportional to the square of the magnetic dipolar or electric quadrupolar coupling constant.[75,78,79] If we use an electric quadrupole constant of at least 50 kHz, as has been estimated for Li_7PS_6,[46] we obtain $(R_1)_{max} \approx 2\ s^{-1}$ yielding $\log_{10}((R_1)_{max}/s) \approx 0.3$, showing that for Li_6PS_5Cl both dipolar and electric quadrupolar interactions play a role in determining the relaxation mechanism. For Li_6PS_5Br we showed *via* comparative ^7Li and ^6Li SLR NMR measurements that quadrupole fluctuations greatly affect the overall spin–lattice relaxation.[15]

Coming back to the temperature dependence of the SLR NMR rates of Li_6PS_5I, we see that at higher temperatures than ambient the rates $R_{1\rho}$ are increasingly governed by R_1, which produces an apparent maximum at *ca.* 330 K. Unfortunately, the peak maximum of $R_{1\rho}(1/T)$ cannot be detected as Li_6PS_5I undergoes a phase transition at 160 K;[31,39,40,49] see the abrupt change in $R_{1\rho}$ in Fig. 11c. The ion dynamics in the low-T (LT) phase is characterised by a much higher activation energy of 0.44 eV. Below 160 K the rates R_1 are no longer induced by diffusive Li jump processes.

To explain the evident differences between the results from conductivity measurements and nuclear spin relaxation in Li_6PS_5I we anticipate that the fast diffusion Li processes in the I compound are not interconnected to give rise to long-range, through-going ion transport. As has been pointed out in detail by Wagemaker and co-workers, and first mentioned by Rao and Adams,[35] the jump probability between two rings in Li_6PS_5I is very low.[50] Intercage jump processes with higher activation energies lead to poor ion transport in Li_6PS_5I. On a shorter length scale, however, the same structural motifs in Li_6PS_5X cause very similar NMR rate peaks. Anion disorder, taking advantage of anions with radii that do not differ much to that of S^{2-}, switches on the intercage exchange processes, making Li_6PS_5Br a fast ion conductor. This design principle causes the overall activation energy to increase in the following order: $Li_6PS_5Br < Li_6PS_5Cl < Li_6PS_5I$.

To verify whether some intragrain translational processes needed for long-range diffusion in Li_6PS_5I are indeed missing or governed by higher activation energies we carefully looked at the $R_{1\rho}$ transients and recorded ^7Li NMR line shapes over a broad temperature range (Fig. 13). Interestingly, the above-mentioned slow magnetization component seen for Li_6PS_5Cl and Li_6PS_5Br (Fig. 12) is missing for the I compound. Furthermore, the intercage jumps are expected to contribute to the averaging of homonuclear (Li–Li) dipole–dipole interactions. If missing at low temperatures, for Li_6PS_5I the change in line width $\Delta\nu$ should occur in two steps. Full averaging is expected at temperatures for which the intercage exchange rate reaches sufficiently high values on the order of some kHz. Indeed, whereas for Li_6PS_5Br and Li_6PS_5Cl the ^7Li NMR line width continuously decreases with temperature revealing typical narrowing curves (Fig. 13a), that of Li_6PS_5I is different.

For Li_6PS_5Br and Li_6PS_5Cl the extreme narrowing regime is already reached at 250 K ($\nu_\infty \approx 300$ Hz); the final line width is caused by external field inhomogeneities. In contrast to the situation observed for Li_6PS_5Br and Li_6PS_5Cl, at 250 K the ^7Li NMR line of Li_6PS_5I is still relatively broad and shows a width of $\nu = 2.2$ kHz. At 350 K it finally reaches ν_∞. Thus, for Li_6PS_5I full averaging of the NMR line width is shifted by $\Delta T = 100$ K toward higher T. Most likely, the latter step corresponds to intercage ion dynamics which are governed by a larger activation barrier. Hence, it is clear from NMR motional narrowing data that in Li_6PS_5I a much slower process kicks in only at higher T. The fact that $\Delta\nu$ of Li_6PS_5I and Li_6PS_5Cl is very similar, at least at temperatures just above the phase transition, shows that mainly fast intracage jump processes are responsible for the narrowing seen in this T range. Differences show up, however, if we consider the rotating-frame spin–lattice relaxation rates, see above. The activation energies of the two samples differ by *ca.* 0.11 eV. Interestingly, the $R_{1\rho}(1/T)$ peak of Li_6PS_5I is expected at a similar temperature to that of Li_6PS_5Br (0.20 eV), again pointing to very fast intracage jump processes in the iodide compound. Most likely, so-called doublet-jump processes[50] have to be considered to explain this feature, see below.

Unfortunately, we cannot probe the rigid-lattice line width ν_0 of the Li_6PS_5I compound because of the phase transition that occurs at 160 K.[31,39,40,49] For both Li_6PS_5Br and Li_6PS_5Cl the value of ν_0 is very similar; ν_0 turned out to be *ca.* 6.1 kHz. Therefore, the magnetic dipolar Li–Li interactions, which are determined by the Li–Li distances, are almost the same in the two compounds. The inflexion point of the motional narrowing curve of Li_6PS_5Br is located at $T = 150$ K (Fig. 13a). $R_{1\rho}(1/T)$ tells us that at this temperature the motional correlation rate τ_c^{-1} ($\approx 2\omega_1$) should be on the order of $2.51 \times 10^5\ s^{-1}$. This value clearly exceeds ν_0 and causes full averaging of the spin–spin interactions in this T range. The changes of the corresponding ^7Li NMR lines are shown in Fig. 13b. Li_6PS_5Br shows one of the lowest onset temperatures seen by NMR motional line narrowing; already at 86 K the shape of the NMR line starts to change as a result of rapid Li^+ self-diffusion.[15] This observation excellently agrees with results from density functional theory molecular dynamics simulations.[50]

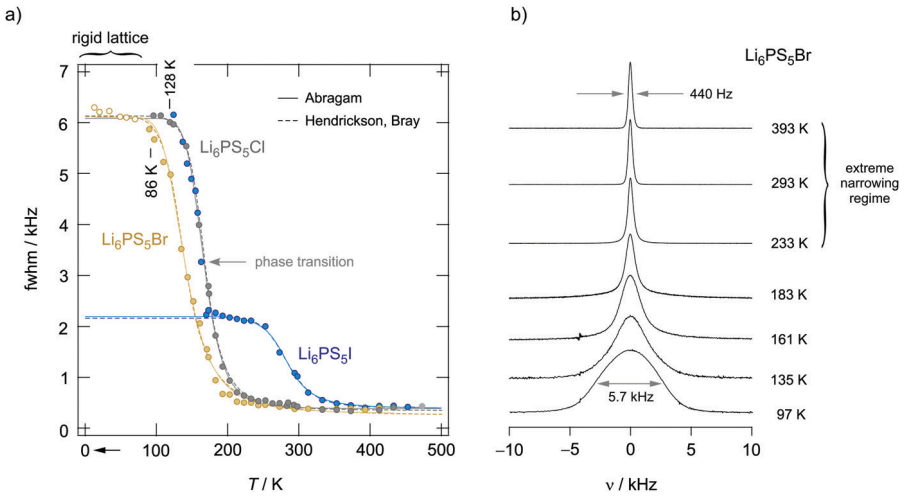

Fig. 13 (a) Temperature dependence of the ^{7}Li NMR line widths (FWHM = full width at half maximum) of the aryrodites Li_6PS_5X (X: Cl, Br and I). Some of the data points referring to Li_6PS_5Br and measured at temperatures lower than 80 K were taken from Epp *et al.*;[15] they perfectly complement the results of the sample studied here. Line widths $\Delta\nu_r(T)$ of Li_6PS_5Br start to narrow at temperatures as low as 86 K indicating ultrafast hopping processes that average homonuclear dipole–dipole interactions being responsible for the rigid lattice line width $\Delta\nu_r \approx 6.1$ kHz. Li diffusion in the compound with Cl is slightly slower as the onset of line narrowing is shifted toward higher T. The line of $\Delta\nu_r(T)$ of Li_6PS_5I narrows in steps of two. At $T < 160$ kHz it indicates dipole averaging in the low-T phase. Because inter-ring jump processes are absent, the line does not reach its extreme value at a temperature comparable to that of Li_6PS_5Br and Li_6PS_5Cl. Higher temperatures are necessary to obtain a fully narrowed ^{7}NMR line. Lines represent fits according to the models of Hendrickson and Bray (dashed lines) and Abragam (solid lines). (b) ^{7}NMR line shapes of Li_6PS_5Br recorded at the temperatures indicated; the line transforms from a Gaussian shape at low T to a Lorentzian one at elevated temperatures.

Extracting quantitative information from NMR motional line narrowing is always fraught with difficulties.[80] Abragam[81] and Hendrickson and Bray[82,83] introduced models to use the change in line widths to deduce activation energies for the hopping process behind. There is still debate over whether these models are accurate enough for this purpose. Hence, we should not over-interpret the results but regard them as estimates. The dashed lines in Fig. 13 refer to the following relationships[82]

$$\Delta\nu(T) = \Delta\nu_0\left\{1 + [(\Delta\nu_0/B) - 1]\exp\left(-\frac{E_{a,HB}}{k_B T}\right)\right\}^{-1} + \nu_\infty \quad (6)$$

$\Delta\nu(T)$ is the line width of the central transition at a given temperature and B is a parameter that is related to the number of thermally activated ions.[82] The final line width ν_∞ is determined by the inhomogeneities of the external magnetic field B_0. Another possibility to deduce activation energies is given by the formalism of Abragam[81] (see the solid line in Fig. 13):

$$\Delta\nu^2(T) = \Delta\nu_0{}^2\frac{2}{\pi}\arctan\left[\alpha\Delta\nu(T)\tau_\infty\exp\left(\frac{E_{a,A}}{k_B T}\right)\right] + \Delta\nu_\infty{}^2 \quad (7)$$

α is a fitting parameter, here chosen to be 1. τ_∞ is the pre-factor of the underlying Arrhenius law of the correlation time τ_c. With the Abragam fit we obtained activation energies $E_{a,A}$ of 0.06 eV (Li_6PS_5Br), 0.11 eV (Li_6PS_5Cl) and 0.23 eV (Li_6PS_5I), respectively. Typically, the formalism of Hendrickson and Bray yields somewhat higher activation energies; here, we found $E_{a,HB} = 1.6 \times E_{a,A}$, see Table 3. Interestingly, although line narrowing is expected to be sensitive to long-range ion dynamics which can fully average all dipolar interactions, the activation energies $E_{a,A}$ and $E_{a,HB}$ are remarkably similar to those governing the low-T flank of the $R_1(1/T)$ peaks, see also Table 3.

Table 3 Activation energies obtained when analysing the motional narrowing curves shown in Fig. 13. We used the Abragam (A) and Hendrickson–Bray (HB) formalism to extract activation energies; the error is in the last digit. For comparison, activation energies describing the slopes of the $R_1(1/T)$ peaks in the limit $\tau_c\omega_0 \gg 1$ are also shown

	$E_{a,A}$ (eV)	$E_{a,HB}$ (eV)	E_a (low-T flank) (eV)
Li_6PS_5Cl	0.11(1)	0.18(2)	0.17(4)
Li_6PS_5Br	0.06(1)	0.09(1)	0.10(4)
Li_6PS_5I	0.23(1)	0.38(2)	0.18(5)

Finally, we will quantitatively compare jump rates τ^{-1} from NMR with electrical relaxation rates from impedance and conductivity spectroscopy. Using the Nernst–Einstein equation[84] we can convert σ' into diffusion coefficients and, thus, jump rates. The easiest way, being also independent of any relaxation model, is to determine jump rates τ^{-1} at the temperatures where the NMR relaxation rate peaks show up. With the conditions $\tau_c\omega_{1(\rho)} = 1(0.5)$, valid at T_{max}, and the jump distances ℓ obtained from XRD we estimated diffusion coefficients according to the Einstein–Smoluchowski relation[84] for 3D diffusion

$$D_{NMR} = \frac{\ell^2}{6\tau}. \quad (8)$$

For ℓ we used the jump distance of the 48h–48h jump process, which is assumed to be the slowest one. The results are listed in Table 4. At T_{max} the jump rate turned out to be on the order of 1.36×10^{-9} s^{-1}. As an example, the mean residence time of the Li ions in Li_6PS_5Br at 286 K is on the order of 1 ns only. Such a short residence time, which is already reached below room temperature, corresponds to ionic conductivities on the order of 10^{-3} to 10^{-2} S cm^{-1}.

Table 4 Results of the diffusion coefficient D. τ was calculated from the $R_1(1/T)$ rate peak measurements performed at 116 MHz

	ℓ/Å	$T_{max}(R_1)$/K	D_{NMR}/cm^2 s^{-1}	n_{Li}/m^{-3}
Li_6PS_5Cl	2.34	316	6.7×10^{-8}	6.3×10^{27}
Li_6PS_5Br	2.41	286	7.1×10^{-8}	6.0×10^{27}
Li_6PS_5I	2.66	329	8.6×10^{-8}	5.8×10^{27}

For ℓ we used the 48h–48h distance, which is the longest jump distance in Li_6PS_5Br, when we consider cation hopping processes near the regularly occupied Li sites.

Using structural data from our Rietveld analysis we also estimated the charge carrier density n_{Li} in Li_6PS_5Br. n_{Li}, which is on the order of 10^{27} m^{-3}, is needed to convert D_{NMR} into conductivities expected at or near T_{max}. Disregarding any correlation effects for our estimation of σ_{NMR}, the following relation holds[11]

$$\sigma_{NMR} = \frac{e^2 \cdot n}{k_B T} D_{NMR} = \frac{e^2 \cdot n_{Li} \cdot \ell^2}{6 k_B T} \cdot \frac{1}{\tau}. \quad (9)$$

where e denotes the elementary charge. Here, a residence time τ of 1 ns results in conductivities of the order of 2 mS cm^{-1}. In Table 5 the estimated results from NMR are compared with those measured by conductivity spectroscopy. Assuming no correlation effects or other influences for this estimation means that H_R/f in $D_{NMR} = (H_R/f)D_\sigma$ is approximated by $H_R/f = 1$; while H_R denotes the Haven ratio connecting the tracer diffusion coefficient D_{tr} with D_σ, the correlation factor f links D_{NMR} with D_{tr}.[11]

While good agreement is seen for σ_{NMR} and σ_{DC} of Li_6PS_5Br, we have to notice a somewhat larger difference for the Cl compound. In general, conductivities indirectly deduced from NMR should be regarded as estimates because relaxation NMR and conductivity spectroscopy sense different kinds of motional correlation functions. Agreement over a large temperature is only obtained if both techniques are sensitive to the same diffusion process and the same correlation function.[51]

As expected, for Li_6PS_5I the values listed in Table 5 differ by three orders of magnitude. Whereas σ_{DC} is mainly governed by successful jump processes resulting in long-range ion transport, σ_{NMR} reflects short-range ion dynamics. The difference can easily be explained by the fact that in Li_6PS_5I the intercage jump processes are less probable; these processes hinder the ions in long-range diffusion. Note that the comparison in Table 5 only refers to $T \approx T_{max}$ at which the NMR peaks show up. Comparing dynamic parameters over the full temperature range will show deviations between nuclear spin relaxation and conductivity spectroscopy as the techniques deliver different activation energies in the present case. Such a comparison is presented in Fig. 14. Squares represent jump rates obtained at the NMR rate peaks; at $T \rightarrow 0$ we have indicated the pre-factors of the Arrhenius lines.

Table 5 Estimated conductivity values (σ_{NMR}) from NMR data. For comparison, the measured values σ_{DC} are also listed

	σ_{NMR}/mS cm^{-1}	σ_{DC}/mS cm^{-1}
Li_6PS_5Cl	2.46 (316 K)	9.00 (313 K)
Li_6PS_5Br	2.78 (286 K)	2.20 (293 K)
Li_6PS_5I	2.80 (329 K)	8.60×10^{-3} (333 K)

In Fig. 14a τ_{NMR}^{-1} as deduced from the joint fits of Li_6PS_5Cl and Li_6PS_5Br are shown. The line belonging to Li_6PS_5I refers to the R_1 rates only. First of all, we notice a correlation between $E_{a,NMR}$ and the pre-factor τ_0^{-1} (see also Table 2). The decrease in $E_{a,NMR}$, which changes from 0.273 eV to 0.218 eV and further to 0.198 eV (R_1 of Li_6PS_5I), is accompanied by a decrease in τ_0^{-1}. The attempt frequency τ_0^{-1} decreases by a factor of 80 when going from Li_6PS_5Cl to Li_6PS_5I. This small variation either reflects a decrease in phonon frequencies or a change in migration entropy ΔS of the ions as $\tau_0^{-1} = \nu_{p,0}\exp(\Delta S/k_B)$. Phonon frequencies, to which $\nu_{p,0}$ is proportional, usually take values on the order of 10^{12} to 10^{15} s^{-1}. As discussed above, for Li_6PS_5I a decrease in migration entropy is reasonable because of the ordered anion sublattice. The decrease in $E_{a,NMR}$ reflects the increase in anion polarizability (I > Br > Cl), which should, apart from effects due to disorder, also lead to lower hopping barriers. This trend for $E_{a,NMR}$ is at least valid for the elementary Li^+ jumps seen by NMR. If we include τ_σ^{-1} values obtained by transforming σ_{DC} into hopping rates after eqn (9), we notice that good agreement is only seen at temperatures around T_{max}, see Fig. 14a and b. Clearly, the fact that $E_{a,NMR} \neq E_{a,DC}$ leads to deviations at temperatures $T \lesssim T_{max}$. For comparison, in Fig. 14b hopping rates from $\rho'(T)$ have also been included.

The pre-factors of the Arrhenius lines referring to τ_σ^{-1} estimated from σ_{DC} also vary with X. While we cannot see any large difference between $\tau_{0,\sigma}^{-1}$ from Li_6PS_5I and Li_6PS_5Br as mentioned above, we see that $\tau_{0,\sigma}^{-1}$ of the Cl-compound is much higher than expected. This increase is caused by a change in slope of σ_{DC} at a temperature slightly below 400 K; it is also seen for Li_6PS_5I. Below 400 K the ionic conductivity σ_{DC} (as well as τ_σ^{-1}) follows an Arrhenius law with an activation energy very similar to that of Li_6PS_5Br (0.273 eV). As σ_{DC} of Li_6PS_5Br and Li_6PS_5Cl almost coincide in this T range, also the corresponding pre-factors $\tau_{0,\sigma}^{-1}$ would be the same. Here, the fact that $\tau_{0,\sigma}^{-1}$ of Li_6PS_5Cl is larger than that of Li_6PS_5Br originates the kink in the Arrhenius line causing $\sigma_{DC}T(1/T)$ to be characterised by an activation energy (0.396 eV) much larger than that in the low-T range. Obviously, another Li^+ diffusion process, being characterised by an activation energy larger than 0.3 eV, contributes to τ_σ^{-1} of Li_6PS_5Cl.

Such an additional process, which we assume could stem from an ordered Li sublattice in Li_6PS_5Cl, has been seen by $R_{1\rho}$, see Fig. 12. The $R_{1\rho}$ magnetization transients of Li_6PS_5Cl are characterised by a second decay process that is thermally activated by 0.48 eV. The same feature is also seen for Li_6PS_5Br with both a disordered anion structure and Li^+ sublattice. The corresponding activation energy of 0.30 eV (see Fig. 12) is, however, very similar to that of $\sigma_{DC}T(1/T)$. This similarity thus gives rise to no increase in $\sigma_{DC}T$ above $T \approx 400$ K.

The pre-factors seen by conductivity spectroscopy, especially those of Li_6PS_5Cl, clearly represent mean values. In materials with several diffusion processes taking place in parallel, each process needs to be characterised by its individual pre-factor.

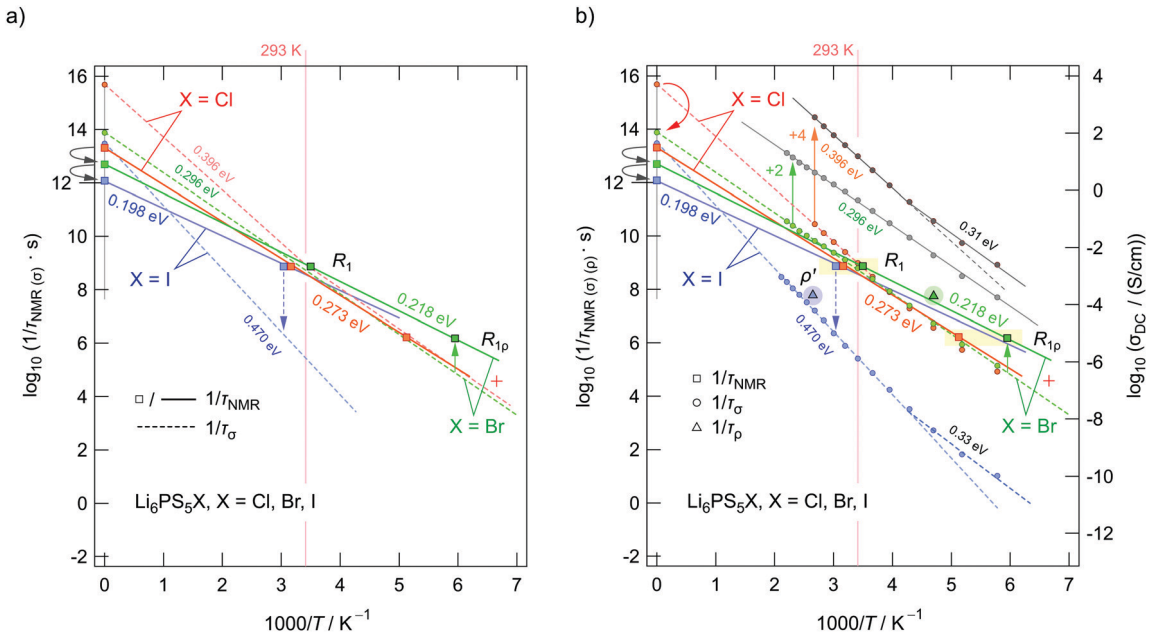

Fig. 14 Arrhenius plot of the jump rates deduced from the ^{7}Li NMR rate peaks shown in Fig. 11c, 12a and (b). (a) Squares represent either pre-factors or jump rates at the maxima of the peaks. Solid lines represent the Arrhenius lines according to the joint fits. Dashed lines indicate the position of τ_σ^{-1}, *i.e.*, estimated from σ_{DC}. (b) The same data points as in (a) but with τ_{DC}^{-1} included as data points. The lines referring to Li_6PS_5Cl and Li_6PS_5Br have been shifted by a factor of +4 (+2) (on the log scale) to illustrate the kink seen in $\tau_{DC}^{-1}(1/T)$ for Li_6PS_5Cl. It is absent for Li_6PS_5Br. Electrical relaxation rates τ_ρ^{-1} from our $\rho'(1/T)$ analyses have been included as well. The vertical arrow drawn with a dashed line indicates the large difference in jump rates seen for Li_6PS_5I. The arrows near the ordinate illustrate the change in pre-factors. See the text for further explanation.

Table 6 Activation energies as deduced from the various methods applied here to investigate the ion dynamics in Li_6PS_5X by conductivity spectroscopy and NMR relaxometry

	Li_6PS_5Cl (eV)	Li_6PS_5Br (eV)	Li_6PS_5I (eV)
σ_{DC}	0.396(3)	0.296(2)	0.470(5)
ρ', high-T flank[a]	0.321(3)	0.250(3)	0.347(7)
ρ', low-T flank[a]	0.153(2)	0.115(9)	0.305(2)
M''	—	—	0.349(5)
R_1, high-T flank[a]	0.320(1)	0.213(1)	0.198(1)
R_1, low-T flank[a]	0.170(4)	0.102(4)	0.182(5)
$R_{1\rho}$, high-T flank[a]	0.248(9)	0.201(9)	0.137(3)
$R_{1\rho}$, low-T flank[a]	0.134(1)	0.083(1)	—
R_1 (global fit)[b]	0.273(5)	0.218(1)	—
	(0.165(8))	(0.105(4))	—
$R_{1\rho}$ (global fit)[b]	0.273(5)	0.218(1)	—
	(0.129(7))	(0.081(4))	—

[a] The values referring either to the high-T or to the low-T flank were obtained by a line fit. [b] Results from the global fit analysis are obtained by linking E_a and τ_0^{-1} of the individual relaxation rate peaks. Values in brackets refer to the low-T flanks of the global fit.

In the case of ^{7}Li NMR, which is primarily sensitive to the elementary jump processes between 24g and 48h, we see a slight increase in the pre-factor when going from X = I to X = Cl (see above). The change in τ_0^{-1} is, however, small as compared to the drastic decrease in $\sigma_{DC}T(1/T)$ seen for Li_6PS_5I. Hence, the increase in overall migration enthalpy for Li_6PS_5I, for which the intercage diffusion process is characterised by a high hopping barrier, turned out to be mainly responsible for its poor ionic conductivity. On shorter length scales, Li ion hopping in Li_6PS_5I, with its ordered anion sublattice, is as fast as in Li_6PS_5Br. This result is in perfect agreement with the pioneering calculations by Rao and Adams as well as the in-depth study presented by De Klerk *et al.*[50] They already pointed out, as mentioned above, that for Li_6PS_5I the intercage jump processes are interrupted and fast localized motions with very low activation energies are present. By ^{7}Li NMR relaxometry their observation is now fully supported. The calculations by Pecher *et al.* point in the same direction.[40] As an example, De Klerk *et al.* report an activation energy as low as 0.05 eV for the doublet jump process in Li_6PS_5I.[50]

Besides these peculiarities for Li_6PS_5Cl and Li_6PS_5I, the complex ion dynamics in Li-bearing argyrodites with anion disorder is reflected in the distribution of activation energies. Table 6 summarises the activation energies obtained by the different methods applied. Depending on the length-scale and time-scale to which the specific method is sensitive quite different activation energies can be probed. Such a result is typical for ionic conductors whose charge carriers are exposed to an irregularly shaped energy landscape that gives rise to highly correlated forward and backward motions or fast (local) dynamics on the angstrom length scale.

4 Summary and conclusion

We studied the Li ion dynamics in argyrodite-type Li_6PS_5X (X: Cl, Br, I) by a wide range of complementary techniques with a special focus on conductivity spectroscopy and nuclear magnetic relaxation. The latter technique is able to probe short-range as

well as long-range bulk ion dynamics. The analysis of electric modulus data also helped us to shed light on the bulk ion dynamics. In all compounds, even in those where two different halogen atoms were used to replace a sulfur anion per formula unit, complex ion dynamics is found. Heterogenous Li ion transport is traced back to the fact of an irregularly shaped potential landscape that the ions are exposed to during diffusion. The vacancy-rich Li sublattice offers a range of hopping barriers between the Li sites involved in the overall ionic transport. Depending on the method applied to study the hopping processes, Li ion translational motions on quite different time scales and lengths scales are probed. This circumstance results in activation energies ranging from 0.08 eV to values as high as 0.48 eV.

Anion disorder in Li_6PS_5Br and Li_6PS_5Cl, as verified by X-ray powder diffraction measurements, boosts the ion dynamics as compared to the parent compound Li_7PS_6. The halogen anions are clearly distributed over the crystallographic sites 4a and 4d. Li_6PS_5Br reveals the lowest activation energies and the bulk ion conductivities follow a single Arrhenius line. Deviations from this behaviour are seen for Li_6PS_5Cl and Li_6PS_5I. For Li_6PS_5Cl an additional dynamic process shows up at higher T, which is also seen in ^{7}Li spin-lock NMR spectroscopy. This process leads to a relatively high mean activation energy in σ_{DC} characterising the overall ion transport.

Most importantly, also for the poor ionic conductor Li_6PS_5I our NMR relaxation measurements reveal very fast Li ion dynamics on a local to medium-range length scale. Obviously, the ions have access to the same, rapid exchange processes as in Li_6PS_5Br but long-range transport is switched off. In the spirit of De Klerk and co-workers we think that the ordered anion sublattice, combined with the larger lattice constant, is responsible for this peculiarity. It leads to a heterogeneous potential landscape with low and high hopping barriers. High activation barriers seem to characterize the intercage jumps; these jump processes are, however, necessary to transport the ions over long distances.

Conflicts of interest

There are no conflicts to declare.

Acknowledgements

Financial support by the Deutsche Forschungsgemeinschaft (DFG Research Unit 1277, grant no. WI3600/2-1(4-1) (FOR1277)) as well as by the Austrian Federal Ministry of Science, Research and Economy, and the Austrian National Foundation for Research, Technology and Development (Christian Doppler Laboratory of Lithium Batteries: Ageing Effects, Technology and New Materials) is greatly appreciated. Furthermore, we thank the FFG in the frame of the K project safe battery.

References

1 M. S. Whittingham, *Chem. Rev.*, 2004, **104**, 4271.
2 J. B. Goodenough and Y. Kim, *Chem. Mater.*, 2010, **22**, 587.
3 *Lithium Ion Batteries*, ed. M. Wakihara and O. Yamamoto, Wiley-VCH, Weinheim, 1998.
4 A. S. Aricó, P. Bruce, B. Scrosati, J.-M. Tarascon and W. V. Schalkwijc, *Nat. Mater.*, 2005, **4**, 366.
5 P. G. Bruce, B. Scrosati and J.-M. Tarascon, *Angew. Chem., Int. Ed.*, 2008, **47**, 2930.
6 B. L. Ellis and L. F. Nazar, *Curr. Opin. Solid State Mater. Sci.*, 2012, **16**, 168.
7 V. Etacheri, R. Marom, R. Elazari, G. Salitra and D. Aurbach, *Energy Environ. Sci.*, 2011, **4**, 3243–3262.
8 V. Thangadurai, S. Narayanan and D. Pinzaru, *Chem. Soc. Rev.*, 2014, **43**, 4714–4727.
9 J. C. Bachman, S. Muy, A. Grimaud, H.-H. Chang, N. Pour, S. F. Lux, O. Paschos, F. Maglia, S. Lupart, P. Lamp, L. Giordano and Y. Shao-Horn, *Chem. Rev.*, 2016, **116**, 140–162.
10 Z. Zhang, Y. Shao, B. Lotsch, Y.-S. Hu, H. Li, J. Janek, L. F. Nazar, C.-W. Nan, J. Maier, M. Armand and L. Chen, *Energy Environ. Sci.*, 2018, **11**, 1945–1976.
11 M. Uitz, V. Epp, P. Bottke and M. Wilkening, *J. Electroceram.*, 2017, **38**, 142–156.
12 A. Hayashi and M. Tatsumisago, *Electron. Mater. Lett.*, 2012, **8**, 199.
13 N. Kamaya, K. Homma, Y. Yamakawa, M. Hirayama, R. Kanno, M. Yonemura, T. Kamiyama, Y. Kato, S. Hama, K. Kawamoto and A. Mitsui, *Nat. Mater.*, 2011, **10**, 682–686.
14 S. Hori, T. Saito, K. Suzuki, M. Hirayama, A. Mitsui, M. Yonemura, H. Iba and R. Kanno, *Nat. Energy*, 2016, **1**, 16303.
15 V. Epp, O. Gün, H.-J. Deiseroth and M. Wilkening, *J. Phys. Chem. Lett.*, 2013, **4**, 2118–2123.
16 D. Brinkmann, *Prog. Nucl. Magn. Reson. Spectrosc.*, 1992, **24**, 527.
17 P. Knauth, *Solid State Ionics*, 2009, **180**, 911.
18 J. Fergus, *J. Power Sources*, 2010, **195**, 4554–4569.
19 C. Julien and G. A. Nazri, *Solid State Batteries: Materials, Design and Optimization*, Kluwer Academic, Boston, 1994.
20 S. Jacke, J. Song, L. Dimesso, J. Brötz, D. Becker and W. Jägermann, *J. Power Sources*, 2011, **196**, 6911–6914.
21 S. Wang, L. Ben, H. Li and L. Chen, *Solid State Ionics*, 2014, **268**, 110–116.
22 R. Murugan, V. Thangadurai and W. Weppner, *Angew. Chem., Int. Ed.*, 2007, **46**, 7778.
23 S. Narayanan, V. Epp, M. Wilkening and V. Thangadurai, *RSC Adv.*, 2012, **2**, 2553.
24 V. Epp, Q. Ma, E.-M. Hammer, F. Tietz and M. Wilkening, *Phys. Chem. Chem. Phys.*, 2015, **17**, 32115–32121.
25 H. Buschmann, J. Dölle, S. Berendts, A. Kuhn, P. Bottke, M. Wilkening, P. Heitjans, A. Senyshyn, H. Ehrenberg, A. Lotnyk, V. Duppel, L. Kienle and J. Janek, *Phys. Chem. Chem. Phys.*, 2011, **13**, 19378.
26 B. Stanje, D. Rettenwander, S. Breuer, M. Uitz, S. Berendts, M. Lerch, R. Uecker, G. Redhammer, I. Hanzu and M. Wilkening, *Ann. Phys.*, 2017, **529**, 1700140.
27 S. Breuer, D. Prutsch, Q. Ma, V. Epp, F. Preishuber-Pflügl, F. Tietz and M. Wilkening, *J. Mater. Chem. A*, 2015, **3**, 21343–21350.

28 S. Lunghammer, Q. Ma, D. Rettenwander, I. Hanzu, F. Tietz and H. Wilkening, *Chem. Phys. Lett.*, 2018, **701**, 147–150.
29 P. Bron, S. Johansson, K. Zick, J. Schmedt auf der Günne, S. Dehnen and B. Roling, *J. Am. Chem. Soc.*, 2013, **135**, 15694–15697.
30 S. Wenzel, S. Randau, T. Leichtweiß, D. A. Weber, J. Sann, W. G. Zeier and J. Janek, *Chem. Mater.*, 2016, **28**, 2400–2407.
31 H.-J. Deiseroth, S.-T. Kong, H. Eckert, J. Vannahme, C. Reiner, T. Zaiss and M. Schlosser, *Angew. Chem., Int. Ed.*, 2008, **47**, 755–758.
32 S. Boulineau, M. Courty, J.-M. Tarascon and V. Viallet, *Solid State Ionics*, 2012, **221**, 1–5.
33 S. Boulineau, J.-M. Tarascon, J.-B. Leriche and V. Viallet, *Solid State Ionics*, 2013, **242**, 45–48.
34 M. A. Kraft, S. P. Culver, M. Calderon, F. Böcher, T. Krauskopf, A. Senyshyn, C. Dietrich, A. Zevalkink, J. Janek and W. G. Zeier, *J. Am. Chem. Soc.*, 2017, **139**, 10909–10918.
35 R. P. Rao and S. Adams, *Phys. Status Solidi*, 2011, **208**, 1804–1807.
36 P. R. Rayavarapu, N. Sharma, V. K. Peterson and S. Adams, *J. Solid State Electrochem.*, 2012, **16**, 1807–1813.
37 H. M. Chen, C. Maohua and S. Adams, *Phys. Chem. Chem. Phys.*, 2015, **17**, 16494–16506.
38 R. P. Rao, N. Sharma, V. Peterson and S. Adams, *Solid State Ionics*, 2013, **230**, 72–76.
39 H.-J. Deiseroth, J. Maier, K. Weichert, V. Nickel, S.-T. Kong and C. Reiner, *Z. Anorg. Allg. Chem.*, 2011, **637**, 1287–1294.
40 O. Pecher, S.-T. Kong, T. Göbel, V. Nickel, K. Weichert, C. Reiner, H.-J. Deiseroth, J. Maier, F. Haarmann and D. Zahn, *Chem. – Eur. J.*, 2010, **16**, 8347–8354.
41 A. Düvel, B. Ruprecht, P. Heitjans and M. Wilkening, *J. Phys. Chem. C*, 2011, **115**, 23784–23789.
42 S. Breuer and M. Wilkening, *Dalton Trans.*, 2018, **47**, 4105–4117.
43 B. Kozinsky, S. A. Akhade, P. Hirel, A. Hashibon, C. Elsässer, P. Mehta, A. Logeat and U. Eisele, *Phys. Rev. Lett.*, 2016, **116**, 055901.
44 K. E. Kweon, J. B. Varley, P. Shea, N. Adelstein, P. Mehta, T. W. Heo, T. J. Udovic, V. Stavila and B. C. Wood, *Chem. Mater.*, 2017, **29**, 9142–9153.
45 E. Fukushima and S. Roeder, *Experimental Pulse NMR*, Addison-Wesley, Reading, 1981.
46 V. Epp, O. Gün, H.-J. Deiseroth and M. Wilkening, *Phys. Chem. Chem. Phys.*, 2013, **15**, 7123–7132.
47 D. C. Look and I. J. Lowe, *J. Chem. Phys.*, 1966, **44**, 2995.
48 D. C. Ailion and C. P. Slichter, *Phys. Rev.*, 1965, **137**, A235.
49 S.-T. Kong, H.-J. Deiseroth, C. Reiner, Z. Gün, E. Neumann, C. Ritter and D. Zahn, *Chem. – Eur. J.*, 2010, **16**, 2198–2206.
50 N. J. J. de Klerk, I. Roslon and M. Wagemaker, *Chem. Mater.*, 2016, **28**, 7955–7963.
51 F. Preishuber-Pflügl, P. Bottke, V. Pregartner, B. Bitschnau and M. Wilkening, *Phys. Chem. Chem. Phys.*, 2014, **16**, 9580–9590.
52 F. Preishuber-Pflügl and M. Wilkening, *Dalton Trans.*, 2016, **45**, 8675–8687.
53 F. Preishuber-Pflügl and M. Wilkening, *Dalton Trans.*, 2014, **43**, 9901–9908.
54 M. Wilkening, A. Düvel, F. Preishuber-Pflügl, K. Silva, S. Breuer, V. Šepelák and P. Heitjans, *Z. Kristallogr. - Cryst. Mater.*, 2016, **232**, 107–127.
55 D. L. Sidebottom, *Rev. Mod. Phys.*, 2009, **81**, 999.
56 R. Metselaar and G. Oversluizen, *J. Solid State Chem.*, 1984, **55**, 320–326.
57 J. T. S. Irvine, D. C. Sinclair and A. R. West, *Adv. Mater.*, 1990, **2**, 132–138.
58 K. L. Ngai, *Relaxation and Diffusion in Complex Systems*, Springer, New York, 2011.
59 K. L. Ngai, G. N. Greaves and C. T. Moynihan, *Phys. Rev. Lett.*, 1998, **80**, 1018.
60 R. Winter, K. Siegmund and P. Heitjans, *J. Non-Cryst. Solids*, 1997, **212**, 215–224.
61 M. Wilkening and P. Heitjans, *Chem. Phys. Chem.*, 2012, **13**, 53–65.
62 P. Heitjans, A. Schirmer and S. Indris, in *Diffusion in Condensed Matter*, ed. P. Heitjans and J. Kärger, Springer, 2005, ch. 9, p. 367.
63 V. Epp, C. Brüning, M. Binnewies, P. Heitjans and M. Wilkening, *Z. Phys. Chem.*, 2012, **226**, 513.
64 M. Wilkening, A. Kuhn and P. Heitjans, *Phys. Rev. B: Condens. Matter Mater. Phys.*, 2008, **78**, 054303.
65 A. Kuhn, S. Narayanan, L. Spencer, G. Goward, V. Thangadurai and M. Wilkening, *Phys. Rev. B: Condens. Matter Mater. Phys.*, 2011, **83**, 094302.
66 P. Heitjans and M. Wilkening, *Defect Diffus. Forum*, 2009, **283–286**, 705.
67 M. Wilkening and P. Heitjans, *Phys. Rev. B: Condens. Matter Mater. Phys.*, 2008, **77**, 024311.
68 M. Wilkening, W. Küchler and P. Heitjans, *Phys. Rev. Lett.*, 2006, **97**, 065901.
69 N. Bloembergen, E. M. Purcell and R. V. Pound, *Phys. Rev.*, 1948, **73**, 679–712.
70 W. Küchler, P. Heitjans, A. Payer and R. Schöllhorn, *Solid State Ionics*, 1994, **70/71**, 434.
71 M. Meyer, P. Maass and A. Bunde, *Phys. Rev. Lett.*, 1993, **71**, 573–576.
72 A. Kuhn, P. Sreeraj, R. Pöttgen, H.-D. Wiemhöfer, M. Wilkening and P. Heitjans, *J. Am. Chem. Soc.*, 2011, **133**, 11018–11021.
73 A. Kuhn, S. Narayanan, L. Spencer, G. Goward, V. Thangadurai and M. Wilkening, *Phys. Rev. B: Condens. Matter Mater. Phys.*, 2011, **83**, 094302.
74 T. M. Kirschgen, M. D. Zeidler, B. Geil and F. Fujara, *Phys. Chem. Chem. Phys.*, 2003, **5**, 5243–5246.
75 R. Bertermann and W. Müller-Warmuth, *Z. Naturforsch., A: Phys. Sci.*, 1998, **53**, 863–873.
76 E. Göbel, W. Müller-Warmuth, H. Olyschläger and H. Dutz, *J. Magn. Reson.*, 1979, **36**, 371–387.
77 C. Yu, S. Ganapathy, E. R. H. van Eck, L. van Eijck, S. Basak, Y. Liu, L. Zhang, H. Zandbergen and M. Wagemaker, *J. Mater. Chem. A*, 2017, **5**, 21178–21188.

78 K. Hayamizu, S. Tsuzuki and S. Seki, *Magn. Reson. Chem.*, 2011, **49**, 6–8.
79 M. Grüne, H. Meierkord, W. Müller-Warmuth, P. Z. Hebel, B. Krebs and M. Wulff, *Ber. Busenges. Phys. Chem.*, 1989, **93**, 1313–1317.
80 M. Wilkening, D. Bork, S. Indris and P. Heitjans, *Phys. Chem. Chem. Phys.*, 2002, **4**, 3246–3251.
81 A. Abragam, *The principles of nuclear magnetism*, Oxford University Press, 1999.
82 J. R. Hendrickson and P. J. Bray, *J. Magn. Reson.*, 1973, **9**, 341–357.
83 J. R. Hendrickson and P. J. Bray, *J. Chem. Phys.*, 1974, **61**, 2754–2764.
84 H. Mehrer, *Diffusion in Solids: Fundamentals, Methods, Materials, Diffusion-Controlled Processes*, Springer, Berlin, 2007.

6.3.1.1 Synthesis and Dynamics of Disordered Crystalline Li_7PS_6

Based on the last paper "Substitutional disorder: Structure and ion dynamics of the Argyrodites Li_6PS_5Cl, Li_6PS_5Br and Li_6PS_5I" further measurements on Li_7PS_6 were carried out.
Lithium thiophosphates are potential candidates for the use as solid electrolytes in all-solid-state batteries due to their softness and high ionic conductivity.[98,183] The crystalline compounds $Li_7P_3S_{11}$, Li_3PS_4 etc., as well thiophosphate glasses are good candidates.[98,184] The ternary phase diagram Li-P-S is shown in Figure 6.1. Inspired by the Argyrodite family and the ternary crystalline thiophosphates Li_6PS_5X, crystalline Li_7PS_6 was prepared.

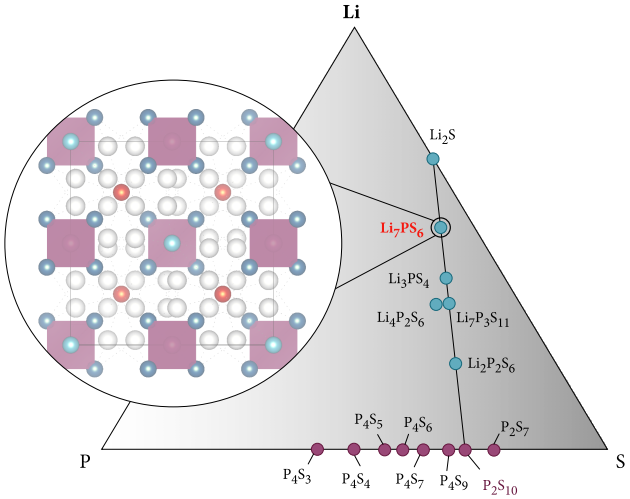

Figure 6.1: Li-P-S ternary phase diagram. In red Li_7PS_6 is marked and as well the cubic crystal structure is shown as an inset. The graphic is adapted from reference Zhu *et al.* and Dietrich *et al.*[185,186]

In 2010 Kong *et al.* have already discussed both phases of Li_7PS_6 (LPS) in detail. LPS appears in two different structures, the high-temperature (HT) and the low-temperature modification (LT). The first results in a cubic structure whereas the second crystallizes in a orthorhombic structure. In the cubic modification of Li_7PS_6, the tetrahedral holes are occupied by P and form the PS_4 tetrahedra. In this structure the lithium ions are in a disordered manner between this PS_4 tetrahedra. However, the orthorhombic modification shows a more ordered structure (see Figure 6.3 a) and b)).[187]

In particular, detailed Rietveld analysis, after the solid-state reaction was finished, and differential scanning calorimetry (DSC) allowed us to get information on the phase transitions of Li_7PS_6. In order to characterize the halogen free Argyrodite component, the synthesis carried out the same way (550 °C / 7 days) as discussed in the article before. The final product shows two different phases of Li_7PS_6: i) cubic (76 wt%), the high temperature phase (HT) and ii) orthorhombic (24 wt%), the low temperature phase (LT). Further information about the Rietveld analysis is included in Figure 6.2.

Differential scanning calorimetry (DSC) measurements were performed with a Netzsch STA-449 coupled with a QMS-403C mass spectrometer. The sample was heated in a closed aluminum

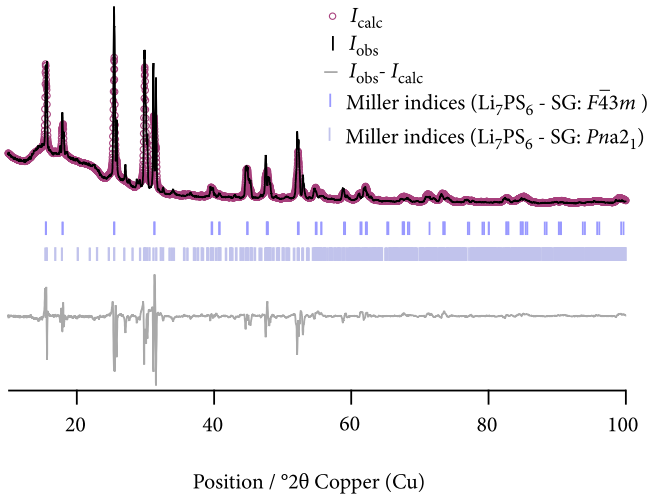

Figure 6.2: Rietveld analysis of the X-ray powder pattern of Li_7PS_6 recorded at 293 K. In this plot the Bragg positions as well the observed and the calculated profiles are shown. The analysis results in Li_7PS_6 existing of a cubic main phase and a orthorhombic secondary phase (<25 wt%). The refinement parameter R_w reaches a value of 14.41 %.

crucible under a constant air flow (flow rate N_2:N_2:O_2 = 40:40:20) with a heating rate of 10 °C/min from room temperature to 500 °C. The aluminum crucible was filled an closed within a argon-filled glovebox to avoid traces of moisture. LPS shows a phase transition at 473 K, from othorhombic to cubic structure, which perfectly matches with previous articles. In Figure 6.3 the crystal structure and the DSC measurement of Li_7PS_6 is shown. The knowledge of the previously mentioned article

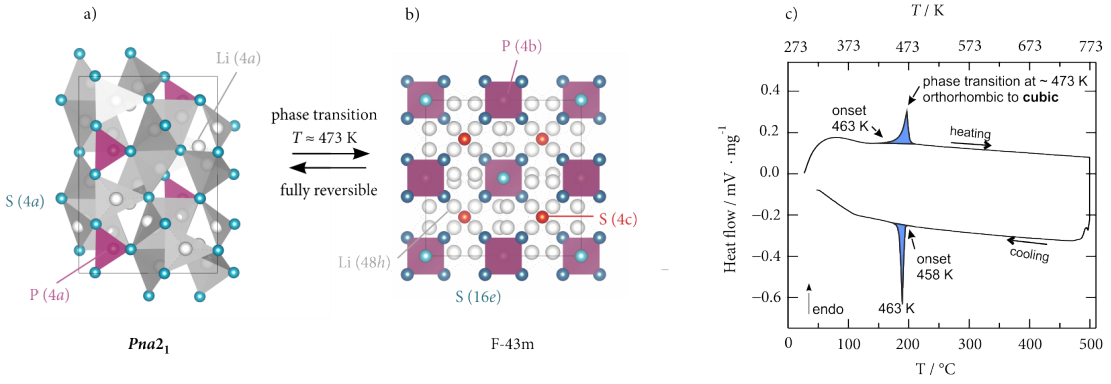

Figure 6.3: a) Orthorhombic and b) cubic modification of Li_7PS_6 with the phase transition at ca. 460 K. c) DSC curve of the prepared Argyrodite-type Li_7PS_6 measured in a aluminum crucible with a heating and a cooling rate of 10 °C/min.

about the Argyrodite-type materials based on the diffusion coefficients and charge chariers determined from NMR, it is also possible to determine these values form the impedance spectroscopy. However, it is important that the conductivity isotherms show a dispersive region to calculate the hopping frequency ν_H, which is determined through $\nu_H = 2 \cdot \sigma_{DC}$ (see Figure 6.4). With the

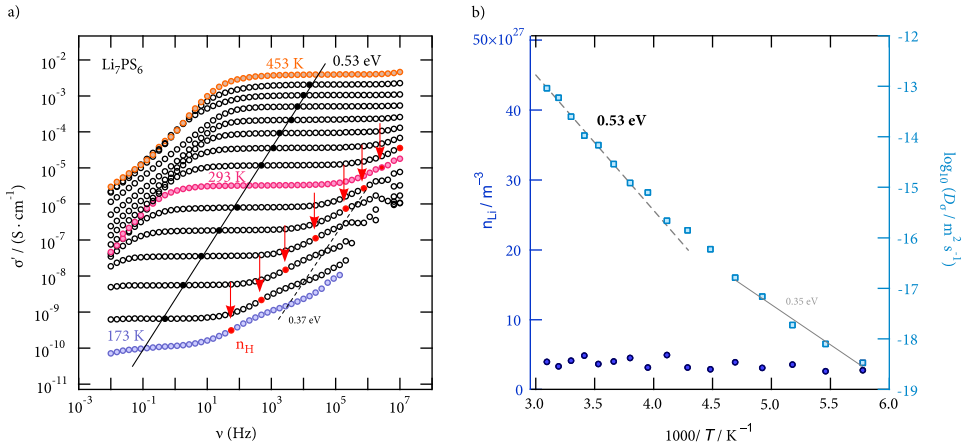

Figure 6.4: a) Conductivity isotherms of Li_7PS_6 ranging from 10 mHz to 10 MHz in a temperature range of 173 K to 453 K. The isotherms have been recorded in steps of 20 K. The red filled dots represent the hopping frequency ν_{H}. b) Diffusion coefficients and charge carrier density n_{Li}. D_σ vs the inverse temperature . As expected, n_{Li} stays constant with a value of 10^{27} m^{-3}. Below 213 K the activation energy is given by 0.35 eV. Above 213 K it increases reaching a value of 0.53 eV. This matches perfect with the activation energies gained by the conductivity isotherms.

conditions $\nu_H = 1/\tau$, and the jump distance a of the Li ions (obtained from the XRPD) a diffusion coefficient D_σ was estimated according to the Einstein-Smoluchowski [115] relation for 3D diffusion

$$D = \frac{a^2 \cdot \nu_H}{6}. \tag{6.1}$$

For a the jump distance of the 48h-48h jump process was used, which has been calculated with ca. 2.91 Å. Using this data D_σ can be calculated for each temperature T. Furthermore, the charge carrier density can be estimated from the Rietveld analysis, as described in the article before, and also through the impedance data taking into account $\sigma_{DC} = e \cdot n \cdot \mu$. e describes the elementary charge and μ the mobility of the ions. So to assemble all facts, the charge carrier denisty n_{Li} can be calculated as follows

$$n_{Li} = \frac{6 \cdot k_B \cdot T \cdot \sigma_{DC}}{e^2 \cdot a^2 \cdot \nu_H}. \tag{6.2}$$

k_{B} represents the Boltzmann constant and σ_{DC} the conductivity in the plateau of the isotherms, that are pointed out in Figure 6.4. The calculated charge carrier density reaches a value in the range of 10^{27} m^{-3} which matches perfect with the XRPD data. Moreover, the diffusion coefficient plotted against the inverse T (see Figure 6.4b)) results in an Arrhenius behavior, that yields an activation energy $E_{\mathrm{a,D}}$ of 0.53 eV which is comparable to $E_{\mathrm{a,DC}}$ (=0.53 eV) obtained from the conductivity isotherms. In Figure 6.4b) a second process is observed, that reaches a $E_{\mathrm{a,DC}}$ of 0.35 eV and is also in a good agreement with $E_{\mathrm{a,DC}}$ (=0.37 eV).

6.3.2 Fast Rotational Dynamics in Argyrodite-type Li_6PS_5X (X: Cl, Br, I) as Seen by ^{31}P Nuclear Magnetic Relaxation – On Cation-Anion Coupled Transport in Thiophosphates

As promising candidate of solid electrolyte for lithium batteries are sulfides with high ionic conductivity. Perfect candidates for such solid electrolytes are Argyrodites due to their ionic conductivity in the mS cm^{-1} range. Li_6PS_5Cl and Li_6PS_5Br show such high ionic conductivities at room temperature, whereas Li_6PS_5I has an three order of magnitude lower ionic conductivity. The lithium ion dynamic *via* ^7Li NMR has shown the ion dynamics of the iodide sample is as fast as for bromide and chloride (see section 6.2.1).

In this article the combination of several NMR techniques have been used, *i.e.* ^7Li and ^{31}P NMR to not only study Li dynamics but also to throw light on the rotational motions of the PS_4^{3-} units. NMR data reveal a high mobile, rotational PS_4^{3-} dynamics. The rate peaks of the PS_4^{3-} tetrahedra shows up at temperatures lower than 280 K. Noticeable, Li_6PS_5Br and Li_6PS_5I show two R_1 $(1/T_1)$ rate peaks while that at higher temperatures corresponds to lithium diffusivity indirectly sensed by the ^{31}P probe. For Li_6PS_5Cl only one rate peak has been observed, which can be explained through a Li anomaly due to the missing 24*g* Wyckoff position.

M2:
Fast Rotational Dynamics in Argyrodite-type Li_6PS_5X (X: Cl, Br, I) as Seen by ^{31}P Nuclear Magnetic Relaxation – On Cation-Anion Coupled Transport in Thiophosphates
I. Hanghofer, B. Gadermaier and H. M. R. Wilkening, *submitted*

Fast Rotational Dynamics in Argyrodite-type Li_6PS_5X (X: Cl, Br, I) as Seen by ^{31}P Nuclear Magnetic Relaxation – On Cation-Anion Coupled Transport in Thiophosphates

Isabel Hanghofer,* Bernhard Gadermaier and H. Martin R. Wilkening*

Graz University of Technology, Institute for Chemistry and Technology of Materials (NAWI Graz), and Christian Doppler Laboratory for Lithium Batteries, Stremayrgasse 9, A-8010 Graz, Austria.

ABSTRACT: Electrolytes with excellent ionic conductivity are needed for all-solid-state batteries to ensure a sage and long-lasting lithium-ion transport. Perfect candidates are Argyrodites, like Li_6PS_5X (X: Cl, Br, I), that show an ionic conductivity in the mS/cm range. Translational Li^+ diffusion in ceramic electrolytes is influenced by many factors such as crystal structure and defect chemistry. Considering thiophosphates, only little information is, however, available about the effects of rotational anion dynamics on Li^+ jump processes. Here, we used ^{31}P spin-lattice relaxation NMR to find out whether rapid Li^+ ion dynamics in Li_6PS_5X is affected by rotational jumps of the PS_4^{3-} units. NMR revealed that in Li_6PS_5I, having an ordered anion sub-lattice, PS_4^{3-} rotational dynamics are much faster than Li^+ self-diffusion. At 223 K the rotational correlation rate, which is obtained from NMR relaxation rate peaks, takes a very high value in the order of 10^9 events per second. It clearly decreases when anion disorder is introduced that, at the same time, contracts the lattice, *i.e.*, when we go from Li_6PS_5I to Li_6PS_5Br and further to Li_6PS_5Cl. While for Li_6PS_5I the rotational jumps of the PS_4^{3-} units are decoupled, that is, independent, from Li^+ translation, in Li_6PS_5Cl, with its small lattice constant, the much slower rotational dynamics seem to influence Li^+ intercage hopping processes. The corresponding rotational jumps do occur almost on the same time scale as the Li^+ exchange processes take place. For Li_6PS_5Br, on the other hand, an optimal balance between lattice properties, site disorder and fast rotational jumps seems to be established that leads to facile translational Li^+ displacements. Our experiments show that rotational motions, if they are in resonance with cation exchange, should be considered when the origins of long-range Li^+ ion transport in argyrodite-type thiophosphates need to be identified.

■ INTRODUCTION

Li-bearing argyrodites, Li_6PS_5X (X: Cl, Br, I), belong to the group of ionic conductors that show rapid Li^+ exchange processes leading to conductivities in the order of several mS/cm at room temperature.[1-7] This property is one of the inevitable prerequisites for the development of all-solid-state lithium-ion batteries taking advantage of non-flammable ceramic electrolytes.[8,9] In general, powerful and safe electrochemical energy storage systems,[10-14] which can efficiently store electricity from renewable sources for both automotive and stationary applications, are expected to pave the way to an environmentally friendly economy that has significantly reduced or even cut its dependency on fossil fuels.[15]

To provide such devices we need chemically and electrochemically stable ceramics with extraordinary high ionic conductivity.[4,8,9] Lifting the lid on the structural and dynamical principles that lead to rapid Li^+ translational motions is one of the big challenges of solid state chemistry.[16-21] Two fundamental aspects, sometimes called the *holy grails* in chemistry,[22] are important to understand rapid cation diffusivity in inorganic materials: i) the coupled *or* independent transport of electrons and cations and ii) the interplay of anion rotational motions and cation self-diffusion. The latter aspect is expected to be met in materials with complex anions such as PS_4^{3-}, SO_4^{2-} and BH_4^- that can undergo rapid rotational jumps. Even for model compounds it turned out to be difficult to decide whether the rapid rotational motions help the smaller cations to perform translational jumps or whether the cation jumps trigger rapid rotational dynamics. As in the famous ballad 'The Fisherman' of J.-W. v. Goethe, where it reads *"half drew she him, and half sank he"* also both partners may influence each other.

For Li_2SO_4 and $LiNaSO_4$ concepts such as the percolation model and the paddle-wheel mechanism have been introduced that assume either direct correlated motions of the anions and cations or, at least, anticipate that rotations and vibrations indirectly produce energetically favorable conduction pathways.[23] In addition, in Li_3InBr_6 and in the family of *closo*-borates, to which $Li_2B_{12}H_{12}$, $Na_2B_{12}H_{12}$ belong, also site frustration, bond and dynamic frustration have been identified as possible origins responsible for superionic conduction.[24,25] The same holds for the dynamics of cluster ions in, e.g., $Li_3S(BF_4)_{0.5}Cl_{0.5}$ and Na_3OBH_4.[26-28]

To study cation-anion coupled transport, spectroscopic methods need to be used that are able to clearly distinguish Li^+ or Na^+ hopping processes from the rotational dynamics of their surroundings. Here, we chose cubic Li_6PS_5X, see Figure 1, as a model system and employed time-domain ^7Li and ^{31}P nuclear magnetic resonance (NMR) spin-lattice relaxation (SLR) measurements[29,30] to probe Li^+ jump diffusion and the rotational jumps of the thiophosphate polyhedra forming the argyrodite structure. For Li_6PS_5I the ^{31}P NMR relaxation rate peak shows up at a temperature as low as 223 K pointing

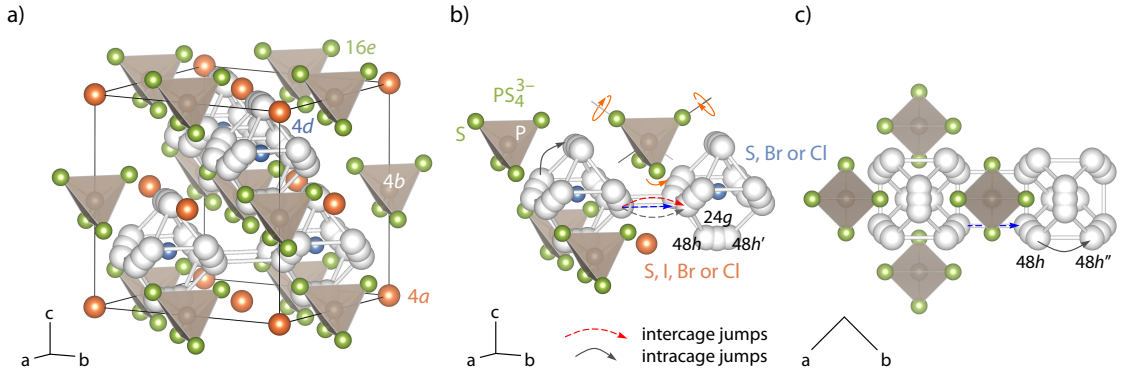

Figure 1 a) Crystal structure of argyrodite-type Li_6PS_5X that crystallizes with cubic symmetry in the space group $F\bar{4}3m$. In Li_6PS_5Cl the Li ions solely occupy the 24*g* positions of the split site 48*h*-24*g*-48*h*′. In compounds with X = Br and I, they are distributed over the 24*g* sites and the 48*h* positions. P resides on 4*b*. 16e is fully occupied by S^{2-} forming PS_4^{3-} tetrahedra. While in Li_6PS_5I the residual S^{2-} anions only occupy the 4*a* sites, in Li_6PS_5Br the occupation factors, according to neutron diffraction, amount to 78% (4*a*) and 22% (4*d*). For Li_6PS_5Cl the occupation factors are 39% (4*a*) and 62% (4*d*), thus the majority of the Cl anions occupies the inner centers of the Li cages, which is too small for I^-. b) Intracage and intercage Li diffusion pathways: hopping between two Li cages (48*h*-48*h*″, see also c)), either following a direct or curved pathway, could be influenced by S^{2-} anions of nearby PS_4^{3-} tetrahedral. The jump distance depends on the lattice constant and, thus, on halogen substitution. Possible rotational jumps are indicated that may open or block the Li^+ pathway. c) The same cutout as in a) but viewed along the *c*-axis. Two S^{2-} anions of the PS_4^{3-} tetrahedra are located slightly above the direct 48*h*-48*h*″ exchange pathway. Rotational jumps of the PS_4^{3-} tetrahedra could also influence the intracage jumps. As seen by ^{31}P SLR NMR, see Figure 2a, the PS_4^{3-} units undergo rapid dynamics if no anion occupies the center of the cages formed by Li^+.

to ultrafast rotational jump processes. Interestingly, depending on the lattice constant and the P-S disorder in the anion sublattice of the three model compounds, which increases in the order Li_6PS_5I < Li_6PS_5Br < Li_6PS_5Cl, we see that this relaxation peak systematically shifts towards higher temperature pointing to a decrease of the rotational correlation rate. For Li_6PS_5Cl this rate approaches the translational Li^+ correlation rate and might affect its Li ion dynamics.

■ RESULTS AND DISCUSSION

Li ion jump processes in Li_6PS_5X. NMR relaxometry, see Figure 2, is a powerful method to characterize both translational and rotational dynamics on the μs to ns time scale.[31] To interpret our findings by ^{31}P NMR relaxometry we need to give a short summary of what has been found out recently about Li ion dynamics in Li_6PS_5X.[19,32]

In a very recent study[32] we characterized Li^+ translational ion dynamics in Li_6PS_5X with the help of broadband conductivity, ^7Li SLR NMR and ^7Li NMR line shape measurements. Extremely rapid Li^+ ion dynamics in Li_6PS_5Br has already been probed by both ^7Li and ^6Li NMR by some of us earlier[2] and later confirmed by Wagemaker and co-workers.[7] Impedance spectroscopy revealed that Li_6PS_5Br and Li_6PS_5Cl show conductivities in the order of some mS/cm at ambient temperature.[3] This finding is highly consistent with ^7Li NMR relaxometry that revealed diffusion-induced R_1 NMR peaks near room temperature.[32]

Astonishingly, although long-range ion transport in Li_6PS_5I is rather poor[3,32] resulting in a room-temperature conductivity σ of only 10^{-6} S/cm at 293 K, the corresponding ^7Li SLR NMR rate peak $R_1(1/T)$ shows up at a temperature as low as 329 K, see Figure 2c.[4,32] According to σ, we would have expected the peak to appear at much higher temperatures. This apparent discrepancy has been explained by the assumption that the important intracage Li^+ exchange, enabling the ions to move over long distances, is characterized by a much higher energy barrier in Li_6PS_5I than that in Li_6PS_5Br and Li_6PS_5Cl, respectively.[32] This view is supported by calculations that show that intercage jumps in Li_6PS_5I, with its larger lattice constant ($a \approx 10.15$ Å), are less frequent than in the sibling compounds.[19] For comparison, the ionic radii *r* of the anions in Li_6PS_5X are given by $r(S^{2-}) = 1.84$ Å, $r(Cl^-) = 1.81$ Å, $r(Br^-) = 1.95$ Å, and $r(I^-) = 2.16$ Å.

Obviously, although intercage jumps are energetically hindered, rapid intracage exchange processes in Li_6PS_5I, including doublet jumps (48*h*-24*g*-48*h*′) and local 48*h*-48*h*′ hops, are sufficient to produce a full ^7Li NMR relaxation rate peak. This peak is symmetric in shape. While the S^{2-} anion distribution in Li_6PS_5I is ordered (the 4*d* site is only occupied by S^{2-}), strong anion disorder is present in Li_6PS_5Br ($a \approx 9.95$ Å) and Li_6PS_5Cl ($a \approx 9.85$ Å); Cl^- and Br^- occupy, according to results from neutron diffraction, the sites 4*a* and 4*d*.[3]

The ^7Li NMR rate peaks of the latter samples appear at T_{max} = 286 K (Li_6PS_5Br) and 316 K (Li_6PS_5Cl), respectively. At T_{max} the associated motional correlation rate $1/\tau_c$, which is within a factor of 2 equal to the jump rate $1/\tau$ is given by $\omega_0 \tau_c \approx 1$ (see Supporting Information); with $\omega_0/2\pi = 116$ MHz we see that $1/\tau$ corresponds to values in the order of 10^9 s^{-1}. The corresponding activation energies E_a deduced of the $R_1(1/T)$ peak of Li_6PS_5Br (0.21 eV, see Figure 2a) is comparable to that of Li_6PS_5I (0.20 eV, Figure 2c). Solid lines in Figure 2 refer to fits using Lorentzian-shaped spectral density functions to approximate the $R_1(^7Li)$ peaks, see Supporting Information, Table 1 lists the activation energies and asymmetry factors obtained. Lines approximating the low-temperature flanks of the peaks are also included in Figure 2, they lead to activation energies ranging from 0.15 eV to 0.2 eV, see Supporting Information. The peaks belonging to X = Cl and X = Br are asymmetric in shape pointing to correlated Li^+ ionic motions in materials with strong substitutional halogen disorder. In general, at the peak maximum the motional correlation rate

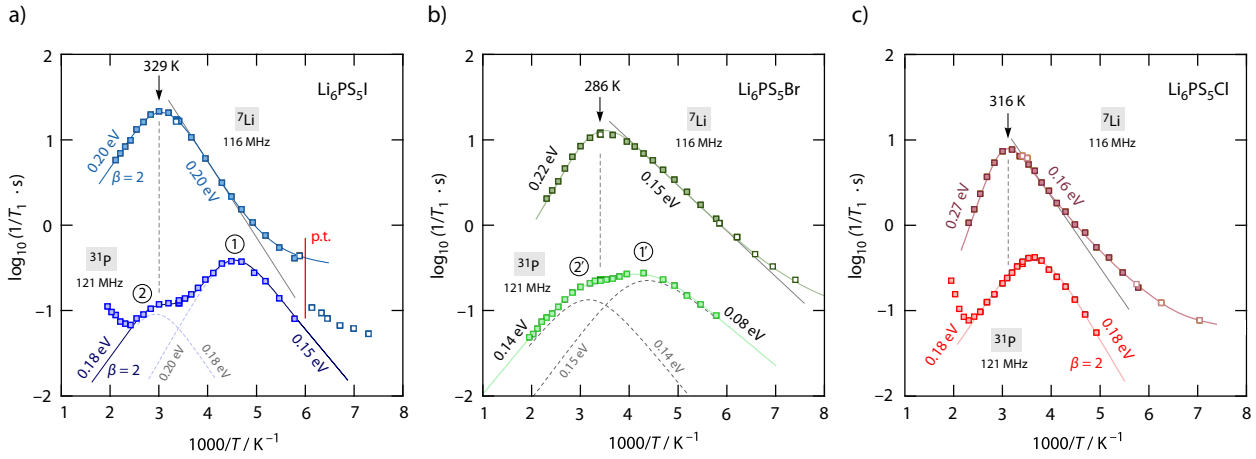

Figure 2 Diffusion-induced ^{7}Li (116 MHz) and ^{31}P (121 MHz) SLR NMR rates ($\log_{10}(R_1)$ plotted *vs.* $1000/T$) of a) Li_6PS_5I, b) Li_6PS_5Br and c) Li_6PS_5Cl. Rates shown with unfilled symbols were recorded with a probe head designed for measurements at cryogenic temperatures. Solid lines represent fits using BPP-type spectral density functions. In the case of ^{7}Li the fits take into account non-diffusive effects seen at low temperature. Linear fits are used to extract activation energies of the $R_1(^7\text{Li})$ peaks in the low-temperature regime. The other values in eV refer to activation energies deduced from BPP-type fits. Dashed lines represent the individual rate peaks that produce the overall two-peak response seen via ^{31}P SLR NMR for X = I, Br. While peak (1) is ascribed to rotational dynamics, peak (2) reflects Li^+ translational jumps indirectly sensed by the ^{31}P spins. Peak (2) shows up at the same temperature T_{max} as $R_1(1/T)$ of ^{7}Li. With increasing anion disorder (and decreasing cation disorder) peak (1) shifts toward higher temperature, *i.e.*, rotational dynamics decreases and is significantly reduced for Li_6PS_5Cl, see Figure 3. The increase of $R_1(^{31}\text{P})$ at high temperature points to a further dynamic process with much higher activation energy. Li_6PS_5I undergoes a phase transition (p.t.) at lower T, as indicated by the jump seen in $R_1(^7\text{Li})$.

$1/\tau_{trans}$ is in the order of the Larmor frequency ω_0 used to probe the SLR NMR rates. Here, at T_{max} the correlation rates are in the order of 7×10^9 s^{-1}, which corresponds to the above-mentioned room temperature ionic conductivities in the order of several mS/cm.

^{31}P SLR NMR measurements of Li_6PS_5X. We begin with the presentation and discussion of the ^{31}P SLR NMR rates of the ordered Li_6PS_5I compound. Provided SLR is solely induced by motional process, as for ^{7}Li NMR, the ^{31}P SLR NMR rate R_1 passes through a maximum on the $\log(R_1)$ *vs.* $1/T$ plot shown in Figure 2a. Coming from very low temperatures $R_1(1/T)$ reveals a very similar temperature dependence as seen for ^{7}Li. $R_1(^7\text{Li})$ is larger than $R_1(^{31}\text{P})$ as the quadrupole nucleus ^{7}Li with its spin-quantum number of $I = 3/2$ is influenced by electric quadrupolar relaxation. Moreover, the spin-1/2 nucleus ^{31}P is subjected to much weaker dipolar homonuclear spin interactions than ^{7}Li. Surprisingly, $R_1(^{31}\text{P})$ passes through a maximum at $T_{max}(^{31}\text{P})$ of only 223 K, that is, by $\Delta T = 106$ K lower than $T_{max}(^7\text{Li})$, see peak (1) in Figure 2a. Obviously, ^{31}P has access to effective magnetic dipolar spin-fluctuations producing a rate peak at such low temperature.

Interestingly, a second rate peak shows up that is located on the high temperature flank of peak (1), see Figure 2a. It appears at a temperature that perfectly agrees with that of the ^{7}Li SLR NMR peak. Hence, we attribute peak (1) to fast PS_4^{3-} rotational dynamics in Li_6PS_5I that are independent of any Li^+ translational motions. Presumably, the large lattice constant of $a \approx 10.15$ Å enables the anions to freely rotate. Peak (2) represents another source of spin-fluctuations that originates from fast Li^+ self-diffusion that is, in the case of Li_6PS_5I, restricted to intracage jump processes. Obviously, at higher temperature the ^{31}P spins indirectly sense the rapid Li exchange processes in their direct neighborhood.

Table 1. Activation energies $E_{a,i}$ and asymmetry parameters β characterizing the ^{7}Li and ^{31}P NMR $R_1(1/T)$ rate peaks of Li_6PS_5X (X = Cl, Br, I) when analyzing with Lorentzian-shaped spectral density functions. For ^{31}P NMR two rate peaks (i = 1,2) are obtained for X = Br and X = I. $\beta = 2$ indicates symmetric peaks; in general it takes values ranging from 1 to 2, see Supporting Information.

Sample	^{7}Li		^{31}P			
	E_a	β	$E_{a,1}$	β_1	$E_{a,2\,(Li)}$	β_2
Li_6PS_5Cl	0.32 eV	1.53	0.18 eV[a]	2	–	–
Li_6PS_5Br	0.21 eV	1.48	0.15 eV	1.59	0.14 eV	2
Li_6PS_5I	0.20 eV	2	0.20 eV	1.75	0.18 eV	2

[a] This value is just an apparent one, as the high-temperature flank is a superposition of two rate peaks belonging to rotational PS_4^{3-} and translational Li^+ dynamics.

The same two sources of spin-fluctuations are also seen for Li_6PS_5Br (Figure 2b, in Figure 3a a comparison of results for X = I and X = Br is shown). Importantly, peak (1′) is slightly shifted toward higher temperature. We conclude that substitutional disorder in the anion sublattice and lattice contraction slightly disturbs PS_4^{3-} rotational dynamics so that the rotational correlation rate $1/\tau_{rot}$ (≈ 121 MHz $\times$ $2\pi = 7.6 \times 10^8$ s^{-1}) is reached at 233 K instead of 223 K for Li_6PS_5I. The fact that some of the larger Br anions occupy the 4*d* sites seems to hinder PS_4^{3-} rotational dynamics; on the other hand, peak (1′) shows a very low activation energy of only 0.08 eV in the limit $\omega_0 \tau_c \gg 1$. As in the case of Li_6PS_5I, $T_{max}(^{31}\text{P})$ of the second peak (2′) agrees well with $T_{max}(^7\text{Li})$, see also Figure 2b. The distance ΔT on the temperature scale of the two peaks (1′ and 2′) decreased from $\Delta T = 106$ K (Li_6PS_5I) to $\Delta T = 53$ K (Li_6PS_5Br), Figure 3a. The two relaxation rate peaks in Figure 2b and 2a have been approximated with two Lorentzian-shaped spectral density terms, see Supporting

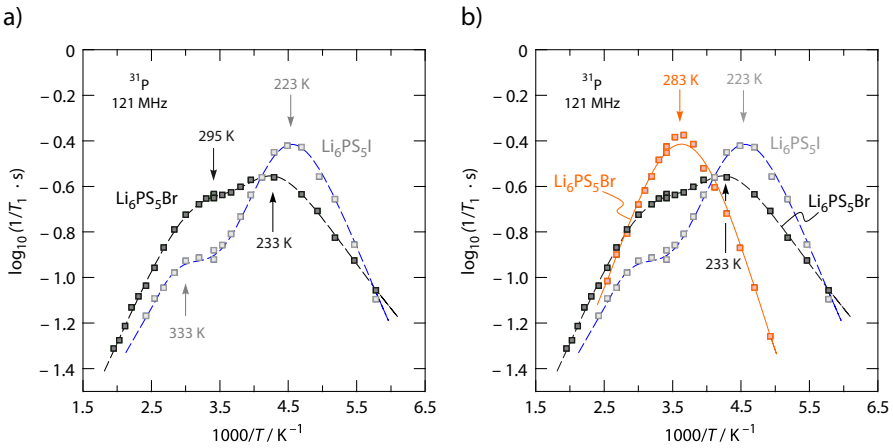

Figure 3 a) Direct comparison of the ^{31}P SLR NMR rate peaks $R_1(1/T)$ seen for Li_6PS_5I and Li_6PS_5Br. The peak at low temperatures refers to a source of spin fluctuations that only affects the ^{31}P spins. The peak at higher temperature indicates Li^+ jump diffusion in the direct neighborhood of the ^{31}P spins. For anion-disordered Li_6PS_5Br translational Li^+ motions are faster as compared to the anion-ordered Li_6PS_5I compound; rotational dynamics, however, are slightly decreased as the corresponding rate peak shifts from 223 K to 233 K. For Li_6PS_5Cl, being characterized by an ordered Li sublattice but strong anion disorder with many Cl anions residing on 4*d*, this shift is even larger. Consequently, the two NMR peaks, if measured at a Larmor frequency of 121 MHz, cannot be distinguished from each other any longer. The significantly slower PS_4^{3-} rotational jump diffusion in disordered Li_6PS_5Cl is expected to influence its Li^+ ion dynamics.

Information; the same fits are shown in Figure 3 as dashed lines. Dashed lines in Figure 2a and 2b shows the individual peaks. Again, activation energies and asymmetry parameters of the two peaks are listed in Table 1 and Arrhenius pre-factors are included in Table S1.

To sum up our results up to here, we found that in Li_6PS_5I very fast rotational dynamics are present and that the Li^+ ions have access to rapid intracage (local) ion dynamics. For Li_6PS_5Br, where some of the S^{2-} ions on 4*d* (and 4*a*) have been replaced by the larger Br^- ions (22.1% (4*d*) *vs* 77.9% (4*a*))[3], rotational dynamics are slightly slowed down. This feature seems to be the consequence of a change in lattice constant and bonding situations. Li^+ dynamics, on the other hand, clearly benefits from anion disorder; the corresponding NMR rate peak is governed by both fast intracage jump processes *and* rapid Li^+ exchange between the Li cages. The latter results in high ionic conductivities being the consequence of facile long-range transport. In general, replacing S^{2-} with a halogen ion having a lower electric charge the Li^+ ions are less attracted by the argyrodite framework leading to higher cation mobilities.

Most interestingly, the ^{31}P SLR NMR response seen for Li_6PS_5I is in stark contrast to what is sensed by ^{31}P for Li_6PS_5Cl (see Figures 2c and 3b). Only a single prominent rate peak $R_1(1/T)$ is obtained for the Cl-compound; this peak is very similar in shape to the main peak (1) of Li_6PS_5I but shifted toward significantly higher temperature. It has been approximated with a single spectral density term (see solid line in Figure 3b and Table 1; the peak appears at $T_{max}(^{31}P)$ = 283 K. For comparison, $R_1(^7Li)(1/T)$ shows up at 316 K and ΔT amounts to only 33 K. Again, we assume that increasing lattice contraction and anion substitutional disorder, which is much stronger for Li_6PS_5Cl than for Li_6PS_5Br, hinders fast rotational jump diffusion. Compared to the Br analogue, in Li_6PS_5Cl the majority of Cl^- anions occupy the 4*d* sites inside the Li cages. The occupation factors are 38.5% (4*a*) and 61.5% (4*d*).[3] Most likely, as ΔT turned out to be only 33 K, the peak $R_1(^{31}P)(1/T)$ seen by ^{31}P NMR is an overall one including the $R_1(^7Li)(1/T)$ peak with its smaller amplitude.

If substitutional anion disorder is beneficial for rapid Li^+ jump diffusion, also involving intercage jumps, we have to wonder why for Li_6PS_5Cl with the smallest lattice constant and the highest degree of anion disorder the $R_1(^7Li)$ peak appears at higher temperature (316 K) than that of Li_6PS_5Br (286 K). To answer this question, it is worth noting that in Li_6PS_5Cl the Li ions solely occupy the 24*g* site, whereas in Li_6PS_5Br the Li ions are distributed over the 24*g* and 48*h* sites.[3] We anticipate, however, that under the conditions of extremely rapid exchange processes this cation site preference might have only moderate influence on the $R_1(^7Li)$ peaks seen near ambient temperature. Here, we assume that, to a greater extent, anion rotations seem to play a decisive role to explain this feature. We have seen that with increasing anion site disorder and lattice contraction, the correlation $1/\tau_{rot}$ decreases. For Li_6PS_5Br it is still rather high and seems to influence $1/\tau_{trans}$ only slightly. For Li_6PS_5Cl, on the other hand, it has significantly been reduced and it might affect interring translational jump diffusion leading to a shift of $R_1(^7Li)(1/T)$ of Li_6PS_5Cl toward T_{max} higher than expected.

Let us think about different Li^+ pathways (P1 and P2, see Figure 1b) connecting the Li cages. Considering the dashed arrows in Figure 1b the Li^+ ions in Li_6PS_5Cl might prefer a curved pathway P2, which, in contrast to P1, escapes from PS_4^{3-} rotation but goes past the 4*a* position, which is occupied by the smaller Cl^- anions. We would expect lower Coulomb attractions between Li and Cl(4*a*) as compared to Li and S(4*a*). For Li_6PS_5Br both pathways connecting the Li cages might play a role giving rise to rapid Li^+ exchange processes between the cages. The latter would result in $R_1(^7Li)$ peaks showing up at the lowest temperatures T_{max} in the series Li_6PS_5X (X = Cl, Br, and I).

In conclusion, for Li_6PS_5I, with its ordered distribution of I^- and S^{2-} over the crystallographic positions 4*a* and 16*e*, the important intercage jump process for long-range Li^+ translational motion is characterized by a much larger activation energy than in the compounds with X = Br and X = Cl.[19] On the other hand, the ordered and widened structure of Li_6PS_5I ensures that the PS_4^{3-} can freely rotate around specific axes. These rotations are decoupled from translational motions ($1/\tau_{rot} \ggg 1/\tau_{trans}$). In Li_6PS_5Br an optimum balance between lattice properties (including polarizabilities[3]) and site disorder is established that leads to fast rotational jumps (0.08 eV in the low-T regime) and facile translational Li^+ displacements ($1/\tau_{rot} \gg 1/\tau_{trans}$). For Li_6PS_5Cl, on the other hand, the small lattice constant and strong anion site disorder significantly reduces $1/\tau_{rot}$ leading to motional correlation rates, $1/\tau_{rot}$ and $1/\tau_{trans}$, being of comparable order of magnitudes. We interpret the latter as a first sign that anion rotational dynamics may influence Li^+ jump dynamics in argyrodite-type Li_6PS_5Cl.

Concisely said, while halogen site disorder is beneficial for Li^+ translational dynamics, it is detrimental for fast rotational ion dynamics. Whereas for Li_6PS_5Br a high $1/\tau_{rot}$ rate does not disturb Li intercage jumps, we anticipate that the much slower rotational dynamics in Li_6PS_5Cl lead to a smaller Li ion intercage diffusivity as one might assume for this compound. The higher activation energy for Li_6PS_5Cl extracted from $R_1(^7Li)$, 0.32 eV compared to 0.2 eV for Li_6PS_5Br,[32] supports this view. Our findings might help rationalize the origins behind fast Li^+ diffusion in inorganic matrices and to refine the currently available design rules to develop powerful electrolytes.

■ MATERIALS AND METHODS

The Li argyrodites Li_6PS_5X (X: Cl, Br, I), have been prepared by mixing stoichiometric amounts of of Li_2S (Sigma-Aldrich 99.98 %), P_2S_5 (Honeywell Fluka 99 %) and LiCl (Sigma-Aldrich, anhydrous, 99 %), LiBr (Sigma-Aldrich, anhydrous, 99.98 %) and LiI (Sigma-Aldrich, 99.9 %), respectively. The starting compounds were mixed using a high-energy planetary ball mill (Fritsch Pulverisette 7 Premium line) at a rotation speed of 400 rpm for 4 hours. Milling was carried out in ZrO_2 beakers (45 mL) filled with 180 balls (ZrO_2, 5 mm in diameter). Afterwards the mixtures were uniaxially pressed (0.4 tons) into pellets with a diameter of 5 mm, filled into quartz ampoules and sealed under vacuum. The ampules were preheated at 573 K under dynamic vacuum to remove traces of water. The reaction was carried out at 823 K (heating rate: 5 K/min, duration 7 days; cooling rate 10 K/min). All preparation steps were strictly carried out in Ar gas atmosphere (H_2O and O_2 < 1 ppm).

According to X-ray diffraction, for which we used a Bruker D8 Advance diffractometer with Bragg Brentano geometry, the 3 compounds, Li_6PS_5Cl, Li_6PS_5Br, Li_6PS_5I, showed the typical argyrodite- type structure (space group *F*-43*m*); Rietveld refinements are shown in Figure S1. High-resolution, *i.e.*, magic angle spinning (MAS), NMR spectra of the nuclei ^6Li (73.6 MHz), ^{31}P (202.4 MHz), which were recorded at a spinning speed of 25 kHz (2.5-mm rotors, ambient bearing gas) on a 500-MHz Bruker Avance III spectrometer, confirmed the phase purity of the samples, see Figure S2.

Time-domain ^{31}P and ^7Li NMR spin-lattice relaxation (SLR) measurements were carried out on a 300-MHz Bruker Avance III spectrometer connected to a shimmed cryo-magnet of a nominal magnetic field of 7 Tesla. This value corresponds to Lamor frequencies of $\omega_0/2\pi$ = 121 MHz and 116 MHz, respectively. We used a high-temperature probe (Bruker Biospin) to record variable-temperature (173 K to 513 K) spectra and spin-lattice relaxation (SLR) rates. The probe is equipped with a type T thermocouple connected to a Eurotherm temperature controller able to guarantee a temperature stability with a precision of ± 2 K. At a power level of 200 W the $\pi/2$ excitation pulse length ranged from 2.0 to 2.7 μs depending on the temperature. Prior to the measurements the sample was vacuum dried and fire-sealed in Duran glass NMR tubes (5 mm in diameter and ca. 3 cm in length).

Longitudinal SLR NMR rates $1/T_1$ (= R_1) in the laboratory frame were measured by means of the saturation recovery pulse sequence: $10 \times \pi/2 - t_d - \pi/2$.[33] This sequence uses a comb of 10 closely spaced $\pi/2$ pulses to destroy any longitudinal magnetization M_z before its recovery is recorded as a function of waiting time t_d. To construct the corresponding magnetization transients $M_z(t_d)$ the area under the free induction decays (FIDs) is plotted vs. t_d. In the case of ^{31}P NMR we used up to 16 FIDs for each waiting time. R_1 was obtained by parameterizing the magnetization curves $M_z(t_d)$ by suitably stretched exponentials: $M_z(t_d) \propto 1 - \exp(-(t_d/T_1)^\gamma)$. For R_1 of ^{31}P the exponent γ ranges from 0.7 to 1; the exponents of $R_1(^7Li)$ take values from 0.9 to 1, that is, the transients are almost of single exponential nature.[32]

AUTHOR INFORMATION

Corresponding Author

* wilkening@tugraz.at; isabel.hanghofer@tugraz.at (see also for correspondence)

Author Contributions

The manuscript was written through contributions of all authors.

Notes

The authors declare no competing financial interest.

ACKNOWLEDGMENT

Financial support by the Deutsche Forschungsgemeinschaft (DFG Research Unit 1277, grant no. WI3600/2-1(4-1) (FOR1277)) as well as by the Austrian Federal Ministry of Science, Research and Economy, and the Austrian National Foundation for Research, Technology and Development (Christian Doppler Laboratory of Lithium Batteries: Ageing Effects, Technology and New Materials) is greatly appreciated. Furthermore, we thank the FFG in the frame of the K project safe battery.

References

1. Deiseroth, H. J.; Kong, S. T.; Eckert, H.; Vannahme, J.; Reiner, C.; Zaiss, T.; Schlosser, M. Li_6PS_5X: A Class of Crystalline Li-Rich Solids with an Unusually High Li^+ Mobility. *Angew. Chem. Int. Ed.* **2008**, *47*, 755-758.

2. Epp, V.; Gün, O.; Deiseroth, H. J.; Wilkening, M. Highly Mobile Ions: Low-Temperature NMR Directly Probes Extremely Fast Li^+ Hopping in Argyrodite-Type Li_6PS_5Br. *J. Phys. Chem. Lett.* **2013**, *4*, 2118-2123.

3. Kraft, M. A.; Culver, S. P.; Calderon, M.; Böcher, F.; Krauskopf, T.; Senyshyn, A.; Dietrich, C.; Zevalkink, A.; Janek, J.; Zeier, W. G. Influence of Lattice Polarizability on the Ionic Conductivity in the

Lithium Superionic Argyrodites Li_6PS_5X (X = Cl, Br, I). *J. Am. Chem. Soc.* **2017**, *139*, 10909-10918.

4. Kraft, M. A.; Ohno, S.; Zinkevich, T.; Koerver, R.; Culver, S. P.; Fuchs, T.; Senyshyn, A.; Indris, S.; Morgan, B. J.; Zeier, W. G. Inducing High Ionic Conductivity in the Lithium Superionic Argyrodites $Li_{6+x}P_{1-x}Ge_xS_5I$ for All-Solid-State Batteries. *J. Am. Chem. Soc.* **2018**, *140*, 16330-16339.

5. Wang, H.; Yu, C.; Ganapathy, S.; van Eck, E. R. H.; van Eijck, L.; Wagemaker, M. A Lithium Argyrodite $Li_6PS_5Cl_{0.5}Br_{0.5}$ Electrolyte with Improved Bulk and Interfacial Conductivity. *J. Power Sources* **2019**, *412*, 29-36.

6. Yu, C.; Ganapathy, S.; Hageman, J.; van Eijck, L.; van Eck, E. R. H.; Zhang, L.; Schwietert, T.; Basak, S.; Kelder, E. M.; Wagemaker, M. Facile Synthesis toward the Optimal Structure-Conductivity Characteristics of the Argyrodite Li_6PS_5Cl Solid-State Electrolyte. *ACS Appl. Mater. Interfaces* **2018**, *10*, 33296-33306.

7. Yu, C.; Ganapathy, S.; van Eck, E. R. H.; van Eijck, L.; Basak, S.; Liu, Y. Y.; Zhang, L.; Zandbergen, H. W.; Wagemaker, M. Revealing the Relation between the Structure, Li-Ion Conductivity and Solid-State Battery Performance of the Argyrodite Li_6PS_5Br Solid Electrolyte. *J. Mater. Chem. A* **2017**, *5*, 21178-21188.

8. Bachman, J. C.; et al. Inorganic Solid-State Electrolytes for Lithium Batteries: Mechanisms and Properties Governing Ion Conduction. *Chem. Rev.* **2016**, *116*, 140-162.

9. Zhang, Z. Z.; et al. New Horizons for Inorganic Solid State Ion Conductors. *Energy Environ. Sci.* **2018**, *11*, 1945-1976.

10. Goodenough, J. B. Evolution of Strategies for Modern Rechargeable Batteries. *Acc. Chem. Res.* **2013**, *46*, 1053-1061.

11. Goodenough, J. B.; Kim, Y. Challenges for Rechargeable Li Batteries. *Chem. Mater.* **2010**, *22*, 587-603.

12. Whittingham, M. S. Lithium Batteries and Cathode Materials. *Chem. Rev.* **2004**, *104*, 4271-4301.

13. Dunn, B.; Kamath, H.; Tarascon, J. M. Electrical Energy Storage for the Grid: a Battery of Choices. *Science* **2011**, *334*, 928-935.

14. Bruce, P. G.; Scrosati, B.; Tarascon, J. M. Nanomaterials for Rechargeable Lithium Batteries. *Angew. Chem. Int. Ed.* **2008**, *47*, 2930-2946.

15. Larcher, D.; Tarascon, J. M. Towards Greener and More Sustainable Batteries for Electrical Energy Storage. *Nat. Chem.* **2015**, *7*, 19-29.

16. Richards, W. D.; Tsujimura, T.; Miara, L. J.; Wang, Y.; Kim, J. C.; Ong, S. P.; Uechi, I.; Suzuki, N.; Ceder, G. Design and Synthesis of the Superionic Conductor $Na_{10}SnP_2S_{12}$. *Nat. Commun.* **2016**, *7*, 1026-1031.

17. Wang, Y.; Richards, W. D.; Ong, S. P.; Miara, L. J.; Kim, J. C.; Mo, Y. F.; Ceder, G. Design Principles for Solid-State Lithium Superionic Conductors. *Nat. Mater.* **2015**, *14*, 1026-1031.

18. Bernges, T.; Culver, S. P.; Minafra, N.; Koerver, R.; Zeier, W. G. Competing Structural Influences in the Li Superionic Conducting Argyrodites $Li_6PS_{(5-x)}Se_xBr$ $(0 < x < 1)$ upon Se Substitution. *Inorg. Chem.* **2018**, *57*, 13920-13928.

19. de Klerk, N. J. J.; Roslon, T.; Wagemaker, M. Diffusion Mechanism of Li Argyrodite Solid Electrolytes for Li-Ion Batteries and Prediction of Optimized Halogen Doping: The Effect of Li Vacancies, Halogens, and Halogen Disorder. *Chem. Mater.* **2016**, *28*, 7955-7963.

20. Yu, C.; Ganapathy, S.; de Klerk, N. J. J.; Roslon, I.; van Eck, E. R. H.; Kentgens, A. P. M.; Wagemaker, M. Unravelling Li-Ion Transport from Picoseconds to Seconds: Bulk versus Interfaces in an Argyrodite Li6PS5Cl-Li2S All-Solid-State Li-Ion Battery. *J. Am. Chem. Soc.* **2016**, *138*, 11192-11201.

21. Yu, C.; Ganapathy, S.; Eck, E. R. H. v.; Wang, H.; Basak, S.; Li, Z.; Wagemaker, M. Accessing the Bottleneck in All-Solid State Batteries, Lithium-Ion Transport over the Solid-Electrolyte-Electrode Interface. *Nat. Commun.* **2017**, *8*, 1086.

22. Smith, P. F.; Takeuchi, K. J.; Marschilok, A. C.; Takeuchi, E. S. Holy Grails in Chemistry: Investigating and Understanding Fast Electron/Cation Coupled Transport within Inorganic Ionic Matrices. *Acc. Chem. Res.* **2017**, *50*, 544-548.

23. Karlsson, L.; Mcgreevy, R. L. Mechanisms of Ionic-Conduction in Li_2SO_4 and $LiNaSO_4$ – Paddle Wheel or Percolation. *Solid State Ionics* **1995**, *76*, 301-308.

24. Adelstein, N.; Wood, B. C. Role of Dynamically Frustrated Bond Disorder in a Li+ Superionic Solid Electrolyte. *Chem. Mater.* **2016**, *28*, 7218-7231.

25. Kweon, K. E.; Varley, J. B.; Shea, P.; Adelstein, N.; Mehta, P.; Heo, T. W.; Udovic, T. J.; Stavila, V.; Wood, B. C. Structural, Chemical, and Dynamical Frustration: Origins of Superionic Conductivity in closo-Borate Solid Electrolytes. *Chem. Mater.* **2017**, *29*, 9142-9153.

26. Fang, H.; Jena, P. Sodium Superionic Conductors Based on Clusters. *ACS Appl. Mater. Interfaces* **2019**, *11*, 963-972.

27. Fang, H.; Jena, P. Li-Rich Antiperovskite Superionic Conductors Based on Cluster Ions. *Proc. Nat. Acad. Sci.* **2017**, *114*, 11046-11051.

28. Sun, Y.; et al. Rotational Cluster Anion Enabling Superionic Conductivity in Sodium-Rich Antiperovskite Na_3OBH_4. *J. Am. Chem. Soc.* **2019**.

29. Uitz, M.; Epp, V.; Bottke, P.; Wilkening, M. Ion Dynamics in Solid Electrolytes for Lithium Batteries. *J. Electroceram.* **2017**, *38*, 142-156.

30. Stanje, B.; Rettenwander, D.; Breuer, S.; Uitz, M.; Berendts, S.; Lerch, M.; Uecker, R.; Redhammer, G.; Hanzu, I.; Wilkening, M. Solid Electrolytes: Extremely Fast Charge Carriers in Garnet-Type $Li_6La_3ZrTaO_{12}$ Single Crystals. *Ann. Phys.* **2017**, *529*, 1700140(1)-1700140(9).

31. Wilkening, M.; Heitjans, P. From Micro to Macro: Access to Long-Range Li^+ Diffusion Parameters in Solids via Microscopic ^6Li, ^7Li Spin-Alignment Echo NMR Spectroscopy. *ChemPhysChem* **2012**, *13*, 53-65.

32. Hanghofer, I.; Brinek, M.; Eisbacher, S.; Bitschnau, B.; Volck, M.; Hennige, V.; Hanzu, I.; Rettenwander, D.; Wilkening, M. Substitutional Disorder: Structure and Ion Dynamics of the Argyrodites Li_6PS_5Cl, Li_6PS_5Br and Li_6PS_5I. *Phys. Chem. Chem. Phys.* **2019**.

33. Epp, V.; Gun, O.; Deiseroth, H. J.; Wilkening, M. Long-Range Li^+ Dynamics in the Lithium Argyrodite Li_7PSe_6 as Probed by Rotating-Frame Spin-Lattice Relaxation NMR. *Phys. Chem. Chem. Phys.* **2013**, *15*, 7123-7132.

..

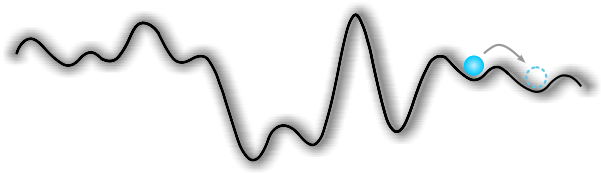

7 Conclusion and Outlook

In this doctoral thesis various types of solid-state ion conductors, especially oxide, halide and sulfide based, have been prepared and studied in detail with respect to their structural features and diffusion properties. Most of the samples were prepared through classical solid-state reactions, including besides mechanochemical treatment also hydrothermal reactions. These techniques allow both the preparation of new compounds as well as the improvement of the ionic transport of existing materials. Materials prepared at various temperatures or pressure, influence the density of the materials and thus also the long-range ion transport through the samples . High-energy ball milling leads to crystallites with a small particle size and introduces structural disorder. X-ray powder diffraction (XRPD) and also neutron powder (NPD) diffraction were used to characterize the samples regarding to purity and crystal structure. To quantify the crystallographic sites resulting from XRPD and NPD, also MAS NMR can be used. The methods of choice to characterize ion transport and diffusion parameters are impedance spectroscopy as well as NMR spectroscopy. Combining both spectroscopic methods allows to characterize the charge carrier motion over a large length scale. In addition, to study the ion motion the combination or comparison of the results contributes to a better understanding of Li or P dynamics; this is especially helpful when corraleted motion have to be studied.

Oxide-based solid electrolyte. – Research on materials for new, chemical energy storage methods, such as solid-state batteries with an oxidic solid electrolyte, have been investigated in this thesis. As model systems materials with NaSICON structure (sodium super ionic conductor) have been studied. The main sample $LiZr_2(PO_4)_3$ was synthesized *via* a solid-state reaction. The same holds for the structurally equivalent materials such as $Li_{1-2x}M_xB_{2-x}(PO_4)_3$ (M=Ca, Hf, Fe; B= Zr, Ti). The rhombohedral NaSICON structure can be stabilized by doping and also the ionic conductivity can be increased significantly. All samples have been characterized *via* XRPD (including Rietveld analysis) and impedance and NMR spectroscopy. Different substitution ions

can lead to a stabilized structure, can densify the sample and can also increase the number of defects, which leads to a higher charge carrier density. All these phenomena are expected to affect ion diffusion in solids and thus influence the Li ion conductivity.

In case of $LiZr_2(PO_4)_3$ and $Li_{1-2x}Ca_xZr_{2-x}(PO_4)_3$ (x = 0.1 and 0.2) it become clear that by doping the rhombohedral phase (space group: R-3c) is stabilized. Since $LiZr_2(PO_4)_3$ does not belong to the family of superionic conductors, it is able to serve as a model substance to learn about the Li ion dynamics in the crystalline grains and across grain boundary. Furthermore, by varying the educts and the substituent, the impurity amount decreases with increasing 10 % Ca^{2+} content which also results in an increase of ionic conductivity related to the grain boundary. ^{7}Li NMR measurements shows a much lower activation energy than impedance spectroscopy revealed. This difference shows length scale dependent ion dynamics. Impedance spectroscopy detects the overall jump process whereas NMR can distinguish between long- and short-range motions. Interestingly by doping with 5 % and 10 % Ca the grain boundary resistance decreases.

Halide-based solid electrolyte. – Halide solid electrolytes can reach a total ionic conductivity in the range of 10^{-8} to 10^{-5} S cm^{-1}, they are stable against metallic lithium and have a good mechanical strength and mechanical flexibility that results in a high electrochemical oxidation stability, which make them promising candidates for all-solid-state batteries. They are attractive candidates also due to the monovalent anions which do not interact the same way with Li as sulfur and oxygen do.

The structure of Li_3OCl has not been studied in detail yet, but it gained great interest due to the recent publication of Braga *et al.* in 2016 that describes the anti-perovskite Li_3OCl as very powerful and promising candidate for ASSB. Li_3OCl and $Li_2(OH)Cl$ have been prepared either through a solid-state reaction and through hydrothermal reaction and characterized XRPD and NPD the structure has been untangled. It turned out that Li_3OCl rapidly decomposes to Li_2CO_3 and $LiCl{\cdot}xH_2O$, which explains the quite high ionic conductivity at room temperature. All prepared samples crystallize a orthorhomic crystal structure and can be associated to $Li_2(OH)Cl$. The sample prepared *via* hydrothermal reaction results in a cubic crystal structure. At the 8g position additional energy density has been observed that can be associated to hydrogen. Here, we were not able to synthesize H-free Li_3OCl only $Li_2(OH)Cl$ with different hydrogen contents was obtained.

Sulfide-based solid electrolyte. – A lot of sufides are known which can reach conductivities in the range of 10^{-2} S cm^{-1} at room temperature. This value is close to that of classical liquid electrolytes. In contrast to the other types of solid electrolytes, oxides and phosphates, sulfides are robust and flexible and therefore they can be densified easier.

The main topic of this thesis is based on the Argyrodite-family Li_6PS_5X (X:Cl, Br and I). Samples have been prepared through a solid-state route in argon atmosphere at 550 °C and result in compounds with cubic crystal structure. Rietveld analyzes of these samples show impurity phases $\leq$ 3 wt%. It turned out that Li_6PS_5Cl and Li_6PS_5Br have shared 4d and 4a sites with X (X:Cl or Br)

and S^{2-}, whereas the Cl-containing sample has a more disordered structure than Br. Li_6PS_5I has a fully occupied 4*d* site by I which results in a ordered structure. Furthermore the disordered sample, Li_6PS_5Cl, has only one Li site at 48*h* whereas the Br- and I- containing Argyrodite occupy the sites 24*g* and a 48*h*. The anion order/disorder in the structure greatly influences ionic conductivities. Li_6PS_5I results in a three orders of magnitude lower conductivity than the others which can be explained through the ordered crystal structure. Interestingly, NMR measurements revealed that Li_6PS_5I is as fast as Li_6PS_5Cl (and Li_6PS_5Br). Structural disorder of these samples clearly appears in NMR rate peaks, $\beta < 2$. This assymetry is also seen in the resistivity measurements. Ion dynamics in Li_6PS_5I is governed by its ordered structure, *i.e.* the fully occupied 4*d* sites and thus the lower ionic conductivity can be explained by the less frequent intercage (48*h*-48*h*) jump process.

In Li_6PS_5X also the P-diffusion can be measured by ^{31}P NMR. Concisely speaking, while halogen site disorder is beneficial for Li^+ translational dynamics, it is detrimental for fast rotational ion dynamics. Whereas for Li_6PS_5Br a high $1/\tau_{rot}$ rate does not disturb Li intercage jumps, we anticipate that the much slower rotational dynamics in Li_6PS_5Cl lead to a smaller Li ion intercage diffusivity as one might assume for this compound.

For the realization of a new, modern chemical energy storage system that are only composed of solids, many more studies of course, are needed. Especially with regard to Li ion batteries, for a better understanding of the elementary jump processes in the materials, basic research is still going on with model systems and must be carried out. Such studies serve to understand the underlying diffusion mechanisms at the atomic level. This thesis helped understanding some of the mechanistic details which seem to be important to develop new materials with tailored diffusion properties.

A final important point concerns the subsequent up-scaling of technologies from the laboratory scale to a large scale. This process includes both the processability of the components, as well as the mechanical properties, other material properties or the production. Here, material science will be facing major problems in the next few years. Despite, year after year, the problem of efficient energy storage increases tremendous progress in research and development is seen paving the way to new solid-state secondary batteries. Selected systems are already commercially available, which is a first promising sign for a possible breakthrough for these technologies.

List of Abbreviations

AC . . . . . Alternating Current

ASSB . . . . . All-Solid-State Battery

BPP . . . . . Bloembergen, Purcell and Pound

DC . . . . . Direct Current

DSC . . . . . Differential Scanning Calorimetry

EFG . . . . . Electric Field Gradient

FID . . . . . Free Induction Decay

FT . . . . . Fourier Transformation

FWHM . . . . . Full Width at Half Maximum

g.b. . . . . . Grain Boundary

GoF . . . . . Goodness of Fit

HT . . . . . High-temperature

LAGP . . . . . $Li_{1+x}Al_xGe_{2-x}(PO_4)_3$

LATP . . . . . $Li_{1.3}Al_{0.3}Ti_{1.7}(PO_4)_3$

LiPON . . . . . $Li_xPO_yN_z$

LiRAP . . . . . Lithium-rich Anti-perovskite

LiSICON . . . . . Lithium Superionic Conductor

LT . . . . . Low-temperature

LTP . . . . . $LiTi_2(PO_4)_3$

LZP . . . . . $LiZr_2(PO_4)_3$

MAS . . . . . Magic Angle Spinning

MFG-NMR . . . . Magnetic Field Gradient - NMR

MN . . . . . Motional Narrowing

MS . . . . . Mössbauer Spectroscopy

NaSICON . . . . Sodium Superionic Conductor

NMR . . . . . Nuclear Magnetic Resonance

NPD . . . . . Neutron Powder Diffraction

QENS . . . . . Quasielastic Neutron Scattering

rf . . . . . Radio Frequency

RT . . . . . Room Temperature

SAE . . . . . Spin Alignment Echo

SLR . . . . . Spin Lattice Relaxation

XRPD . . . . . X-ray Powder Diffraction

List of Symbols

$\Delta G_{\mathbf{s}}$	free surface enthalpy
γ	specific surface energy
A	area
$\Delta\gamma \cdot A$	change in surface energy
$\gamma \cdot \Delta A$	change in total surface area
t	time
$V_{\mathbf{m}}$	volume of a material
J	material flux
D	diffusion coefficient
R	gas constant
T	temperature
p	pressure
$\nabla\sigma$	sintering stress gradient
$E_{\mathbf{a}}$	activation energy
$k_{\mathbf{B}}$	Boltzmann constant
η	viscosity
$\sigma_{\mathbf{DC}}$	DC conductivity
$\sigma_{\mathbf{RT}}$	DC conductivity at room temperature
t	Goldschmidt tolerance factor
$R_{\mathbf{A}}$, $R_{\mathbf{B}}$, $R_{\mathbf{X}}$	radii of ions
$J_{\mathbf{x}}$	particle flux
x	concentration gradient
∇	Nabla operator
j	3D particle flux
c	concentration

r . . . . . radius

ΔG . . . . . Gibbs energy

τ^{-1} . . . . . jump rate

ν . . . . . frequency

ω . . . . . radial frequency

$\boldsymbol{R}$ . . . . . total displacement

$r_{\mathbf{i}}$ . . . . . individual jump

W . . . . . distribution function

d . . . . . dimensionality

f . . . . . correlation factor

$D^{\mathbf{tr}}$ . . . . . tracer diffusion coefficient

$\mu_{\mathbf{i}}$ . . . . . chemical potential

ΔH . . . . . enthalpy

$D_{\mathbf{0}}$ . . . . . pre-factor of the diffusion coefficient

ΔS . . . . . entropy

g . . . . . geometric factor

m . . . . . mass

v . . . . . velocity

e . . . . . charge of an electron

c . . . . . speed of light

λ . . . . . wavelength

$\boldsymbol{k}$ . . . . . magnitude of the wave vector

a, b, c . . . . . dimension of the unit cell

ψ . . . . . angle of the incoming beam

φ . . . . . angle of the outgoing beam

h, k, l . . . . . Miller indices

$I(hkl)$ . . . . . intensity

$S(hkl)$ . . . . . geometrical structure factor

$S(hkl)$ . . . . . structure factor

P . . . . . polarization factor

B . . . . . thickness of the grains

$\rho_{\mathbf{x,y,z}}$ . . . . . electron density

$R_{\mathbf{wp}}$ . . . . . weighted profile (fitting parameter)

$R_{\mathbf{exp}}$ . . . . . R-expected (fitting parameter)

$R_{\mathbf{Bragg}}$ . . . . . R- Bragg indices (fitting parameter)

χ . . . . . goodness of fit

R . . . . . resistance

U . . . . . voltage

I . . . . . current

$\widehat{\rho}$ . . . . . complex resistivity

ρ', ρ'' . . . . . real and imaginary part of the resistivity

C . . . . . capacity

$\widehat{\epsilon}$ . . . . . complex permittivity

ϵ', ϵ'' . . . . . real and imaginary part of the permittivity

$\widehat{M}$ . . . . . complex modulus

M', M'' . . . . . real and imaginary part of the modulus

$\widehat{Y}$ . . . . . complex addmitance

Y', Y'' . . . . . real and imaginary part of the addmitance

$\widehat{Z}$ . . . . . complex impedance

Z', Z'' . . . . . real and imaginary part of the impedance

d . . . . . thickness

φ . . . . . phase shift

νH . . . . . hopping frequency

β . . . . . symmetry factor

$H_{\mathbf{R}}$ . . . . . haven ratio

n . . . . . charge carrier density

$\mathbf{I}$ . . . . . spin quantum number

$\hbar$ . . . . . Planck´s constant

μ . . . . . magnetic moment

$\mathbf{B}_0$ . . . . . external magnetic field

m_I . . . . . magnetic quantum number

N_α, N_β . . . . . high and low energy level

N . . . . . sum of all magnetic moments

$\mathbf{M}$ . . . . . magnetization

$\mathbf{B}_1$ . . . . . linear oscillating magnetic field

$\mathbf{B}_{eff}$ . . . . . effective magnetic field

ϑ . . . . . flipping angle

R_1 **or** $1/T_1$ . . . . SLR in the laboratory frame

$R_{1\rho}$ **or** $1/T_{1\rho}$ . . . SLR in the rotating frame

eQ . . . . . electric quadropol moment

$G^{(q)}$ . . . . . correlation function

$J^{(q)}$ . . . . . spectral density function

S_2 . . . . . decay of echo amplitude

List of Figures

List of Tables

Appendices

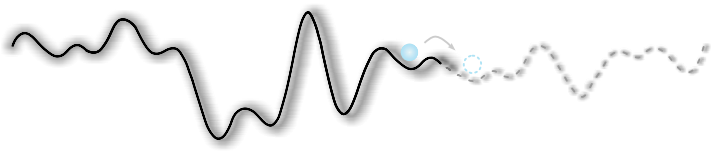

A Supporting Information

A.1 Used Equipment

Gloveboxes: MBraun Model LabMaster Pro SP, MBraun Model LabStar and GS Glovebox Typ: Alpha 2 (H_2O and O_2 < 1 ppm

Analytical balance: METTLER TOLEDO Model XA 303S and Model XA 105

Powder press and press sets: P/O/WEBER Model PW30 and SPECAC; msscientific presssets: 5 mm and 8 mm

High-energy ball mill: FRITSCH Model Pulverisette Premium line 7 with beakers made of ZrO_2 (45 mL) and ZrO_2-balls

Furnances: REETZ model LOBA 1200-45-400-1-OW tube furnace equipped with OMRON E5CK-T temperaturesensor BÜCHI glass furnance B-585 Drying Nabertherm batch furnance C290

Sputtercoater: LEICA Model EM SCD 050 with EM QSG 100 film thickness gauge

X-ray diffractometer: BRUKER D8 Advance Diffraktometer with Bragg-Brentano geometry and CuK_α radiation

Impedance spectrometer: NOVOCONTROL Model Concept 80 broadband analyzer connected to a BDS 1200 cell in combination with an active ZGS cell The temperature is controlled by a QuATRO cryo system

NMR spectrometer: Bruker Avance III 300WB connected to a shimmed cryomagnet with a magnetic field of 7 T.
Bruker Avance III Ultrashield 500WB Plus equipped with a magnet of 11 T.

NMR probe heads: teflon probe head: Bruker PH HPBBHT600WB SOL10
ceramic probe head: Bruker HP BBHT 500WB Sol5 Ceramics
For both heads a Eurotherm thermocouple was used to control the temperature

cryo probe head: HP BB LT Sol5
Temperature is controlled with a LakeShore 331 element equipped with 2 Cernox sensors

Potentiostat/Galvanostat: Biologic Science Instruments multichannel MPG-2 and VMP-3

Thermal analysis spectrometer: Netzsch STA Model STA-449F1 coupled with a QMS-403C mass spectrometer

A.2 Used Software

WinDeta 5.73: Programm to carry out all impedance experiments and export the data obtained

ZView 2.9: Software to fit impedance data, especially Nyquist plots

TopSpin 3.1: Programm to carry out all NMR measurements and export the data obtained.

X´Pert HighScore Plus 3.0: Software to analyze and visualize the X-ray powder diffraction data

Netzsch Proteus-Thermal Analysis-4.8.5 and 6.1: Software to analyze and visualize the thermal analysis and data

EC-LAB: Software to run experiments on the Biologic MPG-2 / VMP-3 potentiostat; evaluation of the data

Igor Pro 6.37: Evaluation software for processing, analysis and presentation of all data

CorelDraw X8: Graphics programm for the processing of illustration and creation of posters or presentations

Vesta 3.4.3: Software to illustrate crystal structures

EndNote X 7.3.1: Software for the management of references and the creation of bibliographies.

LaTeX / TeXnicCenter: Programm for writing texts like this dissertation or some publications

Office2013 (Word, PowerPoint): Text and/or presentation processing

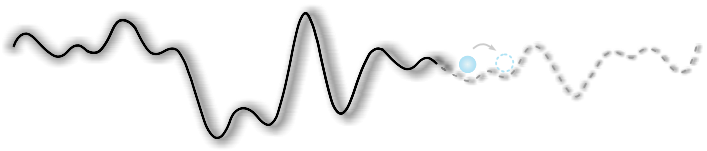

B List of Publications

B.1 Articles

Untangling the Structure and Dynamics of Lithium-Rich Anti-Perovskites Envisaged as Solid Electrolytes for Batteries

I. Hanghofer, G. J. Redhammer, S. Rohde, I. Hanzu, A. Senyshyn, H. M. R. Wilkening and D. Rettenwander, *Chemistry of Materials*, 2018, **30**, 8134–8144.

Substitutional disorder: Structure and ion dynamics of the argyrodites Li_6PS_5Cl, Li_6PS_5Br and Li_6PS_5I

I. Hanghofer, M. Brinek, S. L. Eisbacher, B. Bitschnau, M. Volck, V. Hennige, I. Hanzu, D. Rettenwander and H. M. R. Wilkening, *Phys. Chem. Chem. Phys.*, 2019, **21**, 8489–8507.

B.2 Manuscripts

Ion Dynamics in $LiZr_2(PO_4)_3$ and $Li_{1.4}Ca_{0.2}Zr_{1.8}(PO_4)_3$

I. Hanghofer, B.Gadermaier, A. Wilkening, D. Rettenwander and H. M. R. Wilkening, *in preparation*

Fast Rotational Dynamics in Argyrodite-type Li_6PS_5X (X: Cl, Br, I) as Seen by ^{31}P Nuclear Magnetic Relaxation – On Cation-Anion Coupled Transport in Thiophosphates

I. Hanghofer, B.Gadermaier and H. M. R. Wilkening, *submitted*

B.3 Oral Presentations

Ion Transport in Lithium-Argyrodites Li_6PS_5X (X: Cl, Br, I): Activation Energies, Pre-Factors, Lattice Disorder and Polarizabilities

I. Hanghofer, D. Rettenwander and M. Wilkening

DocDays 2018, 04-05.04.2018, Graz, Austria.

B.4 Poster Presentations

Synthesis and Ionic Conduction of $LiZr_2(PO_4)_3$

I. Hanghofer and M. Wilkening

21st International Conference on Solid State Ionics, 18.-23.06.2017, Padua, Italy

Structure and ion dynamics in solid electrolytes with anti-perovskite structure

I. Hanghofer, S. Rhode, D. Rettenwander and M. Wilkening

6th GÖCH-Symposium 2018: Physikalische Chemistry und Electrochemistry, 16.-17.05.2018, Graz, Austria

Ion Transport in Lithium-Argyrodites Li_6PS_5X (X: Cl, Br, I): Activation energies, Pre-Factors, Lattice Disorder and Polarizabilities

I. Hanghofer, D. Rettenwander and M. Wilkening

19th International Meeting on Lithium Batteries, 18.-22.06.2018, Kyoto, Japan

The Battery's New Clothes: Structure and Li-ion dynamics of the Crystalline Lithium-Rich Anti-Perovskites Li_3OCl and $Li_2(OH)Cl$

I. Hanghofer, S. Rhode, D. Rettenwander and M. Wilkening

19th International Meeting on Lithium Batteries, 18.-22.06.2018, Kyoto, Japan

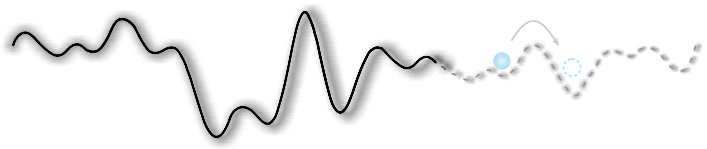

C
Complementary Information

In this chapter the supplementary information of following articles (P) and manuscripts (M) is shown:

- Untangling Structure and Dynamics of Lithium-Rich Anti-Perovskites Envisaged as Solid Electrolytes for Batteries (P1)
- Substitutional disorder: Structure and ion dynamics of the argyrodites Li_6PS_5Cl, Li_6PS_5Br and Li_6PS_5I (P2)
- Fast Rotational Dynamics in Argyrodite-type Li_6PS_5X (X: Cl, Br, I) as Seen by ^{31}P Nuclear Magnetic Relaxation – On Cation-Anion Coupled Transport in Thiophosphates (M2)

Supporting Information

Untangling Structure and Dynamics of Lithium-Rich Anti-Perovskites Envisaged as Solid Electrolytes for Batteries

Isabel Hanghofer[§], Günther J. Redhammer[§], Sebastian Rohde[§], Ilie Hanzu[§], Anatoliy Senyshyn[|], H. Martin R. Wilkening[§,*], and Daniel Rettenwander[§,*]

[§]*Graz University of Technology, Institute for Chemistry and Technology of Materials, and Christian Doppler Laboratory for Lithium Batteries Stremayrgasse 9, A-8010 Graz, Austria.*
[§]*University of Salzburg, Department of Chemistry and Physics of Materials, 5020 Salzburg, Austria.*
[|]*Heinz Maier-Leibnitz Zentrum (MLZ), Technische Universität München, 85748 Garching, Germany*

Table S1. Reports on Li-rich anti-perovskite phases published so far and the degree of experimental evidence

Compound (nominal)	Phase behavior	Methode (grade of evidence)	Reference
$Li_2(OH)Cl$	-	Thermochemical investigations (1)	[1]
$Li_2(OH)Cl$	-	Thermochemical investigations (1)	[2]
$Li_2(OH)Cl$	295 K: orthorhombic *Pmma;* $a = 7.680(8)$, $b = 4.001(7)$, $c = 3.899(6)$	Rietveld refinement on PXRD data, phase purity of the samples (4)	[3]
$Li_2(OH)Cl$	<57 °C: orthorhombic SG *Amm*2; $a = 3.8220(1)$, $b = 7.9968(2)$ $c = 7.7394(2)$ >57 °C: cubic SG; *Pm*-3*m* $a = 3.9103(1)$	Rietveld refinement of NPD, and SCXRD data combined with NMR data, phase purity of the samples (5)	[4]
$Li_2(OH)Cl$	<35 °C: orthorhombic SG *Amm*2 >35 °C: cubic SG *Pm*-3*m*	PXRD without refinement data, pattern similar to previous reports (3)	[5]
$Li_2(OH)Cl$	< 35 °C: orthorhombic SG $Pmc2_1$; $a = 3.8749(8)$, $b = 3.8257(8)$, $c = 7.999(1)$ >35 °C: cubic SG *Pm*-3*m* $a = 3.9345(1)$	Rietveld refinement on PXRD data (4)	[6]
$Li_2(OH)_{1-x}FCl_x$	with F: cubic without F: orthorhombic	PXRD, adding LiF leads to an increase of the LiCl reflexions in the PXRD pattern	[7]
$Li_2(OH)Cl$	<35 °C: orthorhombic SG *Amm*2; $a = 3.8220(1)$, $b = 7.9968(2)$ $c = 7.7394(2)$ >35 °C: cubic SG *Pm*-3*m*; $a = 3.9103(1)$	PXRD without refinement, Composition determined by ICP-OES	[8]
$Li_{2.17}(OH_{0.83})Cl$	tetragonal (<-60 °C) SG unknown cubic (> −60 °C) *Pm*-3*m*; a = 3.9135(1)	PXRD without refinement, Composition determined by ICP-OES	[8]
$Li_{1.16}(OH_{1.84})Cl$	cubic, SG *Pm*-3*m* $a = 3.9103(1)$	PXRD without refinement, Composition determined by ICP-OES	[8]
$LiCl \cdot H_2O$	orthorhombic, SG *Amm*2; $a = 7.65884(5)$, $b = 7.73813(4)$, $c = 7.67267(5)$	SCXRD and PXRD with Rietveld refinement	[9]

$Li_4(OH_3)Cl$	monoclinic, SG $P2_1/m$; a = 5.4096(8), b = 7.382(2), c = 6.2076(8), β = 94.40(1)°	SCXRD, first definitive report on this phase – proposed to be the composition previous reported as Li5(OH)2Cl3	[3]
$Li_5(OH)_2Cl_2$	-	PXRD without refinement, analysis was not possible due to the high amount of reflections, assuming its existence	[10]
$Li_5(OH)_3Cl_2$	-	PXRD without refinement, assuming its existence. LiCl reflection increase in the pattern with increasing amount of LiCl in the starting material.	[5]
$Li_3(OH)_2Cl$	-		
$Li_5(OH)_2Cl_3$	-		
$Li_3(OH)Cl_2$	-		
Li3OCl	RT: *Pm*-3*m* DSC: phase changes at 40 °C > 40 °C - tetragonal or orthorhombic	PXRD w.r.	[11]
Li_3OCl	cubic, *Pm*-3*m*: a = 3.91 Å	PXRD without refinement	[12]
$Li_{2.99}Ba_{0.005}OCl_{1-x}(OH)_x$	-	PXRD No refinement, Amount of Li5(OH)2Cl3; at 25◦C after the glass has been conditioned	[12]
$Li_{3-2x}M_xXO$ (M=Mg, Ca)	-	PXRD No refinement	[12]

Table S2: Typical bond lengths in compounds with $Pm\bar{3}m$ and *Pban* symmetry as determined from PND data at 300 K and 4 K

Sample/ T (K)	LRAP_1, 300K	LRAP_3, 4K	LRAP_3, 300K	LRAP_2, 300K
SG	$Pm\bar{3}m$	*Pban*	*Pban*	*Pban*
Li1-O1 x2 (Å)	1.9467(9)	2.0014(5)	2.0244(9)	2.0233(8)
Li1-Cl1 x2 (Å)	2.7531(6)	2.621(6)	2.511(4)	2.515(4)
Li1-Cl2 x2 (Å)	2.7531(6)	2.771(7)	2.951(5)	2.948(4)
Volume (Å^3)	19.67	19.35	19.76	19.77
OQE	1.0499	1.0394	1.0557	1.0553
OAV	0.0	5.3442	43.50	42.10
Li2-O1 x2 (Å)	--	1.9514(18)	1.938(3)	1.940(8)
Li2-Cl1 x2 (Å)	--	2.521(7)	2.73(8)	2.71(12)
Li2-Cl2 x2 (Å)	--	2.995(9)	2.80(8)	2.83(12)
Volume(Å^3)	--	19.35	19.76	19.77
OQE	--	1.0716	1.0539	1.0543
OAV	--	53.46	3.48	5.39
Li3-O1 (Å)	--	1.93(3)	1.768(19)	1.66(2)
Li3-O1 (Å)	--	2.11(3)	2.236(19)	2.26(2)
Li3-Cl2 (Å)	--	2.618(13)	2.36(7)	2.44(7)
Li3-Cl1 (Å)	--	2.124(13)	2.50(7)	2.62(7)
O1-H1 (Å)	0.863(5)	0.864(8)	0.814(11)	0.938(15)
O1-H2 (Å)	--	0.845(8)	0.937(12)	0.883(16)

Polyhedral volume, octahedral quadratic elongation (OQE) and octahedral angle variance (OAV) were calculated using VESTA.

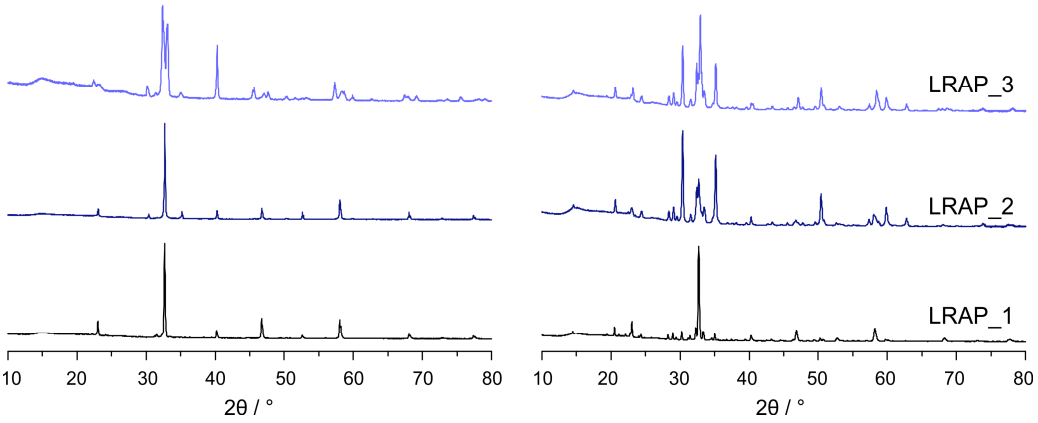

Figure S1. PXRD patterns of LRAP_1, LRAP_2, and LRAP_3, respectively, either recorded before (left) or after (right) the neutron diffraction measurements.

Model finding and refinement of structure

For $Li_2(OH)Cl$ different crystallographic settings are reported in literature: cubic, tetragonal and several orthorhombic unit cells (see Table S1). Indexing of the neutron diffraction data (300 K) of $Li_2(OH)Cl$ (sample LRAP_3) using EXPO2014[15] yields an orthorhombic cell with a = 7.74574(15) Å, b = 7.99730(15) Å and c = 3.82298(7) Å as the best matching model. This corresponds to a 2a, 2b, c setting as compared to the cubic $Pm\bar{3}m$ cell of "Li_3OCl". Using the above mentioned orthorhombic unit cell parameters, all, except two low intensity Bragg peaks at 36.7° 2θ (d = 2.45 Å) and 49.4° 2θ (d = 1.852 Å) could be indexed and refined down to low reliability values. Space group tests on the extracted intensity data were performed using JANA 2006[16], yielding a primitive unit cell with the most probable space group symmetry being *Pbna*. However, it should be noted that also good pattern matching (Le-Bail fits) refinements of data with different space groups could be achieved, using e.g. *Amm*2[8], *Pmma*, *Pmm*2, or *Pmmm* space group symmetry, while *C*-, *F*- or *I*- centered orthorhombic cells do not work at all. Metrics with larger or smaller unit cell parameters were also tested and good matching results are given in Table S3, the results for the different refinements are displayed in Figure S2.

Table S3: Lattice parameters and R_{wp} values, obtained from Le Bail fits with different lattice parameter and symmetry settings to the data of sample LRAP_3 collected at 300 K.

SG	a (Å)	b (Å)	c (Å)	R_{wp}	Reference
*I*4/*mcm*	5.4402(6)	= a	7.9912(14)	7.28	this study
$P4_2/nmc$	7.7806(9)	= a	7.5826(11)	7.07	Weiss *et al.*
*P*4/*mmm*	3.8472(4)	= a	3.9957(7)	6.98	this study
Pmma	7.64582(19)	3.99937(1)	3.87312(9)	2.41	[3]
$Pmc2_1$	3.99923(10)	3.87315(9)	7.64625(18)	2.42	[6]
*Amm*2	3.82317(8)	7.99808(13)	7.74604(16)	2.17	[4]
Pban	7.74574(15)	7.99730(15)	3.82298(7)	1.97	this study
Pmmm	7.74594(15)	7.99645(18)	3.82293(7)	1.91	[18]
Cmcm	7.74644(17)	7.64547(15)	7.9956288(17)	2.12	[19]

Good fits to the data can be achieved with the orthorhombic setting according to ref. 19, *i.e.*, with 2a, 2b, 2c body centred cell *w.r.t.* the cubic cell. However, it is also evident that tetragonal cells do not fit adequately our experimental data at room temperature. To conclude, based on pure Le-Bail fits alone, it is not possible to decide for the correct unit cell and structural setting. Thus, in the next step, using the *Cmcm*, *Pmmm*, *Pmm*2 and *Pban* symmetry, complete structure solutions were conducted. The *Amm*2 space group model was dismissed as analysis of intensity statistics clearly indicated a primitive unit cell for the 2a, 2b, c setting (see above) and first structure solutions did not yield sufficient acceptance at all.

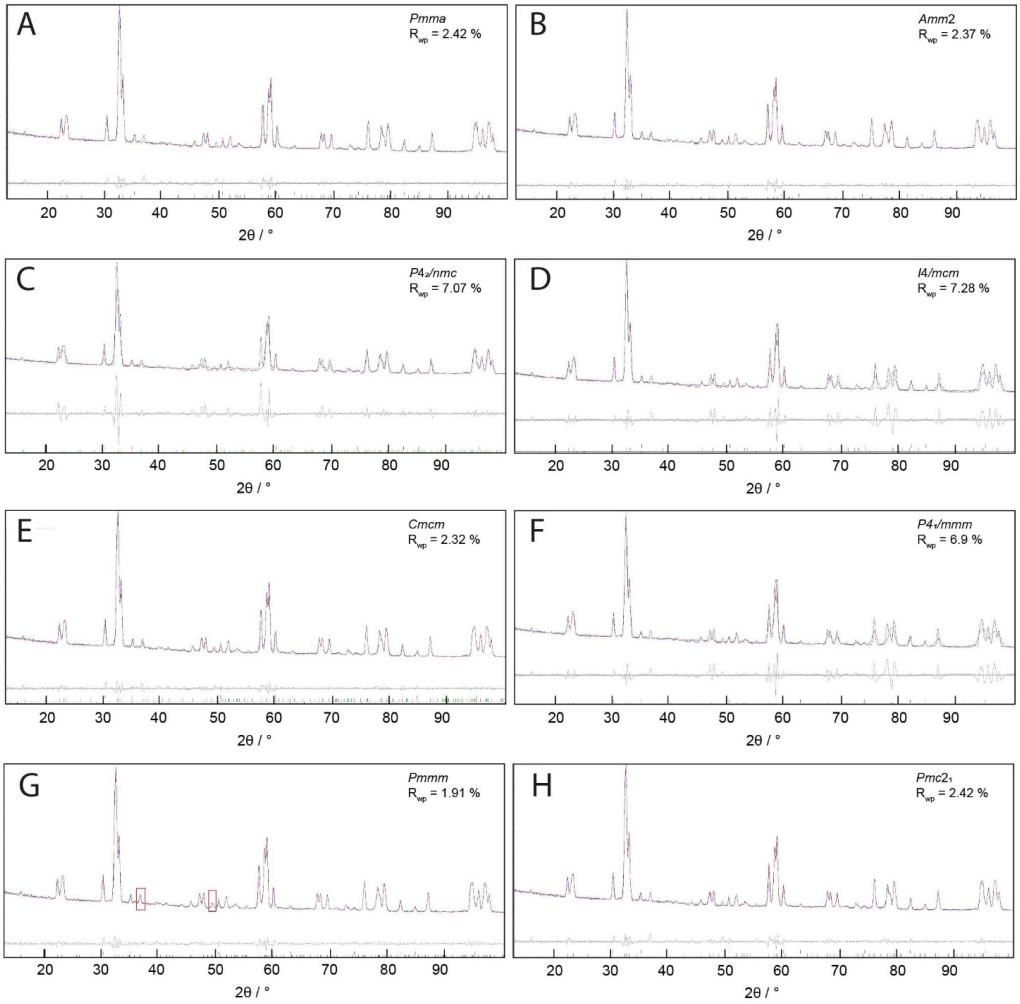

Figure S2: Sections of the diffraction pattern of LRAP_3 at 300 K; the patterns were fitted to different crystallographic settings using Le-Bail refinements, *i.e.*, without a structural model.

In structure solution/refinement it soon turned out that the best and most stable refinements to the neutron diffraction data of LRAP_3 could be obtained with the *Pban* space group symmetry. Thus, we discuss this model within the main text. For this *Pban* model, during refinement of the 300 K data of sample LRAP_3, the occupation and the isotropic equivalent atomic displacement parameters for the hydrogen atoms were restrained to have the same values. They were similar in unconstraint refinements but caused some kind of instability and slow convergence. The data recorded at 4 K were treated similarly. Additionally, it was necessary here to restrain all the atomic displacement parameters for the Li atoms to have the same value. Adequately good results, based on reliability factors, were also possible with *Pmmm* symmetry, the structural data, obtained from the refinements on sample LRAP_3 are given in Table S3.

Table S4: Fractional atomic coordinates and equivalent isotropic atomic displacement parameters for $Li_2(OH)Cl$ (LRAP_3) in *Pmmm* symmetry, S.G. 47, at 300K (*a* =7.74898(10)Å, *b* = 8.00215(12) Å, *c* = 3.82511(5) Å, R_p = 10.8, R_{wp} = 7.40 and R_{Bragg} = 2.04) and 4 K (a = 7.69718(9) Å, *b* = 7.99502(2) Å, *c* = 3.77307(4) Å, R_p = 7.90, R_{wp} = 6.51 and R_{Bragg} = 1.57).

T = 300 K	Wyckoff	*x*	*y*	*z*	$B_{equ.}$	occ
Cl1	1*a*	0	0	0	1.62(14)	0.125
Cl2	1*b*	½	0	0	1.46(13)	0.125
Cl3	1*e*	0	½	0	2.48(14)	0.125
Cl4	1*f*	½	½	0	0.85(10)	0.125
O1	4*z*	0.2517(9)	0.2413(5)	½	1.29(4)	0.5
Li1	2*j*	0.248(5)	0	½	2.8(3)	0.25
Li2	2*l*	0.3077(18)	½	½	0.93(16)	0.25
Li3	2*p*	½	0.241(5)	½	3.9(4)	0.228(9)
Li4	4*y*	0.3178(12)	0.2189(18)	0	0.7(4)	0.263(12)
H1	8α	0.1974(20)	0.275(3)	0.288(4)	3.5(3)	0.253(4)
H2	8α	0.3185(21)	0.264(4)	0.362(4)	3.5(3)	0.253(4)
T = 4 K						
Cl1	1*a*	0	0	0	1.21(10)	0.125
Cl2	1*b*	½	0	0	1.05(10)	0.125
Cl3	1*e*	0	0.5	0	0.58(9)	0.125
Cl4	1*f*	½	½	0	2.76(16)	0.125
O1	4*z*	0.2521(8)	0.2426(8)	½	1.84(5)	0.5
Li1	2*j*	0.2129(23)	0	½	0.68(18)	0.25
Li2	2*l*	0.277(5)	0.5	½	3.7(2)	0.25
Li3	2*p*	½	0.247(6)	½	3.7(2)	0.219(7)
Li4	4*y*	0.3148(15)	0.239(5)	0	3.7(2)	0.255(9)
Li5	2*m*	0	0.283(3)	0	3.7(2)	0.154(7)
H1	8α	0.2133(12)	0.2840(12)	0.3128(22)	1.2(2)	0.222(3)
H2	8α	0.3389(11)	0.2630(24)	0.3852(22)	1.2(2)	0.222(3)

The two models are almost the same, the largest difference is a shift of the Cl atom into the origin to special positions 1*a* to 1*f* (Table S3). Close to the Li4 atom residual nuclear density was observed, which, however, could not be refined. This suggests a disorder of Li over two possible positions, which are close to each other. In the *Pban* model these two positions, over which Li seems to disorder, are related to each other by symmetry. Hence, they can be modelled properly. This is the main reason why the latter model is favoured over the other.

From inspection of the two "good working" models it is evident that O1 and Li1 atoms are displaced from each other along the **b** direction, thus they do not form a straight "line" along the **a** direction (marked by arrows in Figure S3). A similar behaviour is seen along the **a** direction with respect to O1 and Li2 atomic positions. Moreover, the Li3 atoms (for the the *Pban* model) are displaced also from special to more general positions and disordered. Taken together, this forces both the *a* and *b* unit cell dimensions to double; along *c* no such displacement is observed. From this structural evidence we conclude that the orthorhombic setting with the 2*a*, 2*b*, *c* cell setting *w.r.t.* the cubic parent cell is the most probable and correct one.

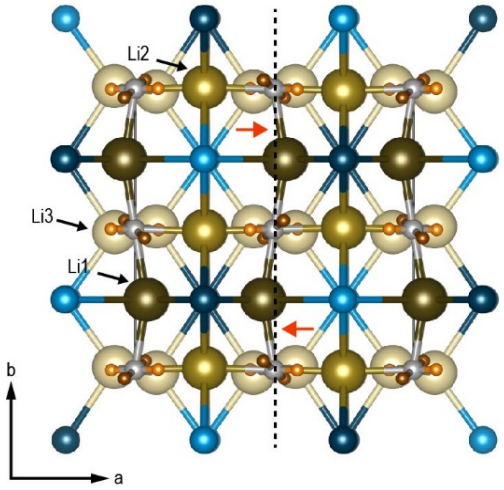

Figure S3: Structure of $Li_2(OH)Cl$ in the *Pban* symmetry in a projection along the *c*-axis. Illustration of the displacements of the Li1, Li2 and Li3 atoms forcing the doubling of *a* and *b* unit cell dimensions with respect to the cubic cell.

For all other space group symmetries, including *Cmcm*, (more) unstable refinements were obtained and *R*-values are distinctly larger. In particular, the Li and H positions could be identified from their negative nuclear densities in difference Fourier analysis. They could, however, could not be refined independently and the structural models partly differ distinctly depending on the refinement strategy. Some of the refinements do not properly converge.

Besides the main component $Li_2(OH)Cl$, the LRAP_3 sample, investigated by ND, contained small amounts of LiCl (9 wt. %). Despite the model used for $Li_2(OH)Cl$, and even if intensity should be allowed with the chosen space group symmetry (*e.g.*, in *Pban*, *Pmm2*, *Pmmm*, *Cmcm*), two reflections at 36.8° 2θ and 49.5° 2θ, respectively, could not be included in any of the refinements. They, however, can be matched with the unit cell parameters of the newly reported phase $LiCl \cdot 2\ H_2O$[20] although it was not possible to use the complete structural model of this compound. We assume that the impurity observed is $LiCl \cdot xH_2O$. It is similar, but structurally not exactly identical with the hydrate $LiCl \cdot 2H_2O$. This holds for both samples investigated. The hypothesis about an additional impurity, which arose during transport of the sample to the neutron source, is supported by the fact that in the samples that were characterized immediately after synthesis by XRD these reflections are absent, see Figure S4.

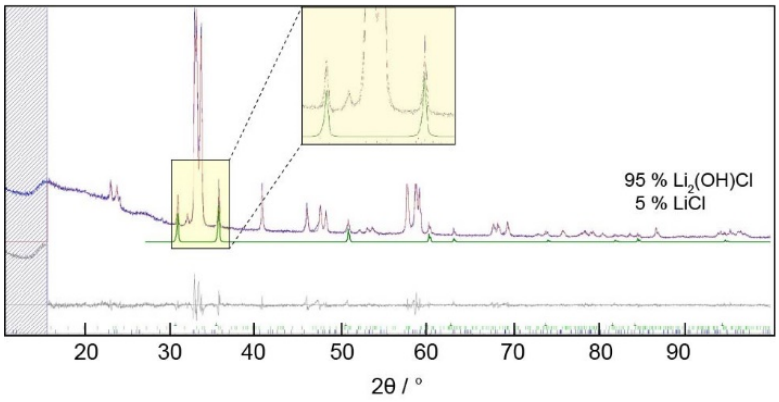

Figure S4: Result of the refinement of the LRAP_3 sample immediately after it has been synthesized.

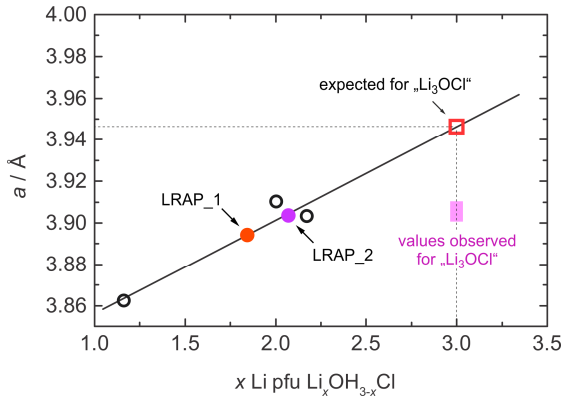

Figure S5. Experimentally probed lattice constant a of $Li_xOH_{3-x}Cl$ as a function of x Li per formula unit (pfu). For "Li_3OCl" one would expect $a \approx 3.95$ Å which has, to our knowledge, never been reported before by any structure refinement.[7,12]

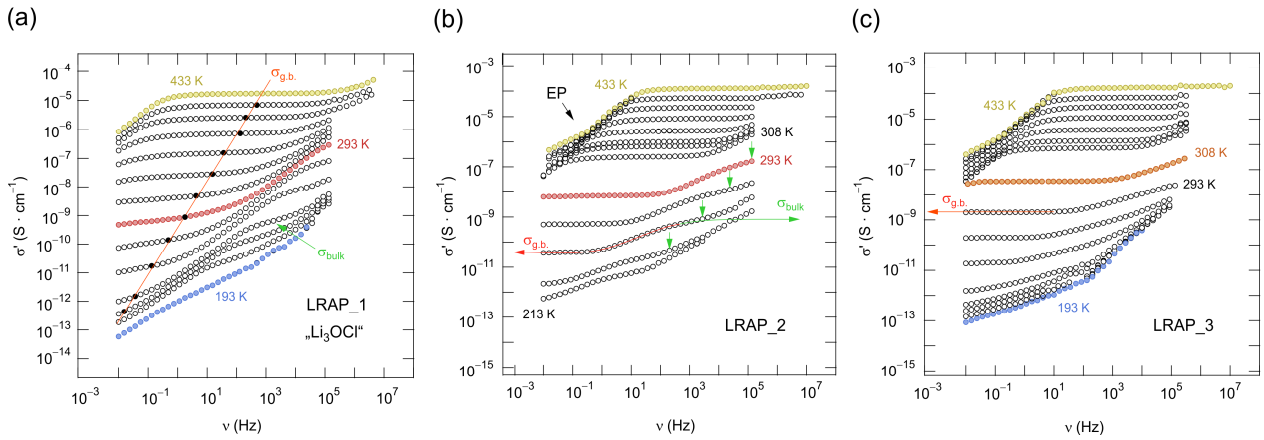

Figure S6: Conductivity isotherms of the hydrothermally synthesized samples LRAP_1 (a) and LRAP_2 (b). In (c) the electrical response of LiRAP_3 is shown that has been prepared via prepared via solid state reaction. Frequencies range from 10 mHz to 10 MHz; the measurements cover a temperature range from 193 K to 473 K in steps of 20 K. To monitor the change in impedance where the phase transition occurs additional isotherms were recorded at 208 K, 218 K, 308 K and 318 K. The broadband conductivity spectra of LRAP_1 and LRAP_2 exhibit two so-called frequency-independent plateaus. The first, seen at intermediate temperatures in the low frequency limit represent long-range ion transport which is usually identified as the direct current (dc) conductivity. Here, it represents the overall conductivity that is determined by the g.b. response; the solid line in (a) illustrates the change in σ_{dc} with temperature. With increasing frequency the dc-plateau of the isotherms passes into a dispersive region which finally reaches a second plateau, see the solid line in (b). From the saddle point seen we estimated bulk conductivities, *cf.* the vertical arrows. At even higher frequencies the isotherms reach the dispersive part of σ_{bulk}. In the ideal case the two plateaus correspond to two semicircles in the Nyquist ($-Z''$ vs. Z') representation, which yield $1/\sigma_{bulk}$ (and $1/\sigma_{g.b.}$) as the intercept with the Z' axis. The latter is only possible after appropriate simulation of the data in the complex plane representation with suitable equivalent circuits. As is well-known, this procedure is often fraught with difficulties since, as it is also in the present case, depressed, intertwined semicircles are obtained if correlation effects are present. Note that at the highest temperatures and the lowest frequencies ion transport is fast enough in order that the charge carriers pile up in front of the ion-blocking electrodes applied. Well-known electrode polarization (EP) causes σ' to decrease in this region, see (b).

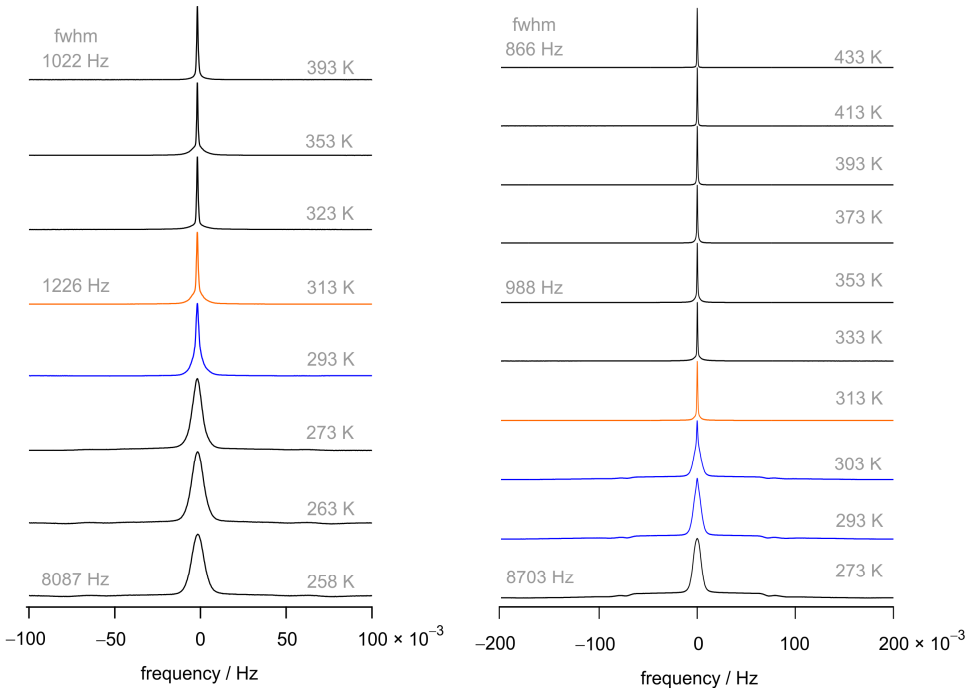

Figure S7: ^{7}Li NMR spectra of LiRAP_1 (left) and LiRAP_3 (right) recorded under static conditions at the temperatures indicated. At low T the central line is dipolarly broadened because of slow Li exchange. For LiRAP_3 we see a (first-order) quadrupole powder pattern as expected for a spin-3/2 nucleus such as ^{7}Li when the spin interacts with a non-vanishing electric field gradient. At ca. 300 K the line heterogeneously narrows indicating the phase transition from orthorhombic to cubic structure. A sharp NMR line is in agreement with Li ion exchange rates being sufficiently fast to average homonuclear dipole-dipole interactions. This observation is in agreement with the jump in electrical conductivity by 2-3 orders of magnitude, see Figure 5 c). A similar, but less pronounced, increase is seen for LiRAP_1. fwhm denotes full width at half maximum and illustrates the change in line width when going from very low to higher temperatures.

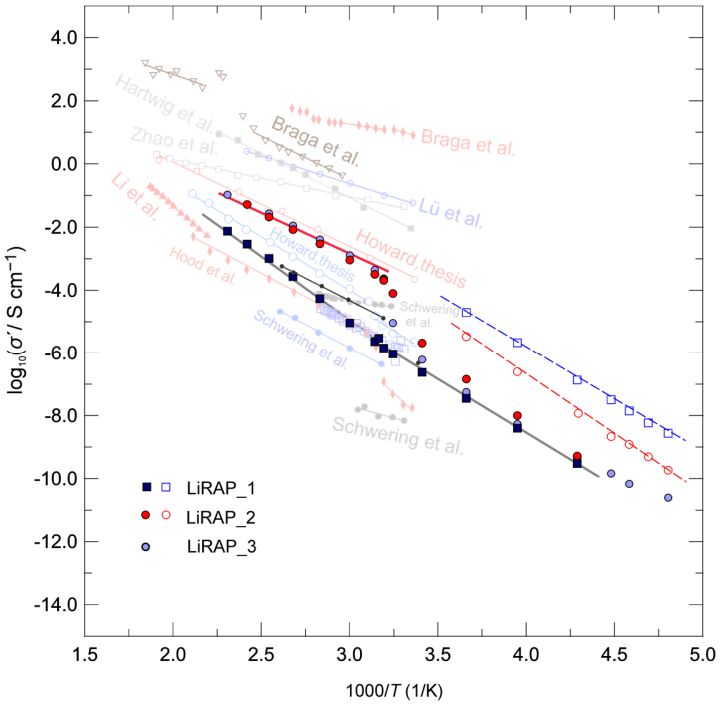

Figure S8: Comparison of conductivity data of the 3 samples investigated in this study with results presented in literature (see Refs. 5-8, 10-14). Here, the logarithm of the real part of the complex impedance σ is plotted as a function of the inverse temperature. Solid lines are to guide the eye.

References

(1) Scarpa G.; Atti R. Thermal analysis of the mixture of the alkali hydroxides with the corresponding halides. *Accad. Naz. Lincci, Sez. II*, **1915**, 24, 476.

(2) Reshcrnikov, N. A.; Unzhakov, G. M. Diagrammy plavkosti sistem LiOH-LiCl, LiOH-NaOH. *Zh. Neorg. Khim.* **1958**, 3, 1433.

(3) Berlange, H.; Jacobs, H.; Ungewöhnliche Koordinationspolyeder um Sauerstoff in $Li_4Cl(OH)_3$*Z. Anorg. Allg. Chem.,* **1994**, *620*, 471-474.

(4) Eilbracht, C.; Kockelmann, W.; Hohlwein, D.; Jacobs, H. *Proceedings of the First European Conference on Neutron Scattering. Phys. B*, **1997**, *234*, 48-50.

(5) Hood, Z. D., Wang, H.; Samuthira Pandian, A.; Keum, J. K. Liang, C. Li_2OHCl Crystalline electrolyte for stable metallic Lithium anodes. *J. Am. Chem. Soc.*, **2016**, *138*, 1768-1771.

(6) Howard, J.; Hood, Z. D.; Holzwarth, N. A. W. Fundamental aspects of the structural and electrolyte properties of Li_2OHCl from simulations and experiment. *Phys. Rev. Mater.,* **2017**, *1*, 075406.

(7) Li, Y.; Zhou, W.; Xin, S.; Li, S.; Zhu, J.; Lü, X.; Cui, Z.; Jia, Q.; Zhou, J.; Zhao, Y.; Goodenough, J. B Fluorine-doped anti-perovskite electrolyte for all-solid-state Lithium-ion batteries. *Angew. Chem. Int. Ed.*, **2016**, *128*, 9965-9968.

(8) Schwering, G.; Hönnerscheid, A.; van Wüllen, L.: Jansen, M. High Lithium ionic conductivity in the Lithium halide hydrates $Li_{3-n}(OH_n)Cl$ $(0.83 \leq n \leq 2)$ and $Li_{3-n}(OH_n)Br$ $(1 \leq n \leq 2)$ at ambient temperatures. *ChemPhysChem,* **2003**, *4*, 343-348.

(9) Hönnerscheid, A.; Nuss, J.; Mühle, C.; Jansen, M. Die Kristallstrukturen der Hydroxyhalogenide $Li_4(OH)_3Br$ und $Li_4(OH)_3I$. *Z. Anorg. Allg. Chem.,* **2003**, *629*, 312-316.

(10) Hartwig, P.; Rabenau, A.; Weppner, W. *J.* Lithium hydroxide halides: phase equilibria and ionic conductivities. *Less-Common Metals*, **1981**, *78*, 227-233.

(11) Zhao, Y.; Daemen, L. L. Superionic conductivity in Lithium-rich anti-perovskites. *J. Am. Chem. Soc.* **2012**, *134*, 15042-15047.

(12) Braga, M. H.; Ferreira, J. A.; Stockhausen, V.; Oliveirad J. E.; El-Azabe, A. Novel Li_3ClO based glasses with superionic properties for lithium batteries. *J. Mater. Chem. A*, **2014**, *2*, 5470-5480.

(13) Howard, J.W. Doctoral Dissertation (retrieved from ProQuest Dissertations and Theses. No. 3686123).

(14) Lü, X.; Wu, G..; Howard, J. W.; Chen, A.; Zhao, Y.; Daemen, L. L.; Jia, Q. Li-rich anti-perovskite Li_3OCl films with enhanced ionic conductivity. *Chem. Comm.* **2014**, *50*, 11520-11522.

(15) Altomare, A.; Cuocci, C.; Giacovazzo, C.; Moliterni, A.; Rizzi, R.; Corriero, N.; Falcicchio, A. A. EXPO2013: a kit of tools for phasing crystal structures from powder data. *J. Appl. Cryst.* **2013**, *46*, 1231-1235.

(16) Petříček, V.; Dusek, M.; Palatinus, L. Crystallographic Computing System JANA2006: General features. *Z. Kristallogr*. **2014**, *229*, 345-352.

(18) Song, A.-Y.; Xiao, Y.; Turcheniuk, K.; Upadhya, P.; Ramanujapuram, A.; Benson, J.; Magasinski, A.; Olguin, M.; Meda, L.; Borodin, O.; Yushin, G. Ion conductivities: Protons enhance conductivities in Lithium halide hydroxide/lithium oxyhalide solid electrolytes by forming rotating hydroxy groups. *Adv. Energy Mater.* **2018**, *8*, 1700971.

(19) Lerner; H.-W.; Bolte, M. An orthorhombic modification of lithium chloride monohydrate. *Acta Cryst. Sec. E* **2003**, *59*, i20-i21.

(20) Sohr, J.; Schmidt. H.; Voigt, W. Higher hydrates of lithium chloride, lithium bromide and lithium iodide. *Acta Cryst. Sec. C*, **2018**, *74*, 194-202.

Substitutional disorder: Structure and ion dynamics of the argyrodites Li_6PS_5Cl, Li_6PS_5Br and Li_6PS_5I

I. Hanghofer,*[a] M. Brinek,[a] S. L. Eisbacher,[a] Brigitte Bitschnau,[b] M. Volck,[c] V. Hennige,[c] I. Hanzu,[a,d] Daniel Rettenwander,[a] and H. M. R. Wilkening*[a,d]

[a] *Christian Doppler Laboratory for Lithium Batteries and Institute for Chemistry and Technology of Materials, Graz University of Technology (NAWI Graz), Stremayrgasse 9, 8010 Graz, Austria.*

[b] *Institute of Physical and Theoretical Chemistry, Graz University of Technology, Stremayrgasse 9, 8010 Graz, Austria*

[c] *AVL List GmbH, 8020 Graz, Austria*

[d] *Alistore-ERI European Research Institute, 33 rue Saint Leu, 80039 Amiens, France.*

E-Mail: wilkening@tugraz.at; E-Mail: isabel.hanghofer@tugraz.at

The electronic supporting information contains results from Rietveld analyses (Figs S1, S2) and further information on NMR settings (Table S1); ^{35}Cl, ^{79}Br and ^{127}I MAS NMR spectra are shown in Fig. S3.

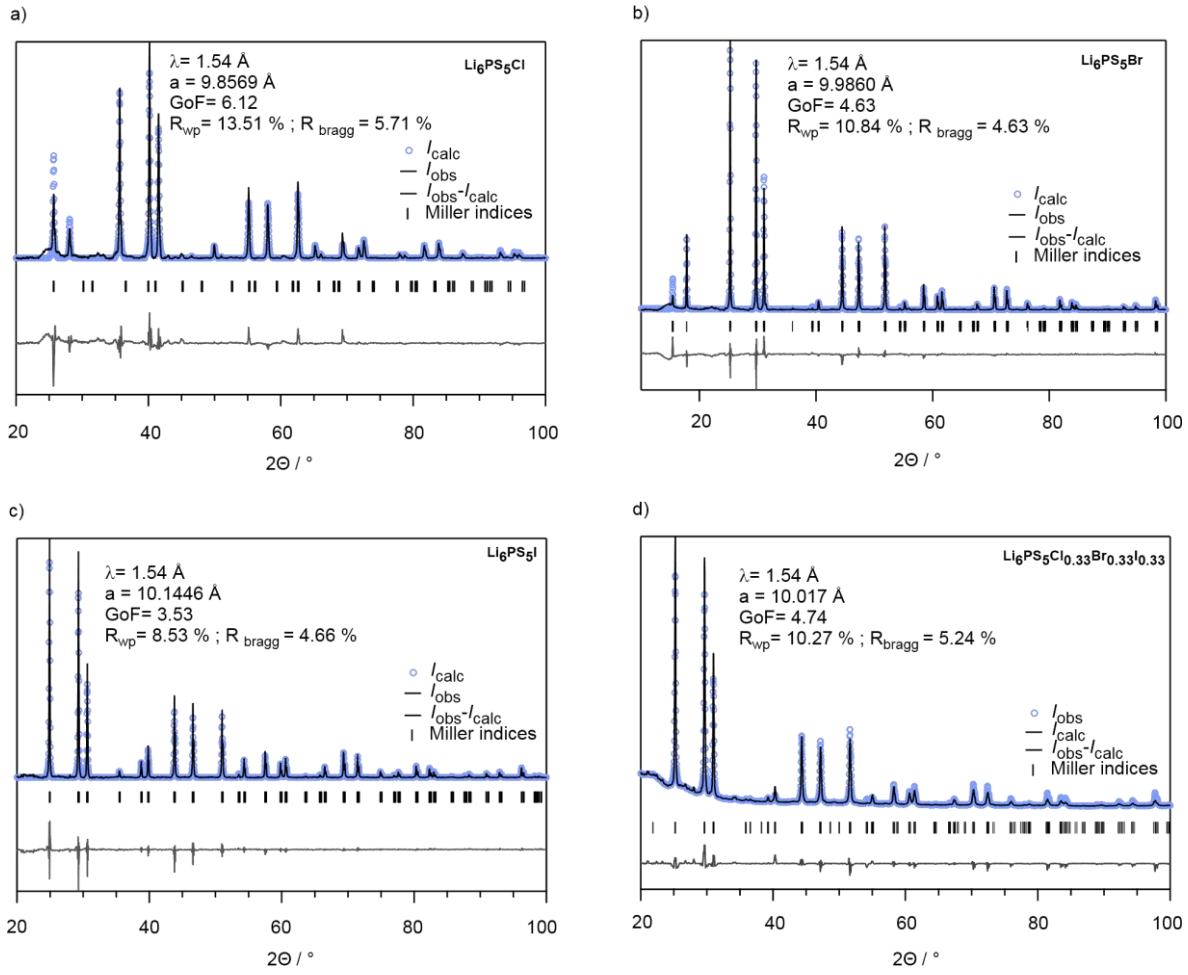

Fig. S1 Crystallographic data of Li_6PS_5Br, Li_6PS_5Cl, Li_6PS_5I, and $Li_6PS_5Cl_{0.50}Br_{0.50}$ obtained from X-ray powder diffraction. GoF means goodness of fit (GoF), the weighted *R*-profile (R_{wp}) and the *R*-Bragg (R_{Bragg}) values are also included. The differential plot as well as the hkl indices are shown, too. The hump at approximately 25° is due to the mercatpo foil, which was used for the measurement

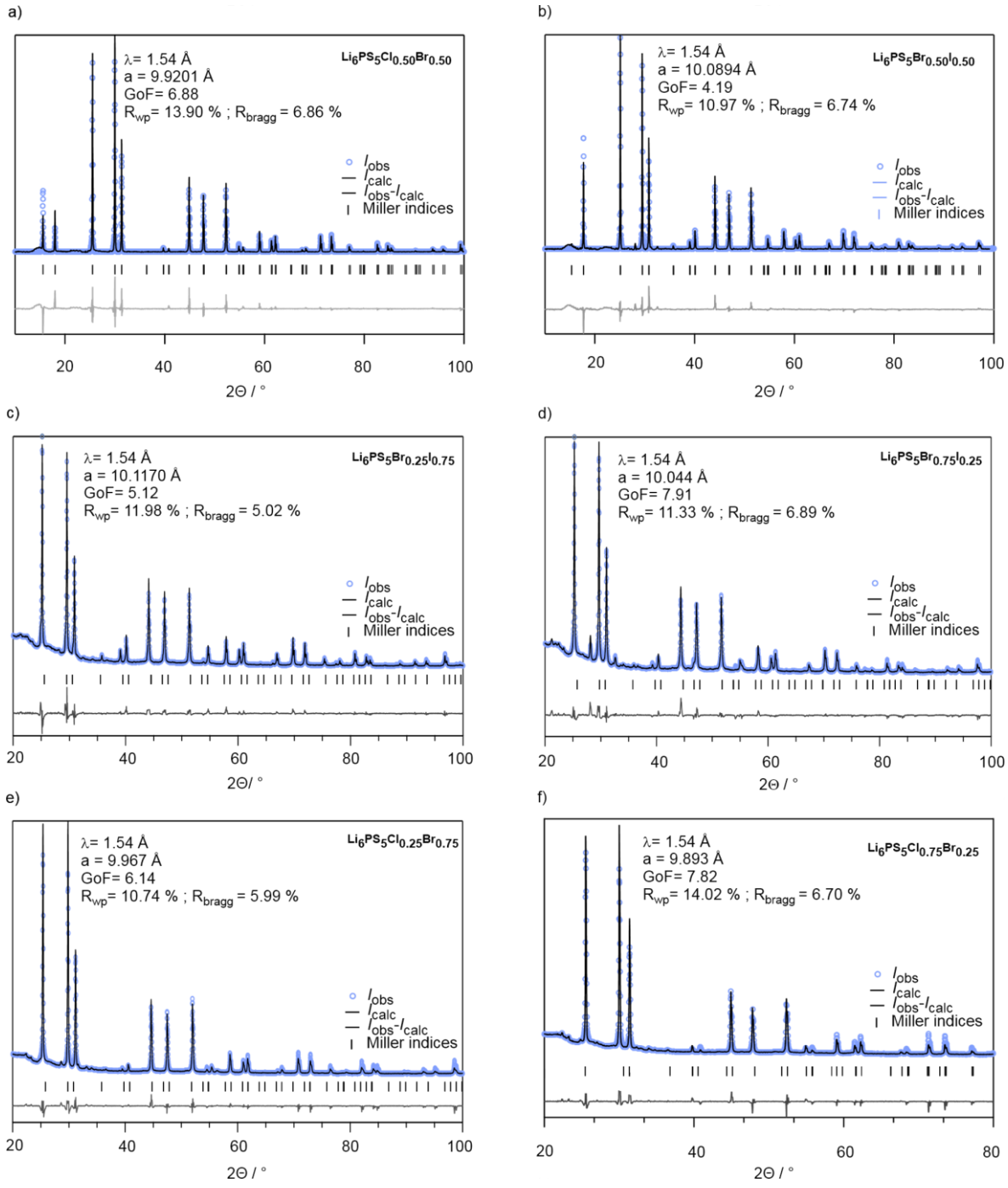

Fig. S2 X-ray powder diffraction patterns and crystallographic data from Rietveld analyses of the Li-argyrodites indicated. As in Fig. S1, GoF means goodness of fit (GoF), the weighted *R*-profile (R_{wp}) and the *R*-Bragg (R_{Bragg}) values are also shown. The differential plot as well as the hkl indices are included, too. The hump at approximately 25° is due to the mercatpo foil, which was used for the measurement

In Table **S1** the experimental settings of the magic angle spinning (MAS) NMR measurements are shown; The table includes pulse lengths and delay times for the ^{6}Li, ^{31}P, ^{35}Cl, ^{79}Br and ^{127}I NMR spectra. In Fig. S1 the corresponding spectra of ^{35}Cl, ^{79}Br and ^{127}I of Li_6PS_5X (X: Cl, Br and I) are presented.

Table S1: Settings to record the MAS NMR spectra of the argyrodites Li_6PS_5Cl, Li_6PS_5Br and Li_6PS_5I, respectively. The pulse length varies from 1 to 4.5 µs and the delay time from 1 s up to 180 s.

sample	measurement	pulse length	delay time
Li_6PS_5Cl	^{6}Li	3.0 µs	10 s
	^{31}P	1.0 µs	10 s
	^{35}Cl	4.5 µs	1 s
Li_6PS_5Br	^{6}Li	3.0 µs	10 s
	^{31}P	1.0 µs	30 s
	^{79}Br	1.3 µs	1.4 s
Li_6PS_5I	^{6}Li	3.0 µs	10 s
	^{31}P	2.0 µs	180 s
	^{127}I	3.0 µs	1 s

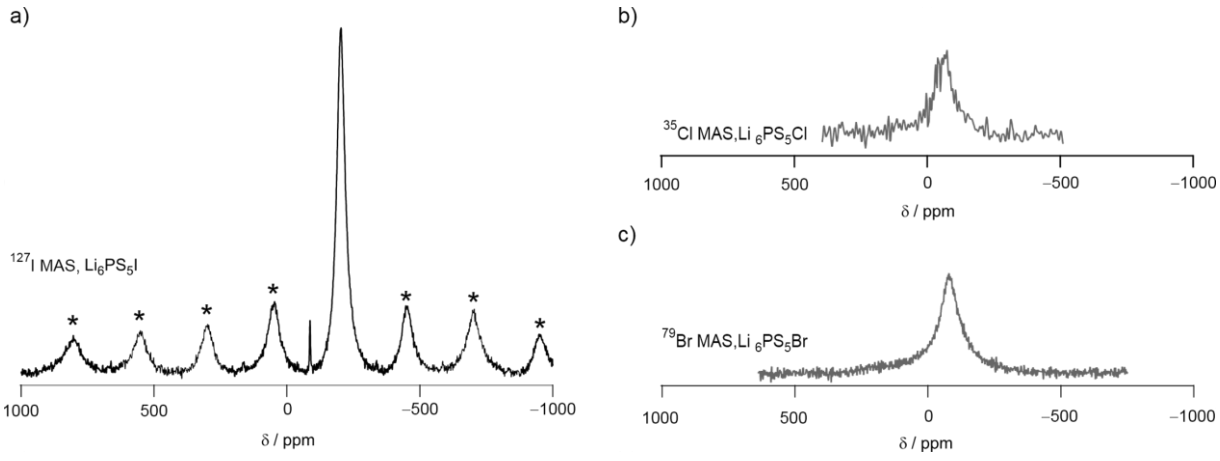

Fig. S3 ^{35}Cl, ^{79}Br and ^{127}I MAS NMR spectra. Asterisks, see the NMR spectrum of Li_6PS_5I, denote spinning sidebands. The narrow line at − 86.4 ppm shows a negligible impurity phase.

Supporting Information

Fast Rotational Dynamics in Argyrodite-type Li_6PS_5X (X: Cl, Br, I) as Seen by ^{31}P Nuclear Magnetic Relaxation — On Cation-Anion Coupled Transport in Thiophosphates

Isabel Hanghofer,* Bernhard Gadermaier and H. Martin R. Wilkening*

Graz University of Technology, Institute for Chemistry and Technology of Materials (NAWI Graz), and Christian Doppler Laboratory for Lithium Batteries, Stremayrgasse 9, A-8010 Graz, Austria.

Corresponding Authors

*wilkening@tugraz.at; isabel.hanghofer@tugraz.at

The quality of the samples investigated was confirmed by X-ray powder diffraction. The corresponding patterns of Li_6PS_5X (X = Cl, Br, I) are shown in Figure S1. Rietveld refinements reveal phase pure samples with only marginal or no contaminations by the starting materials. See Ref. [1] for further information.

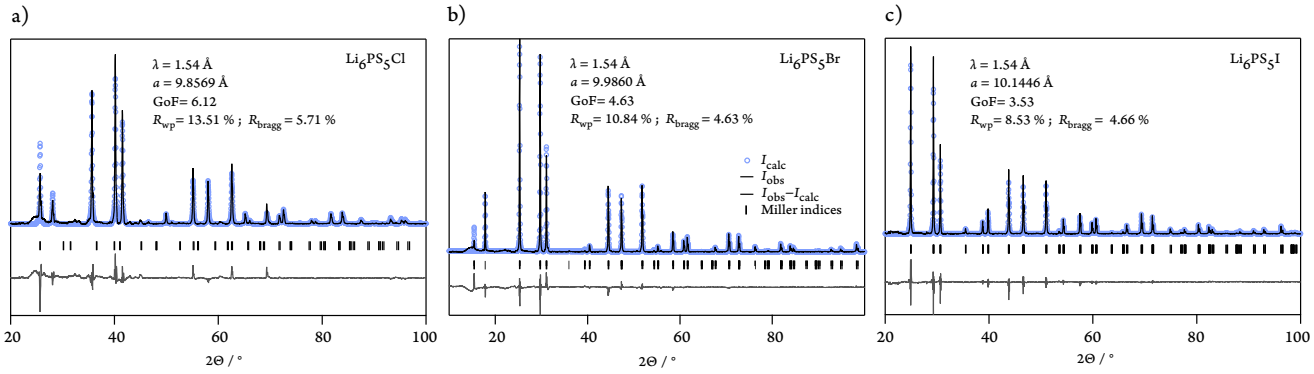

Figure S1 X-ray powder diffraction pattern of Li_6PS_5X (X = Cl, Br, I), see also Ref. [1]. GoF means goodness of fit (GoF), the weighted R-profile (R_{wp}) and the *R*-Bragg (R_{Bragg}) values are also included. The differential plot as well as the hkl indices are shown, too.

^{31}P magic angle spinning (MAS) NMR spectra (see Figure S2a) of Li_6PS_5X (X = Cl, Br, I) reveal a single, sharp line for Li_6PS_5I and confirm its ordered anion lattice. For Li_6PS_5Br several ^{31}P resonances are seen showing a semi-ordered structure. This finding is in stark contrast to Li_6PS_5Cl for which a broad resonance is detected that clearly reveal strong halogen disorder, see also Ref. [1]. ^{6}Li NMR spectra (Figure S2b) reveal both the effect of structural disorder (Li_6PS_5Br, Li_6PS_5Cl) and Li^+ translational motions; for X = I the line is broader as it is less effected by intracage jumps that can effectively reduce residual dipolar contributions that broaden the line but were not eliminated by magic angle spinning.

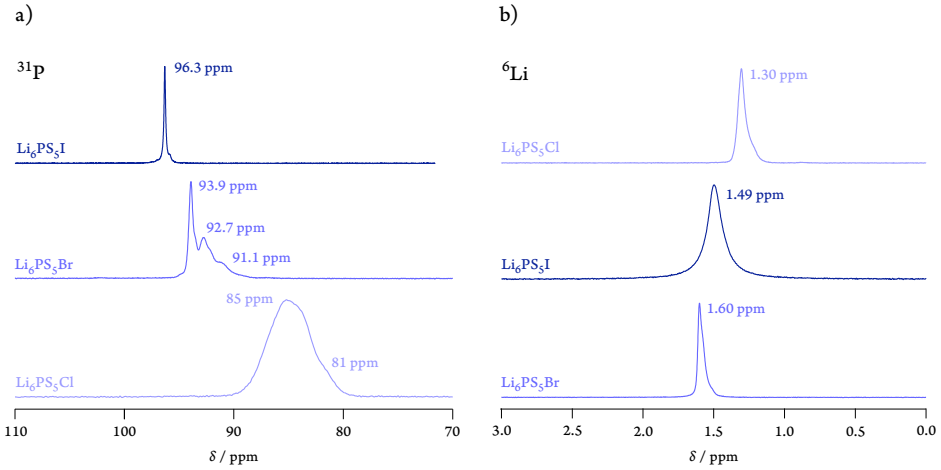

Figure S2 ^{31}P MAS NMR spectra recorded, with a single pulse experiment, using an Avance III NMR spectrometer (Bruker BioSpin). The resonance frequency was 202.4 MHz. We used 2.5-mm rotors to acquire the spectra at a spinning speed of 25 kHz. H_3PO_4 (85 %) served as reference to determine chemical shifts δ_{iso}. ^{6}Li MAS NMR spectra were recorded under the same conditions but at a resonance frequency of 73.6 MHz. The spectra were referenced to crystalline lithium acetate. Data taken from Ref. [1].

To analyze the ^{7}Li and ^{31}P NMR $R_1(1/T)$ rate peaks we used Lorentzian-shaped spectral densities (see eqn. (1)) according to Bloembergen, Purcell and Pound to describe 3D diffusion in Li_6PS_5X [2]. A single term, for each ^{31}P rate peak seen for X = I and X = Br, served as a good approximation to determine activation energies E_a and pre-exponential factors $1/\tau_0$. In general, the relaxation rate R_1 depends on both temperature T and frequency ω_0, $R_1 = f(\omega_0, T)$, see also Refs. [3, 4] for a short introduction. R_1 is directly proportional to $J(\omega_0, T)$ which is the spectral density function describing the temporal magnetic dipolar and electric quadrupolar spin fluctuations. Here, for $J(\omega_0, T)$ we used $R_1(\omega_0, T) \propto J_i^{3D}(\omega_0, T) \propto \Sigma_i \{\tau_{c,i} / [1+(\omega_0 \tau_{c,i})^{\beta}]\}$ with $i = 1, 2$ for ^{31}P NMR. J is the Fourier transform of the motional correlation function $G_i(t)$. If G is a pure exponential a Lorentzian-shaped function J results, *i.e.*, the asymmetry parameter $\beta = 2$. Deviations from exponential behavior result in $\beta < 2$ and point to correlation effects, such as disorder and Coulomb interactions, that govern the shape of J and, thus, that of the rate peak $R_1(1/T)$. The activation energies of the two flnaks in case of an asymmetric rate peak are connected to each other via $E_{a,low} = (\beta - 1)\, E_{a,high}$. As an example, for peak (1) of Li_6PS_5I we obtained $E_{a,high} = 0.2$ eV, whereas $E_{a,low} = 0.15$ eV. The latter value characterizes short-range or local motions when translational ion dynamics are considered.

In general, on the low-T side of the peak, *i.e.*, in the limiting case $\omega_0 \tau_c \gg 1$, we have $R_1 \propto \tau_c^{-1} \omega_0^{-\beta}$, whereas for $\omega_0 \tau_c \ll 1$, that is, on the high temperature flank of $R_1(1/T)$, $R_1 \propto \tau_c$ is valid. For τ_c we assume Arrhenius temperature behavior according to $\tau_c = \tau_{c,0} \times \exp[E_a/(k_B T)]$, where E_a is the activation energy and k_B Boltzmann's constant. $1/\tau_{c,0}$ denotes the pre-exponential factor (or "attempt frequency"), which, typically, takes values in the order of phonon frequencies, of course depending on dimensionality effects and entropy effects. In Table S1 the fitting results are summarized.

Table S1. Fitting results obtained by analyzing the ^{7}Li and ^{31}P NMR rate peaks. For ^{31}P NMR two rate peaks ($i = 1, 2$) are obtained for ^{31}P SLR NMR if we consider the compounds with X = Br and X = I. $E_a = E_{a,high}$, values for $E_{a,low}$ are included in Figure 2.

Sample	^{7}Li			^{31}P					
	E_a	$1/\tau_{c,0}$	β	$E_{a,1}$	$1/\tau_{c,0}$	β_1	$E_{a,2\,(Li)}$		β_2
Li_6PS_5Cl	0.32 eV	7.7×10^{13} s^{-1}	1.53	0.18 eV[a]	2.0×10^{12} s^{-1}	2	–		–
Li_6PS_5Br	0.21 eV	4.4×10^{12} s^{-1}	1.48	0.15 eV[b]	1.1×10^{12} s^{-1}	1.59	0.14 eV	1.1×10^{11} s^{-1}	2
Li_6PS_5I	0.20 eV	1.2×10^{12} s^{-1}	1.92	0.20 eV	1.8×10^{13} s^{-1}	1.74	0.18 eV	2.9×10^{11} s^{-1}	2

[a] This value is just an apparent one, as the high-temperature flank is a superposition of two rate peaks belonging to rotational PS_4^{3-} and translational Li^+ dynamics.
[b] The low-temperature flank is characterized by a very low activation energy of only 0.08 eV for rotational motions.

References

[1] Hanghofer I., Brinek M., Eisbacher S., Bitschnau B., Volck M., Hennige V., Hanzu I., Rettenwander D., Wilkening, H.M.R. Substitutional disorder: Structure and Ion Dynamics of the Argyrodites Li_6PS_5Cl, Li_6PS_5Br and Li_6PS_5I. *Phys. Chem. Chem. Phys.* **2019**, DOI: 10.1039/C9CP00664H.

[2] N. Bloembergen N., Purcell E.M., Pound R.V. Relaxation Effects in Nuclear Magnetic Resonance Absorption. *Phys. Rev.* **1948**, *73*, 679–712.

[3] Epp V., Gün O., Deiseroth H.-J., Wilkening, M. Long-Range Li^+ Dynamics in the Lithium Argyrodite Li_7PSe_6 as Probed by Rotating-Frame Spin-Lattice Relaxation NMR, *Phys. Chem. Chem. Phys.* **2013**, *15*, 7123–7132.

[4] Uitz M., Epp V., Bottke P., Wilkening M. Ion Dynamics in Solid Electrolytes for Lithium Batteries: Probing Jump Rates and Activation Energies through Time-Domain Li NMR. *J. Electroceram.* **2017**, *38*, 142–156.

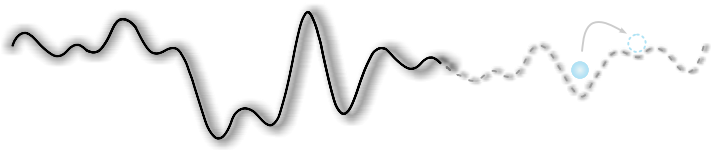

D
Bibliography

[1] R. Korthauer, *Handbuch Lithium-Ionen-Batterien*, Springer, Berlin, 2013.

[2] J.-M. Tarascon, *ChemSusChem*, 2008, **1**, 777–779.

[3] Z. Yang, J. Zhang, M. C. W. Kintner-Meyer, X. Lu, D. Choi, J. P. Lemmon and J. Liu, *Chem. Rev.*, 2011, **111**, 3577–3613.

[4] J.-M. Tarascon and M. Armand, *Nature*, 2001, **414**, 359–367.

[5] E. Quartarone and P. Mustarelli, *Chem. Soc. Rev.*, 2011, **40**, 2525–2540.

[6] A. Manthiram, X. Yu and S. Wang, *Nat. Rev. Mater.*, 2017, **2**, 16103.

[7] V. Thangadurai, S. Narayanan and D. Pinzaru, *Chem. Soc. Rev.*, 2014, **43**, 4714–4727.

[8] J. C. Bachman, S. Muy, A. Grimaud, H.-H. Chang, N. Pour, S. F. Lux, O. Paschos, F. Maglia, S. Lupart, P. Lamp, L. Giordano and Y. Shao-Horn, *Chem. Rev.*, 2016, **116**, 140–162.

[9] M. Uitz, V. Epp, P. Bottke and M. Wilkening, *J. Electroceram.*, 2017, **38**, 142–156.

[10] N. Kamaya, K. Homma, Y. Yamakawa, M. Hirayama, R. Kanno, M. Yonemura, T. Kamiyama, Y. Kato, S. Hama, K. Kawamoto and A. Mitsui, *Nat. mater.*, 2011, **10**, 682–6.

[11] A. Kuhn, M. Kunze, P. Sreeraj, H.-D. Wiemhöfer, V. Thangadurai, M. Wilkening and P. Heitjans, *Solid State Nucl. Magn. Reson.*, 2012, **42**, 2 – 8.

[12] Y. Zhu, X. He and Y. Mo, *ACS Appl. Mater. Interfaces*, 2015, **7**, 23685–23693.

[13] H.-J. Deiseroth, S.-T. Kong, H. Eckert, J. Vannahme, C. Reiner, T. Zaiß and M. Schlosser, *Angew. Chem. Int. Ed.*, 2008, **47**, 755–758.

[14] S. Boulineau, M. Courty, J.-M. Tarascon and V. Viallet, *Solid State Ionics*, 2012, **221**, 1–5.

[15] S. Boulineau, J.-M. Tarascon, J.-B. Leriche and V. Viallet, *Solid State Ionics*, 2013, **242**, 45.

[16] M. A. Kraft, S. P. Culver, M. Calderon, F. Böcher, T. Krauskopf, A. Senyshyn, C. Dietrich, A. Zevalkink, J. Janek and W. G. Zeier, *J. Am. Chem. Soc.*, 2017, **139**, 10909–10918.

[17] R. Prasada Rao and S. Adams, *Phys. Status Solidi*, 2011, **208**, 1804–1807.

[18] P. R. Rayavarapu, N. Sharma, V. K. Peterson and S. Adams, *J. Solid State Electrochem.*, 2012, **16**, 1807–1813.

[19] A. C. Luntz, J. Voss and K. Reuter, *The Journal of Physical Chemistry Letters*, 2015, **6**, 4599–4604.

[20] Y. Kato, S. Shiotani, K. Morita, K. Suzuki, M. Hirayama and R. Kanno, *J. Phys. Chem. Lett.*, 2018, **9**, 607–613.

[21] Y. Kato, S. Hori, T. Saito, K. Suzuki, M. Hirayama, A. Mitsui, M. Yonemura, H. Iba and R. Kanno, *Nat. Energy*, 2016, **1**, 16030.

[22] J. Schnell, T. Günther, T. Knoche, C. Vieider, L. Köhler, A. Just, M. Keller, S. Passerini and G. Reinhart, *J. Power Sources*, 2018, **382**, 160 – 175.

[23] F. Han, J. Yue, X. Zhu and C. Wang, *Adv. Energy Mater.*, 2018, **8**, 1703644.

[24] B. Wu, S. Wang, W. J. Evans IV, D. Z. Deng, J. Yang and J. Xiao, *J. Mater. Chem. A*, 2016, **4**, 15266–15280.

[25] R. Koerver, I. Aygün, T. Leichtweiß, C. Dietrich, W. Zhang, J. O. Binder, P. Hartmann, W. G. Zeier and J. Janek, *Chem. Mater.*, 2017, **29**, 5574–5582.

[26] F. Han, T. Gao, Y. Zhu, K. J. Gaskell and C. Wang, *Adv. Mater.*, 2015, **27**, 3473–3483.

[27] F. Hao, F. Han, Y. Liang, C. Wang and Y. Yao, *MRS Bull.*, 2018, **43**, 775–781.

[28] W. Zhang, D. A. Weber, H. Weigand, T. Arlt, I. Manke, D. Schröder, R. Koerver, T. Leichtweiss, P. Hartmann, W. G. Zeier and J. Janek, *ACS Appl. Mater. Interfaces*, 2017, **9**, 17835–17845.

[29] S. Yu, R. D. Schmidt, R. Garcia-Mendez, E. Herbert, N. J. Dudney, J. B. Wolfenstine, J. Sakamoto and D. J. Siegel, *Chem. Mater.*, 2016, **28**, 197–206.

[30] S. Teragawa, K. Aso, K. Tadanaga, A. Hayashi and M. Tatsumisago, *J. Mater. Chem. A*, 2014, **2**, 5095–5099.

[31] Z. Liu, W. Fu, E. A. Payzant, X. Yu, Z. Wu, N. J. Dudney, J. Kiggans, K. Hong, A. J. Rondinone and C. Liang, *J. Am. Chem. Soc*, 2013, **135**, 975–978.

[32] W. Zhou, S. Wang, Y. Li, S. Xin, A. Manthiram and J. B. Goodenough, *J. Am. Chem. Soc.*, 2016, **138**, 9385–9388.

[33] S. Ohta, J. Seki, Y. Yagi, Y.and Kihira and T. Tani, T. andAsaoka, *J. Power Sources*, 2014, **265**, 40–44.

[34] Y. J. Nam, S.-J. Cho, D. Y. Oh, J.-M. Lim, S. Y. Kim, J. H. Song, Y.-G. Lee, S.-Y. Lee and Y. S. Jung, *Nano Lett.*, 2015, **15**, 3317–3323.

[35] N. Riphaus, P. Strobl, S. J. Sedlmaier, J. Schnell, H. A. Gasteiger and B. Stiaszny, *Meeting Abstracts*, 2018, **MA2018-02**, 323.

[36] D. Y. Oh, D. H. Kim, S. H. Jung, J.-G. Han, N.-S. Choi and Y. S. Jung, *J. Mater. Chem. A*, 2017, **5**, 20771–20779.

[37] D. R. U. W.D. Kingery, H.K. Bowen, *Introduction to Ceramics*, Wiley-Interscience, 1976.

[38] G. W. V. Cave, C. L. Raston and J. L. Scott, *Chem. Commun.*, 2001, 2159–2169.

[39] G. Rothenberg, A. P. Downie, C. L. Raston and J. L. Scott, *J. Am. Chem. Soc.*, 2001, **123**, 8701–8708.

[40] T. Luty and C. J. Eckhardt, *J. Am. Chem. Soc.*, 1995, **117**, 2441–2452.

[41] M. D. Cohen, G. M. J. Schmidt and F. I. Sonntag, *J. Chem. Soc.*, 1964, 2000–2013.

[42] F. Preishuber-Pflügl and M. Wilkening, *Dalton Trans.*, 2016, **45**, 8675–8687.

[43] V. Šepelák, A. Düvel, M. Wilkening, K.-D. Becker and P. Heitjans, *Chem. Soc. Rev.*, 2013, **42**, 7507–7520.

[44] P. Balaz, *Mechanochemistry in Nanoscience and Minerals Engineering*, Springer-Verlag Berlin Heidelberg, 2008.

[45] A. Düvel, J. Bednarcik, V. Šepelák and P. Heitjans, *J. Phys. Chem. C*, 2014, **118**, 7117–7129.

[46] C. Suryanarayana, *Prog. Mater Sci.*, 2001, **46**, 1 – 184.

[47] R. Pampuch, *An Introduction to Ceramics*, Springer, 2013.

[48] W. C. R. Riedel, *Ceramics Science and Technology*, WILEY-VCH Verlag, 2012.

[49] S.-J. L. Kang and Y.-I. Jung, *Acta Mater.*, 2004, **52**, 4573–4578.

[50] T. Gladman, *The theory of abnormal grain growth in steels*, Springer, 1992.

[51] P. Rios, *Acta Mater.*, 1997, **45**, 1785 – 1789.

[52] S. G. Kim and Y. B. Park, *Acta Mater.*, 2008, **56**, 3739 – 3753.

[53] H.-W. Kim, Y.-H. Koh, Y.-M. Kong, J.-G. Kang and H.-E. Kim, *J. Mater. Sci.*, 2004, **15**, 1129–1134.

[54] D. P. R. Fernandez-Prini, A.H. Harvey, *Aqueous Systems at Elevated Temperatures and Pressures*, Academic Press, 2004.

[55] W. Suchanek and R. Riman, *Adv. Sci. Technol.*, 2006, **45**, 184–193.

[56] Y. Ren, K. Chen, R. Chen, T. Liu, Y. Zhang and C.-W. Nan, *J. Am. Ceram. Soc.*, 2015, **98**, 3603–3623.

[57] S. W. Martin, *J. Am. Ceram. Soc.*, 1991, **74**, 1767–1784.

[58] M. K. MURTHY and J. AGUAYO, *J. Am. Ceram. Soc.*, 1964, **47**, 444–447.

[59] O. K., *Phys. Chem. Glasses*, 1966, **7**, 29–37.

[60] W. Widanarto, A. Ramdhan, S. Ghoshal, M. Effendi, W. Cahyanto and Warsito, *Results Phys.*, 2017, **7**, 2277 – 2280.

[61] C.-H. Lee, K. Joo, J. Kim, S. Woo, H.-J. Sohn, T. Kang, Y. Park and J. Oh, *Solid State Ionics*, 2002, **149**, 59 – 65.

[62] I. Raistrick, C. Ho and R. Huggins, *Mater. Res. Bull.*, 1976, **11**, 953 – 957.

[63] H.-P. Hong, *Mater. Res. Bull.*, 1978, **13**, 117 – 124.

[64] J. Kuwano and A. West, *Mater. Res. Bull.*, 1980, **15**, 1661 – 1667.

[65] S. Lunghammer, D. Prutsch, S. Breuer, D. Rettenwander, I. Hanzu, Q. Ma, F. Tietz and M. Wilkening, *SSRN Electronic Journal*, 2018.

[66] A. M. Glass, K. Nassau and T. J. Negran, *J. Appl. Phys.*, 1978, **49**, 4808–4811.

[67] A. Sakuda, H. Kitaura, A. Hayashi, K. Tadanaga and M. Tatsumisago, *Electrochem. Solid-State Lett.*, 2008, **11**, A1–A3.

[68] P. Bruce and A. West, *J. Solid State Chem.*, 1982, **44**, 354 – 365.

[69] P. Knauth, *Solid State Ionics*, 2009, **180**, 911 – 916.

[70] P. Maldonado-Manso, E. R. Losilla, M. Martínez-Lara, M. A. G. Aranda, S. Bruque, F. E. Mouahid and M. Zahir, *Chem. Mater.*, 2003, **15**, 1879–1885.

[71] H. Xie, Y. Li and J. B. Goodenough, *RSC Adv.*, 2011, **1**, 1728–1731.

[72] Y. Maruyama, S. Minamimure, C. Kobayashi, M. Nagao, S. Watauchi and I. Tanaka, *R. Soc. Open Sci*, 2018, **5**, 181445.

[73] R. Murugan, V. Thangadurai and W. Weppner, *Angew. Chem. Int. Ed.*, 2007, **46**, 7778–7781.

[74] J. Goodenough, H.-P. Hong and J. Kafalas, *Mater. Res. Bull.*, 1976, **11**, 203 – 220.

[75] J. E. Iglesias, J. Sanz, A. Martínez-Juárez and J. M. Rojo, *J. Solid State Chem.*, 1997, **130**, 322 – 326.

[76] M. Subramanian, R. Subramanian and A. Clearfield, *Solid State Ionics*, 1986, **18-19**, 562 – 569.

[77] Y. Li, W. Zhou, S. Xin, S. Li, J. Zhu, X. Lü, Z. Cui, Q. Jia, J. Zhou, Y. Zhao and J. B. Goodenough, *Angew. Chem. Int. Ed.*, 2016, **55**, 9965–9968.

[78] Y. Liu, J. Chen and J. Gao, *Solid State Ionics*, 2018, **318**, 27 – 34.

[79] B. Yan, Y. Zhu, F. Pan, J. Liu and L. Lu, *Solid State Ionics*, 2015, **278**, 65–68.

[80] S. Geller, *Solid Electrolytes*, Springer-Verlag Berlin Heidelberg, 1977.

[81] A. Manthiram, X. Yu and S. Wang, *Nat. Rev. Mater.*, 2017, **2**, 16103.

[82] S. Hoshino, T. Sakuma and Y. Fujii, *J. Phys. Soc. Jpn.*, 1979, **47**, 1252–1259.

[83] C. R. Schlaikjer and C. C. Liang, *J. Electrochem. Soc.*, 1971, **118**, 1447–1450.

[84] C. C. Liang, *J. Electrochem. Soc.*, 1973, **120**, 1289–1292.

[85] X. Lü, J. W. Howard, A. Chen, J. Zhu, S. Li, G. Wu, P. Dowden, H. Xu, Y. Zhao and Q. Jia, *Adv. Sci.*, 2016, **3**, 1500359.

[86] K. Kim and D. J. Siegel, *J. Mater. Chem. A*, 2019, **7**, 3216–3227.

[87] V. M. Goldschmidt, *Naturwissenschaften*, 1926, **14**, 477–485.

[88] K. Kim and D. J. Siegel, *J. Mater. Chem. A*, 2019, **7**, 3216–3227.

[89] M. H. Braga, J. A. Ferreira, V. Stockhausen, J. E. Oliveira and A. El-Azab, *J. Mater. Chem. A*, 2014, **2**, 5470–5480.

[90] Z. D. Hood, H. Wang, A. Samuthira Pandian, J. K. Keum and C. Liang, *J. Am. Chem. Soc.*, 2016, **138**, 1768–1771.

[91] M. H. Braga, N. S. Grundish, A. J. Murchison and J. B. Goodenough, *Energy Environ. Sci.*, 2017, **10**, 331–336.

[92] K. Hippler, S. Sitta, P. Vogt and H. Sabrowsky, *Acta Crystallogr., Sect. C: Cryst. Struct. Commun.*, 1990, **46**, 736–738.

[93] I. Hanghofer, G. J. Redhammer, S. Rohde, I. Hanzu, A. Senyshyn, H. M. R. Wilkening and D. Rettenwander, *Chem. Mater.*, 2018, **30**, 8134–8144.

[94] L. Zhou, K.-H. Park, X. Sun, F. Lalère, T. Adermann, P. Hartmann and L. F. Nazar, *ACS Energy Lett.*, 2019, **4**, 265–270.

[95] A.-Y. Song, Y. Xiao, K. Turcheniuk, P. Upadhya, A. Ramanujapuram, J. Benson, A. Magasinski, M. Olguin, L. Meda, O. Borodin and G. Yushin, *Adv. Energy Mater.*, 2018, **8**, 1700971.

[96] S. Chen, D. Xie, G. Liu, J. P. Mwizerwa, Q. Zhang, Y. Zhao, X. Xu and X. Yao, *Energy Storage Mater.*, 2018, **14**, 58 – 74.

[97] L. Zhou, K.-H. Park, X. Sun, F. Lalère, T. Adermann, P. Hartmann and L. F. Nazar, *ACS Energy Lett.*, 2019, **4**, 265–270.

[98] D. Prutsch, B. Gadermaier, H. Brandstätter, V. Pregartner, B. Stanje, D. Wohlmuth, V. Epp, D. Rettenwander, I. Hanzu and H. M. R. Wilkening, *Chem. Mater.*, 2018, **30**, 7575–7586.

[99] J. Lau, R. H. DeBlock, D. M. Butts, D. S. Ashby, C. S. Choi and B. S. Dunn, *Adv. Energy Mater.*, 2018, **8**, 1800933.

[100] R. Kanno and M. Murayama, *J. Electrochem. Soc.*, 2001, **148**, A742–A746.

[101] H. Wada, M. Menetrier, A. Levasseur and P. Hagenmuller, *Mater. Res. Bull.*, 1983, **18**, 189 – 193.

[102] K. Hirai, M. Tatsumisago and T. Minami, *Solid State Ionics*, 1995, **78**, 269 – 273.

[103] T. Minami, A. Hayashi and M. Tatsumisago, *Solid State Ionics*, 2006, **177**, 2715 – 2720.

[104] M. Tatsumisago, F. Mizuno and A. Hayashi, *J. Power Sources*, 2006, **159**, 193 – 199.

[105] J. Trevey, J. S. Jang, Y. S. Jung, C. R. Stoldt and S.-H. Lee, *Electrochem. Commun.*, 2009, **11**, 1830 – 1833.

[106] D. Wohlmuth, V. Epp and M. Wilkening, *ChemPhysChem*, 2015, **16**, 2582–2593.

[107] S. Hori, K. Suzuki, M. Hirayama, Y. Kato, T. Saito, M. Yonemura and R. Kanno, *Faraday Discuss.*, 2014, **176**, 83–94.

[108] Y. Wang, W. D. Richards, S. P. Ong, L. J. Miara, J. C. Kim, Y. Mo and G. Ceder, *Nat. Mater.*, 2015, **14**, 1026–1031.

[109] Y. Inoue, K. Suzuki, N. Matsui, M. Hirayama and R. Kanno, *J. Solid State Chem.*, 2017, **246**, 334 – 340.

[110] Z. Zhu, I.-H. Chu, Z. Deng and S. P. Ong, *Chem. Mater.*, 2015, **27**, 8318–8325.

[111] H.-J. Deiseroth, J. Maier, K. Weichert, V. Nickel, S.-T. Kong and C. Reiner, *Z. anorg. allg. Chem.*, 2011, **637**, 1287–1294.

[112] J. Auvergniot, A. Cassel, D. Foix, V. Viallet, V. Seznec and R. Dedryvère, *Solid State Ionics*, 2017, **300**, 78 – 85.

[113] G. K. G.E. Murch, *Phase Transformations in Materials*, Wiley-VCH Verlag GmbH, 2001.

[114] J. K. P. Heitjans, *Diffusion in condensed matter - Methods, Materials, Models*, Springer, 2005.

[115] H. Mehrer, *Diffusion in Solids.*, Springer, Berlin, 2006.

[116] A. Fick, *Ann. Phys.*, 1855, **170**, 59–86.

[117] A.Einstein, *Ann. Phys.*, 1905, **322**, 549–560.

[118] M. von Smoluchowski, *Ann. Phys.*, 1906, **326**, 756–780.

[119] A.-R. G. und B. Blümich, *Introduction to Solid-State NMR*, Springer-Verlag Berlin Heidelberg, Berlin, 1994.

[120] A. D. SMIGELSKAS, *Trans. AIME*, 1947, **171**, 130–142.

[121] L. S. Darken, *Trans. AIME*, 1948, **175**, 184–201.

[122] D. Schwarzenbach, *Kristallographie*, Springer-Verlag Berlin Heidelberg, Berlin, 2001.

[123] A. R. West, *Solid State Chemistry and Its Applications*, Wiley-VCH Verlag GmbH, 2014.

[124] W. Borchardt-Ott, *Kristallographie - Eine Einführung für Naturwissenschaftler*, Springer-Verlag Berlin Heidelberg, Berlin, 2009.

[125] P. Z. V. K. Pecharsky, *Fundamentals of Powder Diffraction and Structural Characterization of Materials*, Springer-Verlag, 2009.

[126] R. Guinebretiere, *X-ray Diffraction by Polycrystalline Materials*, ISTE, 2007.

[127] L. M. W. David, K. Shankland, *Structure Determination from Powder Diffraction Data*, Oxford Press, 2002.

[128] L. J.I. and L. D., *Reports on Progress in Physics*, 1996, **59**, 131–234.

[129] Z. W. H., *J. Chem. Phys.*, 1948, **16**, 254–254.

[130] G. Caglioti, A. Paoletti and F. P. Ricci, *Nucl. Instrum.*, 1958, **3**, 223–228.

[131] A. A. Coelho, *J. Appl. Crystallogr.*, 2003, **36**, 86–95.

[132] P.-E. Werner, L. Eriksson and M. Westdahl, *J. Appl. Crystallogr.*, 1985, **18**, 367–370.

[133] A. Boultif and D. Louër, *J. Appl. Crystallogr.*, 1991, **24**, 987–993.

[134] H. M. Rietveld, *J. Appl. Crystallogr.*, 1969, **2**, 65–71.

[135] A. A. Coelho, *J. Appl. Crystallogr.*, 2000, **33**, 899–908.

[136] J. Rodriguez-Carvajal, satellite meeting on powder diffraction of the XV congress of the IUCr, 1990.

[137] C. Yu, *Doctoral Thesis*, 2017.

[138] C. J. H. Erich H. Kisi, *Applications of Neutron Powder Diffraction*, Oxford Press, 2008.

[139] V. Lvovich, *Impedance Spectroscopy*, John Wiley and Sons, 2012.

[140] M. Levitt, *Spin Dynamics*, John Wiley and Sons Ltd, 2008.

[141] E. B. und J.R. Macdonald, *Impedance Spectroscopy*, John Wiley and Sons, 2017.

[142] M. Alim, *Immitance Spectroscopy*, John Wiley and Sons, 2017.

[143] J. C. Dyre, P. Maass, B. Roling and D. L. Sidebottom, *Rep. Prog. Phys.*, 2009, **72**, 046501.

[144] J. T. S. Irvine, D. C. Sinclair and A. R. West, *Adv. Mater.*, 1990, **2**, 132–138.

[145] J. C. Kimball and L. W. Adams, *Phys. Rev. B*, 1978, **18**, 5851–5858.

[146] A. Jonscher, *Nature*, 1977, **267**, 673–679.

[147] W. K. Lee, J. F. Liu and A. S. Nowick, *Phys. Rev. Lett.*, 1991, **67**, 1559–1561.

[148] D. L. Sidebottom, P. F. Green and R. K. Brow, *Phys. Rev. Lett.*, 1995, **74**, 5068–5071.

[149] A. K. Rizos, J. Alifragis, K. L. Ngai and P. Heitjans, *J. Chem. Phys.*, 2001, **114**, 931–934.

[150] B. Roling, M. Meyer, A. Bunde and K. Funke, *J. Non-Cryst. Solids*, 1998, **226**, 138 – 144.

[151] F. Preishuber-Pflügl, P. Bottke, V. Pregartner, B. Bitschnau and M. Wilkening, *Phys. Chem. Chem. Phys.*, 2014, **16**, 9580–9590.

[152] B. Gadermaier, B. Stanje, A. Wilkening, I. Hanzu, P. Heitjans and H. M. R. Wilkening, *J. Phys. Chem. C*, 0, **0**, null.

[153] I. Hanghofer, M. Brinek, S. Eisbacher, B. Bitschnau, M. Volck, V. Hennige, I. Hanzu, D. Rettenwander and M. Wilkening, *Phys. Chem. Chem. Phys.*, 2019, –.

[154] W. Nernst, *Z. Phys. Chem*, 1888, 613–637.

[155] A. Einstein, *Zeitschrift für Elektrochemie und angewandte physikalische Chemie*, 1908, **14**, 235–239.

[156] A. Abragam, *Principles of Nuclear Magnetism*, Oxford University Press, New York, 1966.

[157] H. Friebolin, *Basic One- and Two-Dimensional NMR Spectroscopy*, Wiley-VCH Verlag, 2011.

[158] J. Keeler, *Understanding NMR Spectroscopy*, John Wiley and Sons Ltd, Chichester, 2010.

[159] N. Bloembergen, E. M. Purcell and R. V. Pound, *Phys. Rev.*, 1948, **73**, 679–712.

[160] M. Meyer, P. Maass and A. Bunde, *Phys. Rev. Lett.*, 1993, **71**, 573–576.

[161] V. Epp, z. Gün, H.-J. Deiseroth and M. Wilkening, *J. Phys. Chem. Lett.*, 2013, **4**, 2118–2123.

[162] M. Wilkening, D. Bork, S. Indris and P. Heitjans, *Phys. Chem. Chem. Phys.*, 2002, **4**, 3246–3251.

[163] J. R. Hendrickson and P. J. Bray, *J. Magn. Reson.*, 1973, **9**, 341–357.

[164] J. R. Hendrickson and P. J. Bray, *J. Chem. Phys.*, 1974, **61**, 2754–2764.

[165] H. W. Spiess, *J. Chem. Phys.*, 1980, **72**, 6755–6762.

[166] M. Lausch and H. Spiess, *J. Magn. Reson.*, 1983, **54**, 466 – 479.

[167] M. Wilkening, W. Küchler and P. Heitjans, *Phys. Rev. Lett.*, 2006, **97**, 065901.

[168] A. Kuhn, V. Epp, G. Schmidt, S. Narayanan, V. Thangadurai and M. Wilkening, *J. Phys.: Condens. Matter*, 2011, **24**, 035901.

[169] J. Jeener and P. Broekaert, *Phys. Rev.*, 1967, **157**, 232–240.

[170] *Stimulated Echo*, http://mriquestions.com/stimulated-echoes.html, Accessed: 2019-04-08.

[171] B. Ruprecht, H. Billetter, U. Ruschewitz and M. Wilkening, *J. Phys.: Condens. Matter*, 2010, **22**, 245901.

[172] T. Polenova, R. Gupta and A. Goldbourt, *Anal. Chem.*, 2015, **87**, 5458–5469.

[173] A. Alia, S. Ganapathy and H. J. M. de Groot, *Photosynth. Res.*, 2009, **102**, 415.

[174] B. Lang, B. Ziebarth and C. Elsässer, *Chem. Mater.*, 2015, **27**, 5040–5048.

[175] H. El-Shinawi, C. Greaves and J. Janek, *RSC Adv.*, 2015, **5**, 17054–17059.

[176] H. Barlage and H. Jacobs, *Z. anorg. allg. Chem.*, 1994, **620**, 471–474.

[177] H. Yamane, M. Shibata, Y. Shimane, T. Junke, Y. Seino, S. Adams, K. Minami, A. Hayashi and M. Tatsumisago, *Solid State Ionics*, 2007, **178**, 1163 – 1167.

[178] Y. Seino, T. Ota, K. Takada, A. Hayashi and M. Tatsumisago, *Energy Environ. Sci.*, 2014, **7**, 627–631.

[179] I.-H. Chu, H. Nguyen, S. Hy, Y.-C. Lin, Z. Wang, Z. Xu, Z. Deng, Y. S. Meng and S. P. Ong, *ACS Appl. Mater. Interfaces*, 2016, **8**, 7843–7853.

[180] N. J. J. de Klerk, I. Rosłoń and M. Wagemaker, *Chem. Mater.*, 2016, **28**, 7955–7963.

[181] D. Liu, W. Zhu, Z. Feng, A. Guerfi, A. Vijh and K. Zaghib, *Mater. Sci. Eng. C*, 2016, **213**, 169 – 176.

[182] S. Chen, D. Xie, G. Liu, J. P. Mwizerwa, Q. Zhang, Y. Zhao, X. Xu and X. Yao, *Energy Storage Mater*, 2018, **14**, 58 – 74.

[183] Y. Kato, S. Hori, T. Saito, K. Suzuki, M. Hirayama, A. Mitsui, M. Yonemura, H. Iba and R. Kanno, *Nat. Energy*, 2016, **1**, 16030.

[184] Z. Liu, W. Fu, E. A. Payzant, X. Yu, Z. Wu, N. J. Dudney, J. Kiggans, K. Hong, A. J. Rondinone and C. Liang, *J. Am. Chem. Soc.*, 2013, **135**, 975–978.

[185] Y. Zhu, X. He and Y. Mo, *Adv. Sci.*, 2017, **4**,.

[186] C. Dietrich, D. A. Weber, S. Culver, A. Senyshyn, S. J. Sedlmaier, S. Indris, J. Janek and W. G. Zeier, *Inorg. Chem.*, 2017, **56**, 6681–6687.

[187] S.-T. Kong, H.-J. Deiseroth, C. Reiner, z. Gün, E. Neumann, C. Ritter and D. Zahn, *Chem. Eur. J.*, 2010, **16**, 2198–2206.